Theoretical investigations for testing the fundamental symmetries of the Standard Model with diatomic molecules

Hao, Yongliang

DOI:
10.33612/diss.127488441

Theoretical investigations for testing the fundamental symmetries of the Standard Model with diatomic molecules

Yongliang Hao

university of groningen

faculty of science and engineering

Van Swinderen Institute PhD series 2020

ISBN: 978-94-034-2717-1 (printed version)
ISBN: 978-94-034-2718-8 (electronic version)

The work described in this thesis was performed at the Van Swinderen Institute for Particle Physics and Gravity of the University of Groningen.

university of groningen

Theoretical investigations for testing the fundamental symmetries of the Standard Model with diatomic molecules

PhD thesis

to obtain the degree of PhD at the
University of Groningen
on the authority of the
Rector Magnificus Prof. C. Wijmenga
and in accordance with
the decision by the College of Deans.

This thesis will be defended in public on

Tuesday 23 June 2020 at 12:45 hours

by

Yongliang Hao

born on 20 January 1987
in Shandong, China

Supervisors
Dr. A. Borschevsky
Prof. R. G. E. Timmermans

Assessment committee
Prof. J. Berengut
Prof. R. Broer
Prof. A. Zaitsevskii

Contents

1 Introduction **1**

2 The Standard Model and fundamental symmetries **12**
2.1 Overview 12
2.2 The Standard Model 13
2.3 Fundamental symmetries 16
2.3.1 Continuous symmetries 16
2.3.2 Discrete symmetries 16
2.3.3 Charge conjugation symmetry 17
2.3.4 Parity (space inversion symmetry) 18
2.3.5 Time reversal symmetry 19
2.3.6 $\hat{\mathcal{C}}\hat{\mathcal{P}}$ and $\hat{\mathcal{C}}\hat{\mathcal{P}}\hat{\mathcal{T}}$ 20
2.4 $\hat{\mathcal{P}}$ violation 21
2.4.1 Nuclear spin-independent parity violating interaction 23
2.4.2 Nuclear spin-dependent parity violating interaction 24
2.5 $\hat{\mathcal{C}}\hat{\mathcal{P}}$ violation 26
2.6 Variation of fundamental constants 29

3 Computational methods **37**
3.1 Overview 37
3.2 Hamiltonian 38
3.3 Basis sets 41
3.4 Computational methods and electron correlation 43
3.4.1 Dirac-Hartree-Fock method 44
3.4.2 Density Functional Theory 48
3.4.3 Second order Möller-Plesset method 49
3.4.4 Single reference coupled cluster method 50
3.4.5 CCSD(T) 55
3.4.6 Fock-space coupled cluster method 56
3.5 Finite field approach 58

3.6 Uncertainty evaluation 59

4 Molecular structure **68**
4.1 Overview 68
4.2 Molecular symbols 69
4.3 External fields 70
4.4 Born-Oppenheimer approximation 71
4.5 Effective Hamiltonian 72
4.6 Hund's coupling cases 73
4.6.1 Case (a) 74
4.6.2 Case (b) 74
4.6.3 Case (c) 75
4.6.4 Case (d) 75
4.7 Symmetry properties of diatomic molecules 76
4.8 Franck-Condon approximation 78

5 Symmetry-breaking effects and new phenomena **84**
5.1 Overview 84
5.2 Nuclear anapole moment effect 84
5.3 Search for the eEDM and spectroscopic constants 88
5.4 Search for the variation of fundamental constants 91

6 Nuclear anapole moment effect in BaF **98**
6.1 Motivation 98
6.2 Method and computational details 101
6.3 Results and discussion 104
6.4 Conclusions 110

7 Nuclear anapole moment effect in BeCl **119**
7.1 Motivation 119
7.2 Method and computational details 121
7.3 Results and conclusions 122

8 Molecular spectra and structure for eEDM measurements **128**
8.1 Motivation 128
8.2 Previous investigations 130
8.3 Methods 132
8.4 Results and discussion 140
8.4.1 Potential energy curves 140
8.4.2 Spectroscopic constants 140
8.4.3 Frank-Condon factors 142
8.4.4 Static and transition dipole moments 143

8.4.5 Lifetimes of excited states . . . 146
8.5 Impact on laser-cooling . . . 147
8.6 Conclusion . . . 150

9 Variation of fundamental constants **168**
9.1 Motivation . . . 168
9.2 Diatomic results . . . 169
9.3 Solid state results . . . 172
9.4 Conclusion . . . 177

10 Conclusion and Outlook **185**

Appendix A: Dunham expansion **193**

Appendix B: Units **196**

Acknowledgement **197**

Publications **198**

Samenvatting **199**

Chapter 1

Introduction

The Standard Model (SM) of particle physics [1] has achieved great success in describing the fundamental particles and three of the fundamental interactions such as the strong, weak, and electromagnetic interactions. In the SM, the fundamental building blocks of matter, namely fermionic fields including quarks and leptons, can be categorized into three generations and their interactions are mediated by gauge bosons, which can be accommodated into the $SU(3)_c \times SU(2)_L \times U(1)_Y$ gauge group. The discovery of the top quark [2, 3] marks the completeness of the three generation structure of quarks and leptons. In addition, in order to account for the non-zero particle masses, the Higgs mechanism is introduced into the model, where particles acquire masses through their coupling with the Higgs field after the spontaneous breaking of the electroweak symmetry from higher to lower symmetry. Although the discovery of the SM-like Higgs boson [4–6] indicates one of the top achievements of particle physics, there are still many open questions that cannot be explained by the SM. To begin with, in the SM, there are three flavors (types) of neutrinos such as electron-type neutrino, muon-type neutrino, and tau-type neutrino. Neutrino flavor oscillation, which has been confirmed by a variety of experiments, refers to the phenomenon that neutrino flavor can change from one type to another type when neutrino propagates through space. Such phenomenon indicates that neutrinos have mixing among flavors[a] and at least one type of neutrino is massive. However, in the SM, neutrinos are assumed to be massless. In order to account for the nonzero neutrino masses, the SM has to be modified. Furthermore, the dark matter and dark energy problem is one of the biggest challenges we are facing nowadays. Fig. 1.1 shows our current

[a]The neutrino mixing matrix is known as the Pontecorvo–Maki–Nakagawa–Sakata (PMNS) matrix. The complex phase of the PMNS matrix is one of the possible contributions to $\hat{\mathcal{C}}\hat{\mathcal{P}}$ violation (see e.g. Ref. [7]).

knowledge concerning the composition of the Universe. A variety of astrophysical observations have shown that our Universe is dominated by dark matter and dark energy and more than $\sim 80\%$ of the matter in our Universe is composed of dark matter [8, 9]. Dark matter is a type of matter, which barely interacts with ordinary matter via the SM interactions including the strong, weak, and electromagnetic interactions, except via gravity. However, there are no candidates for dark matter in the SM, and a direct detection of dark matter particles has been unsuccessful so far. This is well known as the dark matter problem. Astrophysical observations have shown that our Universe is expanding at an accelerating rate, which indicates the existence of some unknown form of energy, namely dark energy. Although it is believed that the large scale structure of our Universe is dominated by dark energy, the nature of dark energy is still a puzzle. In addition, matter and antimatter asymmetry refers to the observed excess of matter over antimatter in our Universe. However, according to the Big Bang theory, equal amounts of matter and antimatter should have been created in the early Universe. The matter and antimatter asymmetry is also one of the greatest mysteries that cannot be explained by the SM. Last but not least, gravity, as one of the four fundamental interactions, cannot be compatibly incorporated into the framework of the SM. Although almost all the observed gravitational effects can be well described by General Relativity (GR), it is believed that the ultimate theory of gravity should be a quantum field theory, namely quantum gravity [10]. The unification of gravity with the non-gravitational fundamental interactions in the framework of quantum field theory is one of the most challenging problems in modern physics. In short, due to the above-mentioned problems, the SM is considered as an incomplete theory.

In order to solve the problems, many new physics theories (models), such as extra-dimensional theories [12], super-symmetric (SUSY) theories [13, 14], left-right symmetric theories [14], grand unified theories [14], etc., that extend the SM have been mathematically constructed and intensively explored in a wide variety of experiments over the past decades. Recent developments in experimental facilities at the high-energy and high-precision frontier have a significant impact on the searches for new physics beyond the SM. The extra-dimensional theories predict that, in addition to the conventional $(3 + 1)$ spacetime, there may exist extra space or time dimensions. The supersymmetric theories propose new interactions described by the symmetry between fermions and bosons, assuming that each fermion (boson) has an associated boson (fermion), which is called superpartner. In the left-right symmetric models, besides the symmetry between the left handed fermions, a new symmetry between the right handed fermions is also implemented into the model. The grand unified theories suggest that, at high energies, the three fundamental interactions of the SM can be unified into a single interaction, which can be described by the gauge groups with higher

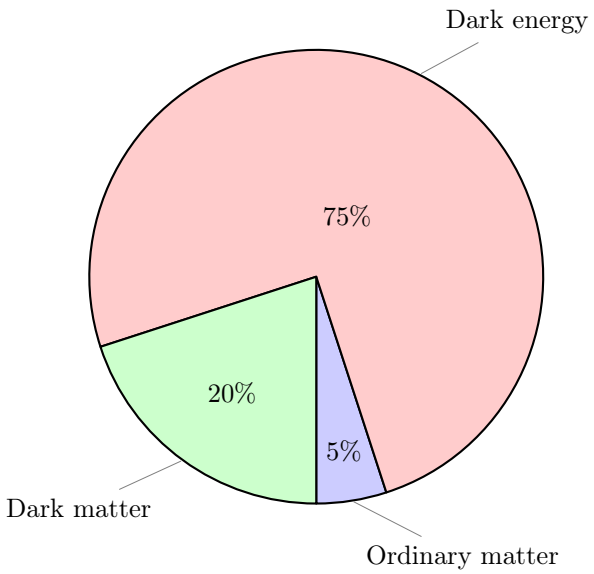

Figure 1.1: Composition of the Universe [11].

symmetry than the conventional $SU(3)_c \times SU(2)_L \times U(1)_Y$ group. Moreover, in order to unify gravity with the remaining fundamental interactions, some other new physics theories, such as quantum gravity and string theory, have also been proposed. The construction of quantum gravity opens a promising window for the unification of all fundamental interactions. All these theories attempt to answer the unresolved problems of the SM. However, unlike the SM, no statistically significant sign of such new physics theories has been confirmed so far.

Compared with the SM, many new physics theories are characterized by more significant symmetry-breaking effects, which can be categorized into the two main classes, depending on whether the symmetries are discrete or continuous. For the former cases, we are interested in the effects related to the breaking of charge conjugation symmetry ($\hat{\mathcal{C}}$), parity ($\hat{\mathcal{P}}$), time reversal symmetry ($\hat{\mathcal{T}}$), $\hat{\mathcal{C}}\hat{\mathcal{P}}$ symmetry, etc. Among such effects, the searches for a non-zero electron electric dipole moment (eEDM) have attracted an enormous level of attention recently. The existence of a non-zero eEDM violates the $\hat{\mathcal{P}}$ and $\hat{\mathcal{T}}$ symmetries. A nonzero eEDM in the SM arises from multi-loop diagrams and thus is greatly suppressed. At the four-loop level, it is estimated to be around the order of 10^{-38} e·cm [15], which is much lower than the present experimental sensitivity. However, in some extensions to the SM, such as the left-right symmetric models, SUSY, etc. [16], the predicted value of the eEDM is in the range from the order of 10^{-27} to the

order of 10^{-30} e·cm [17–22], which is several orders of magnitude higher than that of the SM, possibly leading to an observable effect. According to the $\hat{\mathcal{C}}\hat{\mathcal{P}}\hat{\mathcal{T}}$ theorem, a non-zero eEDM also suggests $\hat{\mathcal{C}}\hat{\mathcal{P}}$ violation. In the SM, $\hat{\mathcal{C}}\hat{\mathcal{P}}$ violation may come from the complex phase of the quark mixing matrix[b] or may come from the θ-term in the QCD[c] Lagrangian. On the one hand, the breaking of the $\hat{\mathcal{C}}$ and $\hat{\mathcal{C}}\hat{\mathcal{P}}$ symmetries is one of the three criteria suggested by Sakharov to explain the observed matter-antimatter asymmetry in our Universe [23]. On the other hand, however, the amount of $\hat{\mathcal{C}}\hat{\mathcal{P}}$ violation in the SM is too small to account for the observed asymmetry between matter and antimatter in our Universe. In order to explain the observed matter-antimatter asymmetry, new physics models with new source of $\hat{\mathcal{C}}\hat{\mathcal{P}}$ violation need to be constructed theoretically and to be explored experimentally.

In addition to the symmetry-breaking effects, we are also interested in the search for new phenomena, such as the variation of dimensionless fundamental constants, etc. The idea of the variation of fundamental constants can be dated back to the big numbers hypothesis proposed by Dirac [24] amid speculation that the gravitational constant may depend on time [25]. Later on, this idea is generalized to the scenario that the fine structure constant α may also vary with time. Many new physics theories that extend the SM or unify all the fundamental interactions are constructed with signatures of varying fundamental constants. The search for the variation of fundamental constants might help to put constraints on such new physics theories. For example, some dark matter candidates, which are oscillating with respect to time, couple to the SM particles and thus lead to the time variation of α and μ [26]. In this case, the studies of the variation of fundamental constants can open a promising avenue for dark matter searches. Another example lies within the new physics theories featured with domain walls generated in the early Universe. Such domain walls couple to the electromagnetic field and may cause the spatial variation of α when the domain walls are passing through the Earth [27]. In this case, the searches for the spatial variation of α might be helpful for the detection of the domain walls.

From an experimental point of view, the new symmetry-breaking phenomena have been intensively investigated at the high-energy and high-precision frontier. In general, the experimental limits on such phenomena are model dependent [28]. As an important feature, parity in the weak interaction is assumed to be maximally violated (100%) due to the interaction structure where only the left-handed (right-handed) chiral components of particle (anti-particle) spinors participate in the weak interaction. The measurement of the polarized muon decay shows that the ratio of the observed parity violation to the expected parity violation is $1.00084 \pm 0.00029(\text{stat.})^{+0.00165}_{-0.00063}(\text{syst.})$ [29], which demonstrates an excellent

[b] The quark mixing matrix is known as the Cabibbo–Kobayashi–Maskawa (CKM) matrix.
[c] QCD denotes Quantum Chromodynamics.

agreement with the SM prediction. In the weak interaction, $\hat{\mathcal{C}}\hat{\mathcal{P}}$ violation has been intensively measured at the high-energy frontier after it was first discovered in the neutral kaon systems. In 2001, $\hat{\mathcal{C}}\hat{\mathcal{P}}$ violation was first established in the B meson decays by BaBar [30] and Belle [31]. In 2013, $\hat{\mathcal{C}}\hat{\mathcal{P}}$ violation was first reported in the strange B meson system. Recently, $\hat{\mathcal{C}}\hat{\mathcal{P}}$ violation was also observed in the D^0 meson decay by LHCb with the asymmetry of -15.4 ± 2.9 (stat. + syst.) $\times 10^{-4}$, which is different from zero with a significance of 5.3 σ [32]. It is believed that the $\hat{\mathcal{C}}\hat{\mathcal{P}}$ symmetry is not necessarily conserved in the strong interaction, where a generic $\hat{\mathcal{C}}\hat{\mathcal{P}}$ violating term may exist and give rise to a non-zero neutron electric dipole moment (nEDM) [33, 34]. However, no significant signal of the nEDM has been observed so far and the experimental upper limit at the 90% confidence level on the nEDM is 2.9×10^{-26} e·cm [35].

Although it is expected that symmetry-breaking effects and new physical phenomena are greatly suppressed by some powers of high-energy scale and are usually considered to be negligible at low energies, tests of fundamental symmetries and searches for new phenomena using atomic and molecular properties have attracted a great deal of attention recently [36]. The reasons why atoms and molecules have very promising applications to the tests of fundamental symmetries and searches for new phenomena can be summarized as follows. To begin with, spectroscopy with high resolution and high sensitivity has been developed enormously over the past years, enabling the observation of tiny optical effects induced by novel interactions. Furthermore, compared with high-energy colliders, the basic facility for research in atomic and molecular physics is usually much smaller, making the search for new physical phenomena in atoms and molecules a complementary and economical way of doing new physics. Thirdly, atoms and molecules have a versatile electronic structure and can be very sensitive to a variety of new physical phenomena, enabling simultaneous investigations of many different effects using a single experimental setup. Remarkably, compared with atoms and polyatomic molecules, diatomic molecules have additional significant advantages in the search for symmetry-breaking effects due to the following considerations. On the one hand, compared with atoms, diatomic molecules have very closely spaced molecular levels with opposite parity, which lead to great enhancement of tiny physical effects when the spacing between neighboring levels is close to zero, or when the external fields are applied to bring them into near degeneracy. On the other hand, compared with polyatomic molecules, the calculations on diatomic molecules are not computationally expensive, allowing highly accurate theoretical investigations. More importantly, previous studies have illustrated that, in some cases, the measurements on diatomic molecules can provide competitive or even more stringent constraints on new physics models than the ones imposed by the high-energy collider experiments. For example, a direct detection of the eEDM is probably beyond the reach of the present high-energy

experiments while it may lie within the detectable regions of the present high-precision experiments due to the significantly enhanced sensitivity in diatomic molecules. The present upper limit at the 90% confidence level on the eEDM with the ThO molecule is 1.1×10^{-29} e·cm [22], and excludes new physics below an energy scale of around 3-30 TeV, which depends on specific models but in general is beyond the detectable regions of the present experiments at the LHC. In addition to the searches for symmetry-breaking effects, atoms and molecules are also considered to be promising probes for the variation of fundamental constants. The searches for the variation of fundamental constants with respect to time and space can be performed through investigations of atomic and molecular spectra [37], including analysis of atomic clock transitions and quasar absorption spectra. On the one hand, recent developments in atomic clocks enable unprecedented level of precision with the uncertainty as low as 10^{-19} [38], allowing precise measurement of the variation of fundamental constants through a comparison of two clock transitions. For example, the experimental limit on the time variation of the constant α imposed by the analysis of atomic transitions in $^{171}Yb^{+}$ is $\dot{\alpha}/\alpha = -0.7 \pm 2.1 \times 10^{-17}$ yr^{-1} [39], which suggests that no evidence for the time variation of the fine structure constant has been observed. On the other hand, the experimental limit imposed by the observation of quasar spectra is $\Delta\alpha/\alpha = 1.2 \pm 1.7$ (stat.) ± 0.9 (syst.) ($\times 10^{-6}$) [40], which does not support the time variation of α either. Another study using the analysis of quasar spectra has reported a possible spatial variation of α with a significance of 4.2 σ [41] but this may possibly arise from undetected systematic effect. Furthermore, the study of the spectra from quasars has also placed constraints on the variation of the proton to electron mass ratio with the result of $\Delta\mu/\mu = -9.5 \pm 5.4$ (stat.) $\pm$ 5.3 (syst.) ($\times 10^{-6}$) [42]. It is worth mentioning that, similar to atoms, molecules are also considered as promising probes for the variation of α and μ, because molecular spectra are expected to be sensitive to both constants too.

Theoretical investigations of the electronic structure and molecular properties for diatomic molecules not only can help to develop an efficient experimental setup for precision measurements, but also can help to interpret the results more correctly after measurements [36]. Furthermore, powerful computational tools and methods have been developed recently, allowing us to rigorously examine electronic structure and molecular properties and to correctly understand the influence of new physics interactions on them. In some cases, they can also be used to identify promising candidates with enhanced sensitivity. In other cases, the measured quantities usually need to be combined with the calculated parameters in order to extract the final values of molecular properties from experiments, where the total uncertainty needs to be included by summing the experimental and theoretical uncertainties in quadrature. Highly accurate calculations of molecular properties and systematic evaluation of theoretical uncertainties can

help to extract the needed molecular properties precisely from the measured signals and can also help to draw conclusions reliably from experiments.

The main purpose of this work is to provide the needed molecular parameters using the state-of-the-art computational methods for successful measurements of various molecular properties and for rigorous interpretations of the results. To be more specific, we are interested in various symmetry-breaking effects arising from the nuclear anapole moment, the eEDM, etc. Among them, the parity-violating nuclear anapole moment effect in diatomic molecules can be used to test nuclear models and gain a deep understanding of nuclear structure. In order to extract the magnitude of nuclear anapole moment from measurements effectively, a $\hat{\mathcal{P}}$-odd interaction parameter W_A, which depends on molecular structure, needs to be calculated with high accuracy. In this case, it is also possible to evaluate the theoretical uncertainties arising from the imperfect or unknown information within the computational methods. The searches for the non-zero eEDM in diatomic molecules can be used as a powerful tool to place constraints on the parameter space of new physics models. A successful measurement of such effect requires the molecules to be effectively laser-cooled [43–46] so that long coherent interaction time could be reached, resulting in an increase in the measurement sensitivity [43–45]. There are a number of factors that determine whether a given molecule is suitable for laser-cooling [47]. In order to develop laser systems more efficiently throughout measurements and interpret the results more correctly after measurements, highly accurate theoretical calculations of the molecular spectroscopic constants for diatomic molecules are necessary. We are also interested in other new physical phenomena such as the variation of fundamental constants. Since a wide variety of new physics theories beyond the SM and GR are featured with the variation of fundamental constants, the searches for such new phenomena can be used to test these new physics theories. In the search for the variation of fundamental constants, we may compare the phase differences between two light beams inside a solid-state laser interferometer [48], instead of comparing two clock transition frequencies over a long period of time. The main goal of the present work is to identify promising systems that lead to great discovery potential, where the DFT calculations of solid-state properties can be employed to achieve such goal. In this case, the coupled cluster calculations of molecular properties can be used to benchmark the accuracy of the DFT calculations of solid-state properties.

This thesis is organized as follows. In Chapter 2, we briefly review some important concepts of the SM and useful aspects of fundamental symmetries therein. Then, we introduce the nature of the symmetry-breaking effects, which can be used to test the SM and search for new physics beyond the SM. In Chapter 3, the computational methods employed for the calculations of molecular properties are reviewed. We summarize the factors that determine the accuracy of the theo-

retical investigations and demonstrate the evaluation of theoretical uncertainties. In Chapter 4, we introduce some useful molecular symbols involved in this work and review the general form of the molecular Hamiltonian, which serves as the basis for the rest of the discussions. In Chapter 5, we summarize the main topics of the present work, including the measurement of symmetry-breaking effects, such as the ones associated with the nuclear anapole moment effect and the electron electric dipole moment (eEDM), and the search for new phenomena, such as the variation of fundamental constants. We address that the main purpose of this work is to provide the needed molecular parameters with the help of the state-of-the-art computational methods for successful measurements of various molecular properties and for rigorous interpretations of the measurements. In Chapter 6, we present high accuracy relativistic coupled cluster calculations of the $\hat{\mathcal{P}}$-odd interaction parameter W_A for the BaF molecule. The influence of various computational parameters on the calculated W_A parameter is analyzed. The uncertainty evaluation is also demonstrated in this chapter. In Chapter 7, we present more detail about the correlation trends of the nuclear anapole moment effect in the BeCl molecule. We highlight the importance of electron correlation in the determination of the W_A parameter by comparing the calculated results from various electron correlation approaches. In Chapter 8, we present high-accuracy theoretical investigations of the spectroscopic constants for the selected alkaline earth metal fluorides and discuss their application to laser cooling. We illustrate that in the search for the eEDM with a slow beam of the BaF molecules, knowledge of the molecular properties for BaF is needed to plan the measurements and, in particular, to determine the optimal laser-cooling schemes. In Chapter 9, we focus on the theoretical investigations of the variation of fundamental constants by examining how crystal parameters in solid-state materials and equilibrium bond distances in diatomic molecules vary with fundamental constants (α and μ). If we assume that the distance between two nearest atoms (lattice points) in a solid can be approximated by the equilibrium bond distance in a diatomic molecule formed by these two atoms, the coupled cluster calculations of the equilibrium bond distances for diatomic molecules can be used to benchmark the performance of the DFT calculations of the lattice parameters for solid-state materials. Finally, in Chapter 10, we present the conclusion for the present work and give an outlook for future work.

References

[1] M. Tanabashi, K. Hagiwara, K. Hikasa, K. Nakamura, Y. Sumino, F. Takahashi, J. Tanaka, K. Agashe, G. Aielli, C. Amsler, *et al.*, Phys. Rev. D **98**, 030001 (2018).

[2] F. Abe, H. Akimoto, A. Akopian, M. G. Albrow, S. R. Amendolia, D. Amidei, J. Antos, C. Anway-Wiese, S. Aota, G. Apollinari, *et al.*, Phys. Rev. Lett. **74**, 2626 (1995).

[3] S. Abachi, B. Abbott, M. Abolins, B. S. Acharya, I. Adam, D. L. Adams, M. Adams, S. Ahn, H. Aihara, G. Alvarez, *et al.*, Phys. Rev. Lett. **74**, 2422 (1995).

[4] G. Aad, T. Abajyan, B. Abbott, J. Abdallah, S. A. Khalek, A. A. Abdelalim, O. Abdinov, R. Aben, B. Abi, M. Abolins, *et al.*, Phys. Lett. B **716**, 1 (2012).

[5] S. Chatrchyan, V. Khachatryan, A. M. Sirunyan, A. Tumasyan, W. Adam, E. Aguilo, T. Bergauer, M. Dragicevic, J. Erö, C. Fabjan, *et al.*, Phys. Lett. B **716**, 30 (2012).

[6] S. Chatrchyan, V. Khachatryan, A. M. Sirunyan, A. Tumasyan, W. Adam, T. Bergauer, M. Dragicevic, J. Erö, C. Fabjan, M. Friedl, *et al.*, JHEP **2013**, 81 (2013).

[7] I. I. Bigi and A. I. Sanda, $\hat{\mathcal{C}}\hat{\mathcal{P}}$ *violation* (Cambridge University Press, 2009).

[8] N. Aghanim, Y. Akrami, M. Ashdown, J. Aumont, C. Baccigalupi, M. Ballardini, A. J. Banday, R. B. Barreiro, N. Bartolo, S. Basak, *et al.*, arXiv:1807.06209 (2018).

[9] N. Song and A. C. Vincent, Phys. Rev. Lett. **124**, 051801 (2020).

[10] C. Kiefer, "Why quantum gravity," in *Approaches to fundamental physics*, edited by I. Stamatescu and E. Seiler (Springer-Verlag, 2007) pp. 123–130.

[11] R. Caldwell and M. Kamionkowski, Nature **458**, 587 (2009).

[12] M. Shifman, Int. J. Mod. Phys. A **25**, 199 (2010).

[13] J. Wess and J. Bagger, *Supersymmetry and supergravity* (Princeton University Press, 1992).

[14] R. N. Mohapatra, *Unification and supersymmetry: The frontiers of quark-lepton physics* (Springer-Verlag, 2003).

[15] D. Ng and J. N. Ng, Mod. Phys. Lett. A **11**, 211 (1996).

[16] T. E. Chupp, P. Fierlinger, M. J. Ramsey-Musolf, and J. T. Singh, Rev. Mod. Phys. **91**, 015001 (2019).

[17] Y. Nakai and M. Reece, JHEP **2017**, 31 (2017).

[18] S. M. Barr, Int. J. Mod. Phys. A **8**, 209 (1993).

[19] J. Engel, M. J. Ramsey-Musolf, and U. Van Kolck, Prog. Part. Nucl. Phys. **71**, 21 (2013).

[20] M. Pospelov and A. Ritz, Ann. Phys. **318**, 119 (2005).

[21] W. Bernreuther and M. Suzuki, Rev. Mod. Phys. **63**, 313 (1991).

[22] V. Andreev and N. R. Hutzler, Nature **562**, 355 (2018).

[23] A. D. Sakharov, JETP Lett. **5**, 24 (1967).

[24] P. A. M. Dirac, Nature **139**, 323 (1937).

[25] E. Teller, Phys. Rev. **73**, 801 (1948).

[26] Y. V. Stadnik and V. V. Flambaum, Phys. Rev. Lett. **114**, 161301 (2015).

[27] K. A. Olive, M. Peloso, and J. Uzan, Phys. Rev. D **83**, 043509 (2011).

[28] S. Rappoccio, Rev. Phys. **4**, 100027 (2019).

[29] J. F. Bueno, R. Bayes, Y. I. Davydov, P. Depommier, W. Faszer, C. A. Gagliardi, A. Gaponenko, D. R. Gill, A. Grossheim, P. Gumplinger, *et al.*, Phys. Rev. D **84**, 032005 (2011).

[30] B. Aubert, D. Boutigny, J. M. Gaillard, A. Hicheur, Y. Karyotakis, J. P. Lees, P. Robbe, V. Tisserand, A. Palano, G. P. Chen, *et al.*, Phys. Rev. Lett. **87**, 091801 (2001).

[31] K. Abe, R. Abe, I. Adachi, B. S. Ahn, H. Aihara, M. Akatsu, G. Alimonti, K. Asai, M. Asai, Y. Asano, *et al.*, Phys. Rev. Lett. **87**, 091802 (2001).

[32] R. Aaij, *et al.*, Phys. Rev. Lett. **122**, 211803 (2019).

[33] P. Cea and G. Nardulli, Phys. Lett. B **144**, 115 (1984).

[34] J. F. Donoghue, E. Golowich, and B. R. Holstein, *Dynamics of the standard model* (Cambridge University Press, 2014).

[35] C. A. Baker, D. D. Doyle, P. Geltenbort, K. Green, M. G. D. Van der Grinten, P. G. Harris, P. Iaydjiev, S. N. Ivanov, D. J. R. May, J. M. Pendlebury, *et al.*, Phys. Rev. Lett. **97**, 131801 (2006).

[36] M. S. Safronova, D. Budker, D. DeMille, D. F. J. Kimball, A. Derevianko, and C. W. Clark, Rev. Mod. Phys. **90**, 025008 (2018).

[37] V. V. Flambaum, in *International Frequency Control Symposium Joint with the 21st European Frequency and Time Forum* (IEEE, 2007) pp. 342–349.

[38] E. Oelker, R. B. Hutson, C. J. Kennedy, L. Sonderhouse, T. Bothwell, A. Goban, D. Kedar, C. Sanner, J. M. Robinson, G. E. Marti, *et al.*, arXiv:1902.02741 (2019).

[39] R. M. Godun, P. B. R. Nisbet-Jones, J. M. Jones, S. A. King, L. A. M. Johnson, H. S. Margolis, K. Szymaniec, S. N. Lea, K. Bongs, and P. Gill, Phys. Rev. Lett. **113**, 210801 (2014).

[40] M. T. Murphy, A. L. Malec, and J. X. Prochaska, arXiv:1606.06293 (2016).

[41] J. K. Webb, J. A. King, M. T. Murphy, V. V. Flambaum, R. F. Carswell, and M. B. Bainbridge, Phys. Rev. Lett. **107**, 191101 (2011).

[42] J. Bagdonaite, W. Ubachs, M. T. Murphy, and J. B. Whitmore, Phys. Rev. Lett. **114**, 071301 (2015).

[43] T. A. Isaev, S. Hoekstra, and R. Berger, Phys. Rev. A **82**, 052521 (2010).

[44] T. A. Isaev and R. Berger, arXiv:1302.5682 (2013).

[45] The NL-eEDM collaboration, P. Aggarwal, H. L. Bethlem, A. Borschevsky, M. Denis, K. Esajas, P. A. B. Haase, Y. Hao, S. Hoekstra, K. Jungmann, T. B. Meijknecht, M. C. Mooij, R. G. E. Timmermans, W. Ubachs, L. Willmann, and A. Zapara, Eur. Phys. J. D **72**, 197 (2018).

[46] Y. Hao, L. F. Pašteka, L. Visscher, P. Aggarwal, H. L. Bethlem, A. Boeschoten, A. Borschevsky, M. Denis, K. Esajas, S. Hoekstra, *et al.*, J. Chem. Phys. **151**, 034302 (2019).

[47] M. D. Di Rosa, Eur. Phys. J. D **31**, 395 (2004).

[48] Y. V. Stadnik and V. V. Flambaum, Phys. Rev. A **93**, 063630 (2016).

Chapter 2

The Standard Model and fundamental symmetries

2.1 Overview

This chapter aims to give a brief introduction to the formalism of the Standard Model (SM) and to highlight the importance of fundamental symmetries in the construction and verification of the SM, as well as in the search for new phenomena beyond the SM. The concept of symmetry has profound implications and widespread manifestations in the SM [1], as it not only governs the construction of the SM, but also predicts new particles and new phenomena. Since many new physics theories are characterized by more significant symmetry-breaking effects, examining symmetry-breaking effects is the main topic of this work. There are many different types of symmetries, which can be classified into two main classes, depending on whether they are continuous or discrete. Conservation laws in physics are usually arising from symmetry properties of a system [2]. The connection between conservation laws and continuous symmetry properties can be elucidated mathematically by Noether's theorem (see e.g. Ref. [2]). Besides continuous symmetries, we briefly review some important discrete symmetries in the SM, such as charge conjugation symmetry $\hat{\mathcal{C}}$, parity (space inversion symmetry) $\hat{\mathcal{P}}$, time reversal symmetry $\hat{\mathcal{T}}$, as well as their combinations such as $\hat{\mathcal{C}}\hat{\mathcal{P}}$ and $\hat{\mathcal{C}}\hat{\mathcal{P}}\hat{\mathcal{T}}$ (for more detail, see e.g. Ref. [3]). We give a brief overview of various symmetry-breaking effects that we investigate, and explain their nature and properties.

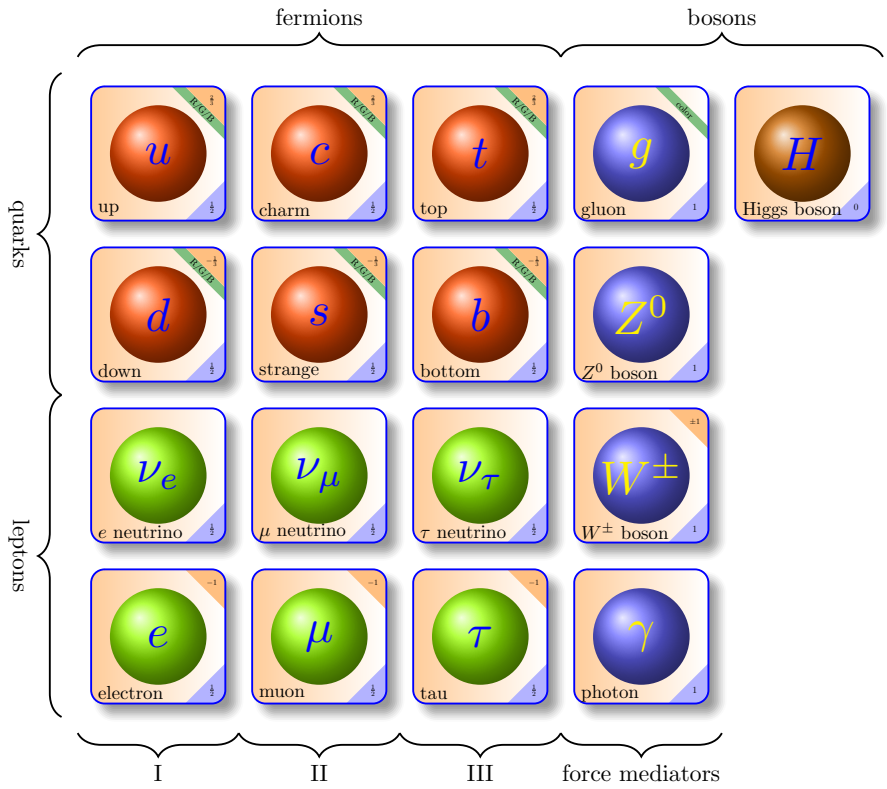

Figure 2.1: Pictorial summary of the SM particles (adapted from Ref. [4]).

2.2 The Standard Model

The Standard Model of particle physics is built on the $SU(3)_c \times SU(2)_L \times U(1)_Y$ gauge group, where the subscripts c, L, and Y represent color, left-handed spinor, and hypercharge, respectively. Fig. 2.1 is a pictorial summary of the SM particles and their properties known to date. The SM describes the fundamental interactions among three sectors, such as the building blocks of matter (fermionic fields including quarks and leptons), the force mediator sector (gauge bosons including gluons, $W^\pm$, Z^0 bosons, and photon), and the Higgs sector. Under the $SU(3)_c \times SU(2)_L \times U(1)_Y$ symmetry, the three-generation fermionic fields,

namely quarks and leptons, take the following form:

$$\begin{aligned}
q_{\alpha L}\Big(3,2,\frac{1}{3}\Big) &\equiv \begin{pmatrix} u \\ d' \end{pmatrix}_L, \quad \begin{pmatrix} c \\ s' \end{pmatrix}_L, \quad \begin{pmatrix} t \\ b' \end{pmatrix}_L, \\
l_{\alpha L}\Big(1,2,-1\Big) &\equiv \begin{pmatrix} \nu_e \\ e \end{pmatrix}_L, \quad \begin{pmatrix} \nu_\mu \\ \mu \end{pmatrix}_L, \quad \begin{pmatrix} \nu_\tau \\ \tau \end{pmatrix}_L, \\
u_{\alpha R}\Big(3,1,\frac{4}{3}\Big) &\equiv u_R, \quad c_R, \quad t_R, \\
d'_{\alpha R}\Big(3,1,-\frac{2}{3}\Big) &\equiv d'_R, \quad s'_R, \quad b'_R, \\
e_{\alpha R}\Big(1,1,-2\Big) &\equiv e_R, \quad \mu_R, \quad \tau_R.
\end{aligned} \tag{2.1}$$

Here, the index α enumerates the three generations of fermionic fields. The right and left handed spinors are defined as $\psi_{R/L} \equiv P_{R/L}\psi$ with $P_{R/L} \equiv (1 \pm \gamma^5)/2$ being the right and left chiral projection operators. The primed and unprimed quark states represent the flavor and mass eigenstates, respectively. The flavor eigenstates d', s', and b' can be related to the mass eigenstates d, s, and b by the Cabibbo–Kobayashi–Maskawa (CKM) matrix (see e.g. Ref. [5]):

$$\begin{pmatrix} d' \\ s' \\ b' \end{pmatrix} = V_{\mathrm{CKM}} \begin{pmatrix} d \\ s \\ b \end{pmatrix} = \begin{pmatrix} V_{ud} & V_{us} & V_{ub} \\ V_{cd} & V_{cs} & V_{cb} \\ V_{td} & V_{ts} & V_{tb} \end{pmatrix} \begin{pmatrix} d \\ s \\ b \end{pmatrix}. \tag{2.2}$$

Here, the CKM matrix V_{CKM} describes quark mixing among the three generations. Under the same gauge symmetry, the SM Higgs doublet takes the following form:

$$\Phi\Big(1,2,1\Big) = \begin{pmatrix} \phi^+ \\ \phi^0 \end{pmatrix}. \tag{2.3}$$

In Equations (2.1) and (2.3), the first two numbers in the parentheses denote the representations of the non-Abelian gauge groups $SU(3)_c$ and $SU(2)_L$, respectively. The third numbers in the parentheses denote the hypercharge, which is related to the electromagnetic charge Q by the following expression:

$$Y = 2\Big(Q - \frac{\sigma_3}{2}\Big). \tag{2.4}$$

Here, σ_3 represents the third component of the weak isospin.

The SM Lagrangian for the α-th generation of particles can be defined as [6]

$$\begin{aligned}\mathscr{L}_{\alpha}^{\mathrm{SM}} \equiv & \, i\bar{q}_{\alpha L}\not{D}q_{\alpha L} + i\bar{l}_{\alpha L}\not{D}l_{\alpha L} + i\bar{u}_{\alpha R}\not{D}u_{\alpha R} + i\bar{d}_{\alpha R}\not{D}d_{\alpha R} + i\bar{e}_{\alpha R}\not{D}e_{\alpha R} \\ & - \frac{1}{2}\mathrm{Tr}\Big(G_{\mu\nu}G^{\mu\nu}\Big) - \frac{1}{2}\mathrm{Tr}\Big(W_{\mu\nu}W^{\mu\nu}\Big) - \frac{1}{4}B_{\mu\nu}B^{\mu\nu} \\ & - y_u\bar{q}_{\alpha L}\tilde{\Phi}u_{\alpha R} - y_d\bar{q}_{\alpha L}\Phi d_{\alpha R} - y_e\bar{l}_{\alpha L}\Phi e_{\alpha R} + \mathrm{h.c.} \\ & + \frac{1}{2}|\not{D}_{\mu}\Phi|^2 - \frac{1}{2}\mu_H^2|\Phi|^2 - \frac{1}{4}\lambda_H^2|\Phi|^4,\end{aligned} \tag{2.5}$$

where μ_H and λ_H represent the Higgs coupling constants. Here, $\not{D}$ is defined as $\not{D} \equiv \gamma^{\mu}D_{\mu}$ and D_{μ} represents the covariant derivative, which is defined as

$$D_{\mu} = \partial_{\mu} - \frac{i}{2}g_1 Y B_{\mu} - \frac{i}{2}g_2\sigma_i W_{\mu}^{i} - \frac{i}{2}g_3\lambda_a G_{\mu}^{a}. \tag{2.6}$$

Here, σ_i and λ_a represent the Pauli and Gell-Mann matrices, respectively. The parameters g_1, g_2 and g_3 are the corresponding coupling constants for the electromagnetic, weak, and strong interactions. The interaction tensors for the electromagnetic, weak and strong interactions are defined, respectively, as follows:

$$B_{\mu\nu} = \partial_{\mu}B_{\nu} - \partial_{\nu}B_{\mu}, \tag{2.7}$$

$$W_{\mu\nu} = \partial_{\mu}W_{\nu} - \partial_{\nu}W_{\mu} + ig_2[W_{\mu}, W_{\nu}], \tag{2.8}$$

$$G_{\mu\nu} = \partial_{\mu}G_{\nu} - \partial_{\nu}G_{\mu} + ig_3[G_{\mu}, G_{\nu}]. \tag{2.9}$$

In the above equations, W_{ν} and G_{μ} are defined as $W_{\nu} \equiv \sigma_i W_{\mu}^{i}/2$ and $G_{\mu} \equiv \lambda_a G_{\mu}^{a}/2$, respectively. The parameters y_u, y_d, and y_e are the Yukawa coupling constants. The conjugate Higgs doublet is defined as $\tilde{\Phi} = i\sigma_2\Phi^*$. In the SM, particles acquire masses when the Higgs field develops a non-zero vacuum expectation value after the electroweak symmetry is broken from the $SU(2)_L \times U(1)_Y$ symmetry to the $U(1)_{\mathrm{em}}$ symmetry in the following way (see e.g. Ref. [5])[a]:

$$\Phi = \begin{pmatrix} 0 \\ \frac{v+h}{\sqrt{2}} \end{pmatrix}, \tag{2.10}$$

where h is the scalar Higgs field and v is the vacuum expectation value.

Despite the great success in the interpretation of the observed data and in the prediction of the new phenomena at the electroweak energy scale, the SM fails to explain many open problems and thus is considered as an incomplete theory.

[a] This expression is obtained in the unitary gauge (see e.g. Ref. [5]).

In order to solve the problems, many new physics theories (models) that extend the SM have been proposed and intensively explored in various experiments over the past decades. However, no statistically significant evidence has been found for such new physics theories so far. Since, compared with the SM, many new physics theories are characterized by more significant symmetry-breaking effects, examining symmetry-breaking effects can be used to test new physics theories and to search for new phenomena beyond the SM.

2.3 Fundamental symmetries

In this section, we give a brief introduction to some important fundamental symmetries and highlight their importance in the verification of the SM and in the search for new phenomena beyond the SM. There are many different types of symmetries, which can be classified in two main classes, depending on whether they are continuous or discrete.

2.3.1 Continuous symmetries

A valid theoretical description of a system requires that it obeys some fundamental conservation laws, such as the conservation of energy, momentum, angular momentum, etc. In the SM, conservation laws refer to the existence of quantities that are independent of the dynamical evolution of the whole system or the existence of quantities that do not change with respect to time. In general, conservation laws in physics are usually connected to continuous symmetry properties of a physical system [2]. The connection between conservation laws and symmetry properties can be elucidated mathematically by Noether's theorem (see e.g. Ref. [2]). According to Noether's theorem [7], each continuous symmetry transformation implies a conserved quantity. Tab. 2.1 summarizes the most common group of continuous symmetry transformations and the associated conserved quantities [8]. Energy and momentum conservation is related to the temporal and spatial translation symmetries, respectively. Angular momentum conservation arises from the rotational symmetry. The global $U(1)$ symmetry implies charge conservation, etc.

2.3.2 Discrete symmetries

In this section, we focus on the symmetry property with respect to discrete transformations, which play an important role in particle physics (see e.g. Ref. [3]), as well as in atomic and molecular physics. The most common discrete symmetry transformations include charge conjugation $\hat{\mathcal{C}}$, space inversion (or parity) $\hat{\mathcal{P}}$, time

Symmetry transform	Description	Conserved quantity
Translation in time	$t \longrightarrow t' = t + \Delta t$	Energy
Translation in space	$x \longrightarrow x' = x + \Delta x$	Linear momentum
Rotation (about x axis)	$y \longrightarrow y' = y\cos\theta + z\sin\theta$ $z \longrightarrow z' = -y\sin\theta + z\cos\theta$	Angular momentum
Global $U(1)$	$\phi \longrightarrow \phi' = e^{i\theta}\phi$	Charge, etc.

Table 2.1: Continuous symmetry transformations and the corresponding conserved quantities (see e.g. Ref. [8]).

reversal $\hat{\mathcal{T}}$, and their combinations, such as $\hat{\mathcal{C}}\hat{\mathcal{P}}$ and $\hat{\mathcal{C}}\hat{\mathcal{P}}\hat{\mathcal{T}}$. Since the transformation properties of the (quantized) scalar, spinor, and vector fields are different, we discuss such fields separately in the following discussions.

2.3.3 Charge conjugation symmetry

The charge conjugation transformation $\hat{\mathcal{C}}$ switches a particle with the corresponding anti-particle or vice versa. This transformation not only changes the sign of the charge but also changes the sign of other quantum numbers such as baryon number, lepton number, etc. The important feature, which is distinct from the space inversion and time reversal transformations, is that the charge conjugation transformation does not depend on space-time coordinates.

Under charge conjugation transformation, the charged scalar field $\hat{\phi}(t, \boldsymbol{r})$ transforms in the following way:

$$\hat{\mathcal{C}}\hat{\phi}(t, \boldsymbol{r})\hat{\mathcal{C}}^{-1} = \eta_c \hat{\phi}(t, \boldsymbol{r})^\dagger, \tag{2.11}$$

where the transformation factor satisfies the condition: $|\eta_c| = \pm 1$. The spinor field $\hat{\psi}(t, \boldsymbol{r})$ transforms in the following way:

$$\hat{\mathcal{C}}\hat{\psi}(t, \boldsymbol{r})\hat{\mathcal{C}}^{-1} = C\hat{\bar{\psi}}^T(t, \boldsymbol{r}), \tag{2.12}$$

where $\hat{\bar{\psi}}(t, \boldsymbol{r}) = \hat{\psi}^\dagger(t, \boldsymbol{r})\gamma^0$ is the adjoint spinor. Since the spinor field is a matrix, the transformation factor C should also be a matrix, which satisfies the following relations [2]:

$$C^\dagger = C^{-1} = C^T = -C. \tag{2.13}$$

The transformation factor C can be chosen as [2]

$$C = i\gamma^2\gamma^0. \tag{2.14}$$

In order to keep the coupling between the electromagnetic current and the vector field invariant, the vector field should transform in the following way [2]:

$$\hat{\mathcal{C}}\hat{A}^{\mu}(t,\boldsymbol{r})\hat{\mathcal{C}}^{-1} = -\hat{A}^{\mu}(t,\boldsymbol{r}). \tag{2.15}$$

The transformation property of observable quantities, such as energy and momentum, under the charge conjugation transformation is as follows [2]:

$$\hat{\mathcal{C}}p(E,\boldsymbol{p})\hat{\mathcal{C}}^{-1} = p(E,\boldsymbol{p}), \tag{2.16}$$

where $p(E,\boldsymbol{p})$ is the four-momentum.

2.3.4 Parity (space inversion symmetry)

Another important discrete symmetry transformation in physics is the space inversion symmetry transformation or parity transformation $\hat{\mathcal{P}}$, which is defined as

$$\hat{\mathcal{P}}x(t,\boldsymbol{r})\hat{\mathcal{P}}^{-1} = x(t,-\boldsymbol{r}), \tag{2.17}$$

where t and $\boldsymbol{r}$ represent the time and space coordinates, respectively. Unlike the charge conjugation transformation, the parity transformation depends on space-time coordinates.

Under parity transformation, the scalar field $\hat{\phi}(t,\boldsymbol{r})$ transforms in the following way:

$$\hat{\mathcal{P}}\hat{\phi}(t,\boldsymbol{r})\hat{\mathcal{P}}^{-1} = \eta_p\hat{\phi}(t,-\boldsymbol{r}), \tag{2.18}$$

where the transformation factor can be chosen as $\eta_p = \pm 1$, which implies the intrinsic parity of a scalar particle is either positive or negative, corresponding to scalar and pseudo-scalar, respectively. The spinor field $\hat{\psi}(t,\boldsymbol{r})$ transforms in the following way [2]:

$$\hat{\mathcal{P}}\hat{\psi}(t,\boldsymbol{r})\hat{\mathcal{P}}^{-1} = P\hat{\psi}(t,-\boldsymbol{r}). \tag{2.19}$$

Similarly, the transformation factor P should also be a matrix and, up to an arbitrary phase factor of modulus 1, can be chosen as [2]

$$P = \gamma^0. \tag{2.20}$$

Obviously, the transformation factor satisfies the following expression:

$$P = P^{\dagger} = P^{-1}. \tag{2.21}$$

Again, in order to keep the coupling between the electromagnetic current and the vector field invariant, the vector field should transform as follows [2]

$$\hat{\mathcal{P}}\hat{A}^{\mu}(t,\boldsymbol{r})\hat{\mathcal{P}}^{-1} = \hat{A}_{\mu}(t,-\boldsymbol{r}). \tag{2.22}$$

It is worth mentioning that, in classical mechanics, space inversion symmetry does not lead to conserved quantity, while in quantum mechanics space inversion symmetry implies conserved quantity, namely parity. The transformation properties of observable quantities, such as four-momentum and angular momentum, under the parity transformation are as follows [2]:

$$\hat{\mathcal{P}} p(E, \boldsymbol{p}) \hat{\mathcal{P}}^{-1} = p(E, -\boldsymbol{p}), \tag{2.23}$$

$$\hat{\mathcal{P}} \boldsymbol{J} \hat{\mathcal{P}}^{-1} = \boldsymbol{J}. \tag{2.24}$$

where $p(E, \boldsymbol{p})$ is the four-momentum and $\boldsymbol{J}$ is the total angular momentum, which is defined as

$$\boldsymbol{J} = \boldsymbol{L} + \frac{\hbar}{2} \boldsymbol{\Sigma}. \tag{2.25}$$

Here, $\boldsymbol{L}$ is the orbital angular momentum and $\hbar\boldsymbol{\Sigma}/2$ is the spin angular momentum, where $\boldsymbol{\Sigma}$ is defined as

$$\boldsymbol{\Sigma} = \begin{pmatrix} \sigma & \boldsymbol{0} \\ \boldsymbol{0} & \sigma \end{pmatrix}. \tag{2.26}$$

2.3.5 Time reversal symmetry

The third discrete symmetry transformation is the time reversal symmetry transformation $\hat{\mathcal{T}}$, which is defined as

$$\hat{\mathcal{T}} x(t, \boldsymbol{r}) \hat{\mathcal{T}}^{-1} = x(-t, \boldsymbol{r}). \tag{2.27}$$

The time reversal transformation flips the direction of motion and exchanges the incoming and outgoing particles. Similar to the space inversion transformation, the time reversal transformation also depends on the space-time coordinates. The time reversal transformation can be constructed by an anti-unitary operator as follows:

$$\hat{\mathcal{T}} \equiv \hat{\mathcal{U}} \hat{\mathcal{K}}, \tag{2.28}$$

where $\hat{\mathcal{U}}$ is a unitary operator and $\hat{\mathcal{K}}$ is the operator of complex conjugation.

Under the time reversal transformation, the scalar field $\hat{\phi}(t, \boldsymbol{r})$ transforms in the following way:

$$\hat{\mathcal{T}} \hat{\phi}(t, \boldsymbol{r}) \hat{\mathcal{T}}^{-1} = \eta_t \hat{\phi}(-t, \boldsymbol{r}), \tag{2.29}$$

where the transformation factor satisfies the condition: $|\eta_t| = 1$. The spinor field $\hat{\psi}(t, \boldsymbol{r})$ transforms in the following way:

$$\hat{\mathcal{T}} \hat{\psi}(t, \boldsymbol{r}) \hat{\mathcal{T}}^{-1} = T \hat{\psi}(-t, \boldsymbol{r}). \tag{2.30}$$

Similarly, the transformation factor T is also a matrix and, up to an arbitrary phase factor of modulus 1, can be chosen as [2]

$$T = i\gamma^1\gamma^3. \tag{2.31}$$

In order to keep the electromagnetic interaction invariant, the vector field should have the following transformation property [2]:

$$\hat{\mathcal{T}}\hat{A}^\mu(t,\boldsymbol{r})\hat{\mathcal{T}}^{-1} = \hat{A}_\mu(-t,\boldsymbol{r}). \tag{2.32}$$

The transformation properties of observable quantities, such as four-momentum and angular momentum, are as follows [2]:

$$\hat{\mathcal{T}}p(E,\boldsymbol{p})\hat{\mathcal{T}}^{-1} = p(E,-\boldsymbol{p}), \tag{2.33}$$

$$\hat{\mathcal{T}}\boldsymbol{J}\hat{\mathcal{T}}^{-1} = -\boldsymbol{J}. \tag{2.34}$$

2.3.6 $\hat{\mathcal{C}}\hat{\mathcal{P}}$ and $\hat{\mathcal{C}}\hat{\mathcal{P}}\hat{\mathcal{T}}$

In addition to the above-mentioned discrete symmetries, we can also combine them together to construct new discrete symmetries, such as $\hat{\mathcal{C}}\hat{\mathcal{P}}$, $\hat{\mathcal{C}}\hat{\mathcal{P}}\hat{\mathcal{T}}$, etc. For example, under the $\hat{\mathcal{C}}\hat{\mathcal{P}}$ symmetry, a left-handed fermion can be transformed into a right-handed anti-fermion. If the $\hat{\mathcal{C}}\hat{\mathcal{P}}$ symmetry was conserved, particles and anti-particles would behave exactly in the same manner. Tab. 2.2 summarizes the transformation properties of the three fundamental interactions in the SM under various discrete symmetries. As can be seen from Tab. 2.2, the $\hat{\mathcal{C}}\hat{\mathcal{P}}$ symmetry is believed to be conserved in the electromagnetic and strong interactions, while broken in the weak interaction. In fact, the weak interaction not only violates the $\hat{\mathcal{C}}\hat{\mathcal{P}}$ symmetry, but also violates the $\hat{\mathcal{C}}$, $\hat{\mathcal{P}}$, and $\hat{\mathcal{T}}$ symmetries. This means that experiments with microscopic particles are able to make an absolute distinction between particles and anti-particles, between left and right, as well as between traveling forward and traveling backward in time [2] through the weak interaction. It is remarkable that, in the weak interaction, although $\hat{\mathcal{P}}$ is violated at a maximal level, measurements suggest that $\hat{\mathcal{C}}\hat{\mathcal{P}}$ violation is very small. The dominant source of $\hat{\mathcal{C}}\hat{\mathcal{P}}$ violation in meson decays comes from the CKM matrix. Unlike the $\hat{\mathcal{C}}\hat{\mathcal{P}}$ symmetry, it is believed that the $\hat{\mathcal{C}}\hat{\mathcal{P}}\hat{\mathcal{T}}$ symmetry should be conserved in all known fundamental interactions described by a locally Lorentz-invariant Hermitian Hamiltonian or Lagrangian [2]. This is the so-called $\hat{\mathcal{C}}\hat{\mathcal{P}}\hat{\mathcal{T}}$ theorem, which guarantees that a particle and its anti-particle have the same mass and lifetime. The validity of the $\hat{\mathcal{C}}\hat{\mathcal{P}}\hat{\mathcal{T}}$ theorem has been tested by various experiments with very high precision [9].

Table 2.2: Transformation properties of the three fundamental interactions in the SM under discrete symmetries.

Force	Mediator	Spin	$\hat{\mathcal{C}}$	$\hat{\mathcal{P}}$	$\hat{\mathcal{T}}$	$\hat{\mathcal{C}}\hat{\mathcal{P}}$	$\hat{\mathcal{C}}\hat{\mathcal{P}}\hat{\mathcal{T}}$
Strong[a]	gluons	1	✓	✓	✓	✓	✓
Electromagnetic	photon	1	✓	✓	✓	✓	✓
Weak	$W^{\pm}$, Z^0	1	✗	✗	✗	✗	✓

[a] Although it is believed that $\hat{\mathcal{C}}\hat{\mathcal{P}}$ violation might occur in the strong interaction, no significant evidence has been found so far.

2.4 $\hat{\mathcal{P}}$ violation

Since the nuclear anapole moment effect is characterized by parity ($\hat{\mathcal{P}}$) violation, we first focus on the history of atomic parity violation. Parity violation was first proposed and discovered in the β decay of nucleus through the weak interaction [11, 12]. Subsequently, Zel'dovich pointed out that, unlike the situation in the β decay, parity violation in atomic transitions might be too small to be detectable [13]. However, many years later Bouchiat showed that parity violating effects roughly scale as the cubic power of nuclear charge Z and thus can be significantly enhanced in heavy atoms, possibly leading to observable signals [14, 15]. The experimental measurements of $\hat{\mathcal{P}}$ violation in atoms were pioneered by Barkov *et al.* [16] and Conti *et al.* [17] using the optical rotation and Stark-interference techniques on the Bi and Tl atoms, respectively.

Atomic parity violation has been measured in a variety of atoms such as ^{209}Bi, ^{208}Pb, ^{205}Tl, ^{174}Yb, ^{133}Cs, etc. What is actually measured in such experiments is the ratio between the imaginary part of the parity violating amplitude $\mathrm{Im}(E_{\mathrm{PV}})$ and the vector transition polarizability β [18], which can be used to extract the nuclear weak charge with the help of theoretical calculations. The most precise result is provided by the measurement on the Cs atom through the transition $6S_{1/2} - 7S_{1/2}$ and the measured quantity is $-\mathrm{Im}(E_{\mathrm{PV}})/\beta \simeq 1.538\ (40)\ \mathrm{mV{\cdot}cm^{-1}}$ [19]. Here, the number in the parenthesis represents the experimental uncertainty. Further measurements have also been proposed on heavy atoms with similar electronic structure, such as Fr [20].

In molecules, parity violation can be greatly enhanced because of closely spaced molecular levels with opposite parity [21], making it more likely to be detectable. It has been suggested that molecular parity violation could be observed by comparing the transition spectra of chiral molecules [22]. However, no statistically significant signal has been observed so far. Alternatively, the measurements of the nuclear spin dependent parity violating effects in molecules such as the nuclear anapole moment effect have also been proposed (see e.g. Ref.

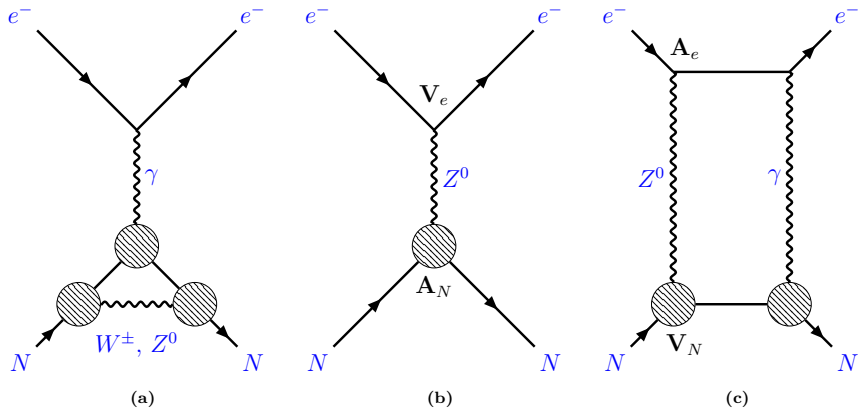

Figure 2.2: Nuclear spin dependent parity violating interactions [10]: (a) nuclear anapole moment interaction, (b) weak neutral coupling between the electronic vector current ($\mathbf{V}_e$) and nuclear axial-vector current ($\mathbf{A}_N$), (c) combined interaction between the nuclear spin independent weak interaction and the hyperfine interaction. The blobs represent the effective interactions between gauge bosons and nucleons (protons and neutrons), simply due to the consideration that nucleons are composite particles made up of quarks, and we do not know all the detail about their interactions.

[23, 24]).

In the SM, parity violation comes from the weak interaction through the exchange of $W^{\pm}$ or Z^0 bosons. In atoms and molecules, the weak interaction between electrons and nucleons gives rise to parity violating effects. In particular, the parity violating effects arising from the exchange of the Z^0 boson can be given by the following effective Lagrangian,

$$\mathscr{L}_{\text{eff}} = \frac{G_F}{\sqrt{2}}\Big[\bar{\psi}_e\gamma_\mu\Big(1-\gamma^5\Big)\psi_e\Big]\Big[\bar{\psi}_N\gamma^\mu\Big(C_v - C_a\gamma^5\Big)\psi_N\Big], \tag{2.35}$$

where $G_F = 2.222516(1) \times 10^{-14}\ E_h \cdot a_B^3$ is the Fermi weak interaction coupling constant [25], E_h is the Hartree energy, a_B is the Bohr radius. ψ_e and ψ_N represent the field operators for electron and nucleon, respectively. C_v and C_a are dimensionless constants accounting for the corrections to the vector and axial-vector currents. The following parity-violating terms can be obtained by expanding Eq. (2.35) explicitly [26, 27],

$$\mathscr{L}_{\text{PV}} = \frac{G_F}{\sqrt{2}}\Big[C_1\Big(\bar{\psi}_e\gamma_\mu\gamma^5\psi_e\Big)\Big(\bar{\psi}_N\gamma^\mu\psi_N\Big) + C_2\Big(\bar{\psi}_e\gamma_\mu\psi_e\Big)\Big(\bar{\psi}_N\gamma^\mu\gamma^5\psi_N\Big)\Big]. \tag{2.36}$$

Here, the first parameter $C_1 \equiv -C_v$ describes the strength of the interaction between the electronic axial-vector current ($\mathbf{A}_e$) and the nuclear vector current ($\mathbf{V}_N$), and the second parameter $C_2 \equiv -C_a$ describes the strength of the interaction between the electronic vector current ($\mathbf{V}_e$) and the nuclear axial-vector current ($\mathbf{A}_N$). The first term does not depend on nuclear spin and gives rise to the nuclear weak charge interaction. The second term depends on nuclear spin and contributes to the nuclear spin dependent parity-violating (NSD-PV) interactions. The coefficients C_1 and C_2 are contributed differently from proton and neutron and, to the lowest order, they can be expressed as [27]

$$\begin{aligned} C_{1p} &= \frac{1}{2}\Big(1 - 4\sin^2\theta_w\Big), \\ C_{1n} &= -\frac{1}{2}, \\ C_{2p} &= \frac{1}{2}g_A\Big(1 - 4\sin^2\theta_w\Big), \\ C_{2n} &= -C_{2p}, \end{aligned} \tag{2.37}$$

where the parameter g_A takes the value of around 1.26 [27] and the parameter θ_w is the Weinberg angle.

2.4.1 Nuclear spin-independent parity violating interaction

The first term in Eq. (2.36) describes the nuclear spin-independent parity violating (NSID-PV) interaction and can be expressed by the following effective Hamiltonian [27]:

$$H_{\mathrm{NSID}} \simeq -\frac{G_F}{\sqrt{2}}\Big[C_{1p}Z\rho_p(\boldsymbol{r}) + C_{1n}N\rho_n(\boldsymbol{r})\Big]\gamma_5, \tag{2.38}$$

where the number of protons and neutrons are denoted by Z and N, respectively. $\rho_p(\boldsymbol{r})$ and $\rho_n(\boldsymbol{r})$ represent the density distributions of protons and neutrons, respectively. Since this interaction does not depend on nuclear spin, all the nucleons contribute to the effect. If the proton and neutron distributions are assumed to be the same i.e. $\rho(\boldsymbol{r}) \equiv \rho_p(\boldsymbol{r}) = \rho_n(\boldsymbol{r})$, Eq. (2.38) can be simplified further as [27]

$$H_{\mathrm{NSID}} = -\frac{G_F}{\sqrt{8}}Q_w\gamma_5\rho(\boldsymbol{r}), \tag{2.39}$$

where Q_w is the nuclear weak charge and to the lowest order can be expressed as [27]

$$Q_w \simeq \Big(1 - 4\sin^2\theta_w\Big)Z - N. \tag{2.40}$$

The nuclear weak charge predicted by the SM for the Cs nucleus is approximately $Q_w \simeq -73.23\ (1)$ [9], where the number in the parenthesis represents the uncertainty. The NSID parity violating effects not only can be used to probe the SM parameters like the weak charge Q_w, but also can be used to impose constraints on new physics beyond the SM.

2.4.2 Nuclear spin-dependent parity violating interaction

The second term in Eq. (2.36) is one of the nuclear spin-dependent parity violating (NSD-PV) interaction terms (see below). The possible diagrams responsible for the NSD-PV interactions are depicted in Fig. 2.2, where N and e^- denote nucleons (protons or neutrons) and electrons, respectively. The NSD-PV interactions are contributed by three main sources and can be described by the following effective Hamiltonian [10, 27]:

$$H_{\mathrm{NSD}} = \frac{G_F}{\sqrt{2}} \left(\kappa_A + \kappa_{\mathrm{ax}} + \kappa_{\mathrm{hfs}}\right) \left(\boldsymbol{\alpha} \cdot \hat{\boldsymbol{I}}\right) \rho\left(\boldsymbol{r}\right), \tag{2.41}$$

where $\rho(\boldsymbol{r})$ is the nuclear density distribution, G_F is the Fermi weak interaction constant [25], $\hat{\boldsymbol{I}}$ is the unit vector along the nuclear spin, and $\boldsymbol{\alpha}$ are the Dirac matrices. As can be seen from Eq. (2.41), the NSD-PV effects are only nontrivial for the nucleus with non-zero nuclear spin. The first term, κ_A, comes from the nuclear anapole moment interaction (see Fig. 2.2 (a)) [26, 27] and will be discussed in more detail below. The second term κ_{ax} arises from the weak neutral coupling between the electronic vector current ($\mathbf{V}_e$) and nuclear axial-vector current ($\mathbf{A}_N$) [27, 28] (see Fig. 2.2 (b)). Theoretical prediction of κ_{ax} within the nuclear shell model can be found in Ref. [29]. The third contribution κ_{hfs} originates in the nuclear spin independent weak interaction combined with the hyperfine interaction [30, 31] (see Fig. 2.2 (c)).

The three sources contribute differently to the NSD-PV effects. The parameter κ_{ax} is independent of the atomic mass number A, while the parameter κ_A scales as $\sim A^{2/3}$ [27]. Compared with κ_A, the parameter κ_{hfs} is much smaller [27]. Therefore, it is expected that for molecules containing heavy elements the NSD-PV effects are dominated by the nuclear anapole moment interaction. In this case, it is possible to separate the nuclear anapole moment effect from the remaining NSD-PV effects. For molecules only containing light elements, the measured NSD-PV effects are contributed from all these three major sources, but it is still possible to distinguish the nuclear anapole moment effect from the other two effects by performing measurements with different nuclei (or different isotopes) [32]. Since numerous experiments aim to measure the nuclear anapole moment effect with improved sensitivities [23, 24, 32], we give a special attention to the nuclear anapole moment effect.

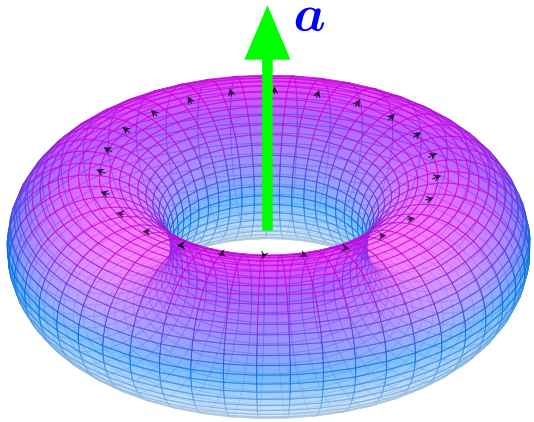

Figure 2.3: Nuclear anapole moment generated by a toroidal current distribution.

The nuclear anapole moment $\boldsymbol{a}$ is a magnetic moment arising from a current distribution $\boldsymbol{j}(\boldsymbol{r})$ within a nucleus and can be expressed as [26]

$$\boldsymbol{a} = -\pi \int |\boldsymbol{r}|^2 \boldsymbol{j}(\boldsymbol{r}) d^3\boldsymbol{r}, \tag{2.42}$$

which gives rise to the following vector potential [26]:

$$\boldsymbol{A} = \boldsymbol{a}\delta(\boldsymbol{r}). \tag{2.43}$$

The interaction between the vector potential and the electromagnetic current leads to the nuclear anapole moment effect. From a classical point of view, the current distribution that gives rise to the nuclear anapole moment can be demonstrated in Fig. 2.3. By definition, the nuclear anapole moment interaction can be factorized into two parts, i.e. the electronic part and the nuclear part. In the nuclear shell model, except for the valence nucleon, all the nucleons with opposite spin are grouped into pairs and form the core of the nucleus. Without parity violating interactions, the spin of the valence nucleon is aligned in the direction perpendicular to the plane where it travels around the core of the nucleus. However, in the presence of parity violating interactions, the spin direction of the valence nucleon would be influenced and no longer aligned in the same direction

when it travels around the core, leading to the current distribution in the windings of a toroidal solenoid [33]. Such current distribution gives rise to the parity violating nuclear anapole moment effect.

In the nuclear shell model, the effective coupling constant κ_A, which describes the strength of the nuclear anapole moment effect, takes the following explicit form [10, 34, 35],

$$\kappa_A \simeq 1.15 \times 10^{-3}(-1)^{I-l+\frac{1}{2}} \left(\frac{I+1/2}{I+1}\right) \mu_i g_i A^{\frac{2}{3}}, \tag{2.44}$$

where I and l represent the quantum numbers of the spin and orbital angular momenta for the unpaired valence nucleon, and A is the total number of nucleons in the nucleus (atomic mass number). g_i is an interaction constant with the absolute values of around 5 [10, 34] and 1 [10, 36] for the proton-nucleus and neutron-nucleus interactions, respectively. μ_i is the nuclear magnetic moment with the absolute values of around 2.8 and 1.9 for proton and neutron, respectively [10].

Non-vanishing nuclear anapole moment effect has been observed in the ^{133}Cs atom with the size of the effect being 0.127 ± 0.019, which is different from zero by a significance of 7 σ [37, 38]. Further measurements with improved sensitivity have been proposed on other atoms, such as ^{137}Ba [39], ^{163}Dy [40], ^{171}Yb [41], ^{212}Fr [42], etc. Recently, the measurements with unprecedented sensitivities have also proposed on diatomic molecules such as BaF [43, 44], and triatomic molecules [32] such as BeNC, MgNC, CaOH, SrOH, BaOH, etc. In Chapter 5, we briefly introduce the methodology behind the measurement of the nuclear anapole moment effect using molecules.

2.5 $\hat{\mathcal{C}}\hat{\mathcal{P}}$ violation

$\hat{\mathcal{C}}\hat{\mathcal{P}}$ violation (and $\hat{\mathcal{C}}$ violation) is one of the three criteria suggested by Sakharov to explain the observed matter-antimatter asymmetry in our Universe [45]. In 1964, $\hat{\mathcal{C}}\hat{\mathcal{P}}$ violation was first observed in the neutral K meson decays through the weak interaction [46]. Many years later, the possibility of finding $\hat{\mathcal{C}}\hat{\mathcal{P}}$ violation in the B meson decays was proposed by Bigi *et al.* [47]. In 2001, $\hat{\mathcal{C}}\hat{\mathcal{P}}$ violation was established in the B meson decays by BaBar [48] and Belle [49]. In 2013, $\hat{\mathcal{C}}\hat{\mathcal{P}}$ violation was first reported in the strange B meson systems [50]. Recently, $\hat{\mathcal{C}}\hat{\mathcal{P}}$ violation has also been observed in the D^0 meson decay by LHCb with the asymmetry of -15.4 ± 2.9 (stat. + syst.) $\times 10^{-4}$, which is different from zero with a significance of 5.3 σ [51]. In the SM, $\hat{\mathcal{C}}\hat{\mathcal{P}}$ violation may come from the complex phase of the three-generation quark mixing (CKM) matrix or may come from the θ-term in the QCD Lagrangian. Although such description of $\hat{\mathcal{C}}\hat{\mathcal{P}}$ violation agrees

well with almost all the current electroweak data, the amount of $\hat{\mathcal{C}}\hat{\mathcal{P}}$ violation predicted by the SM is insufficient to account for the observed matter-antimatter asymmetry. Therefore, a new mechanism for $\hat{\mathcal{C}}\hat{\mathcal{P}}$ violation needs to be proposed from a theoretical perspective and an additional source of $\hat{\mathcal{C}}\hat{\mathcal{P}}$ violation needs to be identified from an experimental perspective.

Compared with the SM, many new physics theories are characterized by more significant $\hat{\mathcal{C}}\hat{\mathcal{P}}$ violating effects. As early as 1950, Purcell *et al.* suggested the probability that elementary particles and nucleons might possess a nonzero permanent electric dipole moment (EDM) [52]. For example, as indicated in Fig. 2.4, a non-zero permanent EDM of an electron is aligned along its spin axis and violates both parity ($\hat{\mathcal{P}}$) and time reversal ($\hat{\mathcal{T}}$) symmetry. According to the $\hat{\mathcal{C}}\hat{\mathcal{P}}\hat{\mathcal{T}}$ theorem of the quantum field theory, the violation of time reversal symmetry implies the violation of the $\hat{\mathcal{C}}\hat{\mathcal{P}}$ symmetry. The searches for the permanent EDM of elementary particles can open a window for identifying new sources of $\hat{\mathcal{C}}\hat{\mathcal{P}}$ violation and can serve as a powerful tool to set constraints on new physics theories beyond the SM.

Particularly, the searches for the permanent EDM of a nucleon may help find the solution to the strong $\hat{\mathcal{C}}\hat{\mathcal{P}}$ problem. In Quantum Chromodynamics (QCD), a nontrivial term induced by non-perturbative effects violates the $\hat{\mathcal{C}}\hat{\mathcal{P}}$ symmetry explicitly through the so-called QCD vacuum angle and can be defined by the following expression [53–55]:

$$\mathscr{L}_\theta = \frac{g_3^2 \theta_{\mathrm{QCD}}}{32\pi^2} \epsilon^{\mu\nu\alpha\beta} G^a_{\mu\nu} G^a_{\alpha\beta}, \tag{2.45}$$

where the parameter g_3 represents the coupling constant for the strong interaction, and θ_{QCD} represents the QCD vacuum angle. This term can induce non-zero neutron electric dipole moment (nEDM). By assuming that this term is the sole source to the nEDM (d_n), the nEDM can be expressed as follows [56]:

$$d_n \simeq 3 \times 10^{-16} \theta_{\mathrm{QCD}} \quad e \cdot \mathrm{cm}. \tag{2.46}$$

The searches for the nEDM have reached a very high level of precision. However, no significant signal of the nEDM has been observed so far. The experimental upper limit at the 90% confidence level on the nEDM is 2.9×10^{-26} e·cm [57], which imposes an upper bound on the QCD vacuum angle with the value of $\theta_{\mathrm{QCD}} \lesssim 10^{-10}$, suggesting that such term is tiny and the $\hat{\mathcal{C}}\hat{\mathcal{P}}$ symmetry in the strong interaction should be preserved to a very high degree [57]. The smallness of strong $\hat{\mathcal{C}}\hat{\mathcal{P}}$ violation remains a puzzle.

Besides the term with the QCD vacuum angle, several other terms also involve non-zero EDM and violate the $\hat{\mathcal{C}}\hat{\mathcal{P}}$ symmetry. Recently, exploring new source of $\hat{\mathcal{C}}\hat{\mathcal{P}}$ violation with electron electric dipole moment (eEDM) has been a subject of

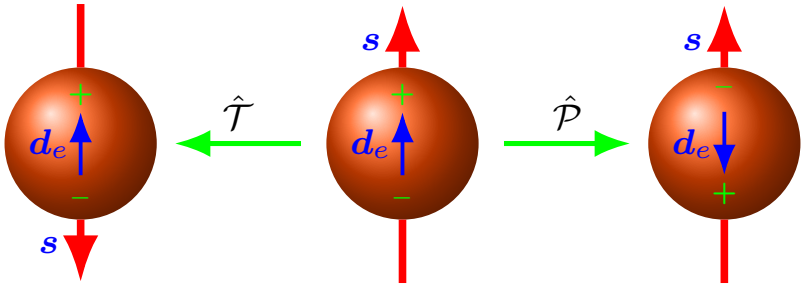

Figure 2.4: The electron electric dipole moment ($\boldsymbol{d}_e$) violates parity ($\hat{\mathcal{P}}$) and time reversal symmetry ($\hat{\mathcal{T}}$).

active research. The interaction between a non-zero eEDM and electromagnetic field can be described by the following effective Lagrangian [58, 59]:

$$\mathscr{L}^{\mathrm{eEDM}} = \frac{-i}{2} d_e \bar{\psi}_e \sigma^{\mu\nu} \gamma^5 \psi_e F_{\mu\nu}, \tag{2.47}$$

where $\sigma^{\mu\nu} = (\gamma^\mu\gamma^\nu - \gamma^\nu\gamma^\mu)/(2i)$, ψ_e is the field operator for electron, $F_{\mu\nu}$ is the field strength operator for electromagnetic field. Since the effects induced by a non-zero eEDM can be greatly enhanced in atoms and molecules [10, 59], the searches for the eEDM using atoms and molecules can be used as a powerful tool to place constraints on new physics theories beyond the SM and have attracted an enormous level of attention recently. Fig. 2.5 summarizes the constraints on new physics models beyond the SM imposed by the searches for the eEDM. As can be seen, the eEDM predicted by the SM is many orders of magnitude smaller than the ones predicted by new physics theories beyond the SM. A large fraction of such new physics models have been excluded by the recent results from the measurement on ThO [60]. At present, the NL-eEDM collaboration is building an experimental setup to search for the eEDM in a slow beam of cold BaF molecules [61] with unprecedented sensitivity. Knowledge of molecular properties of BaF is thus needed to plan the measurements and in particular to determine the optimal laser-cooling scheme, which can help to increase the interaction time and to improve the measurement sensitivity. In Chapter 5, we briefly introduce the searches for the eEDM using atoms and molecules. In Chapter 8, we demonstrate the theoretical investigations of molecular properties for the eEDM measurements, as an application of *ab initio* methods.

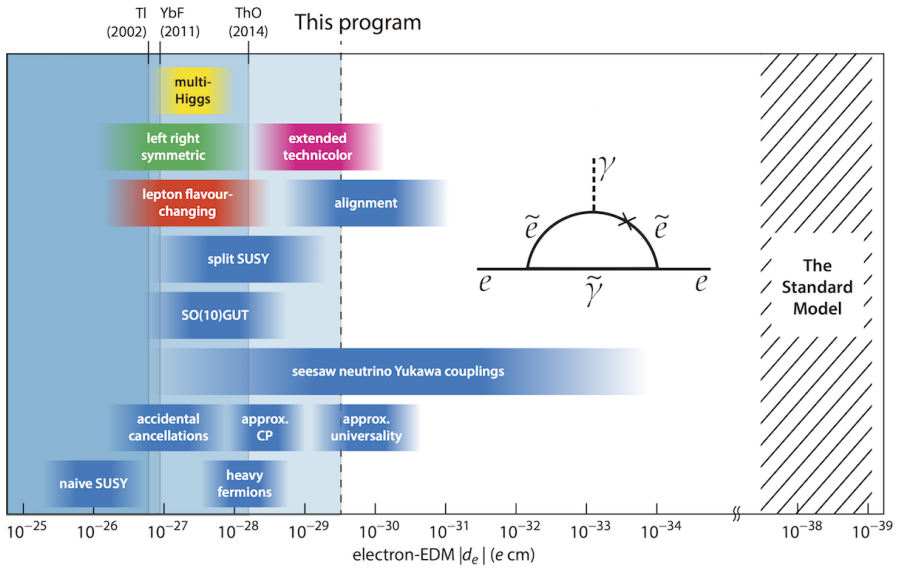

Figure 2.5: Constraints on new physics models beyond SM imposed by the searches for the eEDM (image courtesy of the NL-eEDM collaboration [62]).

2.6 Variation of fundamental constants

Constructing new physics theories, such as quantum gravity, that unify gravity with the other three fundamental interactions in a self-consistent manner is one of the most challenging problems in modern physics. A variety of new physics theories that extend the Standard Model (SM) and General Relativity (GR) have been proposed with the signature of time and space dependence on dimensionless fundamental constants, such as fine structure constant (α), proton to electron mass ratio (μ), etc. The idea that fundamental constants may vary with respect to time and space can be traced back to the big numbers hypothesis proposed by Dirac [63] amid speculation that the gravitational constant may depend on time [64]. Later on, this idea is generalized to the scenario that the fine structure constant α may also vary with time. The searches for the variation of fundamental constants not only can help test the SM and GR, but also can help put constraints on new physics theories.

New physics theories, such as quantum gravity, string theories, M-theories, brane-world models, etc., that unify gravity with other fundamental interactions are usually featured with extra space-time dimensions, which provide a natural framework in describing the variation of fundamental constants [65]. The true

fundamental constants exist in the whole space including the common $(3+1)$ dimensional space and the extra dimensional space. Any change in the size of the extra-dimensional space may give rise to the variation of fundamental constants in the common $(3+1)$ dimensional space. For example, in the Kaluza-Klein model (one type of string theory), extra spatial dimensions are introduced as an attempt of unifying gravity with other fundamental interactions in a form of small compact manifold called internal space, which leads to the time variation of fundamental constants like α [66]. Therefore, the search for the time variation of α may help find evidence for extra space-time dimensions. Some superstring theories with extra space-time dimensions are also considered as promising theories for unifying gravity with other fundamental interactions. In such theories, fundamental constants may vary with time through the coupling between the electromagnetic field and a dynamical field called dilaton, which is a hypothetical particle that could appear when the volume of the (extra) internal space varies [67]. Similarly, in M-theories, the change in the volume of internal space could also manifest itself as the variation of fundamental constants in the common $(3+1)$ dimensional space [68]. In the brane-world models, the existence of scalar fields called moduli fields are predicted and such fields are related to the variation of fundamental constants through the size change of extra-dimensional space as well [69].

Besides extra dimensional theories, some new physics theories give rise to the variation of fundamental constants through scalar dark matter candidates. In such theories, the scalar dark matter candidates oscillate with respect to time and cause the time variation of fundamental constants through their coupling to the SM particles [70]. For example, the newly added scalar field interacts with the SM fermionic and electromagnetic fields respectively in the following way ($\hbar \equiv 1$, $c \equiv 1$) [70]:

$$\mathscr{L}_1 = \frac{Y_\gamma \cos(\omega t)}{4\Lambda_\gamma} F_{\mu\nu} F^{\mu\nu}, \tag{2.48}$$

$$-\mathscr{L}_2 = \frac{Y_f \cos(\omega t)}{\Lambda_f} m_f \bar{\psi}_f \psi_f. \tag{2.49}$$

Here, ω is the oscillating frequency for the new scalar field, $F_{\mu\nu}$ represents electromagnetic tensor and ψ_f represents the fermionic field. The parameters Y_γ and Y_f describe the coupling strengths between the new scalar field and the SM fields and have units of mass, Λ_γ and Λ_f represent the energy scales associated with new physics, m_f represents the mass of the SM fermionic field. The temporal variation of fundamental constants, such as the fine structure constant (α) and fermionic mass m_f, arises from the interactions given by Equations (2.48) and

(2.49) and can be expressed as [70]

$$\alpha'(t) = \frac{\alpha}{1 - \frac{Y_\gamma \cos(\omega t)}{\Lambda_\gamma}}, \tag{2.50}$$

$$m'_f(t) = \Big[1 + \frac{Y_f \cos(\omega t)}{\Lambda_f}\Big] m_f. \tag{2.51}$$

In this case, the studies of the temporal variation of fundamental constants can be helpful for dark matter searches.

Alternatively, the variation of fundamental constants with respect to the space variables is also suggested by new physics theories that unify gravity with other fundamental interactions. Moreover, the spatial variation of fundamental constants can naturally explain the existence of life and the fine-tuning problem, because it suggests that in some regions of the Universe the value of fundamental constants may be in favor of the existence of life and may fit well with certain observations [71]. In some dark matter and dark energy models, the inhomogeneous distribution of dark scalar fields gives rise to the spatial variation of fundamental constants via the coupling between the dark scalar fields and the SM fields, bringing forward the variation of the fundamental constants in accordance with gravitational potential [72–74]. Another example of the spatial variation of fundamental constants lies within the new physics theories featured with domain walls generated in the early Universe. Such domain walls couple to the electromagnetic field and may cause the spatial variation of α when the domain walls are passing through the Earth [75]. In this case, the searches for the spatial variations of α may be helpful for the detection of such domain walls. However, it is suggested by some new physics models that, compared with the time variation of fundamental constants, the spatial variation is less significant [76].

The searches for the variation of fundamental constants with respect to time and space have attracted increasing attention over the past years. Such studies can be performed in a number of ways, such as Big Bang nucleosynthesis, Oklo natural nuclear reactor data, meteorite data, laser interferometer, quasar absorption spectra, and atomic clocks [71]. In Chapter 5, we briefly introduce the methodology behind the search for the variation of fundamental constants using a laser interferometer in particular and discuss its connection with the solid-state and molecular properties. In Chapter 9, we demonstrate the role of *ab initio* methods in the search for the variation of fundamental constants with an application to some solid-state materials and diatomic molecules. Since it is impossible to distinguish between the variation of dimensional constants and the variation of units, it does not make sense to search for the variation of dimensional constants. Throughout the present work, unless otherwise specified explicitly, the fundamental constants under discussion refer to dimensionless fundamental constants.

References

[1] A. Zee, *Fearful symmetry: The search for beauty in modern physics*, Vol. 48 (Princeton University Press, 2015).

[2] W. Greiner and J. Reinhardt, *Field quantization* (Springer-Verlag, 2013).

[3] I. I. Bigi and A. I. Sanda, $\hat{\mathcal{C}}\hat{\mathcal{P}}$ *violation* (Cambridge University Press, 2009).

[4] C. Burgard, *The Standard Model of physics* (Texample, 2016).

[5] M. Thomson, *Modern particle physics* (Cambridge University Press, 2013).

[6] H. M. Lee, arXiv:1907.12409 (2019).

[7] E. Noether, Trans. Theor. Statist. Phys. **1**, 186 (1971).

[8] S. Haywood, *Symmetries and conservation laws in particle physics: an introduction to group theory for particle physicists* (World Scientific, 2011).

[9] M. Tanabashi, K. Hagiwara, K. Hikasa, K. Nakamura, Y. Sumino, F. Takahashi, J. Tanaka, K. Agashe, G. Aielli, C. Amsler, *et al.*, Phys. Rev. D **98**, 030001 (2018).

[10] M. S. Safronova, D. Budker, D. DeMille, D. F. J. Kimball, A. Derevianko, and C. W. Clark, Rev. Mod. Phys. **90**, 025008 (2018).

[11] T. D. Lee and C. N. Yang, Phys. Rev. **104**, 254 (1956).

[12] C. S. Wu, E. Ambler, R. W. Hayward, D. D. Hoppes, and R. P. Hudson, Phys. Rev. **105**, 1413 (1957).

[13] Y. B. Zel'dovich, Sov. Phys. JETP **9**, 682 (1959).

[14] M. A. Bouchiat and C. C. Bouchiat, J. de Phys. **35**, 899 (1974).

[15] M. A. Bouchiat and C. Bouchiat, J. de Phys. **36**, 493 (1975).

[16] L. M. Barkov and M. S. Zolotorev, JETP Lett. **27** (1978).

[17] R. Conti, P. Bucksbaum, S. Chu, E. Commins, and L. Hunter, Phys. Rev. Lett. **42**, 343 (1979).

[18] B. M. Roberts, V. A. Dzuba, and V. V. Flambaum, Ann. Rev. Nucl. Part. Sci. **65**, 63 (2015).

[19] J. Guéna, M. Lintz, and M. A. Bouchiat, Phys. Rev. A **71**, 042108 (2005).

[20] M. Tandecki, J. Zhang, S. Aubin, J. A. Behr, R. Collister, E. Gomez, G. Gwinner, H. Heggen, J. Lassen, L. A. Orozco, *et al.*, JINST **9**, P10013 (2014).

[21] P. Sushkov and V. V. Flarnbaurn, Zh. Eksp. Teor. Fiz **75**, 1208 (1978).

[22] V. S. Letokhov, Phys. Lett. **53**, 275 (1975).

[23] E. Altuntaş, J. Ammon, S. B. Cahn, and D. DeMille, Phys. Rev. A **97**, 042101 (2018).

[24] E. Altuntaş, J. Ammon, S. B. Cahn, and D. DeMille, Phys. Rev. Lett. **120**, 142501 (2018).

[25] P. J. Mohr, D. B. Newell, and B. N. Taylor, J. Phys. Chem. Ref. Data **45**, 043102 (2016).

[26] I. B. Khriplovich, *Parity nonconservation in atomic phenomena* (Gordon and Breach Science Publishers, 1991).

[27] J. S. M. Ginges and V. V. Flambaum, Phys. Rep. **397**, 63 (2004).

[28] V. N. Novikov, O. P. Sushkov, V. V. Flambaum, and I. B. Khriplovich, Sov. Phys. JETP **46**, 420 (1977), or Zh. Eksp. Theor. Fiz **73**, 802 (1977).

[29] V. V. Flambaum and I. B. Khriplovich, Sov. Phys. JETP **52**, 835 (1980), or Zh. Eksp. Teor. Fiz **79**, 1656 (1980).

[30] V. V. Flambaum and I. B. Khriplovich, Sov. Phys. JETP **62**, 872 (1985), or Zh. Eksp. Theor. Fiz **89**, 1505 (1985).

[31] C. Bouchiat and C. A. Piketty, Phys. Lett. B **269**, 195 (1991).

[32] E. B. Norrgard, D. S. Barker, S. Eckel, J. A. Fedchak, N. N. Klimov, and J. Scherschligt, Commun. Phys. **2**, 77 (2019).

[33] E. Altuntas, *Measurement of nuclear spin dependent parity violation in* ^{138}BaF, Ph.D. thesis, Yale University (2017).

[34] V. V. Flambaum, I. B. Khriplovich, and O. P. Sushkov, Phys. Lett. B **146**, 367 (1984).

[35] K. I. B. Flambaum, V. V., Phys. Lett. A **110**, 121 (1985).

[36] V. V. Flambaum and D. W. Murray, Phys. Rev. C **56**, 1641 (1997).

[37] C. S. Wood, S. C. Bennett, D. Cho, B. P. Masterson, J. L. Roberts, C. E. Tanner, and C. E. Wieman, Science **275**, 1759 (1997).

[38] W. C. Haxton and C. E. Wieman, Ann. Rev. Nucl. Part. Sci. **51**, 261 (2001).

[39] D. DeMille, S. B. Cahn, D. Murphree, D. A. Rahmlow, and M. G. Kozlov, Phys. Rev. Lett. **100**, 023003 (2008).

[40] N. Leefer, L. Bougas, D. Antypas, and D. Budker, arXiv:1412.1245 (2014).

[41] D. Antypas, A. Fabricant, L. Bougas, K. Tsigutkin, and D. Budker, Hyperfine Interact. **238**, 21 (2017).

[42] S. Aubin, J. A. Behr, R. Collister, V. V. Flambaum, E. Gomez, G. Gwinner, K. P. Jackson, D. Melconian, L. A. Orozco, M. R. Pearson, D. Sheng, G. D. Sprouse, M. Tandecki, J. Zhang, and Y. Zhao, Hyperfine Interact. **214**, 163 (2013).

[43] E. Altuntaş, J. Ammon, S. B. Cahn, and D. DeMille, Phys. Rev. A **97**, 042101 (2018).

[44] E. Altuntaş, J. Ammon, S. B. Cahn, and D. DeMille, Phys. Rev. Lett. **120**, 142501 (2018).

[45] A. D. Sakharov, JETP Lett. **5**, 24 (1967).

[46] J. H. Christenson, J. W. Cronin, V. L. Fitch, and R. Turlay, Phys. Rev. Lett. **13**, 138 (1964).

[47] I. I. Bigi and A. I. Sanada, Nucl. Phys. B **193**, 85 (1981).

[48] B. Aubert, D. Boutigny, J. M. Gaillard, A. Hicheur, Y. Karyotakis, J. P. Lees, P. Robbe, V. Tisserand, A. Palano, G. P. Chen, *et al.*, Phys. Rev. Lett. **87**, 091801 (2001).

[49] K. Abe, R. Abe, I. Adachi, B. S. Ahn, H. Aihara, M. Akatsu, G. Alimonti, K. Asai, M. Asai, Y. Asano, *et al.*, Phys. Rev. Lett. **87**, 091802 (2001).

[50] R. Aaij, C. A. Beteta, B. Adeva, M. Adinolfi, C. Adrover, A. Affolder, Z. Ajaltouni, J. Albrecht, F. Alessio, M. Alexander, *et al.*, Phys. Rev. Lett. **110**, 221601 (2013).

[51] R. Aaij, *et al.*, Phys. Rev. Lett. **122**, 211803 (2019).

[52] E. M. Purcell and N. F. Ramsey, Phys. Rev. **78**, 807 (1950).

[53] G. t'Hooft, Phys. Rev. Lett. **37**, 8 (1976).

[54] Y. Nagashima, *Elementary particle physics: Foundations of the standard model*, Vol. 2 (John Wiley & Sons, 2013).

[55] M. D. Schwartz, *Quantum field theory and the standard model* (Cambridge University Press, 2014).

[56] J. Ellis, Nucl. Instrum. Methods Phys. Res. A **284**, 33 (1989).

[57] C. A. Baker, D. D. Doyle, P. Geltenbort, K. Green, M. G. D. Van der Grinten, P. G. Harris, P. Iaydjiev, S. N. Ivanov, D. J. R. May, J. M. Pendlebury, *et al.*, Phys. Rev. Lett. **97**, 131801 (2006).

[58] M. Pospelov and A. Ritz, Ann. Phys. **318**, 119 (2005).

[59] T. E. Chupp, P. Fierlinger, M. J. Ramsey-Musolf, and J. T. Singh, Rev. Mod. Phys. **91**, 015001 (2019).

[60] V. Andreev and N. R. Hutzler, Nature **562**, 355 (2018).

[61] P. Aggarwal, H. L. Bethlem, A. Borschevsky, M. Denis, K. Esajas, P. A. B. Haase, Y. Hao, S. Hoekstra, K. Jungmann, T. B. Meijknecht, M. C. Mooij, R. G. E. Timmermans, W. Ubachs, L. Willmann, and A. Zapara, Eur. Phys. J. D **72**, 197 (2018).

[62] *The NL-eEDM Collaboration:* `https://www.rug.nl/research/vsi/newtopics/eedm`.

[63] P. A. M. Dirac, Nature **139**, 323 (1937).

[64] E. Teller, Phys. Rev. **73**, 801 (1948).

[65] P. Loren-Aguilar, E. Garcia-Berro, J. Isern, and Y. A. Kubyshin, Class. Quant. Grav. **20**, 3885 (2003).

[66] W. J. Marciano, Phys. Rev. Lett. **52**, 489 (1984).

[67] K. Maeda, Mod. Phys. Lett. A **3**, 243 (1988).

[68] H. B. Sandvik, J. D. Barrow, and J. Magueijo, Phys. Rev. Lett. **88**, 031302 (2002).

[69] P. Brax, C. van de Bruck, A. C. Davis, and C. S. Rhodes, Astrophys. Space Sci. **283**, 627 (2003).

[70] Y. V. Stadnik and V. V. Flambaum, Phys. Rev. Lett. **114**, 161301 (2015).

[71] V. V. Flambaum, in *International Frequency Control Symposium Joint with the 21st European Frequency and Time Forum* (IEEE, 2007) pp. 342–349.

[72] D. F. Mota and J. D. Barrow, Mon. Not. Roy. Astron. Soc. **349**, 291 (2004).

[73] K. A. Olive and M. Pospelov, Phys. Rev. D **77**, 043524 (2008).

[74] P. Molaro, S. A. Levshakov, and M. G. Kozlov, Nucl. Phys. Proc. Suppl. **194**, 287 (2009).

[75] K. A. Olive, M. Peloso, and J. Uzan, Phys. Rev. D **83**, 043509 (2011).

[76] K. A. Olive, M. Peloso, and A. J. Peterson, Phys. Rev. D **86**, 043501 (2012).

Chapter 3

Computational methods

3.1 Overview

Theoretical investigations of molecular properties for diatomic molecules not only can help develop an experimental setup for precision measurements, but also can help correct the errors and interpret the results after measurements [1]. Compared with the semi-empirical methods, the *ab initio* methods are more mathematically rigorous and do not depend on empirical parameters, making it possible to perform calculations on molecules when there is no experimental information available or the experimental spectra are too complicated to be analyzed. Such methods allow a careful examination of electronic structure and enable us to understand the possible mechanism for the influence of new physics interactions on molecular properties. In some cases, they can also be used to identify promising molecular candidates with enhanced sensitivity and provide the needed molecular parameters for a successful interpretation of the measurements.

In this chapter, we briefly review the computational methods that are used for the calculation of molecular properties in the present work. In order to calculate molecular properties with high-accuracy, we need to take into account a number of factors, such as relativistic effects (Hamiltonian), basis set quality, treatment of electron correlation, etc. The treatment of relativistic effects and electron correlation plays an increasingly important role in accurately determining the properties of molecules containing heavy elements. Light molecules are more feasible for highly accurate investigations, because sufficiently large and high-quality basis sets can be used. A comprehensive analysis of the impact of such factors might help find strategies to systematically improve the accuracy of the calculated molecular properties. In particular, we focus our attention on the performance of various electron correlation methods that have been widely

employed in the calculations of molecular properties.

Theoretical uncertainty not only can help quantitatively evaluate the quality of the calculations, but also can help draw reliable conclusions from measurements. In some cases, theoretical values cannot be directly compared to the experimental values if the corresponding uncertainties are not acknowledged properly [2]. In other cases, the experimental values usually need to be combined with the theoretical values in order to extract the final values of molecular properties from measurements, where the total uncertainties need to be included by summing the experimental and theoretical uncertainties in quadrature [3]. In order to put theoretical uncertainties on the calculated parameters, various factors that determine the theoretical uncertainties are explored and discussed in this chapter as well.

3.2 Hamiltonian

Before proceeding with many-body systems, we first introduce the solution to the Dirac equation for an electron in a central field, which provides the basis for relativistic computational methods. In this case, the Dirac equation can be written as

$$\Big[c\boldsymbol{\alpha}\cdot\boldsymbol{p} + \beta m_e c^2 + V(r)\Big]\psi = E\psi, \tag{3.1}$$

where m_e represents the electron mass, c represents the speed of light, and $\boldsymbol{\alpha}$ and β are the Dirac matrices which are defined as

$$\boldsymbol{\alpha}_i = \begin{pmatrix} \mathbf{0} & \sigma_i \\ \sigma_i & \mathbf{0} \end{pmatrix}, \qquad \beta = \begin{pmatrix} \mathbb{1} & \mathbf{0} \\ \mathbf{0} & -\mathbb{1} \end{pmatrix}. \tag{3.2}$$

The corresponding solution can be chosen as the following form [4]:

$$\psi = i\begin{pmatrix} \frac{G(r)}{r}\chi_{\kappa m} \\ i\frac{F(r)}{r}\chi_{-\kappa m} \end{pmatrix}, \tag{3.3}$$

where n represents the principal quantum number, m represents the magnetic quantum number. The quantum number κ is defined as [4]

$$\kappa = \mp\big(j + \frac{1}{2}\big). \tag{3.4}$$

Here, j represents the total angular momentum quantum number. With the help of Eq. (3.3), the Dirac equation can be written conveniently in following matrix form [4]

$$\begin{pmatrix} m_e c^2 + V(r) & -\hbar c\frac{d}{dr} + \hbar c\frac{\kappa}{r} \\ \hbar c\frac{d}{dr} + \hbar c\frac{\kappa}{r} & -m_e c^2 + V(r) \end{pmatrix} \begin{pmatrix} G(r) \\ F(r) \end{pmatrix} = E \begin{pmatrix} G(r) \\ F(r) \end{pmatrix}. \tag{3.5}$$

Relativistic effects can significantly influence atomic and molecular properties [5], especially for atoms and molecules containing heavy elements. The eigenvalue (energy) for an electron in a Coulomb potential produced by an infinite-mass point charge Ze takes the following form [4, 6]:

$$E = m_e c^2 \Big[1 + \frac{(Z\alpha)^2}{\Big(n - |\kappa| + \sqrt{\kappa^2 - (Z\alpha)^2} \Big)^2} \Big]^{-\frac{1}{2}}. \tag{3.6}$$

It is easy to see that, in the scenario where $Z\alpha \ll 1$, the importance of relativistic effects is approximately proportional to $(Z\alpha)^2$ [4], and thus relativistic effects have more important consequences for heavy elements. Furthermore, parity violating properties are usually induced by the operators containing four-by-four gamma matrices, which reveal their relativistic nature. In such cases, relativistic effects have to be incorporated into the calculation. In this work, the *ab initio* calculations of molecular properties are mainly carried out using the developer's version of the DIRAC package [7], which is a relativistic electronic structure program. Specifically, in the many-electron system, the following (relativistic) 4-component Dirac-Coulomb Hamiltonian is employed with respect to the treatment of relativistic effects,

$$\begin{aligned} H^{\mathrm{DC}} &= \sum_i H_i + \sum_{i<j} \frac{e^2}{r_{ij}} \\ &= \sum_i \Big[c\boldsymbol{\alpha}_i \cdot \boldsymbol{p}_i + \beta_i m_e c^2 + V_n(r_i) \Big] + \sum_{i<j} \frac{e^2}{r_{ij}}, \end{aligned} \tag{3.7}$$

where $V_n(r_i)$ is the nuclear Coulomb potential, which can be chosen as the potential of a point charge or a finite-size charge [8]. In the latter case, the finite-size charge (nucleus) can be modeled by a Gaussian type distribution [9]. The use of Gaussian charge distribution has the advantage that the nucleus-electron attraction integrals and the electron-electron repulsion integrals can be evaluated by the same efficient routines and thus leads to the easy computational implementation [9]. The sum runs over all the electrons in the system. The distance between two electrons is defined as $r_{ij} \equiv |\boldsymbol{r}_i - \boldsymbol{r}_j|$. In practice, the Hamiltonian shifted by the electron rest mass energy ($m_e c^2$) has been widely used [6]:

$$\begin{aligned} H^{\mathrm{DC}} &= \sum_i H_i + \sum_{i<j} \frac{e^2}{r_{ij}} \\ &= \sum_i \Big[c\boldsymbol{\alpha}_i \cdot \boldsymbol{p}_i + (\beta_i - \mathbb{1}) m_e c^2 + V_n(r_i) \Big] + \sum_{i<j} \frac{e^2}{r_{ij}}. \end{aligned} \tag{3.8}$$

The corresponding eigenequation for a given electron can be conveniently written as [6, 10]

$$\begin{pmatrix} V_n & c(\boldsymbol{\sigma}_i \cdot \boldsymbol{p}_i) \\ c(\boldsymbol{\sigma}_i \cdot \boldsymbol{p}_i) & V_n - 2m_e c^2 \end{pmatrix} \begin{pmatrix} \phi_i^L \\ \phi_i^S \end{pmatrix} = \epsilon_i \begin{pmatrix} \phi_i^L \\ \phi_i^S \end{pmatrix}. \tag{3.9}$$

Here, ϕ_i^L and ϕ_i^S represent the large and small components of the relativistic wavefunction. In most cases, the relativistic effects can be sufficiently accounted by the Dirac-Coulomb Hamiltonian. However, the Coulomb potential is not Lorentz invariant and thus is not fully relativistic. In order to compensate for the error due to this limitation, we need to incorporate some important terms arising from higher-order QED [a] corrections in a more rigorous manner. Actually, the relativistic effects are contributed by an infinite number of terms. Among them, the leading contribution to the relativistic effects comes from the Breit term, which is defined as [6, 11–14]

$$B_{ij} = -\frac{e^2 \boldsymbol{\alpha}_i \cdot \boldsymbol{\alpha}_j}{2r_{ij}} - \frac{e^2 (\boldsymbol{\alpha}_i \cdot \boldsymbol{r}_{ij})(\boldsymbol{\alpha}_j \cdot \boldsymbol{r}_{ij})}{2r_{ij}^3}. \tag{3.10}$$

In practice, the Breit term could be rewritten in the following way [14],

$$B_{ij} = -\frac{e^2 \boldsymbol{\alpha}_i \cdot \boldsymbol{\alpha}_j}{r_{ij}} - \frac{e^2 (\boldsymbol{\alpha}_i \cdot \boldsymbol{\nabla}_i)(\boldsymbol{\alpha}_j \cdot \boldsymbol{\nabla}_j) r_{ij}}{2}, \tag{3.11}$$

where the first term is the Gaunt term [15], which gives rise to the leading effects from the Breit term, and the second term is the gauge term, which is less important [13, 14]. Considering the Gaunt term, the following Dirac-Coulomb-Gaunt Hamiltonian has also been widely used [14]:

$$H^{\mathrm{DCG}} = \sum_i H_i + \sum_{i<j} \Big(\frac{e^2}{r_{ij}} + G_{ij} \Big), \tag{3.12}$$

with

$$G_{ij} = -\frac{e^2 \boldsymbol{\alpha}_i \cdot \boldsymbol{\alpha}_j}{r_{ij}}. \tag{3.13}$$

In some cases, the Gaunt term [15] is considered to be important even for some light molecules [16] and thus needs to be taken into account.

In order to decrease computational time and expense while without losing too much predictive accuracy [17–19], the molecular mean-field implementation of the 2-component relativistic (X2Cmmf) Hamiltonian [18, 20, 21] can be employed in the calculations of molecular properties. The main idea behind the

[a] QED denotes Quantum Electrodynamics.

construction of the 2-component (2C) Hamiltonian is to choose an appropriate unitary transformation $\boldsymbol{U}$ to decouple the large and small components of the 4-component (4C) Hamiltonian via a block diagonalization procedure, so that the spectrum of the 4-component Hamiltonian can be reproduced as well as possible [14, 18]. Such procedure can be illustrated by the following expression [14, 18]:

$$\begin{aligned} H^{4\mathrm{C}} &= \boldsymbol{U}^{\dagger} \begin{pmatrix} H_{LL} & H_{LS} \\ H_{SL} & H_{SS} \end{pmatrix} \boldsymbol{U} \\ &= \begin{pmatrix} H_{+} & \mathbf{0} \\ \mathbf{0} & H_{-} \end{pmatrix}, \end{aligned} \tag{3.14}$$

where $H^{2\mathrm{C}} \equiv H_{+}$ is the 2-component Hamiltonian. In order to reduce the computational effort, the smaller component H_{-} can be ignored without losing too much accuracy.

3.3 Basis sets

In computational physics or chemistry, a basis set is a group of functions that can be used to model the nuclear, atomic, and molecular wavefunctions (orbitals). A molecular orbital ϕ_i can be constructed by a linear combination of atomic orbitals (LCAO),

$$\phi_i = \sum_{\beta} C_{i\beta} \xi_{\beta}, \tag{3.15}$$

where ξ_{β} represents atomic orbitals (basis functions). The expansion coefficients $C_{i\beta}$ can be optimized in a manner that the determined energy tends to be converged to a minimum. It is motivated by the form of the electronic wavefunction of a hydrogen atom that a reasonable guess of the atomic orbitals can be the following Slater-type orbitals (STOs) [22]:

$$\xi_{\beta}(\lambda, \boldsymbol{r}) = N_S x^a y^b z^c e^{-\lambda r}, \tag{3.16}$$

which has a well-defined behavior and describes the atomic orbitals more accurately, but has computationally expensive constraints. Alternatively, the following Gaussian-type orbitals (GTOs) have been widely chosen as the basis functions to model atomic orbitals [22]:

$$\xi_{\beta}(\lambda, \boldsymbol{r}) = N_G x^a y^b z^c e^{-\lambda r^2}. \tag{3.17}$$

In the above two equations, the orbital angular momentum quantum number l satisfies the relation $l = a + b + c$, and the radial distance r satisfies the relation $r^2 = x^2 + y^2 + z^2$. The factors N_S and N_G represent the normalization constants.

The exponent of the STOs is a linear function of r while the exponent of the GTOs is a quadratic function of r. The parameter λ describes the radial extent of the orbital. Since the STOs contain the factor $e^{-\lambda r}$, they could model the required characteristics of atomic orbitals naturally. Although the STOs have physically more accurate picture, they are computationally more expensive than the GTOs [23]. Furthermore, the accuracy of the calculation can be improved by linearly combining more GTOs. For these reasons, the GTOs have been widely used in practice.

In the relativistic case, the four-spinor molecular orbitals can be constructed in the following way [24, 25]

$$\phi_i = \begin{pmatrix} \sum\limits_{\mu} C_{i\mu}^{L\alpha} \xi_{\mu}^{L} \\ \sum\limits_{\mu} D_{i\mu}^{L\beta} \xi_{\mu}^{L} \\ i \sum\limits_{\nu} C_{i\nu}^{S\alpha} \xi_{\nu}^{S} \\ i \sum\limits_{\nu} D_{i\nu}^{S\beta} \xi_{\nu}^{S} \end{pmatrix}, \qquad \bar{\phi}_i = \hat{\mathcal{T}} \phi_i = \begin{pmatrix} \sum\limits_{\mu} C_{\bar{i}\mu}^{L\alpha} \xi_{\mu}^{L} \\ \sum\limits_{\mu} D_{\bar{i}\mu}^{L\beta} \xi_{\mu}^{L} \\ i \sum\limits_{\nu} C_{\bar{i}\nu}^{S\alpha} \xi_{\nu}^{S} \\ i \sum\limits_{\nu} D_{\bar{i}\nu}^{S\beta} \xi_{\nu}^{S} \end{pmatrix}. \tag{3.18}$$

Here, ξ_{μ}^{L} and ξ_{ν}^{S} represent the large and small component atomic orbitals, respectively. $\bar{\phi}_i$ represents the Kramers partner of ϕ_i generated by applying the time reversal operator $\hat{\mathcal{T}}$ [6, 25, 26]. In the relativistic case, the molecular orbitals have large and small components and all such components can be modeled by Eq. (3.17). The expansion coefficients $C_{i\mu}^{L\alpha}$, $D_{i\mu}^{L\beta}$, $C_{i\nu}^{S\alpha}$, and $D_{i\nu}^{S\beta}$, in general, are complex numbers. The basis functions employed in describing the large component atomic orbitals are different from the ones employed in describing the small component atomic orbitals. In order to reproduce the non-relativistic limit, the small component atomic orbitals are related to the large component atomic orbitals by the following expression [24, 27, 28]:

$$\xi_{\nu}^{S}(\lambda, \boldsymbol{r}) \simeq \frac{\boldsymbol{\sigma} \cdot \boldsymbol{p}}{2 m_e c} \xi_{\mu}^{L}(\lambda, \boldsymbol{r}). \tag{3.19}$$

The exponents of the basis functions for the small component atomic orbitals are much smaller than the ones for the large component atomic orbitals [29].

In principle, sufficiently large and high-quality basis sets should be used, so that the behavior of the electrons can be well described. However, we also need to take into account the balance between the accuracy and computational feasibility. Actually, various types of basis sets have been developed and used in practice. Among them, we employ the so-called ζ basis sets in the present work. Such basis sets use multiple-ζ basis functions to describe each atomic orbital and could contain both the core and valence orbitals. The ζ basis sets used in this work are Dyall's relativistic valence and core-valence basis sets with various sizes, such

as dyall.v3z, dyall.v4z, dyall.cv3z, and dyall.cv4z [30, 31]. Here, dyall.v3z and dyall.v4z stand for the valence basis sets with triple-ζ and quadruple-ζ functions. The other two stand for the core-valence basis sets with triple-ζ and quadruple-ζ functions. The valence basis sets contain the functions accounting for the electron correlation between the outer shells while the core-valence basis sets contain additional functions for the electron correlation from deep shells. Besides Dyall's standard basis sets, their enlarged versions with additional tight and diffuse functions for each shell are also employed in our calculations.

Basis sets are usually constructed by systematically optimizing them with respect to energies, and thus have sufficiently good performance for predicting energies but may have inadequacies for predicting other properties. In order to compensate for the inadequacies of the basis sets in predicting other properties, an enlargement scheme of basis sets needs to be applied until the convergence of the calculated properties is reached. From a practical point of view, such enlargement of basis sets can be achieved by augmenting Dyall's relativistic basis sets with more tight and diffuse functions. The tight functions are associated with the orbitals that are more contracted on the origin and thus play a significant role in modeling the behavior of electrons close to nucleus. The diffuse functions are associated with the orbitals that are more spread out from the origin and thus take a leading role in modeling the behavior of electrons far away from nucleus. In particular, since the atomic and molecular parity-violating effects mainly arise in the vicinity of the nucleus, augmenting additional tight functions could help improve the accuracy of the calculation. By contrast, chemical bonding mainly depends on the behavior of the electrons in the peripheral region of each atom, where the diffuse functions play an important role, and thus augmenting more diffuse functions would be beneficial for increasing the accuracy of the calculation.

3.4 Computational methods and electron correlation

Electron correlation, which is an instantaneous many-body effect in a quantum system, includes the contributions from the influence of all other electrons on the movement of one electron and from the inadequacy of a single reference determinant in describing the system. The former is known as the dynamical correlation while the latter is known as non-dynamical (or static) correlation [32]. From a practical point of view, electron correlation quantifies inadequacy of the Hartree-Fock (HF) method in describing a quantum system, due to the assumption that the electrons travel independently in a mean field produced by the nuclei and all other electrons [32]. Electron correlation energy can be defined as the difference in the energies between the correlation method and the HF

method and should always be negative because when the electrons travel around they would tend to distribute as far as possible from each other and thus a more adequate method would lower down the energy [32]. The development of various correlation methods that handle electron correlation effects more accurately and more efficiently has been a subject of active research.

In order to investigate the influence of electron correlation on the calculated molecular properties, various electron correlation methods, such as the perturbation method, the coupled cluster method, etc., are employed in this work. The electron correlation methods under discussion in this work are all based on the Dirac-Hartree-Fock (DHF) method, except for the density functional theory (DFT) method. Before proceeding with various correlation methods, we first introduce the HF method in both the non-relativistic and relativistic scenarios. To illustrate the performance of the perturbation method, we perform the calculations using the second-order Møller-Plesset (MP2) method [33]. The coupled cluster method is considered as the state-of-the-art methods in the treatment of electron correlation. In the present work, the molecular properties are investigated by both the relativistic single-reference and multi-reference Fock-space coupled cluster theories. The single-reference coupled cluster calculations are carried out by including single, double, and perturbative triple excitation, namely CCSD and CCSD(T) [34]. The multi-reference Fock-space coupled cluster calculations are carried out by taking into account the single and double excitation, namely FSCCSD. Although the relativistic DFT method [35] does not treat electron correlation in a robust way, in order to compare the performance of various correlation methods, the DFT method is also employed in this work. Furthermore, in order to test the performance of the DFT method, we also perform the calculations with various functionals.

In addition to examining various correlation methods, we also analyze the effects from the truncation of the occupied and virtual orbitals on the calculated molecular properties. It is worth mentioning that, in some cases, if the deep core orbitals and the high virtual orbitals do not play an important role in determining the molecular properties, such orbitals can be safely excluded from the correlation schemes so that computational effort can be considerably reduced without losing too much accuracy.

3.4.1 Dirac-Hartree-Fock method

The Hartree-Fock (HF) method is based on the assumption that each electron travels in the potential generated by the nuclei and in the mean fields generated by all the remaining electrons. Before proceeding with the relativistic HF method, namely the Dirac-Hartree-Fock (DHF) method, a general formalism of the HF method will be briefly reviewed, starting with the definition of the HF

wavefunctions and molecular orbitals. As a basic assumption, the Pauli exclusion principle requires that the HF wavefunction (Φ) for a N-electron system is defined as the following Slater determinant composed of the molecular orbitals ϕ_i [36]:

$$\Phi = \frac{1}{\sqrt{N!}} \begin{vmatrix} \phi_1(1) & \phi_2(1) & \dots & \phi_i(1) & \dots & \phi_N(1) \\ \phi_1(2) & \phi_2(2) & \dots & \phi_i(2) & \dots & \phi_N(2) \\ \dots & \dots & \dots & \dots & \dots & \dots \\ \phi_1(N) & \phi_2(N) & \dots & \phi_i(N) & \dots & \phi_N(N) \end{vmatrix}. \tag{3.20}$$

As defined in Sec. 3.3, the spatial part of the molecular orbitals ϕ_i can be constructed by a linear combination of atomic orbitals (or equivalently basis functions) [37]:

$$\phi_i = \sum_{\beta}^{m} C_{i\beta}\xi_\beta, \tag{3.21}$$

where ξ_β represents atomic orbitals (basis functions), and the sum runs over m atomic orbitals contained in a specific basis set employed in a calculation.

The HF equations can be obtained from the variation principle. If the Hamiltonian (H) of a many-body system, such as an atom or a molecule, is known while the wavefunction (Φ) of this system is unknown, we could use the variational principle to evaluate the ground state energy. For the many-body problem, the exact wavefunction of the system is assumed to be a linear superposition of all the eigen-states of the Hamiltonian. According to the variational principle, the expansion coefficients can be obtained by minimizing the energy. This could result in the following HF equations [36]:

$$F\phi_i = \epsilon_i\phi_i, \tag{3.22}$$

where F is the Fock operator and can be defined as [36, 37]

$$F(\boldsymbol{r}_1) = H(\boldsymbol{r}_1) + \sum_s \Big[j_s(\boldsymbol{r}_1) - k_s(\boldsymbol{r}_1) \Big]. \tag{3.23}$$

Here, the sum runs over all the occupied spin orbitals. In particular, for a closed-shell system with N electrons, the so-called spin-restricted Fock operator can be defined as [37]

$$F(\boldsymbol{r}_1) = H(\boldsymbol{r}_1) + \sum_j^{N/2} \Big[2j_j(\boldsymbol{r}_1) - k_j(\boldsymbol{r}_1) \Big]. \tag{3.24}$$

Here, N is an even number and the sum runs over all the occupied spatial orbitals. $j_j(\boldsymbol{r}_1)$ is the Coulomb operator, which describes the mean potential on electron 1 in orbital i arising from the presence of electron 2 in orbital j, and $k_j(\boldsymbol{r}_1)$ is

the exchange operator, which describes the mean potential on electron 1 due to the exchange process. Such operators can be defined as follows [37, 38]:

$$\begin{aligned} j_j(\boldsymbol{r}_1)\phi_i(\boldsymbol{r}_1) &= \Big[\int d\boldsymbol{r}_2 \frac{e^2|\phi_j(\boldsymbol{r}_2)|^2}{r_{12}}\Big]\phi_i(\boldsymbol{r}_1) \\ &\equiv \langle\phi_j(2)|\frac{e^2}{r_{12}}|\phi_j(2)\rangle|\phi_i(1)\rangle, \end{aligned} \tag{3.25}$$

$$\begin{aligned} k_j(\boldsymbol{r}_1)\phi_i(\boldsymbol{r}_1) &= \Big[\int d\boldsymbol{r}_2 \frac{e^2\phi_j^\dagger(\boldsymbol{r}_2)\phi_i(\boldsymbol{r}_2)}{r_{12}}\Big]\phi_j(\boldsymbol{r}_1) \\ &\equiv \langle\phi_j(2)|\frac{e^2}{r_{12}}|\phi_i(2)\rangle|\phi_j(1)\rangle. \end{aligned} \tag{3.26}$$

In Eq. (3.22), the orbital energy ϵ_i can be expressed (using the final form of orbitals) as follows [37]

$$\begin{aligned} \epsilon_i &= \int d\boldsymbol{r}_1\phi_i^\dagger(\boldsymbol{r}_1)F(\boldsymbol{r}_1)\phi_i(\boldsymbol{r}_1) \\ &= \int d\boldsymbol{r}_1\phi_i^\dagger(\boldsymbol{r}_1)\Big[H(1)+\sum_j\Big(2j_j-k_j\Big)\Big]\phi_i(\boldsymbol{r}_1) \\ &= \int d\boldsymbol{r}_1\phi_i^\dagger(\boldsymbol{r}_1)H(1)\phi_i(\boldsymbol{r}_1)+\sum_j\Big[2\int d\boldsymbol{r}_1\phi_i^\dagger(\boldsymbol{r}_1)j_j\phi_i(\boldsymbol{r}_1)-\int d\boldsymbol{r}_1\phi_i^\dagger(\boldsymbol{r}_1)k_j\phi_i(\boldsymbol{r}_1)\Big] \\ &\equiv E_i+\sum_j\Big(2j_{ij}-k_{ij}\Big). \end{aligned} \tag{3.27}$$

The total HF energy can be obtained by summing over all the orbitals and eliminating double counting [37]:

$$E^{\mathrm{HF}} = 2\sum_i E_i - \sum_{i,j}\Big(2j_{ij}-k_{ij}\Big). \tag{3.28}$$

Using Eq. (3.21), the HF equation (Eq. (3.22)) can be expressed in terms of atomic orbitals as follows [37],

$$F\sum_\beta^m C_{i\beta}\xi_\beta = \epsilon_i\sum_\beta^m C_{i\beta}\xi_\beta. \tag{3.29}$$

On both side of Eq. (3.29), if we multiply by $\xi_\alpha^\dagger$ and integrate, then the following equation can be obtained [37]:

$$\sum_\beta F_{\alpha\beta}C_{i\beta} = \epsilon_i\sum_\beta S_{\alpha\beta}C_{i\beta}, \tag{3.30}$$

which can be written compactly in the following matrix form (Roothaan-Hall equation) [37]:

$$\boldsymbol{FC} = \boldsymbol{\epsilon SC}. \tag{3.31}$$

Here, $\boldsymbol{S}$ is the overlap integral matrix, and its matrix element $S_{\alpha\beta}$ can defined as [37]

$$\begin{aligned} S_{\alpha\beta} &= \int d\boldsymbol{r}_1 \xi_\alpha^\dagger(\boldsymbol{r}_1)\xi_\beta(\boldsymbol{r}_1) \\ &\equiv \langle \xi_\alpha(1)|\xi_\beta(1)\rangle. \end{aligned} \tag{3.32}$$

In Eq. (3.31), $\boldsymbol{F}$ is the Fock matrix, and its matrix element $F_{\alpha\beta}$ can be defined as [37]

$$\begin{aligned} F_{\alpha\beta} &= \int d\boldsymbol{r}_1 \xi_\alpha^\dagger(\boldsymbol{r}_1)F(\boldsymbol{r}_1)\xi_\beta(\boldsymbol{r}_1) \\ &\equiv \langle \xi_\alpha(1)|F(1)|\xi_\beta(1)\rangle. \end{aligned} \tag{3.33}$$

In the relativistic case, with the help of Eq. (3.8), the Fock matrix can be written as [6]

$$\begin{aligned} \boldsymbol{F} &= \begin{pmatrix} F^{LL} & F^{LS} \\ F^{SL} & F^{SS} \end{pmatrix} \\ &= \begin{pmatrix} V_n + \sum\limits_j \Big(j_j - k_j^{LL}\Big) & c(\boldsymbol{\sigma}\cdot\boldsymbol{p}) - \sum\limits_j k_j^{LS} \\ c(\boldsymbol{\sigma}\cdot\boldsymbol{p}) - \sum\limits_j k_j^{SL} & V_n - 2m_e c^2 + \sum\limits_j \Big(j_j - k_j^{SS}\Big) \end{pmatrix}, \end{aligned} \tag{3.34}$$

where j_j represents the relativistic Coulomb operator, which can be written as [39]

$$j_j = \int d\boldsymbol{r}_2 \frac{e^2\phi_j^{L\dagger}(\boldsymbol{r}_2)\phi_j^L(\boldsymbol{r}_2) + e^2\phi_j^{S\dagger}(\boldsymbol{r}_2)\phi_j^S(\boldsymbol{r}_2)}{r_{12}}. \tag{3.35}$$

Here, k_j^{LL}, k_j^{LS}, k_j^{SL}, and k_j^{SS} represent the relativistic exchange operators. We take the operator k_j^{LS} as an example to illustrate the action of such operators on the relativistic wavefunction. The operator k_j^{LS} mixes the large and small components of the relativistic wavefunction in the following way [39]:

$$k_j^{LS}\phi_i^S(\boldsymbol{r}_1) = \Big[\int d\boldsymbol{r}_2 \frac{e^2\phi_j^{S\dagger}(\boldsymbol{r}_2)\phi_i^S(\boldsymbol{r}_2)}{r_{12}}\Big]\phi_j^L(\boldsymbol{r}_1). \tag{3.36}$$

In the relativistic case, the HF equation, i.e. Eq. (3.31), can be written in the following matrix form (the relativistic Roothaan-Hall equation) [6, 40]:

$$\begin{pmatrix} F^{LL} & F^{LS} \\ F^{SL} & F^{SS} \end{pmatrix} \begin{pmatrix} C^L \\ C^S \end{pmatrix} = \boldsymbol{\epsilon} \begin{pmatrix} S^{LL} & 0 \\ 0 & S^{SS} \end{pmatrix} \begin{pmatrix} C^L \\ C^S \end{pmatrix}. \tag{3.37}$$

As can be seen from Eq. (3.31) (or Eq. (3.37)), the Fock matrix $\boldsymbol{F}$ depends on the expansion coefficients $\boldsymbol{C}$. In practice, the HF (or DHF) calculation can be performed by the following steps. To begin with, a trial Fock matrix $\boldsymbol{F}$ and a trial overlap integral matrix $\boldsymbol{S}$ can be constructed with an initial guess of the atomic orbitals ξ_β and the expansion coefficients $C_{i\beta}$. Then, the orbital energies ϵ_i and the new expansion coefficients $C'_{i\beta}$ can be obtained by solving Eq. (3.31). This is a feedback process and can be repeated by constructing a new Fock matrix again using the new expansion coefficients from the last step until the change in the energy or in the expansion coefficients is smaller than a specific threshold.

3.4.2 Density Functional Theory

The density functional theory (DFT) method can treat electron correlation in a computationally cheaper way than the post-HF methods, such as the coupled cluster method, etc. Due to this feature, the DFT method has become one of the most popular tools in many branches of science, such as molecular physics, material physics, etc. Furthermore, compared with other computational methods in this chapter, the DFT method is not based on the wavefunction. Instead, it is based on functionals of electron density. In this formalism, appropriate functionals can be constructed in describing the electron-electron interactions, such as the exchange-correlation interaction, etc. In the relativistic case, the basic equation for the DFT method, namely the Kohn-Sham (KS) equation, can be written as [41–43]

$$\Big[c(\boldsymbol{\alpha}\cdot\boldsymbol{p}) + \beta m_e c^2 + a_\mu v^\mu(\boldsymbol{r})\Big]\phi_i(\boldsymbol{r}) = \epsilon_i \phi_i(\boldsymbol{r}). \tag{3.38}$$

Here, the vector a_μ is defined as $a_\mu \equiv \gamma_0\gamma_\mu$ with γ_0 and γ_μ being the Dirac gamma matrices. The 4-dimensional effective potential operator v^μ, which depends on four-dimensional current $j(\boldsymbol{r})$, is defined as [41–43]

$$v^\mu(\boldsymbol{r}) = v^\mu_{\text{ex}}[j(\boldsymbol{r})] + v^\mu_H[j(\boldsymbol{r})] + v^\mu_{\text{xc}}[j(\boldsymbol{r})]. \tag{3.39}$$

Here, $v^\mu_{\text{ex}}[j(\boldsymbol{r})]$ is the external potential operator, $v^\mu_H[j(\boldsymbol{r})]$ is the direct Hartree energy operator, and $v^\mu_{\text{xc}}[j(\boldsymbol{r})]$ is the exchange-correlation potential operator. The four-dimensional current $j(\boldsymbol{r})$ is defined as [41–43]

$$j(\boldsymbol{r}) = \Big(n(\boldsymbol{r}), \frac{\boldsymbol{j}(\boldsymbol{r})}{c}\Big), \tag{3.40}$$

where $n(\boldsymbol{r})$ is the traditional electron density. The solution to Eq. (3.38) can also be obtained iteratively by requiring that the change in the four-dimensional current $j(\boldsymbol{r})$ between two consecutive iterations is smaller than a specific threshold.

The (relativistic) DFT method does not treat electron correlation in a robust way. Many new density functionals with improved accuracy for the treatment of electron correlation have been proposed. In order to further test the performance of the DFT method, we perform the calculations with various functionals, such as the Slater local exchange (SVWN5) functional [44], the Perdew-Burke-Ernzerhof (PBE) functional [45, 46], the Becke-Lee-Yang-Parr (B3LYP) hybrid functional [47–49] and its adapted version (CAMB3LYP) [50, 51]. The B3LYP functional has improved performance in determining the molecular properties, such as vibrational frequencies, equilibrium bond lengths, etc. The CAMB3LYP has been optimized by reproducing the accurate electron correlation effects obtained from the coupled cluster method and thus is expected to work well for parity-violating effects [51].

3.4.3 Second order Möller-Plesset method

Usually, since the correlation energy is much smaller than the Hartree-Fock (HF) energy, the HF Hamiltonian can be taken as the lowest order approximation to the exact Hamiltonian of the system. In this case, the correlation effect can be treated as a perturbation term in the exact Hamiltonian, which can be formally written as

$$H = H^{\mathrm{HF}} + H^{\mathrm{corr}}, \tag{3.41}$$

where H^{corr} is the perturbation term. The exact energy can be expressed in terms of the corrections of various orders:

$$E = E_0 + E_1 + E_2 + \dots \tag{3.42}$$

Similarly, the exact wavefunction can be expressed as

$$\Psi = \Psi_0 + \Psi_1 + \Psi_2 + \dots \tag{3.43}$$

In Equations (3.42) and (3.43), E_0 is the HF energy and Ψ_0 is the HF wavefunction.

The simplest and widely used correlation method is the second order Möller-Plesset (MP2) method. The general form of the non-relativistic energy correction from the MP2 method can be expressed as [29, 52]

$$E^{\mathrm{MP2}} = \frac{1}{4} \sum_{ij}^{\mathrm{occ}} \sum_{ab}^{\mathrm{vir}} \frac{|\langle ab||ij\rangle|^2}{\epsilon_i + \epsilon_j - \epsilon_a - \epsilon_b}, \tag{3.44}$$

with

$$\langle ab||ij\rangle = \langle ab|ij\rangle - \langle ab|ji\rangle \tag{3.45}$$

and

$$\langle ab|ij\rangle = \int d\boldsymbol{r}_1 \int d\boldsymbol{r}_2 \phi_a^\dagger(\boldsymbol{r}_1)\phi_i(\boldsymbol{r}_1)\frac{e^2}{r_{12}}\phi_b^\dagger(\boldsymbol{r}_2)\phi_j(\boldsymbol{r}_2). \tag{3.46}$$

Here, the indices i and j denote the occupied orbitals and the indices a and b denote the (unoccupied) virtual orbitals. As can be seen, this method is only applicable for atoms or molecules with a large energy gap between the highest occupied and lowest virtual orbitals. In the relativistic case, the energy correction can be expressed as follows [25, 29]:

$$\begin{aligned} E^{\mathrm{MP2}} = \frac{1}{2}\sum_{ij}\sum_{ab}\frac{1}{\epsilon_i+\epsilon_j-\epsilon_a-\epsilon_b}\Big[&|\langle ij||ab\rangle|^2 + |\langle \bar{i}j||ab\rangle|^2 + |\langle i\bar{j}||ab\rangle|^2 \\ &+ |\langle ij||\bar{a}b\rangle|^2 + |\langle ij||a\bar{b}\rangle|^2 + |\langle \bar{i}\bar{j}||a\bar{b}\rangle|^2 + |\langle ij||\bar{a}\bar{b}\rangle|^2 + |\langle \bar{i}\bar{j}||\bar{a}b\rangle|^2\Big], \end{aligned} \tag{3.47}$$

where the barred-spinor represents the Kramers partner of unbarred-spinor generated by the time reversal operator $\hat{\mathcal{T}}$ in Eq. (3.18). The MP2 method takes the virtual orbitals into account, and can improve the HF results significantly and straightforwardly, without requiring very high computational cost. Although it is expected that higher-order Möller-Plesset methods can improve the treatment of electron correlation further, this method faces the slow convergence problem in some cases [53].

3.4.4 Single reference coupled cluster method

In this section, we review the formalism of the single reference coupled cluster (CC) method, which is based on the exponential form of the wave operators and is considered as a powerful tool for the treatment of electron correlation. Before proceeding with the CC method, we first introduce relevant concepts, such as the normal ordering, Wick's theorem, etc. In the second quantization formalism of quantum field theory, a normal ordering means that all the annihilation operators a_j are placed to the right side of all the creation operators $a_i^\dagger$. As an example, the normal-ordered product ($\hat{\mathcal{N}}$) of two operators can be defined as

$$\hat{\mathcal{N}}\left(a_j a_i^\dagger\right) = \epsilon a_i^\dagger a_j, \tag{3.48}$$

where ϵ is a permutation sign and takes the values of $+1$ and -1 for the bosonic and the fermionic field, respectively. The important feature of the normal-ordered product is that its vacuum expectation value is vanishing:

$$\langle\Phi|\hat{\mathcal{N}}\Big(\mathrm{ABCD}\ldots\mathrm{WXYZ}\Big)|\Phi\rangle = 0. \tag{3.49}$$

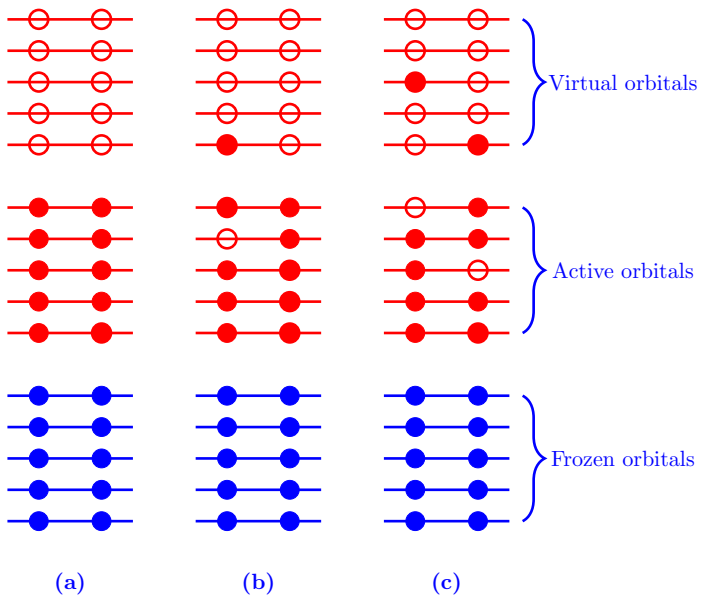

Figure 3.1: Possible diagrams for electron excitation: (a) Hatree-Fock, (b) single excitation, (c) double excitation.

Here, $|\Phi\rangle$ represents the vacuum state and can be chosen as the HF state. The HF energy can be defined as

$$E^{\mathrm{HF}} = \langle\Phi|H|\Phi\rangle. \tag{3.50}$$

In the correlation method, for a specific state, we are interested in the relative energy with respect to the energy for the vacuum state (E^{HF}). According to the definition of the normal-ordered product, the Hamiltonian is normal-ordered in such a way that all the annihilation operators are placed to the right side of the creation operators, and thus in this form the energy for the vacuum state is subtracted automatically [54]:

$$\bar{H} = H - \langle\Phi|H|\Phi\rangle. \tag{3.51}$$

In what follows, the Hamiltonian under discussion refers to the normal-ordered Hamiltonian and for convenience we omit the bar over it. With the help of the normal-ordered product, the contraction between two operators A and B can be written as

$$\overbrace{AB} = AB - \hat{\mathcal{N}}\Big(AB\Big). \tag{3.52}$$

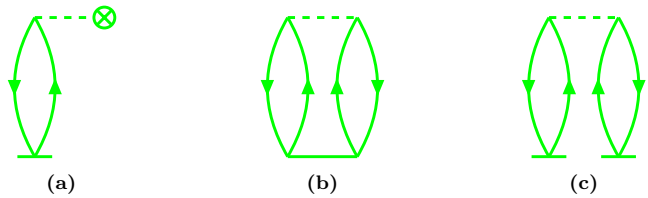

Figure 3.2: All contracted diagrams [55].

Wick's theorem implies that a product of annihilation and creation operators can be expressed as a sum of normal-ordered products with all possible contractions between two operators [54]:

$$\begin{aligned} &ABCD\dots WXYZ \\ =&\hat{\mathcal{N}}\Big(ABCD\dots WXYZ\Big) \\ +&\hat{\mathcal{N}}\Big(\overbracket{A}BCD\dots XYZ + \overbracket{AB}CD\dots WXYZ + \dots + ABCD\dots WX\overbracket{YZ}\Big) \\ +&\hat{\mathcal{N}}\Big(\overbracket{A}B\overbracket{C}D\dots XYZ + \overbracket{A\overbracket{BC}}D\dots WXYZ + \dots + ABCD\dots \overbracket{W}X\overbracket{YZ}\Big) \\ +&\dots \end{aligned} \tag{3.53}$$

where the dots represent all possible other (normal-ordered) contractions.

In the single-reference coupled cluster (CC) approach, in order to construct other configurations, an exponential of the excitation operator $e^{\hat{T}}$ is introduced to act on the HF wavefunction (a Slater-determinant) [56, 57]:

$$|\Psi\rangle = e^{\hat{T}}|\Phi\rangle, \tag{3.54}$$

where $|\Phi\rangle$ and $|\Psi\rangle$ represent the HF and CC wavefunctions, respectively. Here, the excitation operator $\hat{T}$ is defined as [57]

$$\hat{T} = \hat{T}_1 + \hat{T}_2 + ... + \hat{T}_n, \tag{3.55}$$

with

$$\begin{aligned} \hat{T}_n|\Phi\rangle &= \frac{1}{(n!)^2}\sum_{i_1 i_2 \dots i_n}^{\text{occ}}\sum_{a_1 a_1 \dots a_n}^{\text{vir}} t_{i_1 i_2 \dots i_n}^{a_1 a_1 \dots a_n} a_{a_1}^\dagger a_{a_2}^\dagger \dots a_{a_n}^\dagger a_{i_n} \dots a_{i_2} a_{i_1}|\Phi\rangle \\ &= \frac{1}{(n!)^2}\sum_{i_1 i_2 \dots i_n}^{\text{occ}}\sum_{a_1 a_1 \dots a_n}^{\text{vir}} t_{i_1 i_2 \dots i_n}^{a_1 a_1 \dots a_n}|\Phi_{i_1 i_2 \dots i_n}^{a_1 a_1 \dots a_n}\rangle, \end{aligned} \tag{3.56}$$

where the indices i_n and a_n represent the occupied and virtual orbitals, respectively. The CC method with single and double excitation, namely CCSD, is defined by truncating Eq. (3.55) up to the $\hat{T}_2$ level:

$$\hat{T}_{\mathrm{CCSD}} \equiv \hat{T}_1 + \hat{T}_2, \tag{3.57}$$

where the operators $\hat{T}_1$ and $\hat{T}_2$ represent single and double excitation, respectively, and can be defined as [57]

$$\hat{T}_1 = \sum_{i}^{\mathrm{occ}} \sum_{a}^{\mathrm{vir}} t_i^a a_a^\dagger a_i, \tag{3.58}$$

$$\hat{T}_2 = \frac{1}{4} \sum_{ij}^{\mathrm{occ}} \sum_{ab}^{\mathrm{vir}} t_{ij}^{ab} a_a^\dagger a_b^\dagger a_j a_i. \tag{3.59}$$

Fig. 3.1 shows the possible diagrams for the single and double excitation and their connection to the vacuum state, namely the HF state.

The energy of the system can be obtained by acting the Hamiltonian to Eq. (3.54) [57],

$$He^{\hat{T}}|\Phi\rangle = Ee^{\hat{T}}|\Phi\rangle, \tag{3.60}$$

which can be written equivalently as [57]

$$E = \langle\Phi|e^{-\hat{T}}He^{\hat{T}}|\Phi\rangle. \tag{3.61}$$

The operator on the right side of Eq. (3.61) can be expanded explicitly with the help of the Baker-Campbell-Hausdor formula [57],

$$e^{-\hat{T}}He^{\hat{T}} = H + [H,\hat{T}] + \frac{1}{2}[[H,\hat{T}],\hat{T}] + \frac{1}{6}[[[H,\hat{T}],\hat{T}],\hat{T}] + ... \tag{3.62}$$

Furthermore, the following requirements on the amplitude should also be satisfied [57]:

$$\langle\Phi_{ijk...}^{abc...}|e^{-\hat{T}}He^{\hat{T}}|\Phi\rangle = 0. \tag{3.63}$$

In particular, for the CCSD method, the basic equations can be written as [57, 58]

$$\langle\Phi|e^{-\hat{T}}He^{\hat{T}}|\Phi\rangle = E^{\mathrm{CCSD}}, \tag{3.64}$$

$$\langle\Phi_i^a|e^{-\hat{T}}He^{\hat{T}}|\Phi\rangle = 0, \tag{3.65}$$

$$\langle\Phi_{ij}^{ab}|e^{-\hat{T}}He^{\hat{T}}|\Phi\rangle = 0. \tag{3.66}$$

According to Wick's theorem, Equations (3.64), (3.65), and (3.66) can be evaluated in terms of all possible (normal-ordered) contractions. The CCSD energy, arising from the contracted diagrams depicted in Fig. 3.2, can be written as [57, 59]

$$E^{\mathrm{CCSD}} - \langle\Phi|H|\Phi\rangle = \sum_{ia} f_{ia} t_i^a + \frac{1}{4}\sum_{aibj}\langle ij||ab\rangle t_{ij}^{ab} + \frac{1}{2}\sum_{aibj}\langle ij||ab\rangle t_i^a t_j^b. \tag{3.67}$$

Here, the two-particle integral $\langle ab||ij\rangle$ is an anti-symmetrized integral and can be defined as [b] [55]

$$\langle ab||ij\rangle = \langle ab|ij\rangle - \langle ab|ji\rangle. \tag{3.68}$$

The Fock matrix element f_{ia} is defined as [58]

$$f_{ia} = \langle i|H|a\rangle + \sum_s \langle is||as\rangle. \tag{3.69}$$

For $\hat{T}_1$, the amplitude equation, which is related to the diagrams in Fig. 3.3, can be written explicitly as [57, 59]

$$\begin{aligned}
&f_{ai} + \sum_c f_{ac} t_i^c - \sum_k f_{ki} t_k^a + \sum_{kc}\langle ka||ci\rangle t_k^c + \sum_{kc} f_{kc} t_{ik}^{ac} + \frac{1}{2}\sum_{kcd}\langle ka||cd\rangle t_{ki}^{cd} \\
&-\frac{1}{2}\sum_{klc}\langle kl||ci\rangle t_{kl}^{ca} - \sum_{kc} f_{kc} t_i^c t_k^a - \sum_{klc}\langle kl||ci\rangle t_k^c t_l^a + \sum_{kcd}\langle ka||cd\rangle t_k^c t_i^d \\
&-\sum_{klcd}\langle kl||cd\rangle t_k^c t_i^d t_l^a + \sum_{klcd}\langle kl||cd\rangle t_k^c t_{li}^{da} - \frac{1}{2}\sum_{klcd}\langle kl||cd\rangle t_{ki}^{cd} t_l^a \\
&-\frac{1}{2}\sum_{klcd}\langle kl||cd\rangle t_{kl}^{ca} t_i^d = 0.
\end{aligned} \tag{3.70}$$

The explicit form of the amplitude equation for $\hat{T}_2$ is cumbersome and can be found in Refs. [57, 59]. Here, we shall not repeat it in detail. In some cases, the contributions from triple excitation need to be taken into account. In the next subsection, the CCSD method combined with the perturbative triple correction will be discussed.

Similar to the configuration interaction (CI) method, the CC method can also incorporate different orders of excitation into the treatment of electron correlation. In the CI method, the wavefunctions can be constructed by a linear combination of Slater determinants formed from a set of relevant orbitals and

[b] The integral $\langle ab|ij\rangle$ is defined in Eq. (3.46).

the expansion coefficients can be determined variationally by minimizing the total energy. In principle, the accuracy of the CI method can be improved gradually by incorporating more determinants until the full CI limit is reached. The full CI calculation is computationally expensive and usually can not be practically available. In order to make it less computationally demanding, we need to truncate the series of the determinants up to a certain order. Among various truncation schemes, the CI method with single and double excitation (CISD) has been widely employed. Compared with the CISD method, the CCSD method offers a number of competitive advantages. To begin with, unlike the CISD method, the CCSD method employs the so-called exponential parameterization of the wave operators, making it size consistent in such a manner that correct dissociation limits can be yielded in terms of wavefunction and energy [32, 60]. In addition, the CCSD method is also size extensive in such a way that a proper scaling behavior of energy can be obtained with regard to the size of the system [29, 32]. Furthermore, compared with the CISD method, the accuracy of the CCSD method is highly improved, because the CISD method only includes correlation effects up to double excitations while the CCSD method not only includes correlation effects up to double excitations but also approximately includes additional correlation effects from higher-order excitations through the combination of the single and double excitations [61]. However, the CC methods might have difficulties in handling excited states in some cases, where the CI methods would become more suitable [36].

3.4.5 CCSD(T)

A combination of the coupled cluster and perturbation theories has a good performance in describing electron correlation while reducing computational expense considerably. The CC method with triple excitation is computationally demanding [29]. In the present version of the DIRAC program, the triple excitation has not been implemented into the CC equations in an iterative way. Instead, it has been added into the calculations perturbatively based on the CCSD amplitudes [62, 63]. This method is usually denoted as CCSD(T) in *ab initio* calculations. The correlation energy in the CCSD(T) method can be expressed as follows [29, 57, 64, 65]:

$$E_{\mathrm{CCSD(T)}} = E_{\mathrm{CCSD}} + E_{4\mathrm{th}} + E_{5\mathrm{th}}, \tag{3.71}$$

with

$$E_{4\mathrm{th}} = \sum_{i<j<k} \sum_{a<b<c} t_{ijk}^{abc} \Big[P(i|jk) P(a|bc) \Big(\sum_{d} \langle bc||di\rangle t_{jk}^{ad} - \sum_{l} \langle la||jk\rangle t_{il}^{bc} \Big) \Big], \tag{3.72}$$

$$E_{5\mathrm{th}} = \sum_{i,j<k} \sum_{a,b<c} \langle bc||jk\rangle t_{ijk}^{abc} t_{i}^{a}. \tag{3.73}$$

Here, $P(i|jk)$ denotes the permutation operator and is defined in the following way [29, 57, 64, 65]:

$$P(i|jk)f(ijk) = f(ijk) - f(jik) - f(kij). \tag{3.74}$$

In Eq. (3.71), E_{CCSD} represents the CCSD energy, $E_{4\mathrm{th}}$ and $E_{5\mathrm{th}}$ represent the energy corrections from the perturbative triple amplitude in the fourth and fifth orders, respectively. The energy corrections in the second and third orders are contributed from only double substitutions and, as a consequence, all commonly employed iterative techniques incorporate corrections up to the third order [62, 66].

The CCSD(T) method has a wide range of application area in both physics and chemistry, because of its substantial improvements in terms of accuracy-to-cost ratio. However, due to the perturbative nature, the applicability of the CCSD(T) method is restricted to the non-degenerate cases. Besides the CCSD(T) approach, similar methods, such as the CCSD-T and CCSD+T methods, have also been proposed to handle the electron correction from the triple excitation at different levels. In the CCSD-T method [67], further fifth-order terms from the triple excitation are included, while in the CCSD+T method [68], the corrections from the triple excitation are only treated at the fourth-order level.

3.4.6 Fock-space coupled cluster method

The relativistic Fock-space coupled cluster (FSCC) approach is a powerful electronic structure computational tool for the treatment of electron correlation [8, 64, 69–73]. The main feature of this approach is that one calculation can provide molecular properties simultaneously for multiple electronic states. The main idea behind this approach is to divide the Hilbert space into a model space and a (orthogonal) complementary space and then construct an effective Hamiltonian H_{eff} in the model space, which contains active orbitals directly related to the required electronic states and can be enlarged by including more active orbitals. The diagonalization of the effective Hamiltonian provides approximate energies for the required electronic states. Since the diagonalization of the effective Hamiltonian is performed only within the model space, the FSCC method can relatively reduce the computational effort [74], comparing with the full diagonalization over a very large space in the CI methods. Just like the CCSD method, the starting point of the FSCC method is also the HF method, where the closed shell HF determinant is chosen as the vacuum state. All holes and particles can be defined with respect to this vacuum state. The wavefunctions containing m active holes and n active particles in the model space can be denoted as $\Phi^{(m,n)}$. The effective Hamiltonian can be constructed with the help of

the projection operator P, which is defined as [69]

$$P = \sum_{\alpha}^{d} |\Phi_{\alpha}^{(m,n)}\rangle\langle\Phi_{\alpha}^{(m,n)}|, \tag{3.75}$$

where the index α enumerates all the reference determinants in the model space and d represents the dimension of the model space. The projection operator (Q) for the complementary space is defined as [69]

$$Q = \mathbb{1} - P. \tag{3.76}$$

The FSCC method would be more efficient, if the Hilbert space is divided in such a way that the energy levels are very close to each other in the model space while far way from the ones in the complementary space [75]. The zeroth-order wavefunction for the i-th electronic state in the d-dimensional model space is defined as [73]

$$|\Psi_{i(0)}^{(m,n)}\rangle = \sum_{\alpha}^{d} C_{i\alpha}^{(m,n)} |\Phi_{\alpha}^{(m,n)}\rangle, \tag{3.77}$$

where $C_{i\alpha}^{(m,n)}$ denote the expansion coefficients. The exact wavefunction for the i-th electronic state in the d-dimensional model space can be obtained from the zeroth order wavefunction by the following expression [69, 73]:

$$|\Psi_{i}^{(m,n)}\rangle = \Omega |\Psi_{i(0)}^{(m,n)}\rangle, \tag{3.78}$$

with

$$\Omega = \hat{\mathcal{N}}\left(e^{S}\right). \tag{3.79}$$

Here, Ω is the normal-ordered wave operator with $\hat{\mathcal{N}}$ being the normal ordering operator defined in Eq. (3.48). The normal ordering operator guarantees that the equations for the $(0,0)$ sector can be solved without higher-order amplitudes being involved [76]. The excitation operator S with m valence holes and n valence electrons is defined with regard to the closed-shell reference state by the following expression [71–73]:

$$S = \sum_{m\geqslant 0}\sum_{n\geqslant 0}\left(\sum_{l\geqslant m+n} S_{l}^{(m,n)}\right), \tag{3.80}$$

where l is the number of excited electrons. The major part of $|\Psi_{i}^{(m,n)}\rangle$ comes from $|\Psi_{i(0)}^{(m,n)}\rangle$. According to the intermediate normalization, the following expression is satisfied [69]:

$$|\Psi_{i(0)}^{(m,n)}\rangle = P|\Psi_{i}^{(m,n)}\rangle. \tag{3.81}$$

We take the calculation of an electron affinity as an example to illustrate the FSCC formulation. An electron affinity yields the system with zero active hole and one active particle, and can be denoted as the $(0, 1)$ sector. In this case, the first step is to solve the $(0, 0)$ sector, where a Dirac-Hartree-Fock (DHF) calculation followed by a conventional coupled cluster procedure with single and double excitations (CCSD) is carried out for the closed-shell reference state and the corresponding converged amplitudes are obtained iteratively. Based on the results from the first step, active orbitals are selected and the model space is constructed in the second step. Then, equations for the $(0, 1)$ sector can be solved iteratively until a required convergence criterion is satisfied. After that, the following effective Hamiltonian (H^{eff}) can be constructed in the model space based on the previous steps [8, 69–73]:

$$H_{\text{eff}} = PH\Omega P. \tag{3.82}$$

The current version of DIRAC only allows the relativistic FSCC calculations with single and double excitation (namely, the FSCCSD method), and with the number of excited electrons up to 2 ($l \leqslant 2$) [64, 71, 72]. The eigenvalues (energies) corresponding to the model space can be obtained by the diagonalization of the effective Hamiltonian H^{eff}, with the correlation effects for the core and valence electrons being included [70]. Remarkably, the accuracy of the FSCC method can be largely improved by including more active orbitals into the model space.

3.5 Finite field approach

Molecular properties can be calculated analytically or numerically. Usually, there is a difficulty in finding the analytical solutions, mainly because the analytical methods are technically too difficult to be implemented or computationally too expensive to be employed. In this case, the finite field approach can be employed to calculate molecular properties numerically. In the finite field approach, the total Hamiltonian, including the usual unperturbed term H_0 and a perturbative term H_1 arising from the molecular properties, can be written as

$$H = H_0 + \lambda H_1, \tag{3.83}$$

where H_0 is the Hamiltonian excluding perturbation and can be chosen as the Dirac-Coulomb Hamiltonian H^{DC} defined in Eq. (3.7), and λ is a small perturbation parameter. Since the perturbation parameter λ is very small, the total energy can be expanded around $\lambda = 0$ and, to the lowest orders, can be written as

$$E(\lambda) = E(0) + \sum_{k=1} \frac{\lambda^k}{k!} \frac{\partial^k E(\lambda)}{\partial^k \lambda}\bigg|_{\lambda \to 0}. \tag{3.84}$$

Table 3.1: Main possible sources of theoretical uncertainties.

Error sources	
Basis set quality	
Higher l functions	
Basis set augmentations	
	Tight functions
	Diffuse functions
Electron correlation	
	Truncation of the occupied and virtual orbitals
	Residual triple and higher-order excitations
Relativistic effects	
	Higher-order QED corrections, etc.
Others	

The molecular properties of interest in this work are mainly first-order molecular properties. In this case, the general form of molecular properties can be obtained by invoking the Hellmann-Feynman theorem [26, 29]:

$$\begin{aligned} W_g &\simeq \langle \Psi | H_1 | \Psi \rangle \\ &= \left. \frac{\partial E(\lambda)}{\partial \lambda} \right|_{\lambda \to 0}, \end{aligned} \tag{3.85}$$

where $|\Psi\rangle$ represent the wavefunction of the system, W_g represents a generic molecular property, such as the $\hat{\mathcal{P}}$-odd W_A parameter defined in Chapter 5.

3.6 Uncertainty evaluation

Since theoretical results can only be reproduced at the level of uncertainty, any claimed high-accuracy would be meaningless without incorporating the corresponding uncertainty. Theoretical uncertainty arises from imperfect or unknown information within the computational approach, and thus the evaluation of theoretical uncertainty forms an integral part of theoretical investigations. In order to put uncertainties on the calculated parameters (properties), we systematically quantify the main possible sources of uncertainty within our computational approach or methodology. There are a number of possible sources contributed to the theoretical uncertainty in the calculated molecular properties, such as basis set quality, electron correlation, relativistic effect, etc. Tab. 3.1 summarizes the main possible sources of the uncertainties in our calculations.

The uncertainty from basis sets describes the incompleteness in their size and quality. To begin with, we explore the basis set size effects by testing the standard valence and core-valence basis sets with various sizes. Furthermore, we also examine the contributions from the tight and diffuse functions, and, in some cases, we also take into account any further shortfalls of the basis sets. In particular, since the molecular parity-violating effects mainly arise from the regions of the nucleus, augmenting additional tight functions could help reduce the uncertainty of such calculations. By contrast, chemical bondings mainly depend on the behavior of the electrons in the peripheral regions of each atom, where the diffuse functions play an important role. Therefore, augmenting more diffuse functions would be beneficial for decreasing the uncertainty of such calculations. In this manner, the corresponding uncertainty from the incompleteness of the basis sets can be quantified by taking the difference in the calculated values between the optimized basis sets and the ones with additional diffuse and tight functions.

The uncertainty arising from the treatment of electron correlation is contributed by numerous sources, such as the correlation methods, etc. The uncertainty from the correlation methods is mainly from neglecting higher-order excitations. In the CCSD(T) calculation, the contribution of triple excitations is perturbatively taken into account by completely including the fourth order terms and partially including the fifth order terms, while neglecting all the remaining higher-order terms. For the current version of the DIRAC package, although it is impossible to evaluate the corrections from the quadruple or higher-order excitations, the uncertainty from neglecting such higher-order terms can be estimated by examining the results of the CCSD-T and CCSD+T methods. In the CCSD-T method [67], further fifth order terms from the triple excitation are included, while in the CCSD+T method [68] the corrections from the triple excitation are only treated at the fourth order level. As the triple corrections are not significant, we evaluate the uncertainty from the incompetent treatment of electron correlation by taking twice the difference between the CCSD-T and CCSD+T values.

The truncation of the occupied and virtual orbitals also gives rise to uncertainties. In some cases, if the deep core orbitals and the high virtual orbitals do not play an important role in determining molecular properties, such orbitals can be safely excluded from the treatment of electron correlation so that computational effort can be considerably reduced without losing too much accuracy. However, since electron correlation plays a leading role in determining the $\hat{\mathcal{P}}$, $\hat{\mathcal{T}}$-odd molecular properties, all the deep-lying core orbitals and high-lying virtual orbitals need to be included into the treatment of electron correlation in such calculations. The uncertainty arising from neglecting the higher virtual orbitals can be estimated by taking the difference in the calculated values of molecular properties between two virtual orbital cut-offs.

The uncertainty also comes from the approximate treatment of higher-order relativistic effects. Although in most cases the relativistic effects can be sufficiently accounted by the Dirac-Coulomb Hamiltonian, the Coulomb potential is actually not Lorentz-invariant and thus is not completely relativistic. Currently, there is no possibility to incorporate all the relativistic effects, such as the higher-order QED corrections, in a rigorous manner. In practice, we take into account the leading contributions of the remaining relativistic effects by including the Gaunt interaction, which is a part of the Breit interaction. We assume that the effect of replacing the Breit interaction by the Gaunt interaction and neglecting all other higher-order QED corrections is not more than the contribution of the Gaunt interaction itself. Since the Gaunt interaction is implemented at the HF level in the present version of DIRAC, we take the difference between the results with and without the Gaunt interaction as the uncertainty of neglecting the higher-order QED corrections.

Finally, the total theoretical uncertainty can be given by adding all the above uncertainties in quadrature. Besides the above-mentioned sources of uncertainty, an additional source of uncertainty comes from the numerical nature of the finite field approach, where a slight dependence on the size of the perturbation parameters can emerge. For small perturbation parameters, numerical noise might be a factor but in most cases it is negligible. It is worth pointing out that different source of the theoretical uncertainty contributes differently to the total theoretical uncertainty for different molecules. For light molecules, the theoretical uncertainty might be dominated by the basis set effects while for molecules containing heavy elements, the leading contributions to the theoretical uncertainty may come from electron correlations and relativistic effects.

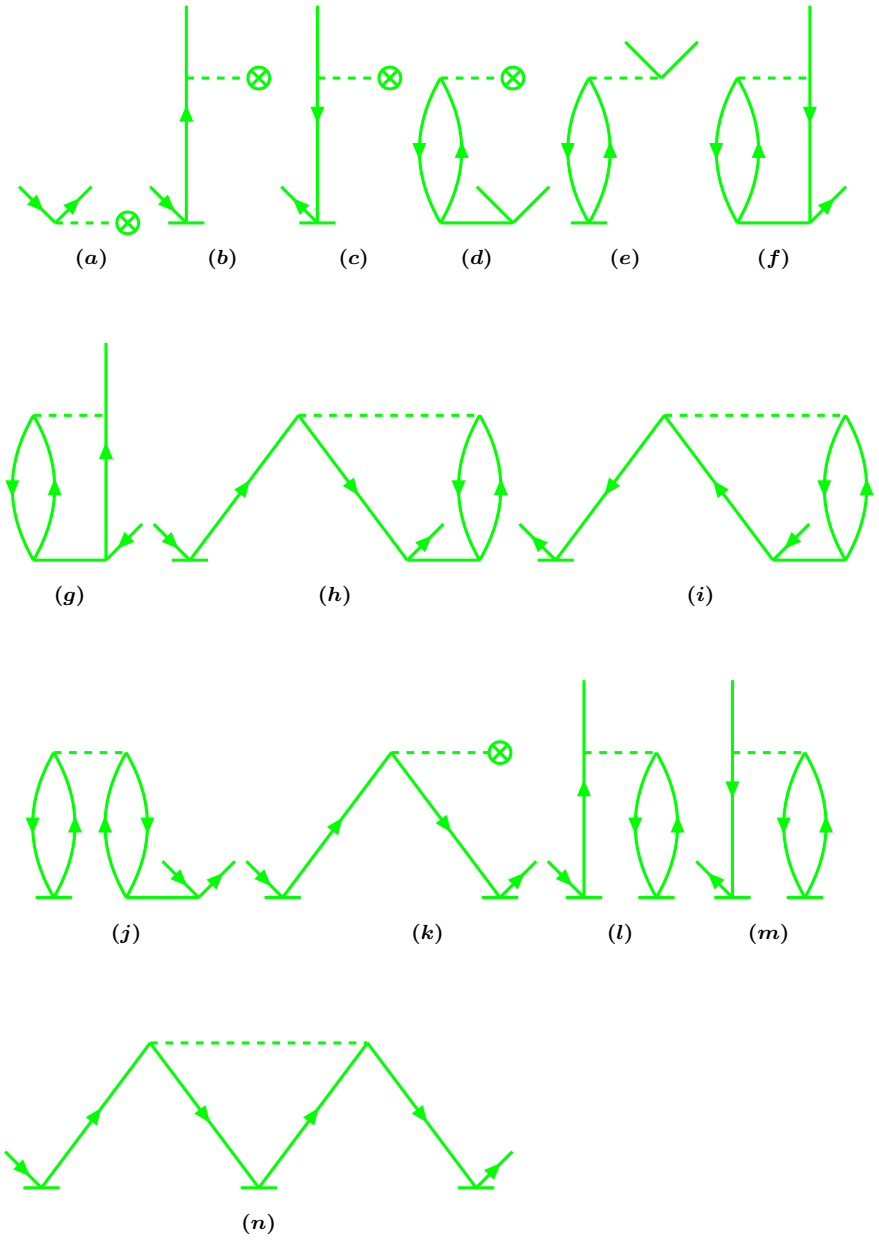

Figure 3.3: One-body intermediate diagrams of the $\hat{T}_1$ amplitude [55]

References

[1] M. S. Safronova, D. Budker, D. DeMille, D. F. J. Kimball, A. Derevianko, and C. W. Clark, Rev. Mod. Phys. **90**, 025008 (2018).

[2] T. G. Bergmann, M. O. Welzel, and C. R. Jacob, Chem. Sci. **11**, 1862 (2020).

[3] A. Derevianko and S. G. Porsev, Eur. Phys. J. A **32**, 517 (2007).

[4] W. Greiner, *Relativistic quantum mechanics* (Springer-Verlag, 1997).

[5] P. Pyykko, Chem. Rev. **88**, 563 (1988).

[6] M. Reiher and A. Wolf, *Relativistic quantum chemistry: the fundamental theory of molecular science* (John Wiley & Sons, 2014).

[7] DIRAC, A relativistic ab initio electronic structure program, Release DIRAC15 (2015), written by R. Bast, T. Saue, L. Visscher, and H. J. Aa. Jensen, with contributions from V. Bakken, K. G. Dyall, S. Dubillard, U. Ekstroem, E. Eliav, T. Enevoldsen, E. Fasshauer, T. Fleig, O. Fossgaard, A. S. P. Gomes, T. Helgaker, J. Henriksson, M. Ilias, Ch. R. Jacob, S. Knecht, S. Komorovsky, O. Kullie, J. K. Laerdahl, C. V. Larsen, Y. S. Lee, H. S. Nataraj, M. K. Nayak, P. Norman, G. Olejniczak, J. Olsen, Y. C. Park, J. K. Pedersen, M. Pernpointner, R. Di Remigio, K. Ruud, P. Salek, B. Schimmelpfennig, J. Sikkema, A. J. Thorvaldsen, J. Thyssen, J. van Stralen, S. Villaume, O. Visser, T. Winther, and S. Yamamoto (see `http://www.diracprogram.org`).

[8] E. Eliav, A. Borschevsky, and U. Kaldor, "High-accuracy relativistic coupled-cluster calculations for the heaviest elements," in *Handbook of relativistic quantum chemistry*, edited by W. Liu (Springer-Verlag, 2017).

[9] L. Visscher and K. G. Dyall, At. Data Nucl. Data Tabl. **67**, 207 (1997).

[10] L. Visscher, P. J. C. Aerts, and O. Visser, in *The Effects of Relativity in Atoms, Molecules, and the Solid State* (Springer-Verlag, 1991) pp. 197–205.

[11] G. Breit, Phys. Rev. **34**, 553 (1929).

[12] H. A. Bethe and E. E. Salpeter, *Quantum mechanics of one-and two-electron atoms* (Springer-Verlag, 1957).

[13] W. Liu, Mol. Phys. **108**, 1679 (2010).

[14] T. Saue, Chem. Phys. Chem. **12**, 3077 (2011).

[15] J. A. Gaunt, Proc. R. Soc. Lond. A **122**, 513 (1929).

[16] O. Visser, L. Visscher, P. Aerts, and W. Nieuwpoort, Theor. Chim. Acta **81**, 405 (1992).

[17] R. Bast, A. J. Thorvaldsen, M. Ringholm, and K. Ruud, Chem. Phys. **356**, 177 (2009).

[18] J. Sikkema, L. Visscher, T. Saue, and M. Iliaš, J. Chem. Phys. **131**, 124116 (2009).

[19] S. Knecht, H. J. A. Jensen, and T. Fleig, J. Chem. Phys. **132**, 014108 (2010).

[20] M. Iliaš and T. Saue, J. Chem. Phys. **126**, 064102 (2007).

[21] T. Saue, J. Chem. Phys. Phys. Chem. **12**, 3077 (2011).

[22] K. I. Ramachandran, G. Deepa, and K. Namboori, *Computational chemistry and molecular modeling: principles and applications* (Springer-Verlag, 2008).

[23] A. J. Thakkar, *Computational chemistry* (2014).

[24] R. E. Stanton and S. Havriliak, J. Chem. Phys. **81**, 1910 (1984).

[25] J. K. Laerdahl, T. Saue, and K. Faegri Jr, Theor. Chem. Account **97**, 177 (1997).

[26] K. G. Dyall and K. Fægri Jr, *Introduction to relativistic quantum chemistry* (Oxford University Press, 2007).

[27] K. G. Dyall, I. P. Grant, and S. Wilson, J. Phys. B: At. Mol. Opt. Phys. **17**, 493 (1984).

[28] P. J. C. Aerts and W. C. Nieuwpoort, Chem. Phys. Lett. **113**, 165 (1985).

[29] M. Iliaš, V. Kelloe, and M. Urban, Acta Phys. Slovaca **60**, 259 (2010).

[30] K. G. Dyall, J. Phys. Chem. A **113**, 12638 (2009).

[31] K. G. Dyall, Theoret. Chem. Acc. **135**, 128 (2016).

[32] R. K. Chaudhuri and S. K. Chattopadhyay, *Many-body methods for atoms and molecules* (CRC Press, 2017).

[33] C. Møller and M. S. Plesset, Phys. Rev. **46**, 618 (1934).

[34] L. Visscher, T. Lee, and K. G. Dyall, J. Chem. Phys. **105**, 8769 (1996).

[35] T. Saue and T. Helgaker, J. Comput. Chem. **23**, 814 (2002).

[36] F. Jensen, *Introduction to computational chemistry* (John Wiley & Sons, 2017).

[37] P. W. Atkins and R. S. Friedman, *Molecular quantum mechanics* (Oxford University Press, 2010).

[38] D. Marx and J. Hutter, *Ab initio molecular dynamics: basic theory and advanced methods* (Cambridge University Press, 2009).

[39] L. Visscher, *Dirac equation and other prerequisites for achieving high accuracy in quantum chemistry* (Vrije Universiteit Amsterdam, 2011).

[40] G. Accaputo, *Advanced quantum chemistry (lecture summary)* (ETH Zurich, 2016).

[41] E. Engel, *Theor. Comput. Chem*, **11**, 523 (2002).

[42] R. Dreizler, in *A primer in density functional theory* (Springer-Verlag, 2003) pp. 123–143.

[43] E. Engel and R. M. Dreizler, *Density functional theory* (Springer-Verlag, 2013).

[44] S. H. Vosko, L. Wilk, and M. Nusair, Canad. J. Phys. **58**, 1200 (1980).

[45] J. P. Perdew, K. Burke, and M. Ernzerhof, Phy. Rev. Lett. **77**, 3865 (1996).

[46] K. Burke, J. P. Perdew, and M. Ernzerhof, Phys. Rev. Lett. **78**, 1396 (1997).

[47] C. Lee, W. Yang, and R. G. Parr, Phys. Rev. B **37**, 785 (1988).

[48] A. D. Becke, J. Chem. Phys. **98**, 5648 (1993).

[49] A. D. Becke, J. Comput. Chem. **20**, 63 (1999).

[50] T. Yanai and D. P. Tew, Chem. Phys. Lett. **393**, 51 (2004).

[51] C. Thierfelder, G. Rauhut, and P. Schwerdtfeger, Phys. Rev. A **81**, 032513 (2010).

[52] C. Møller and M. S. Plesset, Phys. Rev. **46**, 618 (1934).

[53] R. H. Nobes, J. A. Pople, L. Radom, N. C. Handy, and P. J. Knowles, Chem. Phys. Lett. **138**, 481 (1987).

[54] W. Greiner and J. Reinhardt, *Field quantization* (Springer-Verlag, 2013).

[55] R. J. Bartlett and M. Musiał, Rev. Mod. Phys. **79**, 291 (2007).

[56] J. Čížek, Adv. Chem. Phys. **14**, 35 (1969).

[57] T. D. Crawford and H. F. Schaefer, "An introduction to coupled cluster theory for computational chemists," in *Reviews in computational chemistry*, edited by K. B. Lipkowitz and D. B. Boyd (Wiley Online Library, 2000).

[58] T. Papenbrock, *The coupled cluster method* (University of Tennessee, 2018).

[59] D. J. Dean and M. Hjorth-Jensen, Phys. Rev. C **69**, 054320 (2004).

[60] M. Barysz and Y. Ishikawa, *Relativistic methods for chemists*, Vol. 10 (Springer-Verlag, 2010).

[61] L. Meissner, J. GryniakÓw, and I. HubaČ, Mol. Phys. **103**, 2173 (2005).

[62] K. Raghavachari, G. W. Trucks, J. A. Pople, and M. Head-Gordon, Chem. Phys. Lett. **157**, 479 (1989).

[63] R. J. Bartlett, J. D. Watts, S. A. Kucharski, and J. Noga, Chem. Phys. Lett. **165**, 513 (1990).

[64] L. Visscher, T. J. Lee, and K. G. Dyall, J. Chem. Phys. **105**, 8769 (1996).

[65] M. E. Harding, *Large-scale coupled-cluster calculations*, Ph.D. thesis, University of Mainz (2008).

[66] M. Deegan and P. Knowles, Chem. Phys. Lett. **227**, 321 (1994).

[67] M. J. O. Deegan and P. J. Knowles, Chem. Phys. Lett. **227**, 321 (1994).

[68] M. Urban, J. Noga, S. J. Cole, and R. J. Bartlett, J. Chem. Phys. **83**, 4041 (1985).

[69] I. Lindgren and J. Morrison, *Atomic many-body theory* (Springer-Verlag, 1982).

[70] U. Kaldor, Theoretica chimica acta **80**, 427 (1991).

[71] E. Eliav, U. Kaldor, and Y. Ishikawa, Phys. Rev. A **49**, 1724 (1994).

[72] L. Visscher, E. Eliav, and U. Kaldor, J. Chem. Phys. **115**, 9720 (2001).

[73] D. I. Lyakh, M. Musiał, V. F. Lotrich, and R. J. Bartlett, Chem. Rev. **112**, 182 (2011).

[74] P. Tecmer and C. E. González-Espinoza, Phys. Chem. Chem. Phys. **20**, 23424 (2018).

[75] W. Kutzelnigg, "Quantum chemistry in fock space," in *Aspects of many-body effects in molecules and extended systems*, edited by D. Mukherjee (Springer-Verlag, 1988).

[76] L. Ravichandran, D. Bhattacharya, N. Vaval, and S. Pal, J. Chem. Sci. **124**, 223 (2012).

Chapter 4

Molecular structure

4.1 Overview

The spectra and properties of diatomic molecules are determined by numerous motions, such as electronic excitation, vibrations of nuclei, rotations of the whole molecule around its molecular axis [1], etc. The motional characteristics of diatomic molecules provides more detailed information and new insights on dynamics and internal structure of many-body system [2], despite making it more complicated than that of atoms. Furthermore, in order to facilitate the measurement, external fields, such as the electric and magnetic fields, are often applied to molecules, causing the interactions inside them to be even more complicated. For example, in the measurement of parity-violating nuclear anapole moment effects, external magnetic fields need to be applied so that the molecular levels with opposite parity can be brought into near degeneracy, resulting in great enhancement of the effect. Additionally, in order to further amplify the tiny parity-violating effect, external electric fields can be applied in such a way that the interference between the parity-violating amplitudes and the Stark-induced amplitudes leads to dramatic signal amplification [3, 4].

Due to the complexity of many-body systems, such as diatomic molecules, it is impossible to solve the dynamical equations exactly and describe the behavior of the electrons comprehensively without making any approximations. The first approximation we employ is the Born-Oppenheimer approximation, which arises from the consideration that nuclei are much heavier and move much slower than electrons. Although the electronic wavefunction depends on the internuclear distance, the influence of the nuclear motion on the electronic wavefunction is negligible. Similarly, since some of the interactions (or couplings) inside a diatomic molecule are more important than others in determining molecular properties, a

number of additional approximations are necessary in the calculations and analyses. In this chapter, for a better understanding about molecular structure and dynamics, we focus on the interactions and couplings between different degrees of freedoms, such as electronic excitations, vibrations, rotations, etc. We address the hierarchy of these interactions (or couplings) and introduce some important additional approximations, such as the so-called Hund's coupling cases and the Franck-Condon approximation, which have been widely employed for the calculations of the molecular properties under discussion.

This chapter is organized as follows. To begin with, we introduce some useful molecular symbols involved in this work and review the general form of molecular Hamiltonian, which serves as the basis for the rest of the discussions. In order to investigate the parity violating effects, it is necessary to analyze the symmetry properties of a specific molecular state under parity transformation. This can be achieved by examining Hund's coupling cases and choosing approximately good quantum numbers. Hund's coupling cases are the basic assumptions in describing the rotational states of diatomic molecules based on the relative strengths of the couplings between different angular momenta. Moreover, based on such information, we introduce the symmetry properties of diatomic molecules, which play an important role in the measurement of parity-violating effects in such molecules. In addition, we briefly review the Franck-Condon approximation, which plays a leading role in quantitatively describing electromagnetic transitions in molecules. After that, we introduce the corresponding selection rules for electric dipole transitions.

4.2 Molecular symbols

Following Refs. [5–7], the molecular symbols involved in the present work are defined and summarized in Tab. 4.1. The electronic spin angular momentum can be denoted by $\boldsymbol{S}$ and its projection on molecular axis can be denoted by Σ. The electronic orbital angular momentum can be denoted by $\boldsymbol{L}$ and its projection on molecular axis can be denoted by Λ. The nuclear rotation and spin angular momenta can be denoted by $\boldsymbol{R}$ and $\boldsymbol{I}$, respectively. The vector sum of the electronic and orbital angular momenta can be defined as $\boldsymbol{J}_{\mathrm{so}} \equiv \boldsymbol{L} + \boldsymbol{S}$. The total angular momentum excluding the nuclear spin angular momentum can be defined as $\boldsymbol{J} \equiv \boldsymbol{L} + \boldsymbol{S} + \boldsymbol{R}$ and its projection on molecular axis can be denoted by Ω. The total angular momentum can be defined as $\boldsymbol{F} \equiv \boldsymbol{J} + \boldsymbol{I}$. The vector sum of the nuclear rotation and the electronic orbital angular momenta can be defined as $\boldsymbol{N} \equiv \boldsymbol{R} + \boldsymbol{L}$ and its projection on molecular axis can be denoted by Λ too. Throughout this work, unless otherwise specified explicitly, the quantities in bold font represent vectors while the quantities in normal font represent their magnitudes.

4.3 External fields

In the measurement of the nuclear anapole moment effect, external magnetic fields need to be applied so that the molecular levels with opposite parity can be brought into near degeneracy, causing significant enhancement of the effect. Furthermore, in the presence of external electric fields, the interference between the parity-violating amplitudes and the Stark-induced amplitudes provides a huge amplification of the signal. The effective Hamiltonian for a diatomic molecule in the presence of the external electric and magnetic fields can be written as

$$H_{\rm tot} \simeq H_{\rm mol} + H_{\rm s} + H_{\rm z}, \tag{4.1}$$

where $H_{\rm mol}$ represents the effective Hamiltonian for the diatomic molecule in the absence of the external fields and will be discussed in more detail later on. In the presence of an (static) electric field $\boldsymbol{E}$, the interaction can be described by the Stark Hamiltonian $H_{\rm s}$, which can be defined as

$$H_{\rm s} = -\boldsymbol{\mu}_E \cdot \boldsymbol{E} - \frac{1}{2}\boldsymbol{E} \cdot \boldsymbol{\alpha}_E \cdot \boldsymbol{E} + \ldots \tag{4.2}$$

where $\boldsymbol{\mu}_E$ and $\boldsymbol{\alpha}_E$ represent the molecular dipole moment and polarizability tensor, respectively. Here, we only include the linear and quadratic terms. In the presence of an external magnetic field $\boldsymbol{B}$, the interaction can be described by the Zeeman Hamiltonian $H_{\rm z}$, which can be approximately written as

$$H_{\rm z} = -\boldsymbol{\mu}_B \cdot \boldsymbol{B}, \tag{4.3}$$

where $\boldsymbol{\mu}_B$ represents the magnetic dipole moment.

Table 4.1: Molecular symbols involved in the present work (see e.g. Ref. [5–7]).

Angular momenta	Operators	Quantum numbers	Projections
Electronic spin	$\boldsymbol{S}$	S	Σ
Electronic orbital	$\boldsymbol{L}$	L	Λ
Nuclear rotation	$\boldsymbol{R}$	R	-
$\boldsymbol{L}+\boldsymbol{S}$	$\boldsymbol{J}_{\rm so}$	$J_{\rm so}$	-
$\boldsymbol{L}+\boldsymbol{S}+\boldsymbol{R}$	$\boldsymbol{J}$	J	Ω
$\boldsymbol{R}+\boldsymbol{L}$	$\boldsymbol{N}$	N	Λ
$\boldsymbol{J}+\boldsymbol{I}$	$\boldsymbol{F}$	F	-

4.4 Born-Oppenheimer approximation

Without external fields, the general form of the molecular Hamiltonian for a diatomic molecule can be written as

$$H_{\mathrm{mol}} \equiv T_e(\boldsymbol{\nabla}_{\boldsymbol{r}}) + T_n(\boldsymbol{\nabla}_{\boldsymbol{R}}) + V_{\mathrm{ee}}(\boldsymbol{r}) + V_{\mathrm{nn}}(\boldsymbol{R}) + V_{\mathrm{ne}}(\boldsymbol{r}, \boldsymbol{R}), \tag{4.4}$$

which formally satisfies the following equation:

$$H_{\mathrm{mol}}\Psi_{\mathrm{mol}}(\boldsymbol{r}, \boldsymbol{R}) = E_{\mathrm{mol}}\Psi_{\mathrm{mol}}(\boldsymbol{r}, \boldsymbol{R}). \tag{4.5}$$

Here, $\boldsymbol{r}$ and $\boldsymbol{R}$ represent the electronic and nuclear coordinates, respectively. $\Psi_{\mathrm{mol}}(\boldsymbol{r}, \boldsymbol{R})$ and E_{mol} are the total molecular wavefunction and energy, respectively. $T_e(\boldsymbol{\nabla}_{\boldsymbol{r}})$ and $T_n(\boldsymbol{\nabla}_{\boldsymbol{R}})$ represent the electronic and nuclear kinetic energy operators, respectively. $V_{\mathrm{ee}}(\boldsymbol{r})$ represents the electrostatic potential energy operator between electrons. $V_{\mathrm{nn}}(\boldsymbol{R})$ represents the electrostatic potential energy operator between nuclei. $V_{\mathrm{ne}}(\boldsymbol{r}, \boldsymbol{R})$ represents the electrostatic potential energy between nuclei and electrons and depends on the coordinates of the electrons and nuclei.

The Born-Oppenheimer approximation can be divided into two steps [8, 9]. To begin with, since nuclei are much heavier than electrons, they could not respond as fast as the electronic transition occurs. Although the electronic wavefunction depends on the internuclear distance, the influence of the nuclear motion on the electronic wavefunction is negligible. The nuclear coordinate $\boldsymbol{R}$ can be assumed to be fixed in electronic transitions and the nuclear kinetic energy operator $T_n(\boldsymbol{\nabla}_{\boldsymbol{R}})$ can be considered to be negligible in the molecule-fixed frame. In this case, the electronic wavefunction and energy only depend parametrically on the fixed nuclear coordinate $\boldsymbol{R}$. Moreover, the energy arising from the electrostatic interactions between nuclei can be treated as a constant and thus $V_{\mathrm{nn}}(\boldsymbol{R})$ can be isolated from the molecular Hamiltonian. Therefore, Eq. (4.5) can be approximately written as [8, 9]

$$\Big[H_e + T_n(\boldsymbol{\nabla}_{\boldsymbol{R}}) + V_{\mathrm{nn}}(\boldsymbol{R})\Big]\Psi_e(\boldsymbol{r}|\boldsymbol{R})\Psi_n(\boldsymbol{R}) = \Big(E_e + E_n\Big)\Psi_e(\boldsymbol{r}|\boldsymbol{R})\Psi_n(\boldsymbol{R}), \tag{4.6}$$

with

$$H_{\mathrm{mol}} = H_e + T_n(\boldsymbol{\nabla}_{\boldsymbol{R}}) + V_{\mathrm{nn}}(\boldsymbol{R}), \tag{4.7}$$

$$H_e = T_e(\boldsymbol{\nabla}_{\boldsymbol{r}}) + V_{\mathrm{ee}}(\boldsymbol{r}) + V_{\mathrm{ne}}(\boldsymbol{r}, \boldsymbol{R}), \tag{4.8}$$

$$\Psi_{\mathrm{mol}}(\boldsymbol{r}, \boldsymbol{R}) = \Psi_e(\boldsymbol{r}|\boldsymbol{R})\Psi_n(\boldsymbol{R}), \tag{4.9}$$

$$E_{\mathrm{mol}} = E_e + E_n. \tag{4.10}$$

In the above equations, $\Psi_n(\boldsymbol{R})$ and $\Psi_e(\boldsymbol{r}|\boldsymbol{R})$ are the nuclear and electronic wavefunctions, respectively. E_n and E_e represent the nuclear and electronic energies, respectively. To summarize, the Born-Oppenheimer approximation is based on the consideration that nuclei are much heavier and thus move much slower than electrons, making it possible to treat the motions of nuclei and electrons separately. Although the electronic wavefunction depends on the fixed nuclear coordinates, the nuclear motion has negligible effect on the electronic wavefunction.

4.5 Effective Hamiltonian

The effective Hamiltonian for the rotational spectra of a diatomic molecule in the absence of the external fields can be approximately written as [1, 6, 7, 10–13]

$$H_{\text{eff}} \simeq H_{\text{rot}} + H_{\text{cd}} + H_{\text{so}} + H_{\text{ss}} + H_{\text{sr}} + H_{\text{ld}} + H_{\text{hfs}}, \tag{4.11}$$

with

$$H_{\text{rot}} \simeq B_{\text{rot}}\boldsymbol{R}^2, \tag{4.12}$$

$$H_{\text{cd}} \simeq -D_{\text{cd}}\boldsymbol{R}^4, \tag{4.13}$$

$$H_{\text{so}} \simeq A_{\text{so}}\boldsymbol{L}\cdot\boldsymbol{S}, \tag{4.14}$$

$$H_{\text{ss}} \simeq -\frac{2}{3}\lambda_{\text{ss}}\Big(\boldsymbol{S}^2 - 3S_z^2\Big), \tag{4.15}$$

$$H_{\text{sr}} \simeq \gamma_{\text{sr}}\boldsymbol{S}\cdot\boldsymbol{R}. \tag{4.16}$$

Here, H_{rot} represents the rotational interaction term and B_{rot} is the rotational constant. This term will be discussed in more detail in the next section. H_{cd} represents the centrifugal distortion interaction term and D_{cd} represents the quartic centrifugal distortion constant. H_{so} represents the spin-orbit interaction term and A_{so} is the spin-orbit splitting constant. H_{ss} represents the spin-spin interaction term and λ_{ss} is the spin-spin coupling constant. H_{sr} represents the spin-rotation interaction term and γ_{sr} is the spin-rotation coupling constant. H_{ld} represents the Λ-doubling interaction term and its explicit form can be found in Ref. [1]. H_{hfs} represents the hyperfine structure interaction term, which, to the lowest orders, can be written as

$$H_{\text{hfs}} \simeq H_{\text{mhf}} + H_{\text{eqd}}, \tag{4.17}$$

where H_{mhf} represents the magnetic hyperfine interaction term and H_{eqd} represents the electric quadrupole moment interaction term. The magnetic hyperfine interaction term H_{mhf} can be written as

$$H_{\text{mhf}} \simeq a\boldsymbol{I}\cdot\boldsymbol{L} + b\boldsymbol{I}\cdot\boldsymbol{S} + cI_zS_z \tag{4.18}$$

where a, b, and c are the Frosch-Foley parameters [14]. Alternatively, in the presence of axial symmetry, the magnetic hyperfine interaction term can also be written as [15]

$$H_{\mathrm{mhf}} \simeq A_{\parallel} S_z I_z + A_{\perp}\Big(S_x I_x + S_y I_y\Big), \tag{4.19}$$

where $A_{\parallel}$ and $A_{\perp}$ are the parallel and perpendicular components of the magnetic hyperfine structure constant and can be defined as follows [15, 16]:

$$A_{\parallel} = \frac{\mu_N}{I\Omega}\langle \pm| \left(\frac{\boldsymbol{\alpha}\times\boldsymbol{r}}{r^3}\right)_z |\pm\rangle, \tag{4.20}$$

$$A_{\perp} = \frac{\mu_N}{I\Omega}\langle \pm| \left(\frac{\boldsymbol{\alpha}\times\boldsymbol{r}}{r^3}\right)_{x,y} |\mp\rangle. \tag{4.21}$$

Here, μ_N is the nuclear magnetic moment. Obviously, the Frosch-Foley parameters are related to $A_{\parallel}$ and $A_{\perp}$ in the following way [17]

$$b = A_{\perp}, \tag{4.22}$$

$$c = A_{\parallel} - A_{\perp}. \tag{4.23}$$

The electric quadrupole moment interaction term H_{eqd} can be approximately written as [1]

$$H_{\mathrm{eqd}} \simeq \frac{eqQ(3I_z^2 - \boldsymbol{I}^2)}{4I(2I-1)}, \tag{4.24}$$

where eqQ is the electric quadrupole moment coupling constant.

4.6 Hund's coupling cases

In order to investigate the parity-violating effects, it is necessary to analyze the symmetry properties of a specific molecular state under parity transformation. Such symmetry properties can be represented by (approximately) good quantum numbers. The choice of (approximately) good quantum numbers can be classified into Hund's coupling cases [1, 7]. In diatomic molecules, there are three main types of interactions (couplings) between angular momenta, such as the coupling between $\boldsymbol{L}$ and $\boldsymbol{S}$, the coupling between $\boldsymbol{L}$ and molecular axis, and the coupling between $\boldsymbol{J}_{\mathrm{so}}$ and $\boldsymbol{J}$. Hund's coupling cases are the basic assumptions in describing the rotational states of diatomic molecules based on the relative strengths with respect to the above-mentioned types of interactions (couplings). Tab. 4.2 summarizes the coupling strengths between angular momenta and the corresponding Hund's coupling cases. Hund's coupling case (a), (b), (c), and (d) are the most commonly used ones. Figures 4.1 and 4.2 show the vector diagrams for Hund's coupling cases (a), (b), (c), and (d).

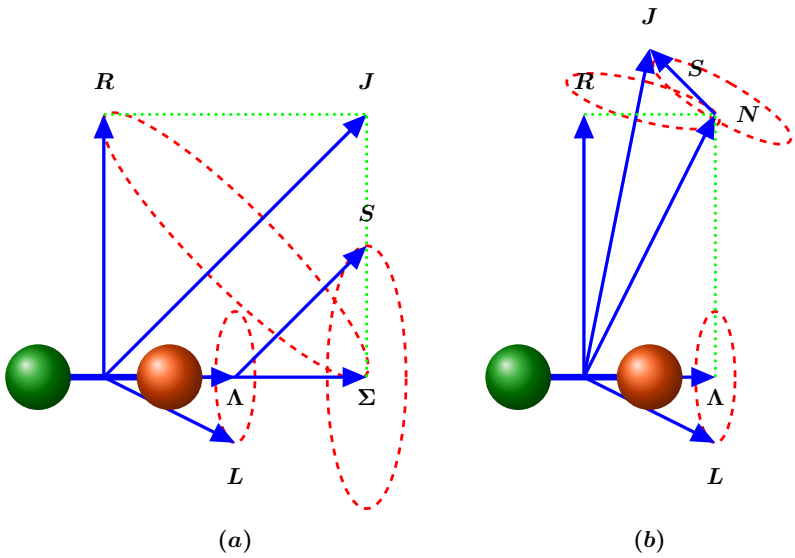

Figure 4.1: Hund's coupling case (a) and (b).

4.6.1 Case (a)

Hund's coupling case (a) assumes that the orbital angular momentum $\boldsymbol{L}$ is strongly coupled to the molecular axis, and both $\boldsymbol{L}$ and $\boldsymbol{S}$ have well-defined projections on the molecular axis, namely Λ and Σ. The good quantum numbers can be chosen as Λ, S, Σ, Ω, and J. In this case, the rotational Hamiltonian can be written as [1, 7]

$$H_{\text{rot}} = B(\boldsymbol{J} - \boldsymbol{L} - \boldsymbol{S})^2, \tag{4.25}$$

where B is the rotational constant. The corresponding rotational energy can be written as [9, 18–20]

$$E(J) = BJ(J+1). \tag{4.26}$$

4.6.2 Case (b)

Hund's coupling case (b) assumes that the spin-orbit coupling is not strong, i.e. $\boldsymbol{L}$ and $\boldsymbol{S}$ are decoupled. In addition, $\boldsymbol{S}$ is coupled to $\boldsymbol{N}$ while $\boldsymbol{L}$ is still coupled to the molecular axis. The good quantum numbers can be chosen as Λ, N, S, and J. In this case, the rotational Hamiltonian can be written as [1, 7]

$$H_{\text{rot}} = B(\boldsymbol{N} - \boldsymbol{L})^2, \tag{4.27}$$

Electrostatic	Rotational	Spin-orbit	Hund's coupling cases
Strong	Weak	Intermediate	(a)
Strong	Intermediate	Weak	(b)
Intermediate	Weak	Strong	(c)
Intermediate	Strong	Weak	(d)

Table 4.2: Coupling strengths between the angular momenta and the corresponding Hund's coupling cases [1, 7].

where B is the rotational constant. The corresponding rotational energy can be written as [9, 18–20]

$$E(N) = BN(N+1). \tag{4.28}$$

4.6.3 Case (c)

Hund's coupling case (c) assumes that, compared with the coupling to the molecular axis, the spin-orbit coupling is much stronger and yields $\boldsymbol{J}_{\mathrm{so}}$. The vector $\boldsymbol{J}$ is given by the coupling between the projection of $\boldsymbol{J}_{\mathrm{so}}$ onto the molecular axis and the nuclear rotation $\boldsymbol{R}$. The good quantum numbers can be chosen as J_{so}, J, and Ω. In this case, the rotational Hamiltonian can be written as [7]

$$H_{\mathrm{rot}} = B(\boldsymbol{J} - \boldsymbol{J}_{\mathrm{so}})^2, \tag{4.29}$$

where B is the rotational constant. The corresponding rotational energy can be written as [18, 19]

$$E(J) = BJ(J+1). \tag{4.30}$$

4.6.4 Case (d)

Hund's coupling case (d) assumes that the coupling between $\boldsymbol{L}$ and $\boldsymbol{R}$ is much stronger than their couplings to the molecular axis and such coupling forms $\boldsymbol{N}$. Then the coupling between $\boldsymbol{N}$ and $\boldsymbol{S}$ yields $\boldsymbol{J}$. The good quantum numbers can be chosen as S, L, J, R, and N. In this case, the rotational Hamiltonian can be written as [1, 7]

$$H_{\mathrm{rot}} = B\boldsymbol{R}^2, \tag{4.31}$$

where B is the rotational constant. The corresponding rotational energy can be written as [1, 9, 13, 18–20]

$$E(R) = BR(R+1). \tag{4.32}$$

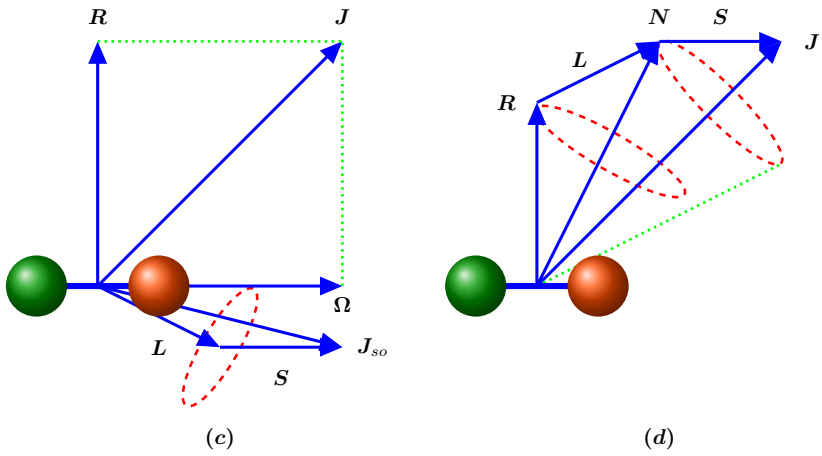

Figure 4.2: Hund's coupling case (c) and (d).

4.7 Symmetry properties of diatomic molecules

In the measurement of parity-violating effects, in order to draw definite conclusions about whether a specific transition violates parity, the symmetry properties of molecular states under parity transformation need to be known. Such symmetry properties can be explored with the help of Hund's coupling cases introduced in Section 4.6. For diatomic molecules, parity is one of the most important symmetry properties we are interested in. All the molecular transitions induced by electromagnetic interactions preserve parity, and thus parity should be taken into account in determining the selection rules for electromagnetic transitions. The total wavefunction of a diatomic molecule can be factorized into three parts [1, 6, 7, 9, 13, 18, 19]:

$$\Psi_{\rm mol} = \Psi_{\rm ele}\Psi_{\rm rot}\Psi_{\rm vib}, \tag{4.33}$$

where $\Psi_{\rm ele}$, $\Psi_{\rm rot}$, and $\Psi_{\rm vib}$ represent (pure) electronic, rotational, and vibrational wavefunctions, respectively. In this case, the symmetry property of a diatomic molecule under parity transformation is determined by the symmetry properties of these three parts. In the molecule-fixed frame, the parity transformation $\hat{\mathcal{P}}$ is equivalent to the reflection transformation $\hat{\sigma}_v$ with respect to the plane containing the rotation axis [1, 6, 7, 9, 13, 18, 19, 21]. For this reason, we only need to focus on the molecule-fixed frame, where parity transformation $\hat{\mathcal{P}}$ can be replaced

with the reflection transformation $\hat{\sigma}_v$ [a]. As an example, we introduce the effect of parity transformation on the wavefunction of a diatomic molecule based on Hund's coupling case (a).

In Hund's coupling case (a), the (pure) electronic part (Ψ_{ele}) of the molecular wavefunction can be written as [1, 6, 7, 9, 13, 18, 19, 21]

$$\Psi_{\text{ele}} = |\chi, \Lambda\rangle|S, \Sigma\rangle. \tag{4.34}$$

Here, $|\chi, \Lambda\rangle$ and $|S, \Sigma\rangle$ represent the orbital and spin parts of the electronic wavefunction, respectively, and χ represents all other quantum numbers. The orbital wavefunction has the following symmetry property under parity transformation [1, 6, 7, 9, 13, 18, 19, 21]:

$$\hat{\mathcal{P}}|\chi, \Lambda\rangle = (-1)^{\Lambda+\Theta}|\chi, -\Lambda\rangle. \tag{4.35}$$

Here, Θ takes the value of 1 for the Σ^- states and takes the value of 0 for all other states. Particularly, for the states with $\Lambda = 0$, the symmetry property under parity transformation takes the following form [9, 18, 19]:

$$\hat{\mathcal{P}}|\Sigma^{\pm}\rangle = \pm|\Sigma^{\pm}\rangle. \tag{4.36}$$

The spin wavefunction has the following symmetry property under parity transformation [1, 6, 7, 9, 13, 18, 19, 21]:

$$\hat{\mathcal{P}}|S, \Sigma\rangle = (-1)^{S-\Sigma}|S, -\Sigma\rangle. \tag{4.37}$$

In diatomic molecules, since the vibrational wavefunction only depends on the magnitude of the internuclear distance R, it does not change sign under parity transformation [1, 6, 7, 9, 13, 18, 19]:

$$\begin{aligned} \hat{\mathcal{P}}\Psi_{\text{vib}} &= \hat{\mathcal{P}}|v\rangle \\ &= (+1)|v\rangle. \end{aligned} \tag{4.38}$$

Here, v represents the vibrational quantum number.

In diatomic molecules, the rotational wavefunction describes how the molecule-fixed coordinates are transformed with respect to the space-fixed coordinates [1, 6, 7, 9, 13, 18, 19, 21]. The symmetry property of the rotational wavefunction under parity transformation is more complicated than that of the electronic and vibrational wavefunctions. In Hund's coupling case (a), it takes the following form [1, 6, 7, 9, 13, 18, 19, 21]:

$$\begin{aligned} \hat{\mathcal{P}}\Psi_{\text{rot}} &= \hat{\mathcal{P}}|J, \Omega, M\rangle \\ &= (-1)^{J-\Omega}|J, -\Omega, M\rangle, \end{aligned} \tag{4.39}$$

[a] Rigorously, a reflection transformation is different from a parity transformation in three dimensional space.

where J represents the quantum number of the total angular momentum excluding the nuclear spin. The second quantum number Ω represents the projection of the total angular momentum on the molecular axis in the molecule-fixed frame. The third quantum number M represents the projection of the total angular momentum on the molecular axis in the space-fixed frame.

Combining Equations 4.35, 4.37, 4.38, and 4.39, we obtain the total symmetry property for the molecular wavefunction of a diatomic molecule under parity transformation [1, 6, 7, 9, 13, 18, 19]:

$$\begin{aligned}\hat{\mathcal{P}}\Psi_{\text{ele}}\Psi_{\text{rot}}\Psi_{\text{vib}} &= \hat{\mathcal{P}}|\chi,\Lambda\rangle|S,\Sigma\rangle|J,\Omega,M\rangle|v\rangle \\ &= (-1)^{\Lambda+\Theta+S-\Sigma+J-\Omega}|\chi,-\Lambda\rangle|S,-\Sigma,M\rangle|J,-\Omega\rangle|v\rangle \\ &= (-1)^{\Theta+S+J-2\Sigma}|\chi,-\Lambda\rangle|S,-\Sigma\rangle|J,-\Omega,M\rangle|v\rangle,\end{aligned} \tag{4.40}$$

where the relation $\Omega = \Lambda + \Sigma$ has been used.

4.8 Franck-Condon approximation

Due to the complexity of many-body systems, such as diatomic molecules, it is impossible to solve the dynamical equations exactly and describe the behavior of the electrons comprehensively without making any approximations. The previous approximations we have introduced are the Born-Oppenheimer approximation and Hund's coupling cases. In this section, we explore another approximation, which plays an important role in the absorption and emission processes in molecular spectroscopy.

In molecules, the absorption and emission intensity in vibronic transitions can be derived based on the so-called Franck-Condon approximation (principle). In electronic transitions, the nuclei are assumed to be stationary, because they are much heavier than the electrons and could not respond as fast as the electronic transitions occur. The Franck-Condon principle is similar to the Born-Oppenheimer approximation and allows us to separate the nuclear wavefunction from the total molecular wavefunction. The intensity of a transition induced by the electric dipole interaction is proportional to the squared transition moment integral $|\langle\Psi'_{\text{mol}}|\boldsymbol{\mu}|\Psi''_{\text{mol}}\rangle|^2$ [9], where Ψ''_{mol} and Ψ'_{mol} represent the molecular wavefunctions of the initial and final states. The operator $\boldsymbol{\mu}$ represents the transition dipole moment and is contributed from the nuclear and electronic parts [9]:

$$\boldsymbol{\mu} = \boldsymbol{\mu}_n(\boldsymbol{R}) + \boldsymbol{\mu}_e(\boldsymbol{r}). \tag{4.41}$$

Here, the nuclear part induces pure rovibrational transitions while the electronic part gives rise to electronic transitions [9]. According to the Born-Oppenheimer approximation, the total molecular wavefunction can be divided into the nuclear

and electronic parts. With the help of Eq. (4.9), the squared transition moment integral can be expressed as [9]

$$\begin{aligned}
|\langle\Psi'_{\mathrm{mol}}|\boldsymbol{\mu}|\Psi''_{\mathrm{mol}}\rangle|^2 =&|\langle\Psi'_e(\boldsymbol{r}|\boldsymbol{R})\Psi'_n(\boldsymbol{R})|\boldsymbol{\mu}|\Psi''_e(\boldsymbol{r}|\boldsymbol{R})\Psi''_n(\boldsymbol{R})\rangle|^2\\
=&|\langle\Psi'_e(\boldsymbol{r}|\boldsymbol{R})\Psi'_n(\boldsymbol{R})|(\boldsymbol{\mu}_n+\boldsymbol{\mu}_e)|\Psi''_e(\boldsymbol{r}|\boldsymbol{R})\Psi''_n(\boldsymbol{R})\rangle|^2\\
=&|\langle\Psi'_e(\boldsymbol{r}|\boldsymbol{R})|\Psi''_e(\boldsymbol{r}|\boldsymbol{R})\rangle\langle\Psi'_n(\boldsymbol{R})|\boldsymbol{\mu}_n|\Psi''_n(\boldsymbol{R})\rangle\\
&+\langle\Psi'_e(\boldsymbol{r}|\boldsymbol{R})\Psi'_n(\boldsymbol{R})|\boldsymbol{\mu}_e|\Psi''_e(\boldsymbol{r}|\boldsymbol{R})\Psi''_n(\boldsymbol{R})\rangle|^2\\
\simeq&|\langle\Psi'_e(\boldsymbol{r}|\boldsymbol{R})\Psi'_n(\boldsymbol{R})|\boldsymbol{\mu}_e|\Psi''_e(\boldsymbol{r}|\boldsymbol{R})\Psi''_n(\boldsymbol{R})\rangle|^2.
\end{aligned} \tag{4.42}$$

In the above equation, we have taken into account the fact that different electronic wavefunctions are orthogonal [9],

$$\langle\Psi'_e(\boldsymbol{r}|\boldsymbol{R})|\Psi''_e(\boldsymbol{r}|\boldsymbol{R})\rangle = 0. \tag{4.43}$$

The electronic transition dipole moment (TDM) operator $\boldsymbol{\mu}_e$ in Cartesian coordinates can be expressed as [19]

$$\boldsymbol{\mu}_e = \sum_i e\boldsymbol{r}_i, \tag{4.44}$$

Here, the sum runs over all the electrons in the system. The transition dipole moment can be decomposed into two components, such as the perpendicular and parallel components, which are defined as [18, 19]

$$\mu_\perp = \frac{1}{\sqrt{2}}\Big(\mu_x \pm i\mu_y\Big), \tag{4.45}$$

$$\mu_\parallel = \mu_z, \tag{4.46}$$

where $\mu_\perp$ and $\mu_\parallel$ represent the perpendicular and parallel components, respectively.

According to the Franck-Condon approximation, the electronic transition moment integral does not depend or only weakly depends on the internuclear distance R [7]. As an approximation (r-centroid approximation), it can be replaced with the value at the equilibrium internuclear distance R_e in the following way

$$\begin{aligned}
D(R) \equiv& \langle\Psi'_e(\boldsymbol{r}|\boldsymbol{R})|\mu_{\parallel(\perp)}|\Psi''_e(\boldsymbol{r}|\boldsymbol{R})\rangle\\
\simeq& D(R_e).
\end{aligned} \tag{4.47}$$

Here, $D(R)$ and $D(R_e)$ represent the transition dipole moments at the arbitrary and equilibrium internuclear distances. In this approximation, Eq. (4.42) can be

rewritten as [8, 19]

$$\begin{aligned}
&|\langle\Psi'_{\mathrm{mol}}|\mu_{\parallel(\perp)}|\Psi''_{\mathrm{mol}}\rangle|^2 \\
\simeq&|\langle\Psi'_n(\boldsymbol{R})|\Psi''_n(\boldsymbol{R})\rangle|^2 D(R_e)^2 \\
\simeq&|\langle\Psi'_{\mathrm{vib}}(\boldsymbol{R})|\Psi''_{\mathrm{vib}}(\boldsymbol{R})\rangle|^2 D(R_e)^2 \\
=&|\langle v'|v''\rangle|^2 D(R_e)^2 \\
=&q_{v'v''} D(R_e)^2.
\end{aligned} \tag{4.48}$$

In the second step of Eq. (4.48), we have considered the fact that, in the molecule-fixed frame, the nuclear wavefunctions of the initial and final states can be approximately replaced with the corresponding vibrational wavefunctions. Here, v'' and v' represent vibrational quantum numbers for the initial and final states, respectively. The newly defined parameter $q_{v'v''} \equiv |\langle\Psi'_{\mathrm{vib}}(\boldsymbol{R})|\Psi''_{\mathrm{vib}}(\boldsymbol{R})\rangle|^2 = |\langle v'|v''\rangle|^2$ is the Franck-Condon factor (FCF).

The FCF is the squared vibrational overlap integral and describes the relative intensity of a transition between the initial and the final vibrational states. Due to the probability conservation, the FCF satisfies the following expression [19, 20]:

$$\sum_{v'} q_{v'v''} = 1. \tag{4.49}$$

Here, the index v' enumerates all the final vibrational states. According to the Born-Oppenheimer approximation, if the motion of nuclei is negligible during a transition, then the intensity of the transition should be dominated by the so-called vertical transition where the relation $v' = v''$ holds.

The selection rules for many-electron systems are more complicated than the ones for hydrogen-like atoms. For simplicity, before proceeding with molecular transitions, we first introduce the selection rules for one-electron transitions. For the electric dipole transitions in hydrogen-like atoms, the possible selection rules can be summarized as follows [22]:

1. $\Delta l = \pm 1$
2. $\Delta m = 0, \pm 1$
3. $\Delta s = 0$

Here, l and s represent the orbital and spin angular momentum quantum numbers, respectively, and m represents the magnetic quantum number. In atoms, the perpendicular component $\mu_\perp$ can induce transitions with the magnetic quantum number being changed by one unit, while the parallel component $\mu_\parallel$ can induce transitions with the magnetic quantum number being unchanged [22]. Since the transition dipole moment operator only depends on the spatial coordinates, the

total spin quantum number before and after transitions should be unchanged under its action. In molecules, angular momenta are coupled to each other, making the selection rules for molecular transitions far more complicated than the ones for atomic transitions. In this case, Hund's coupling cases can be used to choose the (approximately) good quantum numbers. Besides complexity, the molecular selection rules can provide additional insights into the absorption and emission processes, comparing with the atomic selection rules. As an example for the electric dipole transitions in molecules, the possible selection rules based on the (approximately) good quantum numbers assigned by Hund's coupling case (a) can be summarized as follows [2, 19, 20, 23]:

1. $\Delta\Lambda = 0, \pm 1$
2. $\Delta S = 0$
3. $\Delta J = 0, \pm 1$

Similarly, the perpendicular component $\mu_\perp$ shifts the quantum number Λ by one unit, while the parallel component $\mu_\parallel$ keeps the quantum number Λ unchanged [18]. Besides the above selection rules, in all electromagnetic transitions, the total parity of the whole system including photons should be conserved.

References

[1] J. M. Brown, J. M. Brown, and A. Carrington, *Rotational spectroscopy of diatomic molecules* (Cambridge University Press, 2003).

[2] W. Demtröder, *Atoms, molecules and photons*, 7 (Springer-Verlag, 2010).

[3] P. Langacker, *Precision tests of the standard electroweak model* (World Scientific, 1995).

[4] Y. Nagashima, *Elementary particle physics: Foundations of the Standard Model*, Vol. 2 (John Wiley & Sons, 2013).

[5] W. T. Hill and C. H. Lee, *Light-matter interaction: Atoms and molecules in external fields and nonlinear optics* (Wiley-VCH Verlag, 2007).

[6] I. Mukhopadhyay, R. D'Cunha, and K. N. Rao, Int. J. Infrared Millimeter Waves **24**, 1441 (2003).

[7] H. Lefebvre-Brion and R. W. Field, *The spectra and dynamics of diatomic molecules* (Elsevier, 2004).

[8] W. Demtröder, *Molecular physics: theoretical principles and experimental methods* (John Wiley & Sons, 2008).

[9] W. Ubachs, *Notes on molecular physics* (Vrije Universiteit Amsterdam, 2012).

[10] R. N. Zare, A. L. Schmeltekopf, W. J. Harrop, and D. L. Albritton, J. Mol. Spect. **46**, 37 (1973).

[11] I. Kovács, J. Mol. Struct. **80**, 35 (1982).

[12] A. A. Ramos and J. T. Bueno, Astrophys. J. **636**, 548 (2006).

[13] E. Hirota, *High-resolution spectroscopy of transient molecules*, Vol. 40 (Springer-Verlag, 1985).

[14] R. A. Frosch and H. M. Foley, Phys. Rev. **88**, 1337 (1952).

[15] A. Abragam and B. Bleaney, *Electron paramagnetic resonance of transition ions* (Oxford University Press, 1970).

[16] W. Weltner, *Magnetic atoms and molecules* (Courier Corporation, 1989).

[17] E. Y. Misochko, A. V. Akimov, I. U. Goldschleger, D. A. Tyurin, and D. N. Laikov, J. Chem. Phys. **122**, 034503 (2005).

[18] J. T. Hougen and G. G. Wiersma, *The calculation of rotational energy levels and rotational line intensities in diatomic molecules* (National Bureau of Standards, 1970).

[19] P. F. Bernath, *Spectra of atoms and molecules* (Oxford University Press, 2005).

[20] R. W. Field, *Spectra and dynamics of small molecules: Alexander von Humboldt lectures* (Springer-Verlag, 2015).

[21] M. Larsson, Phys. Scrip. **23**, 835 (1981).

[22] H. A. Bethe and E. E. Salpeter, *Quantum mechanics of one-and two-electron atoms* (Springer-Verlag, 1957).

[23] J. M. Hollas, *Basic atomic and molecular spectroscopy*, Vol. 11 (Royal Society of Chemistry, 2002).

Chapter 5

Symmetry-breaking effects and new phenomena

5.1 Overview

This chapter addresses the main topics to be discussed in the present work. The present work is intended to investigate the tests of fundamental symmetries of the Standard Model (SM) and the searches for new phenomena beyond the SM using molecular properties of diatomic molecules. Among such properties, the parity-violating nuclear anapole moment effect in diatomic molecules can be used to test nuclear models and gain deep understanding about nuclear structure. Moreover, the searches for the $\hat{\mathcal{C}}\hat{\mathcal{P}}$-violating eEDM in diatomic molecules not only can provide stringent test of the SM, but also can help put constraints on new physics theories beyond the SM. In addition, the searches for the variation of dimensionless fundamental constants not only can help test the SM, but also can offer a large window for the construction of new physics theories, such as quantum gravity [a]. More importantly, such investigations can also help gain insights into the unsolved problems in physics, such as the nature of dark matter and dark energy, etc.

5.2 Nuclear anapole moment effect

Diatomic molecules are considered as promising candidates for the measurement of the parity-violating nuclear anapole moment effect. For a $^2\Sigma_{1/2}$ ground state

[a] Quantum gravity is considered as a promising approach to the unification of the four fundamental interactions.

of such molecules, the Hamiltonian associated with the nuclear anapole moment interaction in Eq. (2.41) can be rewritten as [1, 2],

$$H_A = \kappa_A W_A \hat{\boldsymbol{I}} \cdot \Big(\hat{\boldsymbol{n}} \times \boldsymbol{S}_{\rm eff} \Big), \tag{5.1}$$

where $\boldsymbol{S}_{\rm eff}$ stands for the effective spin of the open-shell electron, and $\hat{\boldsymbol{n}}$ is the unit vector along the molecular axis. The $\hat{\mathcal{P}}$-odd W_A parameter depends on molecular structure, and can be defined by the following matrix element between two different Ω states [3]:

$$W_A \equiv \frac{G_F}{\sqrt{2}} \langle +\tfrac{1}{2} | \rho(\boldsymbol{r}) \alpha_+ | -\tfrac{1}{2} \rangle, \tag{5.2}$$

with

$$\alpha_+ = \alpha_x + i\alpha_y = \begin{pmatrix} 0 & \sigma_x \\ \sigma_x & 0 \end{pmatrix} + i \begin{pmatrix} 0 & \sigma_y \\ \sigma_y & 0 \end{pmatrix}, \tag{5.3}$$

where σ_x and σ_y are the Pauli matrices.

The nuclear anpole moment effect can be used to probe parity violation in hadronic sector and to gain deep understanding about nuclear structure. The effective coupling constant κ_A can be obtained both experimentally and theoretically. On the one hand, κ_A can be determined by measuring parity-violating transitions in atoms or molecules when the $\hat{\mathcal{P}}$-odd W_A parameter is known. On the other hand, κ_A can also be calculated directly from nuclear theories. From an experimental point of view, the W_A parameter cannot be measured directly and needs to be calculated with high accuracy so that the effective coupling constant κ_A can be extracted precisely from the measured signals. The measured value of κ_A from experiments can be compared with its predicted values from nuclear theories. Any deviation may suggest the incompleteness of our knowledge about nuclear models or even imply hints for new physics beyond the SM.

The nuclear anapole moment interaction violates parity and causes parity-forbidden mixing between molecular states with opposite parity. As an example, the admixture between the molecular states with opposite parity induced by the nuclear anapole moment interaction can be roughly expressed as (see e.g. Ref. [4])

$$\begin{aligned} |\Psi'_{\rm even}\rangle &\simeq |\Psi_{\rm even}\rangle + i \sum_{\rm odd} \epsilon_{\rm odd} |\Psi_{\rm odd}\rangle \\ &= |\Psi_{\rm even}\rangle + \sum_{\rm odd} \frac{\langle \Psi_{\rm odd} | H_A | \Psi_{\rm even} \rangle}{E_{\rm even} - E_{\rm odd}} |\Psi_{\rm odd}\rangle, \end{aligned} \tag{5.4}$$

where the sum runs over all the molecular states with odd parity, and $\Psi_{\rm even}$ ($E_{\rm even}$) and $\Psi_{\rm odd}$ ($E_{\rm odd}$) represent the wavefunctions (energies) with even and

odd parity, respectively. The parameters $\epsilon_{\rm odd}$ represent the mixing coefficients between the molecular states with opposite parity. As can be seen from Eq. (5.4), the parity-violating effect can be enhanced by increasing the mixing coefficients or decreasing the energy gaps between the molecular states with opposite parity. To begin with, the matrix element $\langle\Psi_{\rm odd}|H_A|\Psi_{\rm even}\rangle$ in the mixing coefficient approximately scales as Z^3 (in atoms) [5–7], which indicates that the effect grows rapidly with the nuclear charge Z. Furthermore, the energy levels with opposite parity can be shifted towards each other by applying external magnetic fields, resulting in nearly-degenerate molecular levels and dramatic signal amplification. In particular, diatomic molecules are considered as promising candidates in the search for the nuclear anapole moment effect, because such molecules possess closely-spaced molecular levels with opposite parity, making it more easier to bring such molecular levels into degeneracy. In addition, the tiny parity-violating effect can be effectively detected with the help of the Stark-PV interference technique, where external electric fields can be applied so that the interference between the parity-violating amplitudes and the Stark-induced amplitudes leads to a dramatic signal amplification [8, 9].

In the Stark-PV interference technique, the tiny parity-violating effect can be isolated from the more significant Stark-induced effect through a reversal of the external electric field [10, 11]. In reality, the measurement can be accomplished by two data-acquisition sequences. In the first sequence of data acquisition, the molecules are formed in such a way that the molecular states with even and odd parity are equally populated. Such molecular states with opposite parity can be brought into near degeneracy with the help of magnetic fields generated by a superconducting magnet. Then, the molecular states with even parity are depleted by employing a laser beam. After that, an oscillating electric field parallel to the magnetic field is applied. Some molecules experience a transition from the even parity to the odd parity through the combined interaction of the Stark and parity-violating effects. Next, the molecules with odd parity are depleted by another laser beam. The molecular states with even parity can be detected and counted when the molecules leave the region of the magnetic field. When the first sequence of data acquisition is complete, the external electric field can be reversed and the second sequence of data acquisition can be performed. The parity-violating effect can be extracted from the asymmetry between the two data-acquisition sequences. For molecules containing heavy elements, the nuclear anapole moment effect is the dominant contribution to the NSD-PV effects. However, from heavy to light elements, the nuclear anapole moment effect decreases rapidly, but it is still possible to distinguish such effect from other NSD-PV effects by performing the measurements with different nuclei (or different isotopes) [12].

The alkaline earth metal halides can manifest themselves as promising can-

didates in the measurement of the nuclear anapole moment effect at a variety of levels, due to their structural characteristics. First of all, such molecules contain an unpaired electron with a $^2\Sigma_{1/2}$ ground state, which are more amenable to interpret the measurements because the calculated W_A parameter can be related to the measured signal through a simple expression as indicated in Eq. (5.1). Furthermore, the nuclear anapole moment effect is induced by the interaction between the unpaired electron and nucleon within the region of the nucleus. Since the electronic wavefunction for a $^2\Sigma_{1/2}$ state has a large overlap on the nucleus, the effect can be greatly enhanced in such molecules. More importantly, such molecules possess closely-spaced molecular states with opposite parity. By employing external magnetic fields, these molecular states can be more easily to be brought into near degeneracy, where more significant enhancement of the effect can be achieved. From an experimental point of view, long coherent interaction times can help improve the measurement sensitivity. This requires that the molecules can be effectively laser-cooled. The electronic structure of such molecules reveals that they are promising candidates for laser-cooling. In addition, it is technically available to produce a well-characterized beam source of such molecules, which allows versatile spectroscopic and reaction studies, including the measurement of the nuclear anapole moment effect [10]. Last but not least, such molecules have a wide range of isotopes, allowing the measurements for different nuclear configurations.

In Chapter 6, we present highly accurate relativistic coupled cluster calculations of the $\hat{\mathcal{P}}$-odd interaction parameter W_A, which describes the nuclear anapole moment effect and depends on the molecular structure. The W_A parameter can not be measured directly and can only be calculated by *ab initio* methods. The molecule under study, BaF, is considered as a promising candidate for the measurement of the nuclear anapole moment effect [10, 11]. The experimental setup for the measurement with improved sensitivity has been demonstrated [10, 11]. The influence of various computational parameters, such as basis sets, relativistic effects, and electron correlations, on the calculated W_A parameter is investigated. The uncertainty evaluation is also demonstrated in this chapter.

In Chapter 7, we present more detail about the correlation trends of the nuclear anapole moment interaction for the BeCl molecule. The BeCl molecule is also considered as a good candidate in the search for the nuclear anapole moment effect, due to fact that the molecular and nuclear calculations for the Be element are highly tractable. In this work, the calculations of the W_A parameter for the Be atom in BeCl are carried out with various electron correlation approaches.

5.3 Search for the eEDM and spectroscopic constants

Diatomic molecules also serve as promising probes for detecting the effect from the electron electric dipole moment (eEDM), which violates the $\hat{\mathcal{C}}\hat{\mathcal{P}}$ symmetry. In non-relativistic approximation, the interaction between the eEDM and the effective electric field of a molecule can be written as

$$H^{\mathrm{eEDM}} = -\boldsymbol{d}_e \cdot \boldsymbol{E}_{\mathrm{eff}}, \tag{5.5}$$

where $\boldsymbol{E}_{\mathrm{eff}}$ represents the effective electric field of the molecule and $\boldsymbol{d}_e$ represents the eEDM. At low energies (see Eq. (2.47) for relativistic case), the effective Hamiltonian accounting for the interaction between the eEDM and the total electric field in an atom or a molecule can be written as [13–15]

$$H^{\mathrm{eEDM}} = 2icd_e \sum_i \beta\gamma_5 p_i^2. \tag{5.6}$$

Here, $d_e \equiv |\boldsymbol{d}_e|$ represents the magnitude of the eEDM. The index i enumerates all the electrons inside an atom or a molecule, c represents the speed of light, p_i represents the momentum of the i-th electron. The magnitude of the effective electric field $E_{\mathrm{eff}} \equiv |\boldsymbol{E}_{\mathrm{eff}}|$ can be calculated using *ab initio* methods in the following way:

$$E_{\mathrm{eff}} = -\frac{\langle\Psi|H^{\mathrm{eEDM}}|\Psi\rangle}{d_e}, \tag{5.7}$$

where $|\Psi\rangle$ denotes the normalized wavefunction for the whole system.

From an experimental point of view, the measurement of the eEDM can be illustrated as follows [16]. To begin with, two molecular states with spin being aligned and antialigned with respect to the effective electric fields are produced. After that, such molecules are brought into a magnetically shielded region with the static electric and magnetic fields along the z-axis. Then, the coherent superposition of the two molecular states can be formed by applying a radio-frequency pulse. Over the time of data-taking (T), a phase ϕ is developed between the two molecular states, which can be defined as [17]

$$\phi = \frac{(\pm\mu_B B \mp d_e E_{\mathrm{eff}})T}{\hbar}. \tag{5.8}$$

Here, the phase is contributed from both the electric and magnetic dipole interactions. The contribution from the electric dipole moment can be separated if the external electric field is flipped. This gives rise to a small phase difference, which is proportional to d_e and can be written as [16, 17]

$$\delta\phi = \frac{2d_e E_{\mathrm{eff}} T}{\hbar}. \tag{5.9}$$

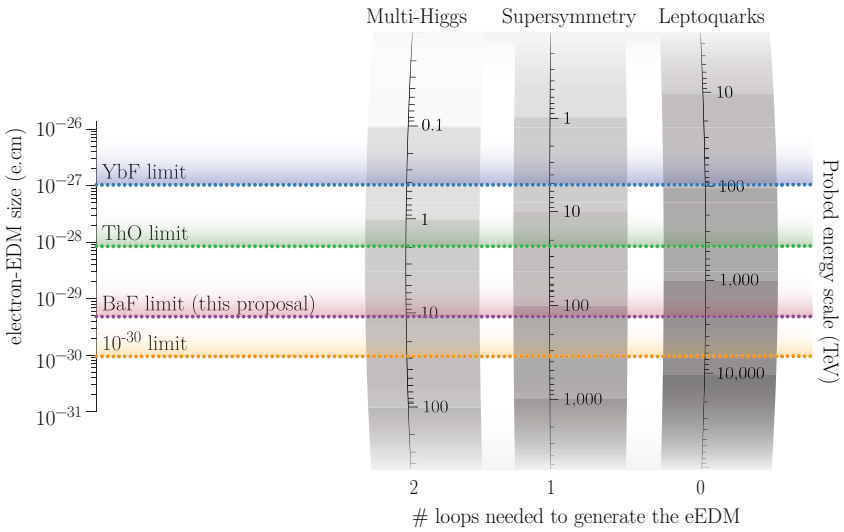

Figure 5.1: The experimental limits (up to the year 2017) on the value of the eEDM and on the probed energy scale associated with new physics beyond the SM (image courtesy of the NL-eEDM collaboration [18]).

The statistical uncertainty of the eEDM measurement can be expressed as [18]

$$\sigma_s = \frac{\hbar}{e} \frac{1}{2|P|E_{\text{eff}}\tau\sqrt{\dot{N}T}}. \tag{5.10}$$

Here, P represents the polarization factor, $\dot{N}$ represents the rate of the detected molecules, T is the time of data taking, τ represents the coherent interaction time.

As can be seen from Eq. (5.10), a successful measurement of the eEDM requires the candidates to satisfy numerous criteria. To begin with, a promising candidate needs to have a large effective electric field. In a molecule, the effect of a non-zero eEDM can be greatly enhanced by the huge surrounding electric fields, which are contributed from both the effective intrinsic electric field and the external electric field. Such electric fields can improve the measurement sensitivity considerably. The measurements of the eEDM with sufficiently high sensitivity using various molecules and molecular ions, such as HfF^+ [19], ThO [20–22], YbF [16], BaF [18], etc., have been carried out or in preparation. Fig. 5.1 shows the experimental limits (up to the year 2017) on the value of the eEDM and on the probed energy scale associated with new physics beyond the SM. The

present best limit at the 90% confidence level on the eEDM is 1.1×10^{-29} e·cm, which is obtained by ACME using the ThO molecule [22]. Further measurements with improved sensitivity have also been proposed on other molecular species such as BaF [18], YbOH [23], etc.

In order to further improve the sensitivity, the experimental setup needs to be designed to achieve a long coherent interaction time [18, 24, 25], which requires that the molecules under study can be effectively laser-cooled [18, 24–26]. There are a number of key factors that determine whether a given molecule is suitable for laser-cooling [27]. To begin with, strong one-photon transitions are more favorable to guarantee high photon-scattering rates and increase momentum transfer efficiency. Since the oscillator strengths of the transitions can be determined by the transition dipole moments (TDMs) between the states, strong one-photon transitions require that the corresponding TDMs cannot be too small. Furthermore, the molecule should possess highly diagonal Franck-Condon factors (FCFs), which provide a near-closed optical cycle in the vibronic structure and thus decrease the number of the required repump lasers. Last but not least, there should either be no intervening electronic states to which the upper state could radiate and cause leaks in the cooling cycle, or at least the transitions to such states should be highly suppressed. Previous studies have demonstrated that calcium monofluoride (CaF) can be successfully laser-cooled to around 5 μK [28, 29]. As a homologue of CaF, barium monofluoride (BaF) has similar electronic structure and thus is considered as a promising candidate for laser-cooling. In order to develop laser systems more efficiently throughout measurements and to interpret the results more correctly after measurements, highly accurate theoretical calculations of molecular spectroscopic constants (see Appendix A) are necessary. At present, the NL-eEDM collaboration is building an experimental setup to search for the permanent eEDM in a slow beam of the BaF molecules [18] with unprecedented sensitivity. Theoretical knowledge concerning molecular properties of BaF is thus needed to design the measurement strategies and in particular to determine the optimal laser-cooling scheme.

In Chapter 8, we present the theoretical investigations of the molecular spectroscopic constants for CaF, SrF, and BaF. We discuss their applications in laser-cooling molecules and investigate different possible laser-cooling schemes. Accurate and reliable theoretical predictions of these spectroscopic constants (properties) require incorporating a number of factors into the calculations, such as large and high-quality basis sets, high-order relativistic effects, and advanced electron correlation methods. In this work, theoretical investigations of the low-lying electronic states of BaF and its lighter homologues, CaF and SrF, are carried out using the relativistic Fock-space coupled cluster (FSCC) method and the multireference configuration interaction (MRCI) method. Using the calculated potential energy curves (PECs), we determine the molecular spectroscopic constants of the

low-lying electronic states and the Franck-Condon factors (FCFs) between these states. We also present the dipole moments of the low-lying electronic states and the transition dipole moments (TDMs) between such states. Finally, using the calculated spectroscopic constants, FCFs, and TDMs, we determine the suitable transition for laser-cooling BaF.

5.4 Search for the variation of fundamental constants

Besides the measurement of the symmetry-breaking effects, the searches for other new phenomena, such as the temporal and spatial variations of fundamental constants, have attracted an enormous level of attention recently. Many new physics theories that extend the SM, or theories that unify gravity with all the non-gravitational interactions are featured with the variation of fundamental constants. The search for the variation of fundamental constants not only can help test the SM and GR, but also can help put constraints on new physics theories. For example, some dark matter candidates, which are oscillating with respect to time, couple to the SM particles and lead to the time variation of fundamental constants [30]. In this case, the search for the variation of fundamental constants can be helpful for dark matter searches. Throughout the present work, we are interested in the variation of dimensionless fundamental constants, such as the fine structure constant α and the proton-to-electron mass ratio μ.

The search for the variation of fundamental constants with respect to time and space can be performed in a number of ways, such as Big Bang nucleosynthesis, Oklo natural nuclear reactor data, meteorite data, laser interferometer, quasar absorption spectra, and atomic clocks [31]. Among them, the last two approaches, namely quasar absorption spectra and atomic clocks, are based on the analysis of atomic and molecular spectra. The advantages of using such approaches are obvious because they not only help gain high sensitivity, but also open windows for evaluating systematic uncertainties [32, 33]. The observation of quasar spectra shows that there has been no sign for the time variation of the fine structure constant and the corresponding limit is $\Delta\alpha/\alpha = 1.2 \pm 1.7$ (stat.) $\pm$ 0.9 (syst.) ($\times 10^{-6}$) [34]. The study of the spectra from quasars has also placed the constraint on the variation of μ with the result of $\Delta\mu/\mu = -9.5 \pm 5.4$ (stat.) $\pm$ 5.3 (syst.) ($\times 10^{-6}$) [35]. The limit on the time variation of α with $^{171}Yb^{+}$ is $\dot{\alpha}/\alpha = -0.7 \pm 2.1 \times 10^{-17}$ yr^{-1} [36]. For the spatial variation of fundamental constants, the example lies in the new physics theories with the signature of domain walls generated in the early Universe. Such domain walls couple to the electromagnetic field and may cause the spatial variation of α when the domain walls are passing through the Earth [37]. In this case, the search for the spatial variation of α

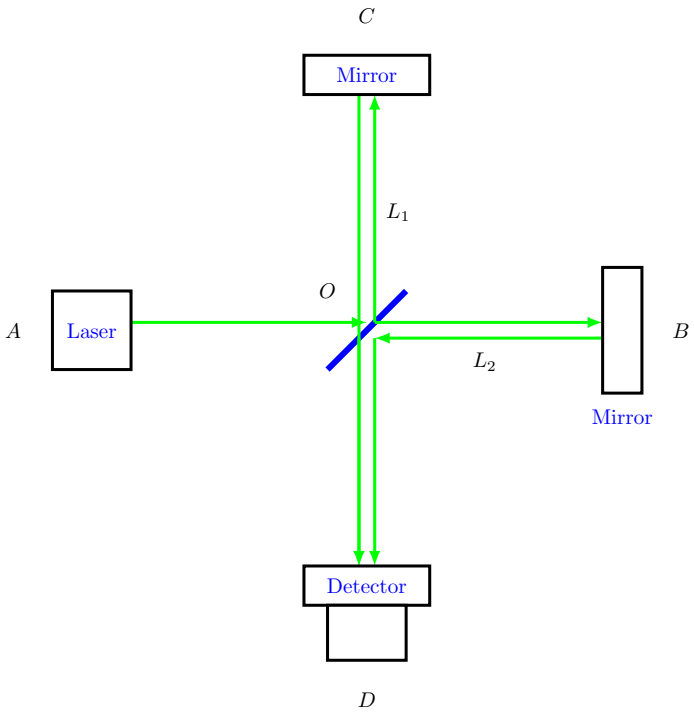

Figure 5.2: Schematic view of a laser interferometer.

can be helpful for the detection of such domain walls. The observation of quasar spectra has indicated a possible spatial variation of α with a significance of 4.2 σ, but it may arise from some undetected systematic effects [38]. Last but not least, recent developments in atomic clocks enable unprecedented level of precision with the uncertainty as low as 10^{-19} [39], making it possible to search for the temporal and spatial variation of fundamental constants with high sensitivity. In practice, atomic clocks can be used to search for the variation of fundamental constants by comparing the transition frequencies between two stable atomic clocks over long period of time or at different locations [40]. Most recently, the analysis of atomic clocks has imposed the constraint on the variation of α with the result of $|\delta\alpha/\alpha| < 5 \times 10^{-17}$ for transients of duration 10^3 s [41].

As an alternative method in the search for the variation of fundamental constants, we may compare the phase differences between two light beams inside the cavities of a laser interferometer [42], instead of comparing two transition frequencies over a long period of time. A schematic view of a laser interferom-

eter that can be used in the search for the variation of fundamental constants is presented in Fig. 5.2, where the green lines stand for the light paths through the laser interferometer. A beam of highly coherent light emitted from a laser device at point A is split into two light beams at point O by a beam splitter, which is used for separating and recombining the light beams and serves as a crucial part of the experiment. One light beam travels inside the cavity of the test arm extending from the beam splitter to the end mirror at point B. The other light beam travels inside the cavity of the reference arm extending from the beam splitter to the end mirror at point C. The reference and test arms have the lengths L_1 and L_2, respectively. The two end mirrors are used to reflect the two light beams back. When the two light beams arrive at the detector at point D, they can be recombined to produce interference. Any changes in the difference between the two arm lengths can give rise to the phase shifts between the two light beams. The laser interferometer is greatly sensitive to length changes between the reference and test beams. The observable in a laser interferometer is the phase difference $\Delta\phi$, which is defined as

$$\Delta\phi = \frac{(L_1 - L_2)\omega}{c}, \tag{5.11}$$

where ω is the reference frequency and c represents the speed of light. The two arm lengths can be adjusted in such a way that the recombined two beams of light give rise to destructive interference in the absence of the variation of fundamental constants [30] and other drifts.

The size of the materials employed in the optical cavity of a laser interferometer depends on the solid-state and molecular properties, such as crystal lattice parameters (e.g. a_e and c_e) and molecular bond lengths (R_e). The changes in such properties can manifest themselves through the changes in the material sizes as well as in the arm lengths. The variation of fundamental constants would affect the crystal lattice parameters and the molecular bond lengths. The main goal of this work is to identify promising materials which are sensitive to the variation of α and μ and thus open windows of opportunity for observing such new phenomena. The sensitivity coefficients K_C can be defined in the following way [30]:

$$\frac{\delta(\Delta\phi)}{\Delta\phi} \equiv \sum_C K_C \frac{\delta C}{C}, \tag{5.12}$$

where the index C enumerates all relevant fundamental constants, such as α, μ, etc.

In Chapter 9, we present an application of *ab initio* methods in the search for the variation of fundamental constants. As a new alternative method to the analysis of atomic clocks and quasar spectra, precision laser interferometry may provide the expected sensitivity to the variation of fundamental constants

through the comparison of the phase differences between two light beams. Ideally, the dependence of the crystal lattice parameters (constants) in a solid needs to be examined by highly accurate computational methods like the coupled cluster method. Highly accurate computational methods can help identify promising candidates which lead to great discovery potential. However, comprehensive and systematic calculations on solid-state materials using the coupled cluster method are not computationally affordable or tractable. Instead, the DFT method has been widely used to predict the solid-state properties, but the accuracy of the DFT results should be assessed. In principle, the exact lattice parameters in a solid depend on the specific crystal structure and on the actual thermal environment. Nonetheless, if we assume that the distance between two nearest atoms (lattice points) in a solid can be approximated by the equilibrium bond distance in a diatomic molecule formed by these two atoms, the coupled cluster calculations of the equilibrium bond distances for diatomic molecules can be used to benchmark the performance of the DFT calculations of the lattice parameters for solid-state materials. Our calculations show that the material sizes can be well-modeled by the equilibrium bond distances of diatomic molecules and the DFT calculations can provide the expected accuracy in predicting the dependence of the material sizes on the variation of fundamental constants. We also provide the accurate values for the dependence of lattice parameters on α and μ in a variety of solid-state materials, such as Cu, Si, Al, Nb, Al_2O_3, etc. Finally, we present the possible experimental setups for the detection of the variation of fundamental constants and reveal the corresponding discovery potential.

References

[1] V. V. Flambaum and I. B. Khriplovich, Phys. Lett. A **110**, 121 (1985).

[2] D. DeMille, S. B. Cahn, D. Murphree, D. A. Rahmlow, and M. G. Kozlov, Phys. Rev. Lett. **100**, 023003 (2008).

[3] A. D. Kudashov, A. N. Petrov, L. V. Skripnikov, N. S. Mosyagin, T. A. Isaev, R. Berger, and A. V. Titov, Phys. Rev. A **90**, 052513 (2014).

[4] E. Altuntas, *Measurement of nuclear spin dependent parity violation in* ^{138}BaF, Ph.D. thesis, Yale University (2017).

[5] M. A. Bouchiat and C. C. Bouchiat, J. de Phys. **35**, 899 (1974).

[6] M. A. Bouchiat and C. Bouchiat, J. de Phys. **36**, 493 (1975).

[7] D. Budker, D. F. Kimball, and D. P. DeMille, (2008).

[8] P. Langacker, *Precision tests of the standard electroweak model* (World Scientific, 1995).

[9] Y. Nagashima, *Elementary particle physics: Foundations of the Standard Model*, Vol. 2 (John Wiley & Sons, 2013).

[10] E. Altuntaş, J. Ammon, S. B. Cahn, and D. DeMille, Phys. Rev. A **97**, 042101 (2018).

[11] E. Altuntaş, J. Ammon, S. B. Cahn, and D. DeMille, Phys. Rev. Lett. **120**, 142501 (2018).

[12] E. B. Norrgard, D. S. Barker, S. Eckel, J. A. Fedchak, N. N. Klimov, and J. Scherschligt, Commun. Phys. **2**, 77 (2019).

[13] E. Lindroth, B. W. Lynn, and P. G. H. Sandars, J. Phys. B **22**, 559 (1989).

[14] A. Mårtensson-Pendrill and P. Öster, Phys. Scr, **36**, 444 (1987).

[15] B. L. Roberts and W. J. Marciano, *Lepton dipole moments*, Vol. 20 (World Scientific, 2010).

[16] J. J. Hudson, D. M. Kara, I. J. Smallman, B. E. Sauer, M. R. Tarbutt, and E. A. Hinds, Nature **473**, 493 (2011).

[17] B. E. Sauer, J. J. Hudson, D. M. Kara, I. J. Smallman, M. R. Tarbutt, and E. A. Hinds, Phys. Proc. **17**, 175 (2011).

[18] P. Aggarwal, H. L. Bethlem, A. Borschevsky, M. Denis, K. Esajas, P. A. B. Haase, Y. Hao, S. Hoekstra, K. Jungmann, T. B. Meijknecht, *et al.*, Eur. Phys. J. D **72**, 197 (2018).

[19] W. B. Cairncross, D. N. Gresh, M. Grau, K. C. Cossel, T. S. Roussy, Y. Ni, Y. Zhou, J. Ye, and E. A. Cornell, Phys. Rev. Lett. **119**, 153001 (2017).

[20] J. Baron, W. C. Campbell, D. DeMille, J. M. Doyle, G. Gabrielse, Y. V. Gurevich, P. W. Hess, N. R. Hutzler, E. Kirilov, I. Kozyryev, *et al.*, Science **343**, 269 (2014).

[21] J. Baron, W. C. Campbell, D. DeMille, J. M. Doyle, G. Gabrielse, Y. V. Gurevich, P. W. Hess, N. R. Hutzler, E. Kirilov, I. Kozyryev, *et al.*, New J. Phys. **19**, 073029 (2017).

[22] V. Andreev and N. R. Hutzler, Nature **562**, 355 (2018).

[23] I. Kozyryev and N. R. Hutzler, Physical review letters **119**, 133002 (2017).

[24] T. A. Isaev, S. Hoekstra, and R. Berger, Phys. Rev. A **82**, 052521 (2010).

[25] T. A. Isaev and R. Berger, arXiv:1302.5682 (2013).

[26] Y. Hao, L. F. Pašteka, L. Visscher, P. Aggarwal, H. L. Bethlem, A. Boeschoten, A. Borschevsky, M. Denis, K. Esajas, S. Hoekstra, *et al.*, J. Chem. Phys. **151**, 034302 (2019).

[27] M. D. Di Rosa, Eur. Phys. J. D **31**, 395 (2004).

[28] L. W. Cheuk, L. Anderegg, B. L. Augenbraun, Y. Bao, S. Burchesky, W. Ketterle, and J. M. Doyle, Phys. Rev. Lett. **121**, 083201 (2018).

[29] L. Caldwell, J. A. Devlin, H. J. Williams, N. J. Fitch, E. A. Hinds, B. E. Sauer, and M. R. Tarbutt, Phys. Rev. Lett. **123**, 033202 (2019).

[30] Y. V. Stadnik and V. V. Flambaum, Physical Rev. Lett. **114**, 161301 (2015).

[31] V. V. Flambaum, in *International Frequency Control Symposium Joint with the 21st European Frequency and Time Forum* (IEEE, 2007) pp. 342–349.

[32] M. T. Murphy, J. K. Webb, V. V. Flambaum, J. X. Prochaska, and A. M. Wolfe, Mon. Not. Roy. Astron. Soc. **327**, 1237 (2001).

[33] J. A. King, J. K. Webb, M. T. Murphy, V. V. Flambaum, R. F. Carswell, M. B. Bainbridge, M. R. Wilczynska, and F. E. Koch, Mon. Not. Roy. Astron. Soc. **422**, 3370 (2012).

[34] M. T. Murphy, A. L. Malec, and J. X. Prochaska, arXiv:1606.06293 (2016).

[35] J. Bagdonaite, W. Ubachs, M. T. Murphy, and J. B. Whitmore, Phys. Rev. Lett. **114**, 071301 (2015).

[36] R. M. Godun, P. B. R. Nisbet-Jones, J. M. Jones, S. A. King, L. A. M. Johnson, H. S. Margolis, K. Szymaniec, S. N. Lea, K. Bongs, and P. Gill, Phys. Rev. Lett. **113**, 210801 (2014).

[37] K. A. Olive, M. Peloso, and J. Uzan, Phys. Rev. D **83**, 043509 (2011).

[38] J. K. Webb, J. A. King, M. T. Murphy, V. V. Flambaum, R. F. Carswell, and M. B. Bainbridge, Phys. Rev. Lett. **107**, 191101 (2011).

[39] E. Oelker, R. B. Hutson, C. J. Kennedy, L. Sonderhouse, T. Bothwell, A. Goban, D. Kedar, C. Sanner, J. M. Robinson, G. E. Marti, *et al.*, arXiv:1902.02741 (2019).

[40] V. V. Flambaum and E. V. Shuryak, in *AIP Conf. Proc.*, Vol. 995 (American Institute of Physics, 2008) pp. 1–11.

[41] B. M. Roberts, P. Delva, A. Al-Masoudi, A. Amy-Klein, C. Baerentsen, C. F. A. Baynham, E. Benkler, S. Bilicki, W. Bowden, E. Cantin, *et al.*, arXiv:1907.02661 (2019).

[42] Y. V. Stadnik and V. V. Flambaum, Phys. Rev. A **93**, 063630 (2016).

Chapter 6

Nuclear anapole moment effect in BaF[a]

6.1 Motivation

The standard model (SM) of particle physics, unifying the electromagnetic, weak, and strong forces by which the fundamental particles interact, has proven to be valid within unprecedented accuracy. However, the SM as we know is incomplete and many open questions remain that lie beyond its current formulation [2]; among the most important are the origin of dark matter and dark energy, neutrino mass and oscillations, matter-antimatter asymmetry and the unification with the gravitational force. These open questions motivate both formulations of new theories beyond the SM and experimental searches for new physical phenomena.

One prominent category of such experiments is the search for violation of parity ($\hat{\mathcal{P}}$) and time ($\hat{\mathcal{T}}$) reversal symmetries in atoms and molecules [3]. In particular, investigation of nuclear spin dependent parity violating (NSD-PV) effects, which are the main focus of this work, can be used to test low-energy quantum chromodynamics and parity nonconservation in nuclei [4].

The effective Hamiltonian responsible for the NSD-PV interaction between an electron and nucleus can be written as [3],

$$H_{\mathrm{NSD}} = \frac{G_F}{\sqrt{2}I}\left(\kappa_{\mathrm{A}} + \kappa_{\mathrm{ax}} + \kappa_{\mathrm{hfs}}\right)\Big(\boldsymbol{\alpha}\cdot\boldsymbol{I}\Big)\rho\left(\boldsymbol{r}\right), \tag{6.1}$$

[a]This chapter is reproduced from our published paper [1]: Yongliang Hao, Miroslav Iliaš, Ephraim Eliav, Peter Schwerdtfeger, Victor V. Flambaum, and Anastasia Borschevsky, Nuclear anapole moment interaction in BaF from relativistic coupled-cluster theory, Phys. Rev. A **98**, 032510 (2018).

where G_F is the Fermi weak interaction coupling constant [5], $\boldsymbol{\alpha}$ are the Dirac matrices in the standard representation, $\boldsymbol{I}$ is the nuclear spin, and $\rho(\boldsymbol{r})$ is the (normalized) nuclear density distribution. This contribution is only present for nuclei with $I \neq 0$, and for open-shell atoms or molecules because of Kramers symmetry. The three dimensionless nuclear κ parameters are associated with the different sources of the NSD-PV effects. The first term, κ_A, comes from the nuclear anapole moment interaction and will be discussed in more detail below. The second term $\kappa_{\rm ax}$ arises from the electroweak neutral coupling between the electronic vector and nuclear axial-vector currents ($\mathbf{V}_e\mathbf{A}_N$) [6]; theoretical prediction of $\kappa_{\rm ax}$ within the nuclear shell model can be found in Ref. [7]. The third contribution $\kappa_{\rm hfs}$ originates in the nuclear-spin-independent weak interaction combined with the hyperfine interaction [8]. The coefficients $\kappa_{\rm hfs}$ were derived using different models, for example in Refs. [9–11].

The anapole moment was first predicted by Zel'dovich [12] in 1958. It appears in the second-order multipole expansion of the magnetic vector-potential simultaneously with the $\hat{\mathcal{P}}$ and $\hat{\mathcal{T}}$ violating magnetic quadrupole moment [13]. In a simple valence nucleon model κ_A has the following form [14],

$$\kappa_A \simeq 1.15 \times 10^{-3}(-1)^{I-l+\frac{1}{2}} \left(\frac{I+1/2}{I+1}\right) \mu_i g_i A^{\frac{2}{3}}. \tag{6.2}$$

Here, $\mathcal{K} = (-1)^{I+\frac{1}{2}-l}(I+1/2)$, l is the orbital angular momentum of the external unpaired nucleon $i = n, p$; $\mu_p = +2.8$, $\mu_n = -1.9$, and A is the atomic mass number. Theoretical estimates give the dimensionless strength constant for nucleon-nucleus weak potential $|g_p| \simeq 4.6$ for a proton [14], and $|g_n| \sim 1$ for a neutron [15]. Due to the $A^{2/3}$ scaling of this effect, the nuclear anapole moment provides the dominant NSD-PV contribution for systems containing heavy nuclei [4]. The determination of nuclear anapole effects can contribute to the fundamental understanding of parity violation in the hadronic sector [4, 16].

To date, only one single observation of a non-zero nuclear anapole moment was achieved using a Stark-PV interference technique in an experiment on the ^{133}Cs atom [17], where the main source of the anapole moment was due to the unpaired proton. The value of κ_A for ^{133}Cs was determined as κ_A=0.364(62)$\times 10^{-1}$ [15]. Further measurements on Cs and other alkali atoms using the ground state hyperfine splitting have been recently proposed [18]. Complementary measurements are also being performed on atoms with unpaired neutrons, such as Yb [19] and Fr [20].

It was shown early on [9, 21, 22] that NSD parity violating effects are enhanced significantly in diatomic molecules with $^2\Sigma_{1/2}$ and $^2\Pi_{1/2}$ electronic states due to the mixing of close rotational states of opposite parity. Thus, these systems provide a different, advantageous route for the search for these phenomena. An experiment to measure NSD-PV effects using the Stark-PV interference technique

in polar diatomic molecules was proposed in 2008 by DeMille and coworkers [23]. In this approach, the opposite parity rotational or hyperfine levels of ground state molecules are tuned to near-degeneracy by a magnetic field, causing dramatic amplification of the parity violating effects [24]. Highly sensitive measurements of this type using the BaF molecule were demonstrated recently [25, 26]. Another experiment based on optical rotation measurements in ^{199}HgH was also proposed [27].

In diatomic molecules with non-zero nuclear spin and $^2\Sigma_{1/2}$ and $^2\Pi_{1/2}$ electronic states, the nuclear anapole moment interaction between an electron and a nucleus can be rewritten in a slightly simplified form

$$H_A = \kappa_A \, \frac{G_F}{\sqrt{2}} \rho(\boldsymbol{r}) \alpha_+ \tag{6.3}$$

with

$$\alpha_+ = \alpha_x + i\alpha_y = \begin{pmatrix} 0 & \sigma_x \\ \sigma_x & 0 \end{pmatrix} + i \begin{pmatrix} 0 & \sigma_y \\ \sigma_y & 0 \end{pmatrix}. \tag{6.4}$$

Here, σ_x and σ_y are the Pauli matrices. The $^2\Sigma_{1/2}$ and $^2\Pi_{1/2}$ open-shell electronic states are twofold degenerate, corresponding to the two possible projections of electronic angular momentum along $\boldsymbol{n}$, i.e., $|\Omega\rangle = \left|\pm\frac{1}{2}\right\rangle$, where $\boldsymbol{n}$ is the unit vector directed along the molecular axis from the heavier to the lighter nucleus. The interaction H_A removes the degeneracy and mixes $|\Omega\rangle$ states with different signs (parities).

The $\hat{\mathcal{P}}$-odd interaction coefficient W_A is usually explored for the expression of the strength of coupling of the two different parity states. This coefficient depends on the electronic structure of the molecule and is defined for a given electronic state; it can be derived from the expression for H_A as the transition element between the two different $|\Omega\rangle$ states [28],

$$W_A = \frac{G_F}{\sqrt{2}} \left\langle +\tfrac{1}{2} \right| \rho(\boldsymbol{r}) \alpha_+ \left| -\tfrac{1}{2} \right\rangle . \tag{6.5}$$

Note that the matrix elements calculated between the same $|\Omega\rangle$ states are zero. Thus, the coefficient W_A defines the amplitude of the expectation value of H_A in the mixed-parity state. Knowledge of W_A is required for extracting the nuclear anapole moment from experiment. It can not be measured directly, and has to be provided by theory. Needless to say the accuracy and reliability of the calculated W_A coefficients is important for the meaningful interpretation of any measurement, and it is thus most desirable to employ state-of-the-art relativistic quantum theoretical methods for such calculations.

Here we perform relativistic coupled cluster calculations to obtain the W_A coefficient for BaF within the framework of a finite-field approach. We investigate the sensitivity of W_A to various computational parameters allowing us to estimate the uncertainty of our result, and finally propose a recommended value for interpretations of future experiments on this molecule.

There have been two previous studies that used coupled cluster theory for the calculation of the W_A coefficient. Relativistic two-component Fock-space coupled cluster theory was used to calculate W_A and other $\hat{\mathcal{P}}$- and ($\hat{\mathcal{P}}$, $\hat{\mathcal{T}}$)-odd parameters for RaF (the authors estimated the uncertainty of the results as 10%). More recently, the relativistic Fock-space coupled cluster method was used to calculate the W_A coefficients of the $^2\Sigma_{1/2}$ and the $^2\Pi_{1/2}$ electronic states of HgH [27].

The majority of earlier investigations of NSD-PV effects in diatomic molecules such as BaF have relied on more approximate approaches such as semiempirical methods [23, 29], where the W_A parameters were estimated using experimental spectroscopic data. Kozlov *et al.* performed relativistic effective core potential (RECP) calculations in the framework of a self-consistent-field (SCF) approach estimating core polarization effects by an effective operator (EO) [30]. Nayak and Das [31] carried out Dirac-Hartree-Fock (DHF) calculation within restricted active space configuration interaction (RASCI). Isaev and Berger [32] used a quasirelativistic two-component zeroth-order regular approximation (ZORA) combined with Hartree-Fock (HF) and density functional theory (DFT), and scaled the results using a semiempirical model described in Ref. [33]. We have previously carried out both DHF and DFT calculations of this property for BaF and many other diatomic molecules [34, 35]. In that work the average of the DHF and the DFT results scaled by the effect of core-polarization (CP) obtained from atomic calculations was taken as the recommended value; these results are designated here as DHF/DFT+CP.

6.2 Method and computational details

The calculations were carried out using the adapted version of the DIRAC program package [36] in the framework of the Dirac-Coulomb Hamiltonian,

$$H_0 = \sum_i [c\boldsymbol{\alpha}_i \cdot \boldsymbol{p}_i + \beta_i m_e c^2 + V(r_i)] + \sum_{i<j} \frac{e^2}{r_{ij}}, \tag{6.6}$$

where $\boldsymbol{\alpha}_i$ and β are the Dirac matrices in standard representation. The Coulomb potential $V(r_i)$ takes into account the finite size of the nuclei, modelled by Gaussian charge distributions [37]. The use of Gaussian charge distribution has the advantage that the nucleus-electron attraction integrals and the electron-electron

repulsion integrals can be evaluated by the same efficient routines and thus leads to the easy computational implementation [37].

The $\hat{\mathcal{P}}$-odd interaction constant is a property of a given nucleus within the molecular environment and for a diatomic molecule we have in principle two W_A values. In this work, however, we entirely focus on the W_A parameter at the heavier nucleus relevant for future experiments.

In order to perform coupled cluster calculations for the W_A parameter, we employ a finite-field approach (FF) [38, 39]. Within this scheme, the entire Hamiltonian of the system H is regarded to be a function of some perturbation parameter λ,

$$H(\lambda) = H_0 + \lambda \frac{G_F}{\sqrt{2}} \rho(\boldsymbol{r}) \alpha_+. \tag{6.7}$$

The nuclear density $\rho(\boldsymbol{r})$ is of Gaussian shape, which is suitable for the fully relativistic framework of the present work, as the $s_{1/2}$ and $p_{1/2}$ spinors are singular at the nucleus. For small values of λ, the total energy can be expanded in Taylor series around $\lambda = 0$,

$$E(\lambda) = E(0) + \sum_{k=1} \frac{\lambda^k}{k!} \frac{\partial^k E(\lambda)}{\partial^k \lambda}\bigg|_{\lambda \to 0}. \tag{6.8}$$

The calculations are performed at various perturbation strengths λ. If these are chosen to be small enough to remain in the linear regime, the higher order terms can be ignored and W_A can be obtained numerically, according to the Hellmann-Feynman theorem, from the first derivative of the energy with respect to λ:

$$W_A = \frac{dE(\lambda)}{d\lambda}\bigg|_{\lambda=0}. \tag{6.9}$$

The perturbation strength needs to be sufficiently large such that the change in total energy is not lost in the precision of the calculations. We have tested the linearity of the above expression with different perturbation strengths applied, i.e. $\lambda = 10^{-6}, 10^{-7}, 10^{-8}$ and 10^{-9}. Based on our results, we found that minimal error in linear fit is obtained for perturbation strengths of the order of $\sim 10^{-8}$. Furthermore, the energy convergence requirement of the coupled cluster iterations had to be set to 10^{-12} a.u.

We have used and compared two variants of relativistic coupled cluster theory: the standard single-reference coupled cluster method with single, double, and perturbative triple contributions, (CCSD(T)) [40], and the multireference Fock-space coupled cluster approach (FSCC) [41]. Within the framework of the valence-universal FSCC approach an effective Hamiltonian is defined and calculated in a low-dimensional model (or P) space, constructed from zero-order

wave functions (Slater determinants), with eigenvalues approximating some desirable eigenvalues of the Hamiltonian. According to Lindgren's formulation of the open-shell CC method [42], the effective Hamiltonian has the form

$$H_{\text{eff}} = PH\Omega P,\ \Omega = \exp\{S\}, \tag{6.10}$$

where Ω is the normal-ordered wave operator and the excitation operator S is defined with respect to a closed-shell reference determinant (vacuum state) and partitioned according to the number of valence holes (m) and valence particles (n) with respect to this reference:

$$S = \sum_{m\geqslant 0}\sum_{n\geqslant 0}\Big(\sum_{l\geqslant m+n} S_l^{(m,n)}\Big). \tag{6.11}$$

Here, l is the number of excited electrons.

BaF has a single valence electron occupying the σ orbital and thus two different computational schemes are appropriate for this system. In the first scheme, designated FSCC(0,1), we start with BaF^+. After solving the relativistic Dirac-Fock equations and correlating this closed shell reference state, an electron is added to reach the neutral state. At each stage, the coupled cluster equations are solved to obtain the correlated ground and excited state energies. The extra electron can be added to the lowest σ orbital, or allowed to also occupy the higher states, thus yielding a number of energy levels and also improving the description of the ground state energy and properties. We have tested the influence of the size of the model space P on the calculated W_A parameters. Within the second computational scheme (FSCC(1,0)) the calculation begins from the closed shell negative ion BaF^-, and an electron is removed to obtain the neutral system. In principle, the two schemes should give very similar results for the ground state, the main difference stemming from the different closed shell reference states yielding different Hartree-Fock orbitals (i.e. relaxation effects). In addition to the coupled cluster results, we also report W_A values from second-order Møller-Plesset (MP2) method [43].

In order to further investigate the effects of electron correlation we performed open-shell single determinant average-of-configuration DHF [44] and relativistic DFT [45] calculations for W_A by evaluating the matrix elements of the $\rho(\boldsymbol{r})\alpha_+$ operator in the molecular spinor basis. To test the performance of various functionals for this property, the DFT calculations were carried out with the Perdew-Burke-Ernzerhof (PBE) functional [46, 47], the Slater local exchange (SVWN5) functional [48], the Becke-Lee-Yang-Parr hybrid functional (B3LYP) [49–51] and its Coulomb-attenuated version (CAMB3LYP*) adapted to accurately describe PV energy shifts in heavy atomic systems obtained from coupled cluster theory [52, 53].

Standard Dyall's basis sets of varying size [54, 55] were employed to investigate the basis set effects on the calculated W_A values. To further improve our results, we augmented the basis sets of the two atoms by additional large (tight) and small (diffuse) exponent functions (see below for details). Further investigated computational parameters were the active space in the electron correlation procedure, i.e. the number of correlated electrons and the chosen virtual energy cut-off. In addition, we include the Gaunt term in our calculations [56] as part of the Breit interaction, which corrects the 2-electron part of the Dirac-Coulomb Hamiltonian up to order $(Z\alpha)^2$ [57]. The Gaunt interaction is included self-consistently at the DHF step. Alongside the detailed investigations of BaF, we also perform calculations for the W_A parameters of its lighter homologues BeF, MgF, CaF, and SrF in order to examine the dependence of W_A on the nuclear charge of the group 2 atom. The positions of the atoms were chosen according to the molecular experimental equilibrium bond lengths (1.361 Å for BeF, 1.750 Å for MgF, 1.967 Å for CaF [58], 2.076 Å for SrF [59], and 2.159 Å for BaF [60]).

6.3 Results and discussion

The first important step in our investigation was a detailed study of the influence of the basis set size on the W_A parameters; we also use this study to determine the best basis set which is still affordable computationally. These tests were performed within the DHF, CCSD, and CCSD(T) framework. In the coupled cluster calculations, 35 electrons were correlated and virtual orbitals with energies above 30.0 a.u. were excluded. We used the standard Dyall's relativistic basis sets of double-, triple-, and quadruple-ζ quality [54, 55]. To check the influence of diffuse functions, we have augmented the dyall.v4z basis with a single diffuse function for each symmetry (s-aug-dyall.v4z) and with two diffuse functions (d-aug-dyall.v4z). While diffuse functions are usually more important for chemical properties, a good description of the electronic wave function in the nuclear region is essential for obtaining reliable results for parity-violating effects [61]. In particular, it was demonstrated in our earlier work [34, 35, 62] that tight s and p functions have a considerable influence on the W_A parameter at the DHF level, especially for the lighter elements. Thus, we also tested the effect of adding different types of tight functions to the basis sets (designated as ts for high exponent s function, tp for high exponent p, etc.). The augmentations (both with the diffuse and the tight functions) were carried out separately for each of the atoms, and the results are summarised in Table 6.1.

Going from double- to triple-ζ quality basis set increases the calculated W_A value by ∼10%; moving to quadruple-ζ quality leads to a further increase of less than a single percent on the coupled-cluster level. The correlation part of the W_A coefficient does not scale smoothly with the size of the basis set, and hence

Table 6.1: Basis set dependence of the calculated W_A coefficient (Hz) of BaF (for the Ba atom).

Basis set (Ba)	Basis set (F)	DHF	CCSD	CCSD(T)
v2z	v2z	99.12	131.04	129.22
v3z	v3z	110.70	143.51	141.42
v4z	v4z	112.27	144.02	141.84
	Diffuse functions			
s-aug-v4z	dyall.v4z	112.25	143.95	141.76
d-aug-v4z	dyall.v4z	112.25	143.95	141.76
dyall.v4z	s-aug-v4z	112.09	143.36	141.16
dyall.v4z	d-aug-v4z	112.04	143.27	141.05
	Tight functions			
v4z+ts	v4z	112.30	144.08	141.89
v4z+tp	v4z	112.39	144.15	141.97
v4z+td	v4z	112.27	144.00	141.82
v4z+tf	v4z	112.32	145.17	143.02
v4z+2tf	v4z	112.33	145.28	143.08
v4z+tg	v4z	112.27	144.42	142.31
v4z	v4z+ts	112.27	144.02	141.84
v4z	v4z+tp	112.27	144.02	141.84
v4z	v4z+td	112.27	144.00	141.82
v4z	v4z+tf	112.27	144.00	141.82

we did not perform extrapolation to the complete basis set limit. Adding diffuse functions for barium has negligible effects on the results, while augmenting the basis of fluorine reduces the W_A value by 0.5% as the fluorine orbitals extend into the domain of the Ba atom. Out of the large exponent functions, only the tight f-type function has a discernible influence on the calculated W_A, raising its value by ∼1% on CCSD and CCSD(T) level (but having no impact on the DHF results). Adding a second tight f orbital leaves the calculated W_A almost unchanged. We thus assume that the results are converged (close to the basis set limit) and perform the rest of our calculations using the optimized dyall.v4z+tf basis set.

Next we explored the effect of the number of correlated electrons and the size of the virtual space on W_A. In the first set of calculations we keep the energy cut-off for the virtual space at a rather high value (500 a.u.) and vary the number of correlated electrons. Figure 6.1 presents the calculated MP2, CCSD, and CCSD(T) W_A values. Overall, the difference between including 35 electrons in the calculation (corresponding to the commonly used cut-off of −20.0 a.u. in

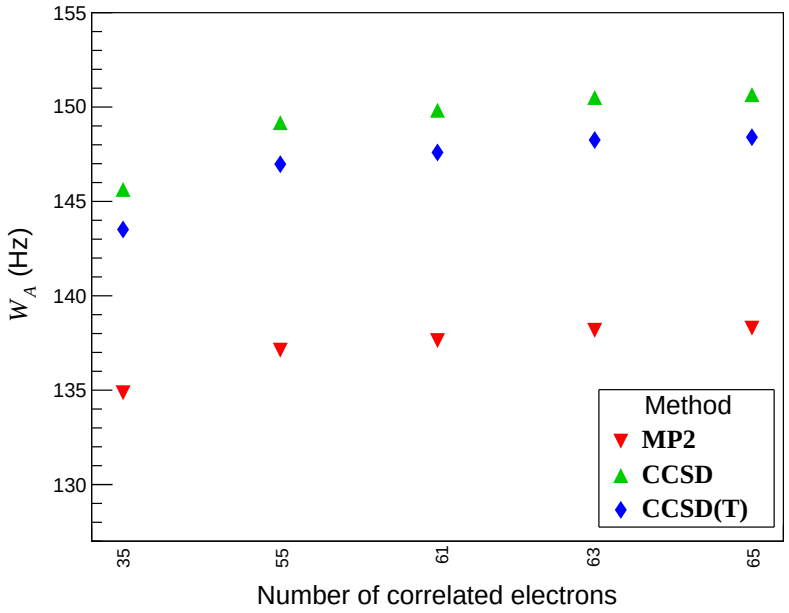

Figure 6.1: Calculated W_A coefficients of BaF (for the Ba atom) using different number of correlated electrons.

the space of the occupied orbitals) and correlating all 65 electrons is ∼3% for the three methods. We note that the major part of this difference does not come from the 1s orbital alone, despite its proximity to the nucleus, but rather comes from all the core shells. In order to achieve $< 1\%$ accuracy, all the electrons should be included in the electron correlation procedure.

In the next step we performed calculations where all electrons are correlated, and vary the energy cut-off in the virtual space (Figure 6.2). Unlike many other atomic or molecular properties, the calculated W_A value does not saturate at the energy cut-off of about 30 a.u., but continues to increase. The difference in the value corresponding to cut-off of 500 a.u. compared to 30 a.u. is ∼3%, and the W_A value continues to increase further beyond this point, albeit at a much lower rate ($W_A = 148.91$ Hz for cut-off of 1000 a.u. vs. 148.40 Hz for 500 a.u.). The importance of inclusion of high lying virtual orbitals for the correlation of the core electrons was also observed by Skripnikov *et al.* [63] for the scalar-pseudoscalar interaction constant R_s in the francium atom. We selected a final

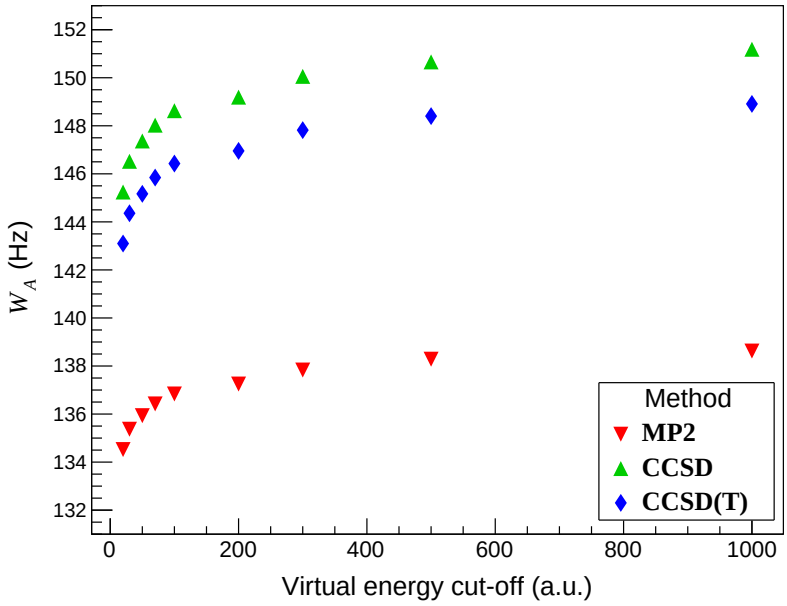

Figure 6.2: Calculated W_A coefficients of BaF (for the Ba atom) using different sizes of the virtual space.

cut-off of 500 a.u. for the following calculations, which is a compromise between optimal accuracy and computational feasibility.

Table 6.2 contains the W_A constant of BaF (for the Ba atom), calculated at the DHF, MP2, and DFT levels of theory, using different functionals, and within various coupled cluster schemes. These results were obtained using the optimised basis set (dyall.v4z augmented by a single tight f function) and in the MP2 and CC calculations all electrons were correlated with the energy cut-off for the virtual space set to 500 a.u.

Electron correlation clearly plays an important role for this property, and the CCSD results are 25% higher than the corresponding DHF values. MP2, however, performs remarkably well and captures the majority of electron correlation, differing from the CCSD value by only 8%.

DFT results tend to be very close to the DHF value; in particular, the result obtained with the CAMB3LYP* functional, which is generally expected to perform well for parity-violating properties [53], is almost identical to the DHF

result, which is somewhat disappointing. Note, similarly disappointing results are obtained for electric field gradients of molecules containing transition metals [64], and arguments about the failure of DFT can be found in Ref. [65]. As we expect that most density functionals lie in-between the DHF and the local density approximation (SVWN5) results, here this deficiency cannot be so easily fixed by adjusting the Hartree-Fock contribution in the hybrid functional as was done for electric field gradients [64].

Moving to the coupled cluster results, the triple excitations contribute very little and they lower the W_A value by $\sim$1.5% only. We thus expect that the higher-order excitations in the CC procedure will not play an important role for this property.

As already mentioned, we have tested two variants of FSCC. In the first one, FSCC(0,1), the calculation starts from BaF^+, and an electron is added into the virtual orbitals. Here we test two sizes of the model space: the minimal one, designated Model space I, where the additional electron is allowed to occupy only the lowest σ orbital (yielding the ground $X^2\Sigma_{1/2}$ state), and Model space II, which contains 2 σ, 2 π, and 2 δ orbitals.

The second FSCC scheme, FSCC(1,0), starts with BaF^- as reference state, and an electron is removed to reach the neutral system. Usually, one expects the FSCC results to be situated between the CCSD and the CCSD(T) values (for recent reviews of relativistic FSCC approach, see Ref. [66]). The sector (0,1) results are extremely close to the CCSD(T) values; superior performance of FSCC in particle sectors compared to single reference CCSD has been observed in the past [66]. It should be noted that in this case increasing the size of the model space has negligible influence on the results. The sector (1,0) values are slightly higher than the CCSD ones, rather than lower as one would expect. This is probably due to the fact that the (1,0) calculation starts from a negative closed shell reference state, and the basis which was optimised for the neutral system does not provide sufficient description of the more diffuse orbitals in BaF^-.

The Gaunt interaction lowers the W_A (on DHF level) by 0.7 Hz. We add the Gaunt contribution from the DHF calculation to the CCSD(T) result to provide the final (recommended) value for the W_A constant of BaF. This value is designated as CCSD(T)+Gaunt in Table 6.2.

In order to put an error bar on this value, we need to examine the remaining sources of uncertainty within our computational approach. These include basis set deficiencies, the unaccounted full triple and higher order contributions in the coupled cluster procedure, the choice of the virtual space cut-off, and neglect of the full Breit and higher-order QED effects. From the investigation of the basis set effects (Table 6.1), we see that the contribution from the diffuse functions on the F atom, which we neglect here, is around -0.6 Hz, while the effect of tight functions beyond tight f (mostly stemming from the tight g) is $+0.5$ Hz. These

two effects cancel out, but we take a conservative estimate of basis set uncertainty of about 0.5 Hz (of the order of magnitude of these effects), to account for any further shortfalls of the basis set. The difference in the values of W_A calculated with a virtual space cut-off of 500 a.u. and 1000 a.u. is about 0.5 Hz and it seems that saturation is reached; we thus take 1 Hz as the corresponding uncertainty. The contribution of perturbative triple excitations in the calculation via the CCSD(T) scheme is -2.26 Hz. In CCSD(T) the triple excitations are included fully in the fourth order in perturbation theory, and part of the fifth-order terms is also included [67]. To test the stability of this scheme, we present the results of CCSD-T calculation where further fifth-order terms are included [68], as well as the CCSD+T approach [69], where the triple corrections are treated only at forth-order level. These values are also shown in Table 6.2. While CCSD+T has the strongest effect on the calculated W_A (-2.77 Hz), addition of the fifth order terms moderates the contribution of the triple excitations, and the difference between CCSD(T) and CCSD-T is negligible. Currently, there is no possibility to evaluate the contribution of quadruple and higher excitation, but as the triple excitation contribution is already quite small, we may safely neglect the higher order ones. We take twice the difference between CCSD+T and CCSD-T (1.5 Hz) as the uncertainty due to incomplete treatment of electron correlation. We assume that the effect of replacing the Breit term by the Gaunt term and neglecting QED effects is not more than the contribution of the Gaunt term itself (~ 0.7 Hz). The final source of uncertainty is in the numerical nature of the finite field approach, where a slight dependence on the size of the perturbation can emerge, and for small fields numerical noise might be a factor. Test calculations we carried out show that these effects are small, up to 0.5 Hz. Summing up all of the above effects we get an uncertainty estimate of 2 Hz, or 1.5%.

Table 6.2 also contains the results of the previous investigations of the W_A parameter of BaF. The majority of these studies used approximate methods, such as DHF and DFT, or semiempirical approaches. Our investigation of this property in BaF is within a relativistic coupled cluster approach, and thus direct comparison with earlier values is perhaps difficult. Our present DHF value is in excellent agreement with the RECP-SCF result of Kozlov *et al.* [30]. However, when these authors include an effective operator (EO) to account for core polarization effects, their final value overshoots the result obtained here. The DHF and DFT results of Ref. [32] are close to the corresponding present values but the scaling scheme seems to overcompensate for the spin-polarization effects, similar to that employed in Ref. [30]. Our earlier DHF and DFT calculations are in good agreement with the present results, as expected, and the final value in that publication, corrected for core polarisation, is in fact very close to our CCSD(T) result, supporting the use of this scaling scheme. The DHF result of Ref. [31] is larger than our value and other uncorrelated calculations [30, 35, 70], but their

RASCI value is again close to our present CCSD(T) result.

It is expected that the magnitude of $|W_A|/R_W$ of the $^2\Sigma_{1/2}$ electronic state scales as Z^2 [8], where the relativistic enhancement parameter R_W ($R_W \geq 1$) is defined as follows [9],

$$R_W = \frac{2\gamma+1}{3}\left(\frac{a_B}{2Zr_0A^{\frac{1}{3}}}\right)^{2-2\gamma}\frac{4}{\left[\Gamma(2\gamma+1)\right]^2}, \tag{6.12}$$

$$\gamma = \sqrt{1-(Z\alpha)^2}. \tag{6.13}$$

Here, α is the fine-structure constant, r_0 is the nucleus radius, taken here as $r_0 = 1.2\times10^{-15}$ m [4], $\Gamma(x)$ is the gamma function, and a_B is the Bohr radius. To test this dependence, we have calculated the W_A parameters of the other alkaline earth metal fluorides (for the alkaline-earth-metal atoms). These calculations were performed with the standard Dyall's v4z basis set; all the electrons were correlated, and the energy cut-off for the virtual space was again set at 500 a.u. Table 6.3 contains the calculated W_A parameters at the DHF, DFT (B3LYP), MP2, and CCSD(T) levels of theory. In Figure 6.3, we show $\log_{10}(|W_A|/R_W)$ as a function of $\log_{10}(Z)$ for these systems. The results are fitted by a linear function:

$$\log_{10}\left(\frac{|W_A|}{R_W}\right) = a\log_{10}(Z) + b. \tag{6.14}$$

For the four computational methods, the scaling factors a are more or less identical (1.77 for DHF, 1.76 for B3LYP, 1.79 for MP2, and 1.80 for CCSD(T)), in spite of very different W_A values, implying that the trend is not sensitive to the treatment of electron correlation. Gaul *et al.* report a similar finding concerning the scaling of the $\hat{\mathcal{P}}$- and $\hat{\mathcal{T}}$-violating parameters W_d and W_s in this group of molecules [71]. It should be mentioned that for other sets of molecules investigated in Ref. [71] (i.e. group 4 oxides and group 12 hydrides), this is not the case, and the Hartree-Fock and DFT scaling differ significantly. The scaling we obtain here is close (if slightly lower) to the expected Z^2 dependence and in good agreement with the scaling derived from the earlier DHF+DFT results [35] and that of Ref. [32]. In this group of molecules, no additional enhancement due to electronic structure effects is observed (unlike in group 12 fluorides, for example, where the scaling is predicted to be 2.4 [35]).

6.4 Conclusions

In this work, we presented high accuracy relativistic coupled cluster calculations for the nuclear spin dependent $\hat{\mathcal{P}}$-odd interaction constant W_A of BaF. The effect of various computational parameters on the obtained result was explored; these

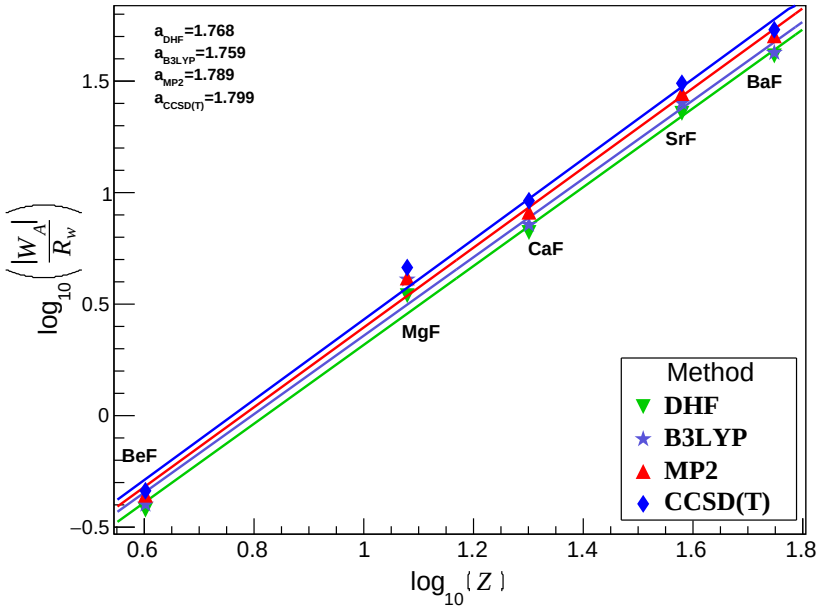

Figure 6.3: Scaling of $\log_{10}(W_A/R_W)$ with $\log_{10}(Z)$ for the selected alkaline earth metal fluorides.

include the choice of the basis set, treatment of electron correlation, number of correlated electrons, size of the virtual space, and inclusion of the Gaunt term. We find that inclusion of electron correlation raises the calculated W_A value by about 25%; the rest of the parameters have a much weaker effect on the results, of the order of a single percent. Furthermore, performance of various DFT functionals for this property was investigated and found lacking. We propose a final recommended value of $W_A = 147.7$ Hz for the barium atom in BaF, obtained from the CCSD(T) calculation using the optimised basis set and corrected for the Gaunt contribution. This result, with its estimated uncertainty of 1.5% will be useful for interpretation of future experiments on this system. We have also investigated the scaling of the W_A parameter for the alkaline-earth-metal atoms in group 2 fluorides, and found it to be close to the expected Z^2 behavior.

Table 6.2: Calculated W_A coefficient (Hz) of BaF (for the Ba atom) within different correlation approaches and compared to previous predictions. The present recommended value (CCSD(T)+Gaunt) is given in bold font.

W_A (Hz)	Method	Reference
112.32	DHF	This work
138.28	MP2	This work
150.66	CCSD	This work
148.40	CCSD(T)	This work
147.89	CCSD+T	This work
148.59	CCSD-T	This work
148.84	FSCC(0,1)-Model space I	This work
148.25	FSCC(0,1)-Model space II	This work
151.98	FSCC(1,0)	This work
147.71	**CCSD(T)+Gaunt**	**This work**
123.50	DFT(SVWN5)	This work
116.18	DFT(B3LYP)	This work
116.08	DFT(PBE)	This work
112.92	DFT(CAMB3LYP*)	This work
210-240	Semiempirical	[29]
111	RECP-SCF	[30]
181	RECP-SCF+EO[a]	[30]
164	Semiempirical	[23]
135	DHF	[31]
160	4c-RASCI	[31]
111	ZORA-HF	[32]
119	ZORA-DFT(B3LYP)	[32]
190	Scaled ZORA-HF[b]	[32]
112.9	DHF	[35]
111.6	DFT(CAMB3LYP*)	[35]
146.0	DHF/DFT+CP[c]	[35]

[a] RECP-SCF+EO: RECP SCF calculation with an effective operator describing valence-core correlations.
[b] ZORA-HF results with semiempirical scaling.
[c] Average of DHF and DFT values, scaled by a core-polarisation parameter.

Table 6.3: Calculated W_A coefficients (Hz) of alkaline-earth-metal fluorides (for the alkaline-earth-metal atoms).

Molecule	DHF	B3LYP	MP2	CCSD(T)
BeF	0.38	0.40	0.44	0.46
MgF	3.67	4.34	4.41	4.91
CaF	7.74	8.39	9.55	10.75
SrF	37.29	41.50	45.79	50.87
BaF	112.27	116.02	138.23	147.16

References

[1] Y. Hao, M. Iliaš, E. Eliav, P. Schwerdtfeger, V. V. Flambaum, and A. Borschevsky, Phys. Rev. A **98**, 032510 (2018).

[2] C. Patrignani *et al.* (Particle Data Group), Chin. Phys. C. **40**, 100001 (2016).

[3] M. S. Safronova, D. Budker, D. DeMille, D. F. J. Kimball, A. Derevianko, and C. W. Clark, Rev. Mod. Phys. **90**, 025008 (2018).

[4] J. Ginges and V. V. Flambaum, Phys. Rep. **397**, 63 (2004).

[5] P. J. Mohr, D. B. Newell, and B. N. Taylor, J. Phys. Chem. Ref. Data **45**, 043102 (2016).

[6] V. N. Novikov, O. P. Sushkov, V. V. Flambaum, and I. B. Khriplovich, Sov. Phys. JETP **46**, 420 (1977), or Zh. Eksp. Theor. Fiz **73**, 802 (1977).

[7] V. V. Flambaum and I. B. Khriplovich, Sov. Phys. JETP **52**, 835 (1980), or Zh. Eksp. Teor. Fiz **79**, 1656 (1980).

[8] V. V. Flambaum and I. B. Khriplovich, Sov. Phys. JETP **62**, 872 (1985), or Zh. Eksp. Theor. Fiz **89**, 1505 (1985).

[9] V. V. Flambaum and I. B. Khriplovich, Phys. Lett. A **110**, 121 (1985).

[10] C. Bouchiat and C. A. Piketty, Z. Phys. C **49**, 91 (1991).

[11] W. R. Johnson, M. S. Safronova, and U. I. Safronova, Phys. Rev. A **67**, 062106 (2003).

[12] Y. B. Zel'dovich, Sov. Phys. JETP **6**, 1184 (1958), or Zh. Eksp. Teor. Fiz **33**, 1531 (1957).

[13] O. Sushkov, V. Flambaum, and I. Khriplovich, Sov. Phys. JETP **60**, 873 (1984), or Zh. Eksp. Teor. Fiz **87**, 1521 (1984).

[14] V. V. Flambaum, I. B. Khriplovich, and O. P. Sushkov, Phys. Lett. B **146**, 367 (1984).

[15] V. V. Flambaum and D. W. Murray, Phys. Rev. C **56**, 1641 (1997).

[16] W. C. Haxton and C. E. Wieman, Annu. Rev. Nucl. Part. Sci. **51**, 261 (2001).

[17] C. S. Wood, S. C. Bennett, D. Cho, B. P. Masterson, J. L. Roberts, C. E. Tanner, and C. E. Wieman, Science **275**, 1759 (1997).

[18] J. Choi and D. S. Elliott, Phys. Rev. A **93**, 023432 (2016).

[19] D. Antypas, A. Fabricant, L. Bougas, K. Tsigutkin, and D. Budker, Hyperfine Interact. **238**, 21 (2017).

[20] S. Aubin, J. A. Behr, R. Collister, V. V. Flambaum, E. Gomez, G. Gwinner, K. P. Jackson, D. Melconian, L. A. Orozco, M. R. Pearson, D. Sheng, G. D. Sprouse, M. Tandecki, J. Zhang, and Y. Zhao, Hyperfine Interact. **214**, 163 (2013).

[21] L. N. Labzovsky, Sov. Phys. JETP **48**, 434 (1978), or Zh. Eksp. Theor. Fiz **48**, 434 (1978).

[22] O. P. Sushkov and V. V. Flambaum, Sov. Phys. JETP **48**, 608 (1978), or Zh. Eksp. Teor. Fiz **75** 1208 (1978).

[23] D. DeMille, S. B. Cahn, D. Murphree, D. A. Rahmlow, and M. G. Kozlov, Phys. Rev. Lett. **100**, 023003 (2008).

[24] M. G. Kozlov, L. N. Labzovskii, and A. O. Mitrushchenkov, Sov. Phys. JETP **73**, 415 (1991), or Zh. Eksp. Theor. Fiz **100**, 761 (1991).

[25] E. Altuntaş, J. Ammon, S. B. Cahn, and D. DeMille, Phys. Rev. A **97**, 042101 (2018).

[26] E. Altuntaş, J. Ammon, S. B. Cahn, and D. DeMille, Phys. Rev. Lett. **120**, 142501 (2018).

[27] A. J. Geddes, L. V. Skripnikov, A. Borschevsky, J. C. Berengut, V. V. Flambaum, and T. P. Rakitzis, Phys. Rev. A **98**, 022508 (2018).

[28] A. D. Kudashov, A. N. Petrov, L. V. Skripnikov, N. S. Mosyagin, T. A. Isaev, R. Berger, and A. V. Titov, Phys. Rev. A **90**, 052513 (2014).

[29] M. G. Kozlov and L. N. Labzowsky, J. Phys. B: At., Mol. Opt. Phys. **28**, 1933 (1995).

[30] M. G. Kozlov, A. V. Titov, N. S. Mosyagin, and P. V. Souchko, Phys. Rev. A **56**, R3326 (1997).

[31] M. K. Nayak and B. P. Das, Phys. Rev. A **79**, 060502 (2009).

[32] T. A. Isaev and R. Berger, Phys. Rev. A **86**, 062515 (2012).

[33] M. G. Kozlov, Sov. Phys. JETP **62**, 1114 (1985).

[34] A. Borschevsky, M. Iliaš, V. A. Dzuba, K. Beloy, V. V. Flambaum, and P. Schwerdtfeger, Phys. Rev. A **85**, 052509 (2012).

[35] A. Borschevsky, M. Iliaš, V. Dzuba, V. Flambaum, and P. Schwerdtfeger, Phys. Rev. A **88**, 022125 (2013).

[36] DIRAC, A relativistic ab initio electronic structure program, Release DIRAC17 (2017), written by L. Visscher, H. J. Aa. Jensen, R. Bast, and T. Saue, with contributions from V. Bakken, K. G. Dyall, S. Dubillard, U. Ekström, E. Eliav, T. Enevoldsen, E. Faßhauer, T. Fleig, O. Fossgaard, A. S. P. Gomes, E. D. Hedegård, T. Helgaker, J. Henriksson, M. Iliaš, Ch. R. Jacob, S. Knecht, S. Komorovský, O. Kullie, J. K. Lærdahl, C. V. Larsen, Y. S. Lee, H. S. Nataraj, M. K. Nayak, P. Norman, G. Olejniczak, J. Olsen, J. M. H. Olsen, Y. C. Park, J. K. Pedersen, M. Pernpointner, R. di Remigio, K. Ruud, P. Sałek, B. Schimmelpfennig, A. Shee, J. Sikkema, A. J. Thorvaldsen, J. Thyssen, J. van Stralen, S. Villaume, O. Visser, T. Winther, and S. Yamamoto (see `http://www.diracprogram.org`).

[37] L. Visscher and K. G. Dyall, At. Data Nucl. Data Tabl. **67**, 207 (1997).

[38] H. J. Monkhorst, Int. J. Quant. Chem. **12**, 421 (1977).

[39] J. Thyssen, J. K. Laerdahl, and P. Schwerdtfeger, Phys. Rev. Lett. **85**, 3105 (2000).

[40] L. Visscher, T. Lee, and K. G. Dyall, J. Chem. Phys. **105**, 8769 (1996).

[41] L. Visscher, E. Eliav, and U. Kaldor, J. Chem. Phys. **115**, 9720 (2001).

[42] I. Lindgren, "Electronic structure and chemistry of the heaviest elements," in *Many-Body Methods in Quantum Chemistry*, edited by U. Kaldor (Springer-Verlag, 1989) p. 293.

[43] C. Møller and M. S. Plesset, Phys. Rev. **46**, 618 (1934).

[44] J. Thyssen, *Development and applications of methods for correlated relativistic calculations of molecular properties*, Ph.D. thesis, University of Southern Denmark (2001).

[45] T. Saue and T. Helgaker, J. Comput. Chem. **23**, 814 (2002).

[46] J. P. Perdew, K. Burke, and M. Ernzerhof, Phy. Rev. Lett. **77**, 3865 (1996).

[47] K. Burke, J. P. Perdew, and M. Ernzerhof, Phys. Rev. Lett. **78**, 1396 (1997).

[48] S. H. Vosko, L. Wilk, and M. Nusair, Canad. J. Phys. **58**, 1200 (1980).

[49] C. Lee, W. Yang, and R. G. Parr, Phys. Rev. B **37**, 785 (1988).

[50] A. D. Becke, J. Chem. Phys. **98**, 5648 (1993).

[51] A. D. Becke, J. Comput. Chem. **20**, 63 (1999).

[52] T. Yanai and D. P. Tew, Chem. Phys. Lett. **393**, 51 (2004).

[53] C. Thierfelder, G. Rauhut, and P. Schwerdtfeger, Phys. Rev. A **81**, 032513 (2010).

[54] K. G. Dyall, J. Phys. Chem. A **113**, 12638 (2009).

[55] K. G. Dyall, Theoret. Chem. Acc. **135**, 128 (2016).

[56] J. A. Gaunt, Proc. Royal Soc. Lond. A: Math. Phys. Eng. Sci. **122**, 513 (1929).

[57] G. Breit, Phys. Rev. **34**, 375 (1929).

[58] P. J. Linstrom and W. G. Mallard (Eds.), *NIST chemistry webbook: NIST standard reference database number 69* (National Institute of Standards and Technology).

[59] R. F. Barrow and J. R. Beale, Chem. Commun. (London) , 606a (1967).

[60] C. Ryzlewicz and T. Törring, Chem. Phys. **51**, 329 (1980).

[61] J. K. Laerdahl and P. Schwerdtfeger, Phys. Rev. A **60**, 4439 (1999).

[62] A. Borschevsky, M. Iliaš, V. A. Dzuba, K. Beloy, V. V. Flambaum, and P. Schwerdtfeger, Phys. Rev. A **86**, 050501 (2012).

[63] L. V. Skripnikov, D. E. Maison, and N. S. Mosyagin, Phys. Rev. A **95**, 022507 (2017).

[64] R. Bast and P. Schwerdtfeger, J. Chem. Phys. **119**, 5988 (2003).

[65] P. Schwerdtfeger, M. Pernpointner, and J. K. Laerdahl, J. Chem. Phys. **111**, 3357 (1999).

[66] E. Eliav, A. Borschevsky, and U. Kaldor, *High-accuracy relativistic coupled cluster calculations for the heaviest elements* (Springer-Verlag, 2014) pp. 825–855.

[67] K. Raghavachari, G. W. Trucks, J. A. Pople, and M. Head-Gordon, Chem. Phys. Lett. **157**, 479 (1989).

[68] M. J. O. Deegan and P. J. Knowles, Chem. Phys. Lett. **227**, 321 (1994).

[69] M. Urban, J. Noga, S. J. Cole, and R. J. Bartlett, J. Chem. Phys. **83**, 4041 (1985).

[70] T. A. Isaev and R. Berger, arXiv:1302.5682 (2013).

[71] K. Gaul, S. Marquardt, T. Isaev, and R. Berger, arXiv:1805.05494 (2018).

Chapter 7

Nuclear anapole moment effect in BeCl[a]

7.1 Motivation

The nuclear anapole moment interaction is one of the three main sources accounting for the nuclear spin dependent parity violating (NSD-PV) effects [2], and comes from the interaction between the electromagnetic current and the nuclear weak current [3]. The effective Hamiltonian, which describes the nuclear anapole moment interaction, takes the following form [4–6],

$$H_A \equiv \frac{\kappa_A G_F}{\sqrt{2}} \Big(\boldsymbol{\alpha} \cdot \hat{\boldsymbol{I}} \Big) \rho(\mathbf{r}) \tag{7.1}$$

where $\rho(\boldsymbol{r})$ is the nuclear density distribution, G_F is the Fermi weak interaction constant [7], $\hat{\boldsymbol{I}}$ is the unit vector along the nuclear spin, and $\boldsymbol{\alpha}$ are the Dirac matrices. κ_A is a dimensionless effective coupling constant, which describes the magnitude of the nuclear anapole moment interaction.

The nuclear anapole moment effect has been observed in the ^{133}Cs atom [8, 9]. Some measurements have also been proposed on other atoms, such as ^{137}Ba [10], ^{163}Dy [11], ^{171}Yb [12], and ^{212}Fr [13]. In diatomic molecules with a $^2\Sigma_{1/2}$ ground state, the effect is strongly enhanced because of close-lying molecular levels with opposite parity, where degeneracy can be very easily occur in external fields and thus a dramatic amplification of the tiny parity-violating effect can be achieved

[a]This chapter is based on our published paper [1]: Yongliang Hao, Miroslav Iliaš, and Anastasia Borschevsky, Correlation trends in the nuclear anapole moment interaction of the Be atom in BeCl, Proceeding of Science, International Conference on Precision Physics and Fundamental Physical Constants, **FFK2019**, 057 (2019).

[14]. Recently, measurements with improved sensitivity were demonstrated for the BaF molecule [15, 16], and the corresponding theoretical investigations for BaF as well as for its homologues have also been carried out [10, 17–21].

For a $^2\Sigma_{1/2}$ ground state, Eq. (7.1) can be written as follows [5, 10],

$$H_A = \kappa_A W_A \hat{\boldsymbol{I}} \cdot \Big(\hat{\boldsymbol{n}} \times \boldsymbol{S}_{\text{eff}} \Big), \tag{7.2}$$

where $\boldsymbol{S}_{\text{eff}}$ stands for the effective spin of the open-shell electron, and $\hat{\boldsymbol{n}}$ is the unit vector along the molecular axis. The effective coupling constant κ_A can be obtained both experimentally and theoretically. On the one hand, κ_A can be determined by measuring parity-violating transitions in atoms or molecules when the W_A parameter is known. On the other hand, κ_A can also be calculated directly from nuclear theories. For instance, κ_A takes the following form in a nuclear model [4–6],

$$\kappa_A \simeq 1.15 \times 10^{-3} (-1)^{I-l+\frac{1}{2}} \left(\frac{I+1/2}{I+1} \right) \mu_i g_i A^{\frac{2}{3}}, \tag{7.3}$$

where l is the orbital angular momentum of the unpaired valence nucleon, g_i is an interaction constant with values of around 4.6 [4] and 1 [22] for the proton-nucleus and neutron-nucleus interactions, respectively, μ_i is the nuclear magnetic moment, and A is the total number of nucleons in the nucleus.

From an experimental point of view, the W_A parameter needs to be known with high accuracy so that the effective coupling constant κ_A can be obtained precisely from the measured signals. The determined values of κ_A from experiments can be compared with the calculated values from nuclear theories. Any deviation may suggest the incompleteness of our current knowledge concerning nuclear structure. However, no meaningful comparison can be made unless κ_A is precisely measured from experiments and accurately calculated from theories. Molecules containing light elements, such as BeCl, etc., are also considered as promising candidates for the study of the nuclear anapole moment effect. The practical advantage of using such molecules is that nuclear calculations for light elements are more computationally tractable. In this case, the effective coupling constant κ_A can be more accurately calculated from nuclear theories and thus a more meaningful comparison can be made.

The nuclear anapole moment interaction is only present in atoms or molecules with unpaired nucleons and unpaired electrons. Due to the scaling factor in Eq. (7.3), it is the dominating contribution to the NSD-PV effects in atoms or molecules containing heavy elements [2]. However, in molecules containing light elements, the observed NSD-PV signals may come from all three sources, but it is still possible to distinguish the nuclear anapole moment signal from the remaining NSD-PV signals by performing the measurements on different nuclei (or different isotopes) [23].

The W_A parameter, which depends on the electronic structure of the atoms or molecules, is defined by the following expression [24],

$$W_{\mathrm{A}} \equiv \frac{G_F}{\sqrt{2}} \left\langle +\tfrac{1}{2} \right| \rho(\boldsymbol{r}) \alpha_+ \left| -\tfrac{1}{2} \right\rangle , \tag{7.4}$$

with

$$\alpha_+ = \alpha_x + i\alpha_y = \begin{pmatrix} 0 & \sigma_x \\ \sigma_x & 0 \end{pmatrix} + i \begin{pmatrix} 0 & \sigma_y \\ \sigma_y & 0 \end{pmatrix} . \tag{7.5}$$

Here, σ_x and σ_y represent the Pauli matrices, and $\left|\pm\frac{1}{2}\right\rangle$ are two Ω-states. The W_A parameter cannot be measured and can only be calculated using theoretical molecular method. In Sec. 7.2, the calculations of the W_A parameter for the beryllium atom in BeCl will be discussed in more detail.

7.2 Method and computational details

In order to calculate the W_A parameter with high accuracy, we need to take into account the following three main factors: relativistic effects (Hamiltonian), basis sets, and electron correlations. To begin with, we need to include relativistic effects into our calculations so that high accuracy is assured. Furthermore, for a good description of the electronic wavefunctions, large basis sets should be employed. More importantly, since electron correlations, which describe the instantaneous interaction among electrons, are crucial in the determination of molecular properties, they should be treated properly in high-accuracy calculations. In this work, we carry out the calculations using various electron correlation methods and compare the corresponding results.

The calculations are performed using the developer's version of the DIRAC package [25] throughout this work. With respect to the treatment of relativistic effect, the following (relativistic) Dirac-Coulomb Hamiltonian is employed,

$$H_0 = \sum_i [c\boldsymbol{\alpha}_i \cdot \boldsymbol{p}_i + \beta_i m_e c^2 + V(r_i)] + \sum_{i<j} \frac{e^2}{r_{ij}}, \tag{7.6}$$

Here, the Coulomb potential takes into account the finite size of the nuclei, modeled by a Gaussian type distribution [26].

In order to have a good description of the electronic wavefunctions, we use Dyall's relativistic standard basis sets [27, 28]. Throughout this work, all the calculations are performed using the dyall.v4z basis set [27, 28] at the experimental equilibrium bond length 1.7971 [29].

In order to further investigate the influence of electron correlation on the calculated W_A parameter, various electron correlation approaches are employed. We

Table 7.1: Calculated W_A parameters (Hz) for the Be atom in BeCl at the equilibrium bond length using various electron correlation methods.

Electron correlation methods	W_A (Hz)	Δ %
DHF	0.3961	0.0%
DFT(CAMB3LYP*)	0.3973	0.3%
DFT(B3LYP)	0.4138	4.5%
DFT(PBE)	0.4245	7.2%
DFT(SVWN5)	0.4282	8.1%
MP2	0.4626	16.8%
CCSD	0.4847	22.4%
CCSD(T)	0.4822	21.7%

first carry out the calculation using the open-shell single determinant average-of-configuration Dirac-Hartree-Fock (DHF) [30] method, which does not include electron correlation effects. The relativistic density functional theory (DFT) [31] does not treat electron correlation in a robust way, and in order to further test the performance of the DFT method, we perform the calculations with various functionals, such as the Slater local exchange (SVWN5) functional [32], Perdew-Burke-Ernzerhof (PBE) functional [33, 34], the Becke-Lee-Yang-Parr (B3LYP) hybrid functional [35–37] and its adapted version (CAMB3LYP*) [38, 39]. Finally, we perform the calculations using the second-order Møller-Plesset (MP2) method [40] and the relativistic coupled cluster method [41]. The relativistic coupled cluster method is considered as the state-of-the-art method in the (relativistic) treatment of electron correlation. In this work, we employ the relativistic coupled cluster method with single, double, and perturbative triple excitation, namely CCSD and CCSD(T) [41]. The nuclear anapole moment interaction is perturbatively added to the coupled cluster calculations using a finite field (FF) approach [21, 42, 43]. In the coupled cluster calculations, the virtual energy cut-off is 500 a.u. and all the electrons are included into the treatment of electron correlation.

7.3 Results and conclusions

The calculated W_A parameters (in units of Hz) for the Be atom in the BeCl molecule using various methods, such as DHF, DFT, MP2, CCSD, and CCSD(T) are presented in Tab. 7.1 and in Fig. 7.1. Such methods treat the electron correlation on different levels. As can be seen from Tab. 7.1 and Fig. 7.1, the calculated W_A parameters (Hz) tend to increase from top to bottom, where the

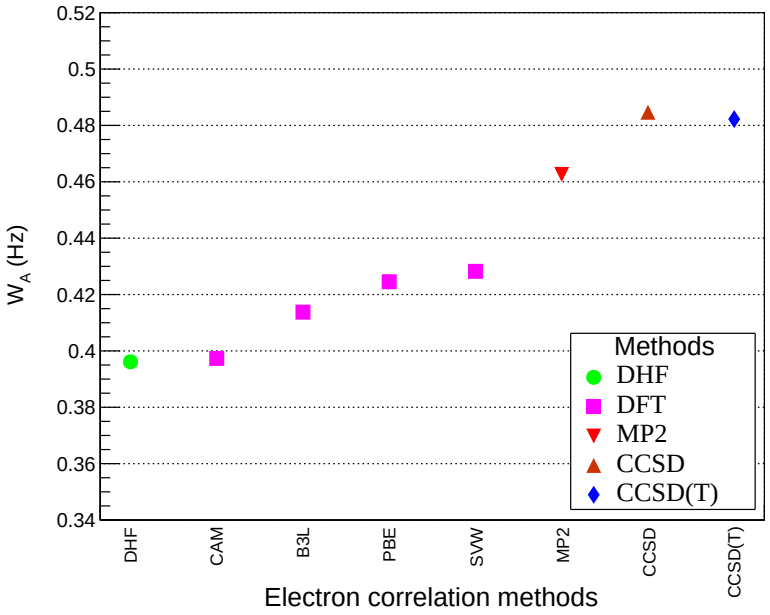

Figure 7.1: Calculated W_A parameters (Hz) for the Be atom in BeCl at the equilibrium bond length using various electron correlation methods. The calculated W_A values tend to increase with electron correlation.

treatment of electron correlation is steadily improving. The parameter Δ, which describes the relative contributions from the electron correlation, is defined as follows,

$$\Delta = \frac{100\Big(Corr - DHF\Big)}{DHF}. \tag{7.7}$$

Here, $Corr$ represents the calculated results from various electron correlation methods, and DHF represents the calculated result from the DHF method. The DHF method does not incorporate the electron correlation effect while the CCSD(T) is considered as the state-of-the-art method in dealing with the electron correlation. A direct comparison between the DHF and the CCSD(T) results suggests that electron correlation contributes to the nuclear anapole moment effect by approximately 20%, and thus it plays an important role in the determination

of the W_A parameter and should be taken into account in high-accuracy calculations. Interestingly, the calculated value from the CCSD method is higher than the calculated value from the CCSD(T) method but the difference is very small. This illustrates that, in our case, the perturbative triple excitation tends to lower down the W_A parameter but its contribution is not significant.

In summary, we have calculated the W_A parameter, which can be used for interpreting the measurement of the nuclear anapole moment effect, for the Be atom in BeCl using various *ab initio* methods such as DHF, DFT, MP2, CCSD, and CCSD(T) and using a large basis set. This is the first result of this effect for the BeCl molecule using the relativistic coupled cluster method. Our results show that electron correlation contributes to the W_A parameter significantly and should be treated properly in high-accuracy calculations.

References

[1] Y. Hao, M. Iliaš, and A. Borschevsky, PoS **FFK2019**, 057 (2019).

[2] J. Ginges and V. V. Flambaum, Phys. Rep. **397**, 63 (2004).

[3] O. Sushkov, V. Flambaum, and I. Khriplovich, Sov. Phys. JETP **60**, 873 (1984), or Zh. Eksp. Teor. Fiz **87**, 1521 (1984).

[4] V. V. Flambaum, I. B. Khriplovich, and O. P. Sushkov, Phys. Lett. B **146**, 367 (1984).

[5] V. V. Flambaum and I. B. Khriplovich, Phys. Lett. A **110**, 121 (1985).

[6] M. S. Safronova, D. Budker, D. DeMille, D. F. J. Kimball, A. Derevianko, and C. W. Clark, Rev. Mod. Phys. **90**, 025008 (2018).

[7] P. J. Mohr, D. B. Newell, and B. N. Taylor, J. Phys. Chem. Ref. Data **45**, 043102 (2016).

[8] C. S. Wood, S. C. Bennett, D. Cho, B. P. Masterson, J. L. Roberts, C. E. Tanner, and C. E. Wieman, Science **275**, 1759 (1997).

[9] W. C. Haxton and C. E. Wieman, Ann. Rev. Nucl. Part. Sci. **51**, 261 (2001).

[10] D. DeMille, S. B. Cahn, D. Murphree, D. A. Rahmlow, and M. G. Kozlov, Phys. Rev. Lett. **100**, 023003 (2008).

[11] N. Leefer, L. Bougas, D. Antypas, and D. Budker, arXiv (2014).

[12] D. Antypas, A. Fabricant, L. Bougas, K. Tsigutkin, and D. Budker, Hyperfine Interact. **238**, 21 (2017).

[13] S. Aubin, J. A. Behr, R. Collister, V. V. Flambaum, E. Gomez, G. Gwinner, K. P. Jackson, D. Melconian, L. A. Orozco, M. R. Pearson, D. Sheng, G. D. Sprouse, M. Tandecki, J. Zhang, and Y. Zhao, Hyperfine Interact. **214**, 163 (2013).

[14] M. G. Kozlov, L. N. Labzovskii, and A. O. Mitrushchenkov, Sov. Phys. JETP **73**, 415 (1991), or Zh. Eksp. Theor. Fiz **100**, 761 (1991).

[15] E. Altuntaş, J. Ammon, S. B. Cahn, and D. DeMille, Phys. Rev. A **97**, 042101 (2018).

[16] E. Altuntaş, J. Ammon, S. B. Cahn, and D. DeMille, Phys. Rev. Lett. **120**, 142501 (2018).

[17] M. G. Kozlov, A. V. Titov, N. S. Mosyagin, and P. V. Souchko, Phys. Rev. A **56**, R3326 (1997).

[18] M. K. Nayak and B. P. Das, Phys. Rev. A **79**, 060502 (2009).

[19] T. A. Isaev and R. Berger, Phys. Rev. A **86**, 062515 (2012).

[20] A. Borschevsky, M. Iliaš, V. Dzuba, V. Flambaum, and P. Schwerdtfeger, Phys. Rev. A **88**, 022125 (2013).

[21] Y. Hao, M. Iliaš, E. Eliav, P. Schwerdtfeger, V. V. Flambaum, and A. Borschevsky, Phys. Rev. A **98**, 032510 (2018).

[22] V. V. Flambaum and D. W. Murray, Phys. Rev. C **56**, 1641 (1997).

[23] E. B. Norrgard, D. S. Barker, S. Eckel, J. A. Fedchak, N. N. Klimov, and J. Scherschligt, Commun. Phys. **2**, 77 (2019).

[24] A. D. Kudashov, A. N. Petrov, L. V. Skripnikov, N. S. Mosyagin, T. A. Isaev, R. Berger, and A. V. Titov, Phys. Rev. A **90**, 052513 (2014).

[25] DIRAC, A relativistic ab initio electronic structure program, Release DIRAC18 (2018), written by L. Visscher, H. J. Aa. Jensen, R. Bast, and T. Saue, with contributions from V. Bakken, K. G. Dyall, S. Dubillard, U. Ekström, E. Eliav, T. Enevoldsen, E. Faßhauer, T. Fleig, O. Fossgaard, A. S. P. Gomes, E. D. Hedegård, T. Helgaker, J. Henriksson, M. Iliaš, Ch. R. Jacob, S. Knecht, S. Komorovský, O. Kullie, J. K. Lærdahl, C. V. Larsen, Y. S. Lee, H. S. Nataraj, M. K. Nayak, P. Norman, G. Olejniczak, J. Olsen, J. M. H. Olsen, Y. C. Park, J. K. Pedersen, M. Pernpointner, R. di Remigio, K. Ruud, P. Sałek, B. Schimmelpfennig, A. Shee, J. Sikkema, A. J. Thorvaldsen, J. Thyssen, J. van Stralen, S. Villaume, O. Visser, T. Winther, and S. Yamamoto (see `http://www.diracprogram.org`).

[26] L. Visscher and K. G. Dyall, At. Data Nucl. Data Tabl. **67**, 207 (1997).

[27] K. G. Dyall, J. Phys. Chem. A **113**, 12638 (2009).

[28] K. G. Dyall, Theoret. Chem. Acc. **135**, 128 (2016).

[29] K. P. Huber and G. Herzberg, *Molecular spectra and molecular structure: IV. Constants of diatomic molecules* (Springer US, 1979).

[30] J. Thyssen, *Development and applications of methods for correlated relativistic calculations of molecular properties*, Ph.D. thesis, University of Southern Denmark (2001).

[31] T. Saue and T. Helgaker, J. Comput. Chem. **23**, 814 (2002).

[32] S. H. Vosko, L. Wilk, and M. Nusair, Canad. J. Phys. **58**, 1200 (1980).

[33] J. P. Perdew, K. Burke, and M. Ernzerhof, Phy. Rev. Lett. **77**, 3865 (1996).

[34] K. Burke, J. P. Perdew, and M. Ernzerhof, Phys. Rev. Lett. **78**, 1396 (1997).

[35] C. Lee, W. Yang, and R. G. Parr, Phys. Rev. B **37**, 785 (1988).

[36] A. D. Becke, J. Chem. Phys. **98**, 5648 (1993).

[37] A. D. Becke, J. Comput. Chem. **20**, 63 (1999).

[38] T. Yanai and D. P. Tew, Chem. Phys. Lett. **393**, 51 (2004).

[39] C. Thierfelder, G. Rauhut, and P. Schwerdtfeger, Phys. Rev. A **81**, 032513 (2010).

[40] C. Møller and M. S. Plesset, Phys. Rev. **46**, 618 (1934).

[41] L. Visscher, T. Lee, and K. G. Dyall, J. Chem. Phys. **105**, 8769 (1996).

[42] H. J. Monkhorst, Int. J. Quant. Chem. **12**, 421 (1977).

[43] J. Thyssen, J. K. Laerdahl, and P. Schwerdtfeger, Phys. Rev. Lett. **85**, 3105 (2000).

Chapter 8

Molecular spectra and structure for eEDM measurements[a]

8.1 Motivation

Heavy diatomic molecules are currently considered to be the most sensitive systems used in the search for the electron electric dipole moment (eEDM) [2]. The large effective electric field, which the valence electron in these molecules is exposed to (Ref. [3]), allows for a huge sensitivity enhancement compared to a measurement on an atom.

In the ongoing experiments on YbF [4] and ThO [5, 6], and the planned experiment on BaF [7], precision measurements are performed on a beam of molecules using the Ramsey separated oscillatory fields method [8]. In the region of the experiment where the molecular beam interacts with carefully defined electric and magnetic fields, the eEDM can become visible in the correlation of an energy level shift with the direction of the electric field. The sensitivity of such a measurement scales with the square root of the total number of molecules used in the experiment, and linearly with the coherent interaction time in the Ramsey

[a]This chapter is reproduced from our published paper [1]: Yongliang Hao, Lukáš F. Pašteka, Lucas Visscher, Parul Aggarwal, Hendrick L. Bethlem, Alexander Boeschoten, Anastasia Borschevsky, Malika Denis, Kevin Esajas, Steven Hoekstra, Klaus Jungmann, Virginia R. Marshall, Thomas B. Meijknecht, Maarten C. Mooij, Rob G. E. Timmermans, Anno Touwen, Wim Ubachs, Lorenz Willmann, Yanning Yin, Artem Zapara, High accuracy theoretical investigations of CaF, SrF, and BaF and implications for laser-cooling, J. Chem. Phys. **151**, 034302 (2019), with the permission of AIP Publishing.

detection scheme. To optimize the sensitivity, the interaction time in these experiments can be increased by reducing the longitudinal velocity of the molecular beam by using a cryogenic beam source or by Stark deceleration. However, if the transverse velocity spread of the molecular beam is not also reduced, the increase in the interaction time will be offset by an increased transverse spreading of the molecular beam during the transition of the interaction zone, and the sensitivity of the experiment will not be improved. Transverse laser-cooling of molecular beams can reduce the spread of the molecular beam to a negligible level, provided the internal structure of the molecule is suitable. This leads to an increase in the number of molecules and thereby opens the way to experiments with very long interaction times and an improved sensitivity for measuring the eEDM. The possibility to exert both laser-cooling and Stark deceleration on the BaF molecule makes this species a candidate for a successful measurement of the eEDM [7].

The prospects of laser-cooling and trapping of molecules [9] have led to a considerable interest in both experimental and theoretical communities. The first molecule to be laser cooled was SrF [10], followed by YO [11], CaF [12], and YbF [13]. Recently, laser-cooling of the first polyatomic molecule, SrOH, was demonstrated [14] and has been proposed for heavier molecules, such as RaOH and YbOH, and larger polyatomic molecules like $YbOCH_3$ [15, 16].

There are a number of key factors that determine whether a given molecule is suitable for laser-cooling [9]. One is having strong one-photon transitions to ensure the high photon-scattering rates needed for efficient momentum transfer. The oscillator strengths of the transitions can be determined using the transition dipole moments (TDMs) between the states. A second requirement is a rotational structure with a closed optical cycle; this is available in ${}^2\Pi - {}^2\Sigma^+$ and ${}^2\Sigma^+ - {}^2\Sigma^+$ transitions. A third condition concerns the Franck-Condon factors (FCFs) which govern the vibronic transitions between different electronic states. Highly diagonal FCFs provide a near-closed optical cycle in the vibronic structure, therewith limiting the required repumping. Finally, there should either be no intervening electronic states to which the upper state could radiate and cause leaks in the cooling cycle, or the transitions to such states should be suppressed.

Thus, the suitability of BaF for laser-cooling depends critically on its energy level structure, lifetimes of its excited states, vibrational branching ratios, and electronic transition probabilities. This paper aims to determine these properties at the highest possible level of computational accuracy, to conclude on the suitability of BaF for laser-cooling, and to suggest the optimal laser-cooling scheme.

We perform high-accuracy relativistic Fock-space coupled cluster (FSCC) calculations of the spectroscopic constants of BaF and its lighter homologues CaF and SrF; based on these values we provide predictions of the FCFs of the $A^2\Pi_{1/2} - X^2\Sigma^+_{1/2}$ laser-cooling transition, the alternative cooling transition $B^2\Sigma^+_{1/2} - X^2\Sigma^+_{1/2}$, and the possible leak transition $A^2\Pi_{1/2} - A'^2\Delta_{3/2}$. We also

carry out calculations of the dipole moments (DMs) and transition dipole moments (TDMs) for the six lowest states of the selected molecules, using in this case the relativistic multireference configuration interaction method (MRCI). These are the first comprehensive relativistic high-accuracy investigations of the spectroscopic properties of these molecules. The ground and the excited state properties are treated on the same footing, and similar accuracy is expected for all the levels investigated here.

In the following, we start in Section 8.2 with a brief overview of previous experimental and theoretical studies of the three molecules. In Section 8.3 the methods employed in our calculations are introduced. Section 8.4 contains our theoretical results for spectroscopic constants, Franck-Condon factors, dipole moments, transition dipole moments, and lifetimes of the excited states. The implications of these results for possible laser-cooling schemes are discussed in Section 8.5.

8.2 Previous investigations

Numerous theoretical studies of the electronic structure and other properties of BaF and its lighter homologues were carried out, using a variety of methods. The majority of these investigations were performed in a nonrelativistic framework. The main system of interest here, BaF, was recently investigated using the effective core potential (ECP) based complete active space self-consistent field approach combined with the multi-reference configuration interaction method (CASSCF+MRCI) [17]. This study provides the spectroscopic constants, the static and the transition dipole moments, and the static dipole polarizabilities of the ground and the 41 lowest doublet and quartet electronic states of this system. The drawbacks of this extensive investigation are in the rather limited size of the employed basis sets and in the fact that spin-orbit coupling is neglected altogether. Shortly after, Kang *et al.* [18] published a paper where a similar approach (CASSCF+MRCI) was used to investigate the properties of BaF, including the Franck-Condon factors for the transitions between the lowest states. Here, much higher quality basis sets were used, and spin-orbit coupling (SOC) effects were included at the MRCI level. The FCFs for the transition between the low-lying states of BaF were reported by Chen *et al.* [19] using the Rydberg-Klein-Rees (RKR) approach, and by Karthikeyan *et al.* [20] and Xu *et al.* [21] within the Morse potential model (MPM). The DM of the ground state of BaF was also studied using the relativistic restricted active space approach combined with configuration interaction method (RASCI) [22], by relativistic coupled cluster method (RCCSD/RCCSD(T)) [23–25], and using relativistic effective core potential approach based on the restricted active space self-consistent-field theory (AREP-RASSCF) [26].

Earlier, in the work of Westin *et al.* [27], the transition energies between low-

lying electronic states of BaF were obtained based on density functional theory (DFT) method. The spectroscopic constants (α_e and $\omega_e\chi_e$) and dipole moments of the ground state of BaF and its homologues were calculated by Törring *et al.* [28] using the ionic Rittner model [29]. Subsequently, these authors applied an electrostatic polarisation model (EPM) [30] to evaluate the energies and the dipole moments of the low-lying excited states of alkaline earth metal monohalides, including BaF. The transition energies as well as the DMs and TDMs of the lowest excited states of CaF, SrF, and BaF were reported by Allouche *et al.* [31] using the Ligand Field Method (LFM), where model potential functions are used to describe the electronic structure of alkaline earth metal ions.

The majority of theoretical investigations on CaF and SrF were carried out using the configuration interaction approach, either within its single reference (CISD) [32] or multireference variant [33–35]. Most recently, two studies were published, presenting the spectroscopic constants and the DMs of the two molecules obtained both by the CASSCF+MRCI approach and using the second-order multireference Rayleigh-Schrödinger perturbation theory (CASSCF+RSPT2) [36, 37]. Some single reference coupled cluster studies are also available [24, 25, 38–42]. Other approaches used for calculations of the spectroscopic constants, the DMs, and the TDMs of CaF and SrF are the ligand field method [31, 43], the electrostatic polarisation model [30, 44], the finite-difference Hartree-Fock (FDHF) approach [45], the second order Møller-Plesset perturbation theory (MP2) [46], the effective one-electron variational eigenchannel R-matrix method (EOVERM) [47], and the ionic model [28]. Barry [10, 48] obtained the potential energy curves of SrF using experimental spectroscopic constants within the first-order Rydberg-Klein-Rees (RKR) approach and subsequently evaluated the FCFs for the transition $A^2\Pi_{1/2} \rightarrow X^2\Sigma^+_{1/2}$.

Many spectroscopic constants of the ground and the lowest excited states of BaF were determined experimentally with high precision [49–53], along with the DM of its ground state [54] and electronic transition dipole moments between its lowest levels [55, 56], which were extracted from the measured lifetimes using calculated FCFs. There is also a significant amount of experimental data available on the properties of its lighter homologues, CaF and SrF. Here, we cite the most recent and precise values available: Refs. [49, 50, 57–68] for the spectroscopic constants, Refs. [69–72] for the static and transition dipole moments, Refs. [58, 73] for the lifetimes, and a single measurement of the FCFs of the $A - X(0 - 0)$ transition in CaF [74].

RaF, the heavier homologue of BaF, was also proposed for laser-cooling and for use in experiments to search for physics beyond the Standard Model. Its spectroscopic properties were investigated within the relativistic Hartree-Fock and the density functional theory methods [75–79], and using the relativistic coupled cluster approach [80]. This molecule, along with the lighter BeF and

MgF, is, however, outside the scope of the present work.

8.3 Methods

Relativistic effects can have a significant influence on atomic and molecular properties [81], in particular in case of heavier atoms and molecules, represented by BaF in this study. Thus, we have carried out all the calculations within the relativistic framework, using the DIRAC15 program package [82]. In order to reduce computational effort, we have replaced the traditional 4-component Dirac-Coulomb (DC) Hamiltonian by the exact 2-component Hamiltonian (X2C) [83, 84]. This approach allows a significant decrease in computational time and expense, while reproducing very well the results obtained using the 4-component DC Hamiltonian, as tested for a variety of species and properties [85–87]. In this work, we have used the molecular mean-field implementation of the approach, X2Cmmf [86] and included the Gaunt interaction [88]. This interaction is part of the Breit term, which corrects the 2-electron part of the Dirac-Coulomb Hamiltonian up to the order of $(Z\alpha)^2$ [89]. The Breit correction was shown to be of importance even for light molecules [90]; we thus include the Gaunt term in our calculations, for achieving optimal accuracy (the full Breit term is to date not implemented in the DIRAC program). All the calculations were performed for the ^{138}BaF, ^{88}SrF, and ^{40}CaF isotopologues.

In order to obtain the spectroscopic constants of the ground and excited states of the molecules and the Franck-Condon factors for transitions between these states, we have calculated the potential energy curves using the multireference relativistic Fock space coupled cluster approach [91]. FSCC is considered one of the most powerful methods for high-accuracy calculations of atomic and molecular properties of small heavy species and it is particularly well suited for treating excited states [92]. Within the framework of this approach an effective Hamiltonian (H_{eff}) is defined and calculated in a low-dimensional model (P) space, constructed from zero-order wave functions (Slater determinants), with eigenvalues approximating some desirable eigenvalues of the physical Hamiltonian. The effective Hamiltonian has the form [93]

$$H_{\text{eff}} = PH\Omega P, \tag{8.1}$$

where Ω is the normal-ordered wave operator,

$$\Omega = \exp(S). \tag{8.2}$$

The excitation operator S is defined with respect to a closed-shell reference determinant (vacuum state), and partitioned according to the number of valence

holes (m) and valence electrons (n) with respect to this reference:

$$S = \sum_{m \geqslant 0} \sum_{n \geqslant 0} \left(\sum_{l \geqslant m+n} S_l^{(m,n)} \right) . \tag{8.3}$$

Here l is the number of excited electrons. Current implementation of the relativistic FSCC method [91] is limited to $l \leqslant 2$, corresponding to single and double excitations, and thus, $m + n \leqslant 2$, which in practice means that we are able to treat atoms and molecules with up to two valence electrons or holes.

Table 8.1: Spectroscopic constants of the ground and the low-lying excited states of CaF.

	$X^2\Sigma^+_{1/2}$	$A'^2\Delta_{3/2}$	$A'^2\Delta_{5/2}$	$A^2\Pi_{1/2}$	$A^2\Pi_{3/2}$	$B^2\Sigma^+_{1/2}$	Method	Reference
R_e(Å)	1.958	1.997	1.996	1.943	1.943	1.961	X2C-FSCC	This work
	1.965						CISD	[32]
	1.975	1.998	1.998	1.957	1.957	1.977	MRCI[a]	[33]
	1.971			1.954	1.954		MRCI[a]	[34]
	2.001	2.027	2.027	1.981	1.981	1.992	MRCI[a]	[35]
	2.015	2.050	2.050	2.001	2.001	2.009	CASSCF+MRCI[a]	[37]
	2.015	2.071	2.071	2.008	2.008	2.043	CASSCF+RSPT2[a]	[37]
	1.967			1.952	1.952		Experiment[a]	[49, 50]
		1.993(3)	1.993(3)				Experiment[a]	[63]
				1.9374(1)	1.9374(1)	1.9555(3)	Experiment[a]	[66]
ω_e(cm^{-1})	586.2	529.4	529.5	594.6	594.6	572.8	X2C-FSCC	This work
	587						CISD	[32]
	581.2	558.9	558.9	579.9	579.9	551.5	MRCI[a]	[33]
	612.5			624.0	624.0		MRCI[a]	[34]
	572.4	506.1	506.1	578.6	578.6	571.4	MRCI[a]	[35]
	524.3	498.2	498.2	563.4	563.4	512.6	CASSCF+MRCI[a]	[37]
	518.6	462.4	462.4	511.4	511.4	472.5	CASCF+RSPT2[a]	[37]
	581.1(9)			586.8(9)			Experiment[a]	[59]
		528.57(1)	528.57(1)				Experiment[a]	[63]
				594.513(50)	594.513(50)	572.424(80)	Experiment[a]	[66]
$\omega_e\chi_e$(cm^{-1})	2.90	2.86	2.85	3.03	3.04	3.13	X2C-FSCC	This work
	3.70			3.77	3.77		MRCI[a]	[34]
	2.65	2.75	2.75	2.60	2.60	3.24	MRCI[a]	[35]
		2.77(9)	2.77(9)				Experiment[a]	[63]
				3.031(20)	3.031(20)	3.101(37)	Experiment[a]	[66]

[a] As this study neglects spin-orbit coupling, the same values of the spectroscopic constants are given for the $A'^2\Delta_{3/2}$ and $A'^2\Delta_{5/2}$ and the $A^2\Pi_{1/2}$ and $A^2\Pi_{3/2}$ states.

Table 8.1: Spectroscopic constants of the ground and the low-lying excited states of CaF (continued).

	$X^2\Sigma^+_{1/2}$	$A'^2\Delta_{3/2}$	$A'^2\Delta_{5/2}$	$A^2\Pi_{1/2}$	$A^2\Pi_{3/2}$	$B^2\Sigma^+_{1/2}$	Method	Reference
$B_e(\mathrm{cm}^{-1})$	0.341	0.328	0.329	0.347	0.347	0.341	X2C-FSCC	This work
	0.335	0.328	0.328	0.342	0.342	0.335	MRCI[a]	[33]
	0.327	0.319	0.319	0.334	0.334	0.330	MRCI[a]	[35]
	0.322	0.311	0.311	0.326	0.326	0.324	CASSCF+MRCI[a]	[37]
	0.322	0.305	0.305	0.324	0.324	0.313	CASSCF+RSPT2[a]	[37]
	0.343704(23)			0.348744(27)	0.348744(27)		Experiment	[61]
		0.3295	0.3295				Experiment[a]	[63]
				0.348781(5)	0.348781(5)	0.342345(10)	Experiment[a]	[66]
$T_e(\mathrm{cm}^{-1})$	0	22187	22207	16647	16720	19191	X2C-FSCC	This work
		24950	24950	17998	17998	22376	LFM	[43]
		17690	17690	16340	16340	18620	EPM	[30]
		24851	24851	17712	17712	20069	MRCI[a]	[33]
		22552	22552	18217	18217	21486	LFM	[31]
				16421	16421		MRCI[a]	[34]
		20697	20697	15627	15627	19512	MRCI(CBS)[a]	[35]
		22113	22113	16544	16544	19013	CASSCF+MRCI[a]	[37]
		25337	25337	16574	16574	21016	CASSCF+RSPT2[a]	[37]
		21567.76(1)	21580.10(1)				Experiment	[63]
				16491.036(50)	16562.465(50)	18840.190(60)	Experiment	[66]

[a] As this study neglects spin-orbit coupling, the same values of the spectroscopic constants are given for the $A'^2\Delta_{3/2}$ and $A'^2\Delta_{5/2}$ and the $A^2\Pi_{1/2}$ and $A^2\Pi_{3/2}$ states.

Table 8.2: Spectroscopic constants of the ground and the low-lying excited states of SrF.

	$X^2\Sigma^+_{1/2}$	$A'^2\Delta_{3/2}$	$A'^2\Delta_{5/2}$	$A^2\Pi_{1/2}$	$A^2\Pi_{3/2}$	$B^2\Sigma^+_{1/2}$	Method	Reference
R_e(Å)	2.083	2.099	2.098	2.069	2.069	2.089	X2C-FSCC	This work
	2.085						CISD	[32]
	2.137	2.147	2.147	2.116	2.116	2.130	CASSCF+MRCI[a]	[36]
	2.124	2.145	2.145	2.097	2.097	2.138	CASSCF+RSPT2[a]	[36]
	2.081						CCSD(T)	[41]
						2.080	Experiment	[49, 50]
	2.0757(5)						Experiment	[57]
ω_e(cm^{-1})	500.1	475.9	476.7	508.4	508.8	492.2	X2C-FSCC	This work
	507						CISD	[32]
	475.0	454.7	454.7	491.9	491.9	480.2	CASSCF+MRCI[a]	[36]
	477.8	449.6	449.6	510.3	510.3	516.6	CASSCF+RSPT2[a]	[36]
	500.25						CCSD(T)	[41]
	502.4(7)					495.8(7)	Experiment	[60]
	501.96496(13)						Experiment	[65]
$\omega_e\chi_e$(cm^{-1})	2.45	2.44	2.41	2.46	2.52	2.16	X2C-FSCC	This work
	2.27(21)					2.34(21)	Experiment	[60]
	2.204617(37)						Experiment	[65]
B_e(cm^{-1})	0.249	0.245	0.245	0.252	0.252	0.247	X2C-FSCC	This work
	0.236	0.234	0.234	0.241	0.241	0.238	CASSCF+MRCI[a]	[36]
	0.239	0.235	0.235	0.245	0.245	0.236	CASSCF+RSPT2[a]	[36]
	0.248						CCSD(T)	[41]
	0.24975935(23)			0.2528335(37)	0.2528335(37)		Experiment	[68]
	0.25053456(34)					0.2494103(21)	Experiment	[62]
				0.25284(3)	0.25284(3)		Experiment[a]	[64]
	0.250534383(25)						Experiment	[65]

[a] As this study neglects spin-orbit coupling, the same values of the spectroscopic constants are given for the $A'^2\Delta_{3/2}$ and $A'^2\Delta_{5/2}$ and the $A^2\Pi_{1/2}$ and $A^2\Pi_{3/2}$ states.

Table 8.2: Spectroscopic constants of the ground and the low-lying excited states of SrF (continued).

	$X^2\Sigma^+_{1/2}$	$A'^2\Delta_{3/2}$	$A'^2\Delta_{5/2}$	$A^2\Pi_{1/2}$	$A^2\Pi_{3/2}$	$B^2\Sigma^+_{1/2}$	Method	Reference
$T_e(\mathrm{cm}^{-1})$	0	19108	19225	15113	15392	17405	X2C-FSCC	This work
		19830	19830	15300	15300	16950	EPM[a]	[30]
		20553	20553	16531	16531	19295	LFM[a]	[31]
		20559	20559	14506	14506	18673	CASSCF+RSPT2[a]	[36]
		20790	20790	16503	16503	19005	CASSCF+RSPT2[a]	[36]
						17264.1446(12)	Experiment	[67]
				15075.6122(7)	15357.0736(7)		Experiment	[68]

[a] As this study neglects spin-orbit coupling, the same values of the spectroscopic constants are given for the $A'^2\Delta_{3/2}$ and $A'^2\Delta_{5/2}$ and the $A^2\Pi_{1/2}$ and $A^2\Pi_{3/2}$ states.

Table 8.3: Spectroscopic constants of the ground and the low-lying excited states of BaF.

	$X^2\Sigma^+_{1/2}$	$A'^2\Delta_{3/2}$	$A'^2\Delta_{5/2}$	$A^2\Pi_{1/2}$	$A^2\Pi_{3/2}$	$B^2\Sigma^+_{1/2}$	Method	Reference
R_e(Å)	2.177	2.207	2.205	2.196	2.195	2.222	X2C-FSCC	This work
	2.204	2.229	2.229	2.197	2.197	2.234	CASSCF+MRCI	[17]
	2.171	2.187	2.192	2.199	2.217	2.226	CASSCF+MRCI+SOC	[18]
				2.183	2.183	2.208	Experiment[a]	[49, 50]
	2.1592964(75)						Experiment	[51]
ω_e(cm^{-1})	468.4	437.3	439.1	440.9	440.5	425.5	X2C-FSCC	This work
	459.3	438.3	438.3	452.7	452.7	437.0	CASSCF+MRCI[a]	[17]
	474.1	446.3	423.3	456.7	417.7	421.7	CASSCF+MRCI+SOC	[18]
	469.4	436.9	438.9	435.5	436.7	424.7	Experiment	[52]
$\omega_e\chi_e$(cm^{-1})	1.83	1.84	1.82	1.90	1.87	1.81	X2C-FSCC	This work
	1.90	2.02	1.32	2.55	1.86	1.83	CASSCF+MRCI+SOC	[18]
	1.79			1.68	1.82	1.88	Experiment[b]	[49, 50]
	1.83727(76)	1.833(27)	1.833(27)	1.854(12)	1.854(12)	1.8524(37)	Experiment[a]	[53]
B_e(cm^{-1})	0.213	0.207	0.208	0.209	0.210	0.205	X2C-FSCC	This work
	0.208	0.203	0.203	0.209	0.209	0.202	CASSCF+MRCI[a]	[17]
	0.214	0.211	0.210	0.209	0.205	0.204	CASSCF+MRCI+SOC	[18]
	0.2165297	0.20975	0.21044			0.20784	Experiment	[52]
T_e(cm^{-1})	0	10896	11316	11708	12341	14191	X2C-FSCC	This work
		7420	7420	9437	9437	12663	DFT[a]	[27]
		11100	11100	12330	12330	14250	EPM[a]	[30]
		11310	11310	11678	11678	13381	LFM[a]	[31]
		12984	12984	11601	11601	13794	CASSCF+MRCI[a]	[17]
		11582	12189	12329	14507	14022	CASSCF+MRCI+SOC	[18]
		10734	11145	11647	12278	14063	Experiment	[52]

[a] As this study neglects spin-orbit coupling, the same values of the spectroscopic constants are given for the $A'^2\Delta_{3/2}$ and $A'^2\Delta_{5/2}$ and the $A^2\Pi_{1/2}$ and $A^2\Pi_{3/2}$ states.

[b] The experimental values for the $\omega_e\chi_e$ constants of the $A^2\Pi_{1/2}$ and the $A^2\Pi_{3/2}$ from Ref. [49, 50] show a surprisingly large difference (0.14 cm^{-1}). Our results do not support this difference, and further study is needed.

The molecules of interest all have a single valence electron and a $^2\Sigma^+_{1/2}$ ground state configuration. We thus start our calculations from the closed-shell positively charged ions, CaF^+, SrF^+, and BaF^+. After solving the coupled cluster equations for these closed-shell reference ions, we proceed to add an electron to reach the neutral states, for which additional CC equations are solved to obtain the correlated ground and excited state energies. In this work, we were interested in the $X^2\Sigma^+_{1/2}$, $A^2\Pi_{1/2}$, $A^2\Pi_{3/2}$, $A'^2\Delta_{3/2}$, $A'^2\Delta_{5/2}$, and $B^2\Sigma^+_{1/2}$ states. We have thus defined the model space P to contain the appropriate σ, π, and δ orbitals.

In order to reach optimal accuracy very large basis sets were used in the calculations, and higher angular momentum basis functions were added manually to the available sets. For all the elements involved in our calculation, we have employed the relativistic basis sets of Dyall [94, 95]. Singly augmented pVQZ basis set (s-aug-pVQZ) was used for fluorine; for Sr and Ba we used the doubly augmented pVQZ basis sets (d-aug-pVQZ), to which we manually added two h-type functions with exponent values of 0.48 and 0.25. For CaF the pVQZ did not provide sufficient quality for description of the Δ states, while on the other hand the h-type functions had very little effect on the calculated transition energies. We thus used the doubly augmented core-valence CVQZ basis set for this element (this basis set has two additional d, one additional f and one additional g functions compared to the d-aug-pVQZ basis). Convergence of the obtained spectroscopic constants (in particular excitation energies) with respect to the basis set size was verified. We have correlated 34 electrons in case of BaF and SrF and 24 electrons for CaF.

After obtaining the potential energy curves, we have used the Dunham [96] programme (written by V. Kellö of the Comenius University, [97]) to calculate the spectroscopic constants: the equilibrium bond lengths (R_e), the harmonic and anharmonic vibrational frequencies (ω_e and $\omega_e\chi_e$), the adiabatic transition energies (T_e), and the rotational constants (B_e). The Frank-Condon factors between the low lying vibrational levels of the ground state and the excited states were extracted using the LEVEL16 program of Le Roy [98].

The calculations of the dipole moments and the transition dipole moments were carried out using the MRCISD method [99] as implemented in the LUCIAREL module [87, 100] of the DIRAC15 program package [82]. The change of method is needed because calculation of TDMs is not yet implemented on the Fock-space coupled cluster level in the present version of the DIRAC program. Since the MF (M=Ca, Sr, Ba) molecule is considerably ionic [101], in first approximation we can describe this system as a metal cation M^+ perturbed by the presence of the F^- anion [36]. Hence, the valence electronic structure of MF is qualitatively similar to M^+: ns^1. All the excited states of interest can be similarly described by the single unpaired valence electron being excited into the low lying empty valence d shell of the M^+ cation. The configuration space was thus

defined as one electron spanning the 6 orbitals corresponding to the metal atomic orbitals: ns and $(n-1)d$, thus describing two $^2\Sigma$, one $^2\Pi$ and one $^2\Delta$ state. In order to describe the orbitals equally well for all states we used the average-of-configuration DHF reference orbitals [102] with one electron occupying the same 6 orbitals as were included in the configuration space. The correlation space extended down to the $(n-1)$ shell of the M^+ cation and $2s$, $2p$ orbitals of F^- anion (i.e. 8 additional occupied orbitals) and virtual orbitals with energies over 10 a.u were cut off. For the DMs, both computational methods are appropriate; there we use the FSCC values to test the performance and the validity of MRCI for the TDM calculations. The same basis sets were employed as for the calculations of the potential energy curves.

8.4 Results and discussion

8.4.1 Potential energy curves

The calculated potential energy curves of the ground and the low-lying excited states of the three molecules are shown in Fig. 8.1. As expected, the energy splitting between the Ω resolved states tends to be larger the heavier the molecule becomes, due to the relativistic effects playing a more important role in heavier species. An important difference in the electronic structure of the three molecules is in the location of the $A'^2\Delta$ states. For CaF and SrF, these states are higher than the $A^2\Pi$ states, even higher than the $B^2\Sigma^+$ state, while for BaF they are lower in energy and transitions to the $A'^2\Delta_{3/2}$ state could constitute a leak in the cooling cycle.

8.4.2 Spectroscopic constants

Tables 8.1, 8.2, and 8.3 contain the calculated spectroscopic constants of the three molecules, along with experimental values where available and earlier theoretical results. Throughout this paper, all the molecular constants are defined in the usual way [103] (for further details, see Appendix A). Overall, our calculations are in excellent agreement with experiment. For most of the values, the error is less than 1%; the largest relative error (of a few percent) is for the anharmonicity correction $\omega_e\chi_e$. However, for these constants the experimental uncertainty is often rather high. The calculated transition energies are generally slightly overestimated due to the neglect of the triple excitations, which are to date not implemented in the FSCC approach.

The present results can be compared to the most recent theoretical investigations. For CaF, these are the nonrelativistic MRCI calculations of Ref. [35] and the nonrelativistic CASSCF+MRCI and CASSCF+RSPT2 values of Ref. [37].

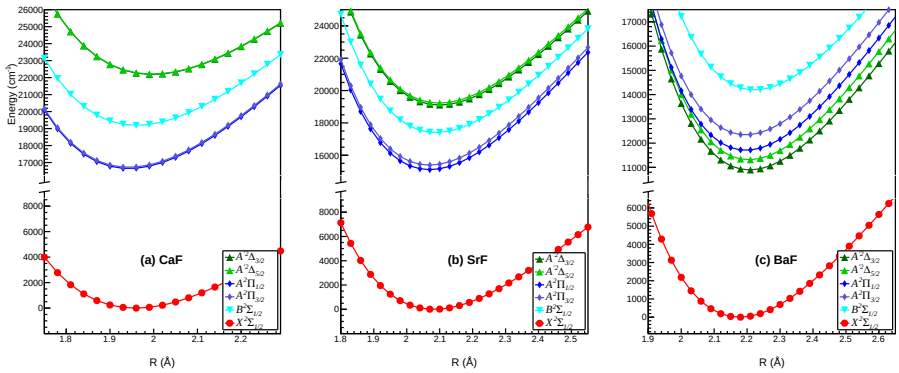

Figure 8.1: Potential energy curves for the low-lying states of CaF, SrF, and BaF (Color online).

In both the previous studies the deviations from experiment were larger than here; in case of Ref. [37] use of a limited basis set led to errors on the order of 2-10%, with MRCI performing better than the RSPT2 approach (MRCI transition energies reproduced the experiment quite well). In Ref. [35] the results were extrapolated to the complete basis set limit, resulting in lower errors of 2-5%.

In case of SrF the nonrelativistic CASSCF+MRCI and CASSCF+RSPT2 [36] methods perform on a similar level, and generally somewhat better than for CaF (overall errors of 2-6%). However, here the errors in excitation energies are larger, due to the small basis set, which is probably insufficient for an adequate description of Sr. In SrF, relativistic effects start coming into play: the spin-orbit splitting of the $A^2\Pi$ state is almost 300 cm^{-1} and therefore, in order to achieve optimal accuracy, including spin-orbit effects is important. The ground state of SrF was also studied by the CCSD(T) approach [41]. As expected, these results are in excellent agreement with the present values. To the best of our knowledge, no experimental information is available for the $A'^2\Delta$ states of SrF; the high-accuracy of our results for the other levels in this system supports our predictions of the properties of these states.

In BaF the order of the excited states is different to that in its lighter homologues, and the $A'^2\Delta$ states are below the $A^2\Pi$ levels. It is thus important to have high-accuracy predictions of their properties in order to estimate whether they will present a challenge in the cooling scheme. The spin-orbit splitting of the $A^2\Pi$ state is around 630 cm^{-1} and of that of $A'^2\Delta$ is around 420 cm^{-1}. Our results reproduce very well the level ordering, the magnitude of the fine-structure splitting, and the absolute positions of the different levels as obtained from experiment. The two recent theoretical investigations of BaF used the CASSCF+MRCI ap-

proach [17, 18]. The results of Ref. [17] show the $A^2\Pi$ states below the $A'^2\Delta$, most likely due to the basis set limitations. In Ref. [18] a larger basis set was used, and the correct ordering of the states was reproduced. This work also included spin orbit coupling contributions, but their effect seems to be greatly overestimated, in particular for the $A^2\Pi$ state, where the calculated splitting is over 2000 cm^{-1}.

The good performance of the relativistic FSCC approach for the spectroscopic constants implies that this method is also successful in reproducing the shape of the potential energy curves (Fig. 8.1). Therefore, we expect high-accuracy for the Frank-Condon factors presented in the next section.

8.4.3 Frank-Condon factors

In this work, we employ the extensively used r-centroid approximation [104] for analyzing the transition rates (see e.g. Ref. [105]). It factorises the transition integrals into electronic transition dipole moments and Franck-Condon factors representing the vibrational wave function overlap. Franck-Condon factors are an important parameter needed for determining whether a given system is suitable for laser-cooling. Highly diagonal FCFs would allow to limit the number of required lasers [9, 106]. Therefore, we use the potential energy curves presented in the previous section to calculate the FCFs of the three molecules; the results are shown in Table 8.4 for the $A^2\Pi_{1/2} - X^2\Sigma^+_{1/2}$ transition, in Table 8.5 for the $A^2\Pi_{1/2} - A'^2\Delta_{3/2}$ transition, in Table 8.6 for the $A'^2\Delta_{3/2} - X^2\Sigma_{1/2}$ transition, and in Table 8.7 for the $B^2\Sigma^+_{1/2} - X^2\Sigma^+_{1/2}$ transition. For completeness sake, we also include the FCFs of the $A^2\Pi_{3/2} - X^2\Sigma^+_{1/2}$ transition in Table 8.14.

For the three molecules, the FCFs of the $A^2\Pi_{1/2} - X^2\Sigma^+_{1/2}$ transitions (the intended cooling transition for BaF) exhibit a highly diagonal behaviour, as can also be seen from Fig. 8.2. This is due to the very similar equilibrium bond lengths of the ground and the $A^2\Pi$ states in all the molecules investigated here, and it makes these molecules excellent species for laser-cooling.

Wall *et al.* [74] have measured the FCF of the $A - X(0-0)$ band in CaF using the saturation of laser-induced fluorescence. Our result (0.974) is consistent with the experimental value (0.968-1.000). We find that the diagonal FCF is largest for the SrF molecule, and the off-diagonal decay in the $(0-1)$ band the smallest. Our results for the diagonal $(0-0)$ and off-diagonal FCF for BaF (0.960 and 0.039 respectively) predict a slightly less diagonal character for this system. Our calculations are also in good agreement with previous theoretical works [18–21, 34, 48].

The $A - A'$ transition constitutes a possible leak in the cooling cycle of BaF; for CaF and SrF the $A'\Delta_{3/2}$ state is higher than the $A^2\Pi_{1/2}$ and therefore not a

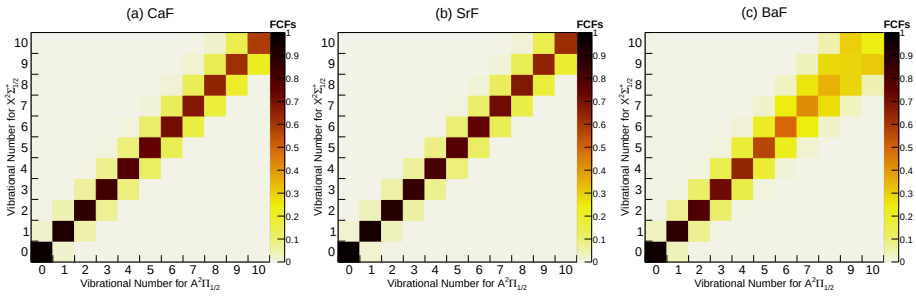

Figure 8.2: Calculated Franck-Condon factors for the vibronic transitions between the $|A^2\Pi_{\frac{1}{2}}, v'\rangle$ and the $|X^2\Sigma^+_{\frac{1}{2}}, v\rangle$ states of CaF, SrF, and BaF (Color online).

concern in this context. To the best of our knowledge no previous calculations or measurements were performed for the FCFs between these two states. The FCF of the $A - A'(0-0)$ transition in BaF is 0.986 (Table 8.5 and Fig. 8.3), due to the similar equilibrium bond length of the two states. We also present the FCFs for the decay of the $A'^2\Delta$ states of the three species to the ground state (Table 8.6). Implications of these results for the laser-cooling of BaF are discussed below.

The $B^2\Sigma^+_{1/2} - X^2\Sigma^+_{1/2}$ transition was demonstrated as an alternative cooling route for CaF [107]. We thus explore the FCFs of this transition in the three molecules (Table 8.7 and Fig. 8.4). In case of CaF, the FCFs are indeed highly diagonal, with the $B - X(0-0)$ FCF extremely close to unity, and in SrF it is 0.996. BaF, however, has an FCF of about 0.800 for the same transition, caused by a significantly larger R_e of the $B^2\Sigma^+_{1/2}$ state compared to the ground state.

8.4.4 Static and transition dipole moments

The calculated DMs at experimental bond lengths R_e are given in Tables 8.8, 8.9, and 8.10 and compared to experimental values (where available) and to previous theoretical investigations.

The majority of previous theoretical investigations of the DMs of these molecules were carried out in a nonrelativistic framework; the only exception being the relativistic coupled cluster studies of the ground state DMs of the three molecules [23–25, 38, 40, 42]. This is the first relativistic study of the DMs of the excited states. We have performed the calculation using two approaches: FSCC and MRCI. The results obtained using the two methods are within a few percent of each other for most of the states considered here, with the exception of the $B^2\Sigma^+_{1/2}$ states of the three molecules, where the differences are significantly

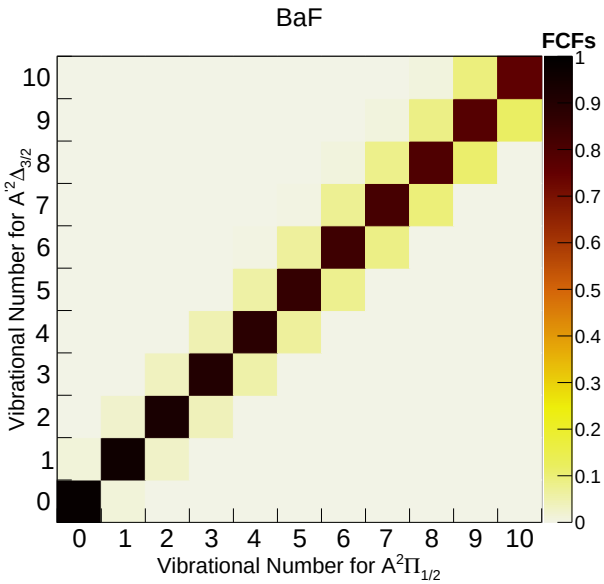

Figure 8.3: Calculated Franck-Condon factors for the vibronic transitions between the $|A'^2\Delta_{\frac{3}{2}}, v\rangle$ and the $|A^2\Pi_{\frac{1}{2}}, v'\rangle$ states of BaF (Color online).

larger.

In case of the ground state DMs our results are generally in good agreement with the majority of the earlier theoretical publications (in particular, as expected, with the relativistic coupled cluster values [23–25, 38, 40, 42]), and within 10% of the measured values. For the excited states, previous data are more scarce. For the $A^2\Pi$ state in CaF and SrF, our FSCC and MRCI results overestimate the experimental values somewhat (5-12%); the error is smaller for MRCI. In case of the $B^2\Sigma^+_{1/2}$ state of SrF, FSCC performs on the same level, but the MRCI results are too low almost by a factor of 2; this is consistent with the deviation of the MRCI and the FSCC values for this state in all the molecules. For BaF, there is no experiment available for the DMs of the excited states. For these states, our DMs are generally lower than those from the earlier calculations, with the best agreement obtained where MRCI approach was also employed [17, 18]; the discrepancy can be attributed to neglect of relativistic effects in the previous works, or the use of a significantly smaller basis set in Ref. [17]. We expect the present predictions to be the most accurate, due to the quality of the methods employed here.

The good agreement of the MRCI DM results with the FSCC values (which

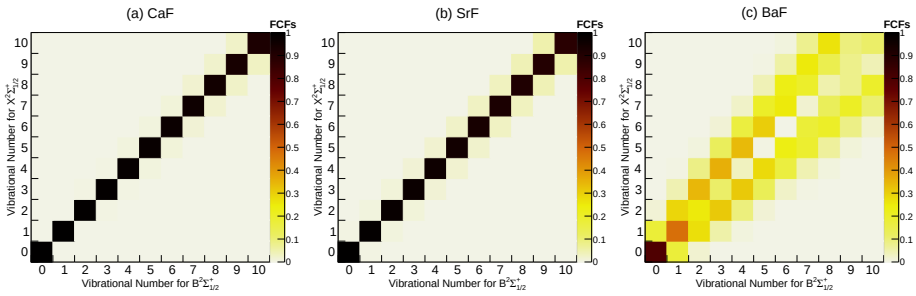

Figure 8.4: Calculated Franck-Condon factors for the vibronic transitions between the $|B^2\Sigma^+_{\frac{1}{2}}, v'\rangle$ and the $|X^2\Sigma^+_{\frac{1}{2}}, v\rangle$ states of CaF, SrF, and BaF (Color online).

are expected to be more accurate) and with experiment validates the use of this method for calculation of the TDMs, where FSCC is not yet applicable.

The calculated transition dipole moments between the ground and the excited states and in between the different excited states are collected in Table 8.11. Experimental verification of the TDM values can be obtained from comparison with measured lifetimes of excited states, as discussed in the next subsection. Also, good agreement is found with previous theoretical investigations, in particular where MRCI approach was used [17, 18]. The new results presented here are, however, the first relativistic calculations of the TDMs of these molecules.

No experimental and limited theoretical information is available for the TDMs between the $A^2\Pi_{1/2}$ and the $A'^2\Delta_{3/2}$ states, the latter being a possible leak channel in the laser-cooling cycle. In case of CaF, our prediction is somewhat higher than the ligand field method calculation of Ref. [43], but of particular note is the discrepancy of almost two orders of magnitude with the predictions of Kang *et al.* [18] for BaF. Our predicted TDM for this transition is 2.33 a.u., which is close to that of CaF and SrF, as expected. The low value presented in Ref. [18] (0.04 a.u.) is appropriate for a forbidden transition, which is not the case for $A^2\Pi_{1/2}$ to $A'^2\Delta_{3/2}$; thus, we view the present prediction as more reliable. We note that the avoided crossing between the $A^2\Pi_{3/2}$ and $A'^2\Delta_{3/2}$ states of BaF, an artifact introduced by the MRCI method, somewhat lowers the expected accuracy of the TDMs for the weak transitions $A'^2\Delta_{5/2} - A'^2\Delta_{3/2}$, $X^2\Sigma_{1/2} - A'^2\Delta_{3/2}$, $A^2\Pi_{3/2} - A'^2\Delta_{3/2}$ and $A^2\Pi_{3/2} - A^2\Pi_{1/2}$. Comparing results obtained from different basis sets, we estimate the size of this error to be up to 20%. This only affects the $A'^2\Delta_{5/2}$ and $A'^2\Delta_{3/2}$ lifetimes of BaF presented in the following subsection.

8.4.5 Lifetimes of excited states

The transition rate of a vibronic transition is defined as

$$\Gamma_{n'v'n''v''} = \frac{16\pi^3 e^2 a_B^2}{3h\epsilon_0} \nu^3_{n'v'n''v''} |\langle v'|M_{n'n''}(R)|v''\rangle|^2. \tag{8.4}$$

Here, $n'v'$ and $n''v''$ denote the upper and lower vibronic states (with n for the electronic and v for the vibrational part), h is the Planck constant, a_B is the Bohr radius, ϵ_0 is the permittivity of free space, $M_{n'n''}(R)$ is the electronic TDM function, and $\nu_{n'v'n''v''}$ is the corresponding transition frequency. In the Franck-Condon (FC) approximation, one assumes the TDM to be independent of R, such that the integral can be factorized to become [108, 109]

$$\begin{aligned} \Gamma_{n'v'n''v''} &\simeq \frac{16\pi^3 e^2 a_B^2}{3h\epsilon_0} \nu^3_{n'v'n''v''} |\langle v'|v''\rangle|^2 M^2_{n'n''} \\ &= \frac{16\pi^3 e^2 a_B^2}{3h\epsilon_0} \nu^3_{n'v'n''v''} q_{v'v''} M^2_{n'n''}. \end{aligned} \tag{8.5}$$

The squared overlaps of vibrational wavefunctions $|\langle v'|v''\rangle|^2 = q_{v'v''}$ are the FCFs obtained in Section 8.4.3. The transition rates $\Gamma_{n'v'n''v''}$ were calculated using the program LEVEL16 [98] and were subsequently used to calculate the lifetimes.

The lifetime $\tau_{n''v''}$ of an excited level can be derived by summing over all vibronic decay channels:

$$\tau_{n''v''} = \frac{1}{\sum\limits_{n'v'} \Gamma_{n'v'n''v''}}. \tag{8.6}$$

All lifetimes listed below were calculated from the transition rates according to Eq. (8.4). However, the FC approximation would also be very appropriate for these molecules, as all errors that would be introduced in the transition rates by the FC approximation lie below 3.5%. This includes the values for the branching ratios of relevance for laser-cooling. This justifies the use of FCFs for the interpretation of the investigated transitions in Sections 8.4.3 and 8.5.

The lifetimes of the excited states of CaF, SrF, and BaF are listed in Table 8.12. The calculated lifetimes are lower by 15-30 % than the experimental values [55, 56, 58, 73], with the discrepancies highest for BaF (the uncertainty on the experimental CaF and SrF lifetimes was estimated as ∼2-4 ns [58], and as low as ∼1 ns for BaF [55, 56]). Furthermore, the calculated difference between the $A^2\Pi_{1/2}$ and the $A^2\Pi_{3/2}$ lifetimes is lower than that obtained in the experiment. Interestingly, for CaF the experimental lifetimes of the two states differ by 3.5 ns, which is higher than the corresponding difference in SrF (1.5 ns), in spite of CaF being a lighter system. A new measurement of the lifetimes in question would thus be instrumental in elucidating the source of the discrepancies between experiment and theory and in verifying the surprising trend in the lifetimes. From

the theory side, a development that would allow calculations of TDMs within the coupled cluster approach would be beneficial in this and in other important applications. We observe a sizeable discrepancy between our value for the lifetime of the $A'^2\Delta_{3/2}$ state of BaF, 5.3 μs, and the theoretical result from Ref. [19], 220 ns. However, the latter value is an estimate based on the $A'^2\Delta_{3/2} - A^2\Pi_{3/2}$ mixing obtained from an effective Hamiltonian matrix, while our results comes from direct *ab initio* calculations.

Finally, the products of transition rates $\Gamma_{n'v'n''v''}$ in Eq. (8.4) with the corresponding lifetimes $\tau_{n''v''}$ in Eq. (8.6) give the radiative branching ratios (relative decay fractions) shown in the Figure 8.5.

8.5 Impact on laser-cooling

In this section we use the results of our molecular structure calculations to discuss the impact of laser-cooling applications for BaF molecules, and compare it to CaF and SrF, for which it has been demonstrated that laser-cooling works efficiently. Typically, scattering of a few thousand photons is sufficient to transversely cool heavy molecules in a molecular beam. In order to slow molecules from a buffer gas beam to below the capture velocity of a magneto-optical trap (MOT), tens of thousands of photons need to be scattered. The requirements for a MOT are even more stringent as the molecules need to continuously scatter photons to remain trapped (at a rate of typically 10^6 photons per second).

Molecules usually exhibit multiple decay paths from the excited state. The excited states under consideration here, the $A^2\Pi$ and the $B^2\Sigma^+$ states, have their lowest vibrational levels below the first dissociation limit, so that pre-dissociation is absent, and decay is purely radiative. As for rotation, the level structure is such that when exciting from an $N = 1$ ground state level, in both $^2\Pi - ^2\Sigma^+$ and $^2\Sigma^+ - ^2\Sigma^+$ electronic transitions, an excited rotational level can be chosen that due to parity and angular momentum selection rules can only decay back to the $N = 1$ ground state level (where it is assumed that rotational mixing due to external electric fields or due to nuclear spin can be neglected) [110]. Therefore, the main problem is decay to vibrationally excited levels in the ground state which are not governed by strict selection rules.

Based on the calculated absolute decay rates associated with the lifetimes listed in Table 8.12, relative decay fractions (branching ratios) have been calculated, taking into account decay from the $B^2\Sigma^+$ to the $A^2\Pi_{1/2}$ state and (for BaF) the decay from the $A^2\Pi$ state to the metastable $A'^2\Delta$ state. The results are depicted in Fig. 8.5. Note that, in principle, laser-cooling via the $A^2\Pi_{3/2}$ state is also possible; however, the small Λ-splitting in this state would require reduction of the external electric fields to an impractically low level, and hence

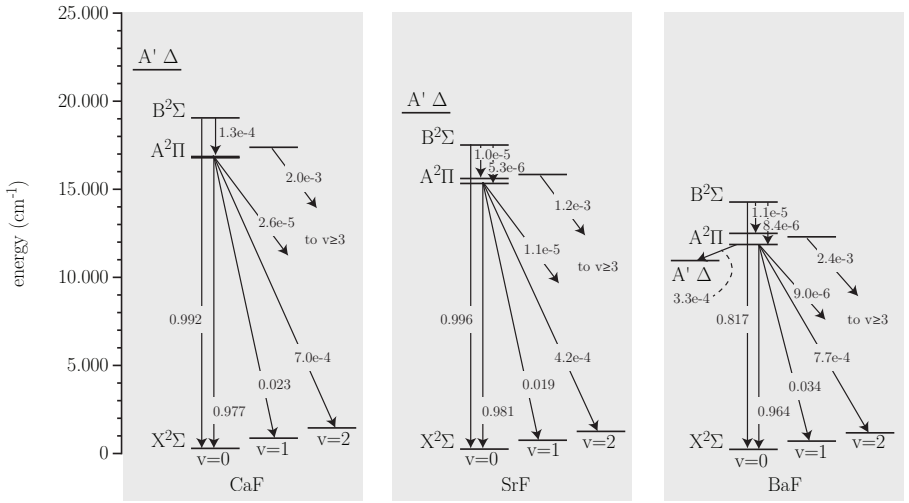

Figure 8.5: The most important energy levels for laser-cooling and the calculated relative decay fractions for CaF, SrF, and BaF.

we will not consider this path further. From the relative decay fractions and the (experimental) transition frequencies, the transition rates have been calculated for the CaF, SrF, and BaF. For BaF, these are depicted in Figure 8.6.

In principle the procedure to find the optimal cooling scheme for each of these molecules is straightforward: start with the strongest transition with good Franck-Condon overlap, and add re-pump lasers to fix the leaks in order of importance. However, strong lasercooling via one excited state leads to an equal distribution of the molecules over all states involved which reduces the maximum optical scattering rate [111]. Hence, for smaller leaks it is more attractive to use an alternative route back to the ground state [112].

Table 8.13 lists the number of photons that can be scattered from CaF, SrF, and BaF via the $A^2\Pi_{1/2}$ and the $B^2\Sigma^+$ states, determined from the calculated transition rates. These numbers represent the maximum number of times that a given transition can be excited before on average half of the molecules will have decayed through a leak to another level. A number of observations can be made from this table. First of all, the large Franck-Condon factor (0.9992) of the $B - X(0\text{-}0)$ in CaF allows one to scatter on average 8.4×10^2 photons before a molecule decays to an unwanted state. It should be noted that specifically this number is very sensitive to small deviations, since the FCF is so close to unity. According to our calculations, adding a re-pumper from the $v = 1$ of the ground state gives only a limited increase as the decay from the B-state to the A-state is

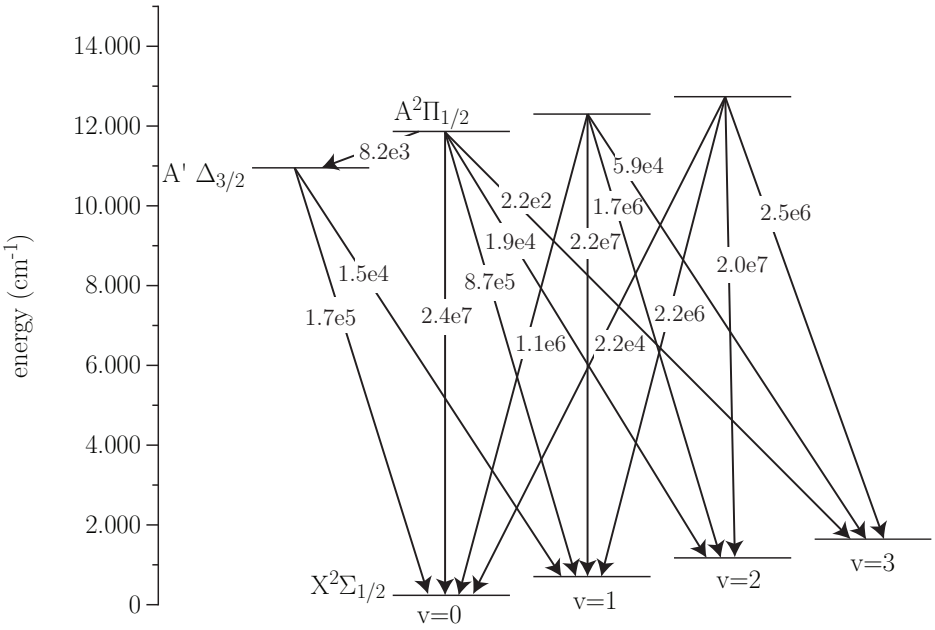

Figure 8.6: Laser cooling level scheme of the $A^2\Pi_{1/2} - X^2\Sigma^+_{1/2}$ system in BaF with the loss channel via the $A'^2\Delta_{3/2}$ state. The absolute transition rates are given in units of s^{-1}.

a significant loss channel. The Franck-Condon factors for the $A-X$ transition in CaF are somewhat less favorable, but still allow to scatter 2.7×10^4 photons using 2 lasers for re-pumping from the first and second vibrationally excited states of the ground state. The Franck-Condon factors of the $B-X$ transition of SrF are not as optimal as those of CaF, but the leak to the A state is reduced. On the other hand, the Franck-Condon factors of the $A-X$ transitions are somewhat better than those of CaF, allowing to scatter on average 6.2×10^4 photons using 2 re-pumpers. Finally, the Franck-Condon factors of the $B-X$ transition of BaF are much smaller than those of CaF and SrF making laser-cooling on the $B-X$ transition impractical. The $A-X$ transition in BaF can be used to scatter 2.0×10^3 photons using 2 re-pumpers. Adding a laser to close the leak from the $v=1$ in the excited state to the $v=3$ in the ground state will not change much because decay to the $A'^2\Delta$ state is a larger limiting factor. If one could close this leak to the $A'^2\Delta$, the number of scattered photons would increase to 7.2×10^4. However, with an energy separation of $\sim$900 cm^{-1} this is not straightforward technically. We conclude from this that although the $A-X$ transition is too

leaky to be used for longitudinal slowing, sufficient photons can be scattered to perform transverse cooling. We note that due to its long lifetime, the $A'^2\Delta$ state has a narrow linewidth. As a consequence, laser-cooling on the $X - \Delta$ transition may be used to reach a very low Doppler limit temperature [113].

8.6 Conclusion

The main goal of this work was investigation of the electronic structure of BaF, which will be used in an experiment to measure the electric dipole moment of the electron. Transverse laser-cooling of the BaF beam is an important component of the planned experiment, and knowledge of the internal structure of the molecule is necessary for identification of an efficient cooling scheme.

We present high-accuracy relativistic Fock space coupled cluster calculations of the potential energy curves and the spectroscopic constants of the ground and the lower excited states of the CaF, SrF, and BaF molecules. Our results for spectroscopic constants are in excellent agreement with experiment, where available, which gives credence to our predictions where no measurements were performed. Using the calculated potential energy curves, we obtain Franck-Condon factors for the $A^2\Pi_{1/2} - X^2\Sigma^+_{1/2}$, $B^2\Sigma^+_{1/2} - X^2\Sigma^+_{1/2}$, $A^2\Pi_{1/2} - A'^2\Delta_{3/2}$, and $A'^2\Delta_{3/2} - X^2\Sigma^+_{1/2}$ transitions. The first two are possible cooling transitions that were previously successfully employed in laser-cooling of CaF and SrF. The investigation of the $A'^2\Delta_{3/2}$ state is due to the fact that it constitutes a potential leak in the BaF cooling cycle. We have also calculated the TDMs of these transitions, using relativistic multireference configuration interaction approach. Based on the calculated TDMs and experimental transition energies we determined the lifetimes of the excited states in BaF and its lighter homologues. The calculated FCFs and TDMs were also used to calculate the relative decay fractions and the transition rates for the three molecules. Finally, using the obtained molecular properties, we investigate the possible cooling schemes in BaF. The $B^2\Sigma^+_{1/2} - X^2\Sigma^+_{1/2}$ cooling transition was shown to be extremely efficient in CaF; however, due to the non-diagonal nature of the FCFs for this transition in BaF, laser-cooling on this transition is impractical. The $A^2\Pi_{1/2} - X^2\Sigma^+_{1/2}$ transition, on the other hand, seems much more promising. We have estimated that it is possible to scatter about 2000 photons on this transition (if two re-pump lasers are added to close the leaks to higher vibrational levels), which is sufficient for transverse laser-cooling.

Table 8.4: Frank-Condon factors (FCFs) for the vibronic transitions between the $|A^2\Pi_{\frac{1}{2}}, v'\rangle$ and the $|X^2\Sigma^+_{\frac{1}{2}}, v\rangle$ states of CaF, SrF, and BaF.

$A^2\Pi_{\frac{1}{2}}$ \ $X^2\Sigma^+_{\frac{1}{2}}$	$v=0$	$v=1$	$v=2$	$v=3$	Method	Reference
$v'=0$	9.739×10^{-1}	2.523×10^{-2}	8.742×10^{-4}	3.588×10^{-5}	X2C-FSCC	This work
	0.964	0.036	0.000	0.000	MRCI	[34]
	$0.968-1.000$				Experiment	[74]
$v'=1$	2.610×10^{-2}	9.236×10^{-1}	4.770×10^{-2}	2.482×10^{-3}	X2C-FSCC	This work
	0.035	0.895	0.070	0.000	MRCI	[34]
$v'=2$	4.427×10^{-5}	5.107×10^{-2}	8.763×10^{-1}	6.760×10^{-2}	X2C-FSCC	This work
	0.001	0.065	0.830	0.103	MRCI	[34]
$v'=3$	2.016×10^{-7}	1.253×10^{-4}	7.494×10^{-2}	8.318×10^{-1}	X2C-FSCC	This work
	0.000	0.004	0.092	0.767	MRCI	[34]

(a) CaF

$A^2\Pi_{\frac{1}{2}}$ \ $X^2\Sigma^+_{\frac{1}{2}}$	$v=0$	$v=1$	$v=2$	$v=3$	Method	Reference
$v'=0$	9.789×10^{-1}	2.054×10^{-2}	5.117×10^{-4}	1.530×10^{-5}	X2C-FSCC	This work
	0.98	0.018	4.30×10^{-4}	1.26×10^{-5}	RKR	[10, 48]
$v'=1$	2.102×10^{-2}	9.377×10^{-1}	3.969×10^{-2}	1.489×10^{-3}	X2C-FSCC	This work
	0.019	0.945	0.035	0.001	RKR	[10, 48]
$v'=2$	4.741×10^{-5}	4.158×10^{-2}	8.978×10^{-1}	5.749×10^{-2}	X2C-FSCC	This work
	2.72×10^{-5}	0.037	0.910	0.051	RKR	[10, 48]
$v'=3$	6.203×10^{-9}	1.411×10^{-4}	6.168×10^{-2}	8.592×10^{-1}	X2C-FSCC	This work
	1.60×10^{-8}	8.15×10^{-5}	0.054	0.876	RKR	[10, 48]

(b) SrF

$A^2\Pi_{\frac{1}{2}}$ \ $X^2\Sigma^+_{\frac{1}{2}}$	$v=0$	$v=1$	$v=2$	$v=3$	Method	Reference
$v'=0$	9.601×10^{-1}	3.892×10^{-2}	9.899×10^{-4}	1.318×10^{-5}	X2C-FSCC	This work
	0.93	0.07			RKR	[55]
	0.951	0.048	0.002	0.000	MPM	[20]
	0.951	0.048	0.002	2.7×10^{-5}	RKR	[19]
	0.981	0.019	3.96×10^{-4}	2.98×10^{-6}	CASSCF+MRCI+SOC	[18]
	0.947	0.051	0.002	0.000	MPM	[21]
$v'=1$	3.923×10^{-2}	8.807×10^{-1}	7.695×10^{-2}	3.051×10^{-3}	X2C-FSCC	This work
	0.049	0.854	0.093	0.005	MPM	[20]
	0.048	0.854	0.093	0.005	RKR	[19]
	0.019	0.940	0.039	0.001	CASSCF+MRCI+SOC	[18]
	0.052	0.845			MPM	[21]
$v'=2$	6.894×10^{-4}	7.812×10^{-2}	8.011×10^{-1}	1.137×10^{-1}	X2C-FSCC	This work
	0.000	0.096	0.758	0.135	MPM	[20]
	9.1×10^{-4}	0.096	0.758	0.135	RKR	[19]
	7.10×10^{-5}	0.040	0.896	0.060	CASSCF+MRCI+SOC	[18]
$v'=3$	3.405×10^{-6}	2.224×10^{-3}	1.162×10^{-1}	7.219×10^{-1}	X2C-FSCC	This work
		0.003	0.141	0.666	MPM	[20]
	1.9×10^{-6}	0.003	0.141	0.664	RKR	[19]
	1.14×10^{-6}	2.88×10^{-4}	0.063	0.849	CASSCF+MRCI+SOC	[18]

(c) BaF

Table 8.5: Frank-Condon factors (FCFs) using X2C-FSCC method for the vibronic transitions between the $|A^2\Pi_{\frac{1}{2}}, v'\rangle$ and the $|A'^2\Delta_{\frac{3}{2}}, v\rangle$ states of BaF (present work, X2C-FSCC).

$A^2\Pi_{\frac{1}{2}}$ \ $A'^2\Delta_{\frac{3}{2}}$	$v = 0$	$v = 1$	$v = 2$	$v = 3$
$v' = 0$	9.856×10^{-1}	1.404×10^{-2}	3.359×10^{-4}	9.470×10^{-6}
$v' = 1$	1.438×10^{-2}	9.578×10^{-1}	2.685×10^{-2}	9.624×10^{-4}
$v' = 2$	2.512×10^{-6}	2.818×10^{-2}	9.314×10^{-1}	3.851×10^{-2}
$v' = 3$	1.443×10^{-7}	6.325×10^{-6}	4.143×10^{-2}	9.063×10^{-1}

Table 8.6: Frank-Condon factors (FCFs) for the vibronic transitions between the $|A'^2\Delta_{\frac{3}{2}}, v'\rangle$ and the $|X^2\Sigma^+_{\frac{1}{2}}, v\rangle$ states of CaF, SrF, and BaF (present work, X2C-FSCC).

$A'^2\Delta_{\frac{3}{2}}$ \ $X^2\Sigma^+_{\frac{1}{2}}$	$v=0$	$v=1$	$v=2$	$v=3$
$v'=0$	8.544×10^{-1}	1.354×10^{-1}	9.884×10^{-3}	4.105×10^{-4}
$v'=1$	1.331×10^{-1}	6.018×10^{-1}	2.355×10^{-1}	2.801×10^{-2}
$v'=2$	1.180×10^{-2}	2.270×10^{-1}	4.009×10^{-1}	3.035×10^{-1}
$v'=3$	7.600×10^{-4}	3.271×10^{-2}	2.860×10^{-1}	2.475×10^{-1}

(a) CaF

$A'^2\Delta_{\frac{3}{2}}$ \ $X^2\Sigma^+_{\frac{1}{2}}$	$v=0$	$v=1$	$v=2$	$v=3$
$v'=0$	9.696×10^{-1}	2.990×10^{-2}	4.924×10^{-4}	3.376×10^{-6}
$v'=1$	2.992×10^{-2}	9.089×10^{-1}	5.961×10^{-2}	1.522×10^{-3}
$v'=2$	4.660×10^{-4}	5.969×10^{-2}	8.477×10^{-1}	8.896×10^{-2}
$v'=3$	2.975×10^{-6}	1.476×10^{-3}	8.903×10^{-2}	7.863×10^{-1}

(b) SrF

$A'^2\Delta_{\frac{3}{2}}$ \ $X^2\Sigma^+_{\frac{1}{2}}$	$v=0$	$v=1$	$v=2$	$v=3$
$v'=0$	9.007×10^{-1}	9.480×10^{-2}	4.361×10^{-3}	1.087×10^{-4}
$v'=1$	9.333×10^{-2}	7.196×10^{-1}	1.739×10^{-1}	1.269×10^{-2}
$v'=2$	5.678×10^{-3}	1.683×10^{-1}	5.623×10^{-1}	2.381×10^{-1}
$v'=3$	2.597×10^{-4}	1.619×10^{-2}	2.261×10^{-1}	4.276×10^{-1}

(c) BaF

Table 8.7: Frank-Condon factors (FCFs) for the vibronic transitions between the $|B^2\Sigma^+_{\frac{1}{2}}, v'\rangle$ and the $|X^2\Sigma^+_{\frac{1}{2}}, v\rangle$ states of CaF, SrF, and BaF (present work, X2C-FSCC).

$B^2\Sigma^+_{\frac{1}{2}}$ \ $X^2\Sigma^+_{\frac{1}{2}}$	$v=0$	$v=1$	$v=2$	$v=3$
$v'=0$	9.992×10^{-1}	7.270×10^{-4}	3.809×10^{-5}	9.834×10^{-8}
$v'=1$	7.396×10^{-4}	9.973×10^{-1}	1.814×10^{-3}	1.176×10^{-4}
$v'=2$	2.473×10^{-5}	1.873×10^{-3}	9.945×10^{-1}	3.322×10^{-3}
$v'=3$	7.981×10^{-7}	6.775×10^{-5}	3.481×10^{-3}	9.907×10^{-1}

(a) CaF

$B^2\Sigma^+_{\frac{1}{2}}$ \ $X^2\Sigma^+_{\frac{1}{2}}$	$v=0$	$v=1$	$v=2$	$v=3$
$v'=0$	9.961×10^{-1}	3.866×10^{-3}	3.604×10^{-6}	7.685×10^{-9}
$v'=1$	3.856×10^{-3}	9.881×10^{-1}	8.000×10^{-3}	1.190×10^{-5}
$v'=2$	1.343×10^{-5}	7.959×10^{-3}	9.796×10^{-1}	1.241×10^{-2}
$v'=3$	7.913×10^{-8}	4.258×10^{-5}	1.231×10^{-2}	9.705×10^{-1}

(b) SrF

$B^2\Sigma^+_{\frac{1}{2}}$ \ $X^2\Sigma^+_{\frac{1}{2}}$	$v=0$	$v=1$	$v=2$	$v=3$
$v'=0$	7.995×10^{-1}	1.811×10^{-1}	1.832×10^{-2}	1.073×10^{-3}
	0.81^a	0.17^a		
$v'=1$	1.760×10^{-1}	4.782×10^{-1}	2.924×10^{-1}	4.915×10^{-2}
$v'=2$	2.221×10^{-2}	2.751×10^{-1}	2.570×10^{-1}	3.482×10^{-1}
$v'=3$	2.105×10^{-3}	5.717×10^{-2}	3.156×10^{-1}	1.159×10^{-1}

(c) BaF

[a] Previous study using the RKR method [55].

Table 8.8: Calculated dipole moments (a.u.) of CaF at the experimental bond length R_e, compared to previous calculations and experiment.

State	DM	Method	Reference
$X^2\Sigma^+_{1/2}$	1.18	X2C-MRCISD	This work
	1.25	X2C-FSCC	This work
	1.31	Ionic model	[28]
	1.18	LFM	[43]
	1.02	CISD	[32]
	1.26	EPM	[44]
	1.18	MRCI	[33]
	1.32	LFM	[31]
	1.26	MP2	[46]
	1.04	FDHF	[45]
	1.24	EOVERM	[47]
	1.20	RCCSD(T)	[38]
	1.24	RCCSD	[23]
	1.30[a]	CASSCF+MRCI	[37]
	1.26	RCCSD(T)	[24]
	1.20	RCCSD(T)	[42]
	1.21(3)	Experiment	[69]
$A'^2\Delta_{3/2}$	2.44	X2C-MRCISD	This work
	2.57	X2C-FSCC	This work
$A'^2\Delta_{5/2}$	2.44	X2C-MRCISD	This work
	2.57	X2C-FSCC	This work
$A'^2\Delta$	2.98	LFM	[43]
	3.04	EPM	[30]
	3.2	CASSCF+MRCI	[37]
$A^2\Pi_{1/2}$	1.04	X2C-MRCISD	This work
	1.08	X2C-FSCC	This work
$A^2\Pi_{3/2}$	1.04	X2C-MRCISD	This work
	1.08	X2C-FSCC	This work
$A^2\Pi$	1.61	LFM	[43]
	1.01	EPM	[30]
	1.00	EOVERM	[47]
	0.96(2)	Experiment	[71]
$B^2\Sigma^+_{1/2}$	0.69	X2C-MRCISD	This work
	0.89	X2C-FSCC	This work
	2.25	LFM	[43]
	0.63	EPM	[30]
	0.73	EOVERM	[47]

[a] This is evaluated around the equilibrium bond distance from Fig. 4 in Ref. [37].

Table 8.9: Calculated dipole moments (a.u.) of SrF at the experimental bond length R_e, compared to previous calculations and experiment.

State	DM	Method	Reference
$X^2\Sigma^+_{1/2}$	1.26	X2C-MRCISD	This work
	1.36	X2C-FSCC	This work
	1.44	Ionic model	[28]
	0.99	CISD	[32]
	1.42	EPM	[44]
	1.49	LFM	[31]
	1.01	FDHF	[45]
	1.42	CASSCF+RSPT2	[36]
	1.32	CASSCF+MRCI	[36]
	1.36	RCCSD	[40]
	1.42	CCSD	[23]
	1.42	RCCSD(T)	[24]
	1.38	RCCSD	[25]
	1.3643(4)	Experiment	[70]
$A'^2\Delta_{3/2}$	2.39	X2C-MRCISD	This work
	2.50	X2C-FSCC	This work
$A'^2\Delta_{5/2}$	2.39	X2C-MRCISD	This work
	2.50	X2C-FSCC	This work
$A'^2\Delta$	3.36	EPM	[30]
	3.18	LFM	[31]
	3.27	CASSCF+MRCI	[36]
$A^2\Pi_{1/2}$	0.85	X2C-MRCISD	This work
	0.91	X2C-FSCC	This work
$A^2\Pi_{3/2}$	0.82	X2C-MRCISD	This work
	0.88	X2C-FSCC	This work
$A^2\Pi$	0.85	EPM	[30]
	1.29	LFM	[31]
	1.53	CASSCF+RSPT2	[36]
	1.64	CASSCF+MRCI	[36]
	0.81(2)	Experiment	[72]
$B^2\Sigma^+_{1/2}$	0.19	X2C-MRCISD	This work
	0.40	X2C-FSCC	This work
	0.41	EPM	[30]
	1.33	LFM	[31]
	1.26	CASSCF+MRCI	[36]
	0.36(2)	Experiment	[72]

Table 8.10: Calculated dipole moments (a.u.) of BaF at the experimental bond length R_e, compared to previous calculations and experiment.

State	DM	Method	Reference
$X^2\Sigma^+_{1/2}$	1.14	X2C-MRCISD	This work
	1.27	X2C-FSCC	This work
	1.26	RASCI	[22]
	1.35	Ionic model	[28]
	1.54	LFM	[31]
	1.15	AREP-RASSCF	[26]
	1.16	CASSCF+MRCI	[17]
	1.33	CASSCF+MRCI+SOC	[18]
	1.34	RCCSD	[23]
	1.34	RCCSD(T)	[24]
	1.34	RCCSD	[25]
	1.247(1)	Experiment	[54]
$A'^2\Delta_{3/2}$	2.31	X2C-MRCISD	This work
	2.38	X2C-FSCC	This work
$A'^2\Delta_{5/2}$	2.31	X2C-MRCISD	This work
	2.38	X2C-FSCC	This work
$A'^2\Delta$	3.57	EPM	[30]
	3.31	LFM	[31]
	2.47	CASSCF+MRCI	[17]
	2.64	CASSCF+MRCI	[18]
$A^2\Pi_{1/2}$	0.40	X2C+MRCISD	This work
	0.53	X2C-FSCC	This work
$A^2\Pi_{3/2}$	0.34	X2C+MRCISD	This work
	0.47	X2C-FSCC	This work
$A^2\Pi$	1.95	EPM	[30]
	1.36	LFM	[31]
	0.86	CASSCF+MRCI	[17]
	1.01	CASSCF+MRCI	[18]
$B^2\Sigma^+_{1/2}$	0.58	X2C-MRCISD	This work
	0.32	X2C-FSCC	This work
	1.61	EPM	[30]
	1.31	LFM	[31]
	0.54	CASSCF+MRCI	[17]

Table 8.11: Calculated transition dipole moments (a.u.) between state 1 and state 2 at the ground state experimental bond length R_e. Present results in italics, experimental values in bold font.

State 1	State 2				
	$A^2\Pi_{1/2}$	$A^2\Pi_{3/2}$	$A'^2\Delta_{3/2}$	$A'^2\Delta_{5/2}$	$B^2\Sigma^+_{1/2}$
CaF					
$X^2\Sigma^+_{1/2}$	*2.406*	*2.406*	*0.004*		*1.881*
	2.32*[a]				1.73[a]
	2.17*[b]				1.64[b]
	2.34*[c]				1.85[c]
					1.79[d]
	2.34*[e]				**1.71**[e]
$A^2\Pi_{1/2}$		*0.012*	*2.473*		*0.373*
$A^2\Pi_{3/2}$			*0.000*	*2.476*	*0.370*
$A^2\Pi$				1.76*[a]	
$A'^2\Delta_{3/2}$				*0.001*	*0.036*
SrF					
$X^2\Sigma^+_{1/2}$	*2.626*	*2.627*	*0.012*		*2.054*
	2.37*[b]				1.86[b]
	2.45*[e]				
					2.45[f]
$A^2\Pi_{1/2}$		*0.035*	*2.711*		*0.210*
$A^2\Pi_{3/2}$			*0.004*	*2.728*	*0.195*
$A'^2\Delta_{3/2}$				*0.009*	*0.173*
BaF					
$X^2\Sigma^+_{1/2}$	*2.810*	*2.797*	*0.272*		*2.226*
	2.18*[b]				1.85[b]
	3.20*†[g]				2.40†[g]
	2.73*[h]			0.20*[h]	
		2.57[i]			**2.10**[i]
	2.41[j]				
$A^2\Pi_{1/2}$		*0.242*	*2.332*		*0.100*
$A^2\Pi_{3/2}$			*0.166*	*2.375*	*0.178*
$A^2\Pi$				0.04*[h]	
$A'^2\Delta_{3/2}$				*0.193*	*0.316*

*Ω-unresolved transitions; †This is evaluated around the equilibrium bond distance from Fig. 10 in Ref. [17]; [a]LFM [43]; [b]LFM [31]; [c]EOVERM [47]; [d]MRCI [37]; [e]Experiment [58]; [f]Experiment [73]; [g]CASSCF+MRCI [17]; [h]CASSCF+MRCI [18]; [i]Experiment [55]; [j]Experiment [56].

Table 8.12: Calculated lifetimes (ns) of the excited states of CaF, SrF, and BaF.

State / Mol.	$A^2\Pi_{\frac{1}{2}}$	$A^2\Pi_{\frac{3}{2}}$	$B^2\Sigma^+_{\frac{1}{2}}$	$A'^2\Delta_{\frac{3}{2}}$	Ref.
CaF	18.3	18.1	19.7	546	Present
	19.48^e	19.48^e			[34]
	$21.9(4.0)^a$	$18.4(4.1)^a$	$25.1(4.0)^a$		Exp.
SrF	20.7	19.6	22.4	1130	Present
	$24.1(2.0)^a$	$22.6(4.7)^a$	$25.5(0.5)^c$		Exp.
BaF	40.4	34.7	37.0	5289	Present
	37.8^f	37.8^f			[18]
				220	[19]
	$56.0(0.9)^d$	$46.1(0.9)^b$	$41.7(0.3)^b$		Exp.

[a]Ref. [58]; [b]Ref. [55]; [c]Ref. [73]; [d]Ref. [56]; [e] This is derived from the calculated TDM using MRCI wave function; [f] This is derived from the calculated TDM with CASSCF+MRCI+SOC method for transition $A^2\Pi - X^2\Sigma^+$.

Table 8.13: Estimated number of photons scattered on a cycling transition before half of the molecules are lost.

Transition	Repump	CaF	SrF	BaF
$X - A$	no repump	29	36	19
	$v = 1$ repump	9.5×10^2	1.6×10^3	6.2×10^2
	$v = 2$ repump	2.7×10^4	6.2×10^4	2.0×10^3
	Δ repump			7.2×10^4
$X - B$	no repump	8.4×10^2	1.9×10^2	3.4
	$v = 1$ repump	4.3×10^3	3.8×10^4	42

Table 8.14: Frank-Condon factors (FCFs) for vibronic transitions between the $|A^2\Pi_{\frac{3}{2}}, v'\rangle$ and the $|X^2\Sigma^+_{\frac{1}{2}}, v\rangle$ states of CaF, SrF, and BaF (present work, X2C-FSCC).

$A^2\Pi_{\frac{3}{2}}$ \ $X^2\Sigma^+_{\frac{1}{2}}$	$v=0$	$v=1$	$v=2$	$v=3$
$v'=0$	9.733×10^{-1}	2.574×10^{-2}	9.036×10^{-4}	3.745×10^{-5}
$v'=1$	2.663×10^{-2}	9.220×10^{-1}	4.861×10^{-2}	2.564×10^{-3}
$v'=2$	4.763×10^{-5}	5.208×10^{-2}	8.738×10^{-1}	6.882×10^{-2}
$v'=3$	2.099×10^{-7}	1.347×10^{-4}	7.639×10^{-2}	8.286×10^{-1}

(a) CaF

$A^2\Pi_{\frac{3}{2}}$ \ $X^2\Sigma^+_{\frac{1}{2}}$	$v=0$	$v=1$	$v=2$	$v=3$
$v'=0$	9.769×10^{-1}	2.245×10^{-2}	5.955×10^{-4}	1.864×10^{-5}
$v'=1$	2.301×10^{-2}	9.320×10^{-1}	4.324×10^{-2}	1.728×10^{-3}
$v'=2$	6.225×10^{-5}	4.541×10^{-2}	8.886×10^{-1}	6.243×10^{-2}
$v'=3$	4.937×10^{-9}	1.850×10^{-4}	6.723×10^{-2}	8.468×10^{-1}

(b) SrF

$A^2\Pi_{\frac{3}{2}}$ \ $X^2\Sigma^+_{\frac{1}{2}}$	$v=0$	$v=1$	$v=2$	$v=3$
$v'=0$	9.640×10^{-1}	3.515×10^{-2}	8.858×10^{-4}	1.122×10^{-5}
$v'=1$	3.554×10^{-2}	8.917×10^{-1}	6.994×10^{-2}	2.742×10^{-3}
$v'=2$	5.060×10^{-4}	7.144×10^{-2}	8.183×10^{-1}	1.040×10^{-1}
$v'=3$	9.061×10^{-7}	1.670×10^{-3}	1.072×10^{-1}	7.443×10^{-1}

(c) BaF

References

[1] Y. Hao, L. F. Pašteka, L. Visscher, P. Aggarwal, H. L. Bethlem, A. Boeschoten, A. Borschevsky, M. Denis, K. Esajas, S. Hoekstra, *et al.*, J. Chem. Phys. **151**, 034302 (2019).

[2] M. S. Safronova, D. Budker, D. DeMille, D. F. J. Kimball, A. Derevianko, and C. W. Clark, Rev. Mod. Phys. **90**, 025008 (2018).

[3] V. A. Dzuba and V. V. Flambaum, Int. J. Mod. Phys. E **21**, 1230010 (2012).

[4] J. J. Hudson, D. M. Kara, I. J. Smallman, B. E. Sauer, M. R. Tarbutt, and E. A. Hinds, Nature **473**, 493 (2011).

[5] J. Baron, W. C. Campbell, D. DeMille, J. M. Doyle, G. Gabrielse, Y. V. Gurevich, P. W. Hess, N. R. Hutzler, E. Kirilov, I. Kozyryev, B. R. O'Leary, C. D. Panda, M. F. Parsons, E. S. Petrik, B. Spaun, A. C. Vutha, and A. D. West, Science **343**, 269 (2014).

[6] V. Andreev, D. G. Ang, D. DeMille, J. M. Doyle, G. Gabrielse, J. Haefner, N. R. Hutzler, Z. Lasner, C. Meisenhelder, B. R. O'Leary, C. D. Panda, A. D. West, E. P. West, and X. Wu, Nature **562**, 355 (2018).

[7] The NL-eEDM collaboration, P. Aggarwal, H. L. Bethlem, A. Borschevsky, M. Denis, K. Esajas, P. A. B. Haase, Y. Hao, S. Hoekstra, K. Jungmann, T. B. Meijknecht, M. C. Mooij, R. G. E. Timmermans, W. Ubachs, L. Willmann, and A. Zapara, Eur. Phys. J. D **72**, 197 (2018).

[8] N. F. Ramsey, Rev. Mod. Phys. **62**, 541 (1990).

[9] M. D. Di Rosa, Eur. Phys. J. D **31**, 395 (2004).

[10] E. S. Shuman, J. F. Barry, and D. DeMille, Nature **467**, 820 (2010).

[11] M. Hummon, M. Yeo, B. Stuhl, A. Collopy, Y. Xia, and J. Ye, Phys. Rev. Lett. **110**, 143001 (2013).

[12] V. Zhelyazkova, A. Cournol, T. E. Wall, A. Matsushima, J. J. Hudson, E. A. Hinds, M. R. Tarbutt, and B. E. Sauer, Phys. Rev. A **89**, 053416 (2014).

[13] J. Lim, J. R. Almond, M. A. Trigatzis, J. A. Devlin, N. J. Fitch, B. E. Sauer, M. R. Tarbutt, and E. A. Hinds, Phys. Rev. Lett. **120**, 123201 (2018).

[14] I. Kozyryev, L. Baum, K. Matsuda, B. L. Augenbraun, L. Anderegg, A. P. Sedlack, and J. M. Doyle, Phys. Rev. Lett. **118**, 173201 (2017).

[15] T. A. Isaev, A. V. Zaitsevskii, and E. Eliav, J. Phys. B **50**, 225101 (2017).

[16] I. Kozyryev and N. R. Hutzler, Phys. Rev. Lett. **119**, 133002 (2017).

[17] S. Tohme and M. Korek, J. Quant. Spec. Rad. Trans. **167**, 82 (2015).

[18] S. Kang, F. Kuang, G. Jiang, and J. Du, Mol. Phys. **114**, 810 (2016).

[19] T. Chen, W. Bu, and B. Yan, Phys. Rev. A **94**, 063415 (2016).

[20] B. Karthikeyan, K. Balachandrakumar, V. Raja, and N. Rajamanickam, J. Appl. Spec. **80**, 790 (2013).

[21] L. Xu, B. Wei, Y. Xia, L. Deng, and J. Yin, Chin. Phys. B **26**, 033702 (2017).

[22] M. K. Nayak and R. K. Chaudhuri, J. Phys. B **39**, 1231 (2006).

[23] V. S. Prasannaa, S. Sreerekha, M. Abe, V. Bannur, and B. P. Das, Phys. Rev. A **93**, 042504 (2016).

[24] M. Abe, V. S. Prasannaa, and B. P. Das, Phys. Rev. A **97**, 032515 (2018).

[25] N. M. Fazil, V. S. Prasannaa, K. V. P. Latha, M. Abe, and B. P. Das, Phys. Rev. A **98**, 032511 (2018).

[26] M. G. Kozlov, A. V. Titov, N. S. Mosyagin, and P. V. Souchko, Phys. Rev. A **56**, R3326 (1997).

[27] E. Westin and A. Rosen, Chem. Phys. Lett. **149**, 239 (1988).

[28] T. Törring, W. E. Ernst, and S. Kindt, J. Chem. Phys. **81**, 4614 (1984).

[29] E. S. Rittner, J. Chem. Phys. **19**, 1030 (1951).

[30] T. Törring, W. Ernst, and J. Kändler, J. Chem. Phys. **90**, 4927 (1989).

[31] A. R. Allouche, G. Wannous, and M. Aubert-Frécon, Chem. Phys. **170**, 11 (1993).

[32] S. R. Langhoff, C. W. Bauschlicher Jr., H. Partridge, and R. Ahlrichs, J. Chem. Phys. **84**, 5025 (1986).

[33] P. Bündgen, B. Engels, and S. D. Peyerimhoff, Chem. Phys. Lett. **176**, 407 (1991).

[34] M. Pelegrini, C. S. Vivacqua, O. Roberto-Neto, F. R. Ornellas, and F. B. Machado, Braz. J. Phys. **35**, 950 (2005).

[35] C. Yang, X. Zhang, F. Gao, and T. Ren, J. Mol. Struct. **807**, 147 (2007).

[36] F. Jardali, M. Korek, and G. Younes, Canad. J. Phys. **92**, 1223 (2014).

[37] N. El-Kork, F. Korjieh, J. A. Chtay, and M. Korek, Spectrochim Acta A: Mol. Biomol. Spectrosc. **177**, 170 (2017).

[38] J. F. Harrison, R. W. Field, and C. C. Jarrold, "Comparison of CaF, ZnF, CaO, and ZnO," in *Low-lying potential energy surfaces*, edited by M. R. Hoffmann and K. G. Dyall (American Chemical Society, 2002) pp. 238–259.

[39] V. S. Prasannaa, M. Abe, and B. Das, Phys. Rev. A **90**, 052507 (2014).

[40] S. Sasmal, H. Pathak, M. K. Nayak, N. Vaval, and S. Pal, Phys. Rev. A **91**, 030503 (2015).

[41] M. B. Kosicki, D. Kedziera, and P. S. Zuchowski, J. Phys. Chem. A **121**, 4152 (2017).

[42] S. Hou and P. F. Bernath, J. Quant. Spec. Rad. Trans. **210**, 44 (2018).

[43] S. F. Rice, H. Martin, and R. W. Field, J. Chem. Phys. **82**, 5023 (1985).

[44] J. M. Mestdagh and J. P. Visticot, Chem. Phys. **155**, 79 (1991).

[45] J. Kobus, D. Moncrieff, and S. Wilson, Phys. Rev. A **62**, 062503 (2000).

[46] A. D. Buckingham and R. M. Olegário, Chem. Phys. Lett. **212**, 253 (1993).

[47] S. Raouafi, G. H. Jeung, and C. Jungen, J. Chem. Phys. **115**, 7450 (2001).

[48] J. F. Barry, *Laser cooling and slowing of a diatomic molecule*, Ph.D. thesis, Yale University (2013).

[49] P. J. Linstrom and W. G. Mallard (Eds.), *NIST chemistry webbook: NIST standard reference database number 69* (National Institute of Standards and Technology, 2018).

[50] K. P. Huber and G. Herzberg, *Molecular spectra and molecular structure: IV. Constants of diatomic molecules* (Springer US, 1979).

[51] C. Ryzlewicz and T. Törring, Chem. Phys. **51**, 329 (1980).

[52] R. F. Barrow, A. Bernard, C. Effantin, J. d'Incan, G. Fabre, A. El Hachimi, R. Stringat, and J. Vergès, Chem. Phys. Lett. **147**, 535 (1988).

[53] A. Bernard, C. Effantin, E. Andrianavalona, J. Verges, and R. Barrow, J. Mol. Spec. **152**, 174 (1992).

[54] W. E. Ernst, J. Kändler, and T. Törring, J. Chem. Phys. **84**, 4769 (1986).

[55] L. E. Berg, T. Olsson, J. C. Chanteloup, A. Hishikawa, and P. Royen, Mol. Phys. **79**, 721 (1993).

[56] L. E. Berg, N. Gador, D. Husain, H. Ludwigs, and P. Royen, Chem. Phys. Lett. **287**, 89 (1998).

[57] R. F. Barrow and J. R. Beale, Chem. Commun. (London) **12**, 606a (1967).

[58] P. J. Dagdigian, H. W. Cruse, and R. N. Zare, J. Chem. Phys. **60**, 2330 (1974).

[59] R. W. Field, D. O. Harris, and T. Tanaka, J. Mol. Spec. **57**, 107 (1975).

[60] T. C. Steimle, P. J. Domaille, and D. O. Harris, J. Mol. Spec. **68**, 134 (1977).

[61] J. Nakagawa, P. J. Domaille, T. C. Steimle, and D. O. Harris, J. Mol. Spec. **70**, 374 (1978).

[62] W. E. Ernst and J. O. Schröder, Chem. Phys. **78**, 363 (1983).

[63] J. Verges, C. Effantin, A. Bernard, A. Topouzkhanian, A. R. Allouche, J. d'Incan, and R. F. Barrow, J. Phys B **26**, 279 (1993).

[64] T. C. Steimle, D. A. Fletcher, and C. T. Scurlock, J. Mol. Spec. **158**, 487 (1993).

[65] P. Colarusso, B. Guo, K. Q. Zhang, and P. F. Bernath, J. Mol. Spec. **175**, 158 (1996).

[66] L. A. Kaledin, J. C. Bloch, M. C. McCarthy, and R. W. Field, J. Mol. Spec. **197**, 289 (1999).

[67] C. Nitsch, J. O. Schröder, and W. E. Ernst, Chem. Phys. Lett. **148**, 130 (1988).

[68] P. M. Sheridan, J. Wang, M. J. Dick, and P. F. Bernath, J. Phys. Chem. A **113**, 13383 (2009).

[69] W. J. Childs, L. S. Goodman, U. Nielsen, and V. Pfeufer, J. Chem. Phys. **80**, 2283 (1984).

[70] W. E. Ernst, J. Kändler, S. Kindt, and T. Törring, Chem. Phys. Lett. **113**, 351 (1985).

[71] W. E. Ernst and J. Kändler, Phys. Rev. A **39**, 1575 (1989).

[72] J. Kändler, T. Martell, and W. E. Ernst, Chem. Phys. Lett. **155**, 470 (1989).

[73] L. E. Berg, K. Ekvall, T. Hansson, A. Iwamae, V. Zengin, D. Husain, and P. Royen, Chem. Phys. Lett. **248**, 283 (1996).

[74] T. E. Wall, J. F. Kanem, J. J. Hudson, B. E. Sauer, D. Cho, M. G. Boshier, E. A. Hinds, and M. R. Tarbutt, Phys. Rev. A **78**, 062509 (2008).

[75] T. A. Isaev, S. Hoekstra, and R. Berger, Phys. Rev. A **82**, 052521 (2010).

[76] T. A. Isaev and R. Berger, Phys. Rev. A **86**, 062515 (2012).

[77] A. Borschevsky, M. Iliaš, V. A. Dzuba, K. Beloy, V. V. Flambaum, and P. Schwerdtfeger, Phys. Rev. A **85**, 052509 (2012).

[78] A. Borschevsky, M. Iliaš, V. A. Dzuba, V. V. Flambaum, and P. Schwerdtfeger, Phys. Rev. A **88**, 022125 (2013).

[79] T. Isaev and R. Berger, J. Mol. Spec. **300**, 26 (2014).

[80] A. D. Kudashov, A. N. Petrov, L. V. Skripnikov, N. S. Mosyagin, T. A. Isaev, R. Berger, and A. V. Titov, Phys. Rev. A **90**, 052513 (2014).

[81] P. Pyykko, Chem. Rev. **88**, 563 (1988).

[82] DIRAC, A relativistic ab initio electronic structure program, Release DIRAC15 (2015), written by R. Bast, T. Saue, L. Visscher, and H. J. Aa. Jensen, with contributions from V. Bakken, K. G. Dyall, S. Dubillard, U. Ekstroem, E. Eliav, T. Enevoldsen, E. Fasshauer, T. Fleig, O. Fossgaard, A. S. P. Gomes, T. Helgaker, J. Henriksson, M. Ilias, Ch. R. Jacob, S. Knecht, S. Komorovsky, O. Kullie, J. K. Laerdahl, C. V. Larsen, Y. S. Lee, H. S. Nataraj, M. K. Nayak, P. Norman, G. Olejniczak, J. Olsen, Y. C. Park, J. K. Pedersen, M. Pernpointner, R. Di Remigio, K. Ruud, P. Salek, B. Schimmelpfennig, J. Sikkema, A. J. Thorvaldsen, J. Thyssen, J. van Stralen, S. Villaume, O. Visser, T. Winther, and S. Yamamoto (see `http://www.diracprogram.org`).

[83] M. Iliaš and T. Saue, J. Chem. Phys. **126**, 064102 (2007).

[84] T. Saue, J. Chem. Phys. Phys. Chem. **12**, 3077 (2011).

[85] R. Bast, A. J. Thorvaldsen, M. Ringholm, and K. Ruud, Chem. Phys. **356**, 177 (2009).

[86] J. Sikkema, L. Visscher, T. Saue, and M. Iliaš, J. Chem. Phys. **131**, 124116 (2009).

[87] S. Knecht, H. J. A. Jensen, and T. Fleig, J. Chem. Phys. **132**, 014108 (2010).

[88] J. A. Gaunt, Proc. R. Soc. Lond. A **122**, 513 (1929).

[89] G. Breit, Phys. Rev. **34**, 553 (1929).

[90] O. Visser, L. Visscher, P. Aerts, and W. Nieuwpoort, Theor. Chim. Acta **81**, 405 (1992).

[91] E. Eliav, U. Kaldor, and Y. Ishikawa, Phys. Rev. A **49**, 1724 (1994).

[92] A. B. E. Eliav and U. Kaldor, "High-accuracy relativistic coupled-cluster calculations for the heaviest elements," in *Handbook of Relativistic Quantum Chemistry*, edited by W. Liu (Springer, 2017).

[93] I. Lindgren and J. Morrison, *Atomic many-body theory* (Springer, Berlin, 1982).

[94] K. G. Dyall, J. Phys. Chem. A **113**, 12638 (2009).

[95] K. G. Dyall, Theor. Chem. Account. **135**, 128 (2016).

[96] J. L. Dunham, Phys. Rev. **41**, 721 (1932).

[97] V. Kellö, private communication (2018).

[98] R. J. Le Roy, J. Quant. Spec. Rad. Transf. **186**, 167 (2017).

[99] I. Shavitt, "The method of configuration interaction," in *Methods of electronic structure theory*, edited by H. F. Schaefer III (Springer-Verlag, 1977) pp. 189–275.

[100] T. Fleig, J. Olsen, and L. Visscher, J. Chem. Phys. **119**, 2963 (2003).

[101] L. B. Knight Jr, W. C. Easley, W. Weltner Jr, and M. Wilson, J. Chem. Phys. **54**, 322 (1971).

[102] J. P. Desclaux, Comp. Phys. Commun. **9**, 31 (1975).

[103] G. Herzberg, *Molecular spectra and molecular structure*, Vol. 1 (Read Books Ltd., 2013).

[104] R. W. Nicholls and W. R. Jarmain, Proc. Phys. Soc. A **69**, 253 (1956).

[105] J. C. McCallum, J. Quant. Spectros. Rad. Transfer **21**, 563 (1979).

[106] J. H. V. Nguyen, C. R. Viteri, E. G. Hohenstein, C. D. Sherrill, K. R. Brown, and B. Odom, New J. Phys. **13**, 063023 (2011).

[107] S. Truppe, H. J. Williams, M. Hambach, L. Caldwell, N. J. Fitch, E. A. Hinds, B. E. Sauer, and M. R. Tarbutt, Nat. Phys. **13**, 1173 (2017).

[108] M. Larsson, Astron. Astrophys. **128**, 291 (1983).

[109] R. Li, X. Zhang, M. Jin, H. Xu, and B. Yan, Chin. Phys. B **23**, 053101 (2014).

[110] B. K. Stuhl, B. C. Sawyer, D. Wang, and J. Ye, Phys. Rev. Lett. **101**, 243002 (2008).

[111] M. R. Tarbutt, B. E. Sauer, J. J. Hudson, and E. A. Hinds, New J. Phys. **15**, 0530034 (2013).

[112] I. J. Smallman, F. Wang, T. C. Steimle, M. R. Tarbutt, and E. Hinds, J. Mol. Spec. **300**, 3 (2014).

[113] A. L. Collopy, M. Hummon, M. Yeo, B. Yan, and J. Ye, New J. Phys. **17**, 055008 (2015).

Chapter 9

Variation of fundamental constants[a]

9.1 Motivation

Several unification theories and standard model (SM) extensions predict variation of fundamental constants (VFC) in space and in time [2, 3]. It has also been hypothesized that interaction of ordinary matter with a massive scalar dark matter (DM) field can produce slow temporal drifts or oscillations in the values of the fundamental constants [4–6], while topological defects in the dark matter field can produce transient VFC [7–9]. The first transient DM detection limits were recently discussed by Wcisło *et al.* [10]. A possible route to observe such drifts or transient effects is through systematic measurements of transitions in atomic and molecular spectra that are sensitive to the variation of dimensionless fundamental quantities such as the fine structure constant $\alpha = e^2/\hbar c$ or the proton-to-electron mass ratio $\mu = m_p/m_e$ [11–16].

Laser interferometers now reach precision far exceeding that of any spectroscopic apparatus and thus offer a new promising direction in the search for VFC [17]. This line of research is directly connected to the dependence of material size on VFC, through the use of resonant-mass detectors [18–21] or cryogenic sapphire and silicon oscillators [22–27]. In order to interpret such experiments, knowledge of dependence of the crystal size on the fundamental constants is needed.

Theoretical investigations of size dependence of molecules and bulk materials on fundamental constants are scarce. Some studies were carried out in the con-

[a]This chapter is reproduced from our published paper [1]: Lukáš F. Pašteka, Yongliang Hao, Anastasia Borschevsky, Victor V. Flambaum, and Peter Schwerdtfeger, Material size Dependence on fundamental constants, Phys. Rev. Lett. **122**, 160801 (2019).

text of relativistic effects and corresponding changes in periodic trends, where the dependence on the fine structure constant is considered [28, 29]. More recently, King *et al.* investigated the dependence of structure and bonding in small molecules on both α and μ, with the objective of finding the hypothetical (α, μ) regimes that support biochemistry and therefore life on our planet [30]. Braxmaier *et al.* [31] performed an investigation of the variation of the resonance frequencies of monolithic crystal cavities with possible variation of fundamental constants through the dependence of the refractive index of the medium on α and μ. To the best of our knowledge, no prior investigations of direct size dependence of bulk materials on fundamental constants have been carried out.

In non-relativistic physics, the size of molecules and solids is proportional to the Bohr radius a_B. This dependence cancels out in the ratio of the sizes. The individual dependence of different compounds on the fine structure constant is determined by the difference in the relativistic effects, which are proportional to $Z^2\alpha^2$ (and higher powers of $Z^2\alpha^2$). Thus, considering the ratio of the resonance frequencies in two optical cavities made from different materials, in the non-relativistic approximation there is no dependence on α, but such dependence appears due to relativistic corrections.

The situation is different when we compare the resonance frequency of an optical cavity with an atomic optical frequency. For example, one measures the ratio of the Sr atomic clock frequency and the resonance frequency in a silicone cavity of length L [10]. Here, the ratio is proportional to α already in the non-relativistic approximation since the resonator frequency depends on the speed of light c. Indeed, the resonator frequency is $\omega_r = ck \sim c/\lambda \sim c/L \sim c/a_B$, atomic frequency $\omega_a \sim e^2/(\hbar a_B)$, therefore $\omega_a/\omega_r \sim e^2/\hbar c = \alpha$. In this case, relativistic corrections produce additional α dependence.

Another dimensionless ratio which affects the properties of different compounds is the ratio of nuclear and electron masses; the nuclear mass is approximately proportional to the proton mass, and thus we consider the proton-to-electron mass ratio μ.

In this work we present a systematic investigation of the variation of crystal lattice parameters (a_e and c_e) and molecular bond lengths (R_e) due to variation of the fine structure constant and the proton-to-electron mass ratio for selected solid state and molecular systems.

9.2 Diatomic results

For our solid-state study, we have selected several elemental and compound crystals. The choice of Cu, Si, Al, Nb and Al_2O_3 was motivated by highly precise experimental setups measuring effects of physics beyond the SM: silicon and sapphire oscillators [22–27] and resonance of Cu, Al and Nb bars [18–20]. In order

Table 9.1: Experimental and calculated bond lengths R_e and their corresponding calculated fractional variation with varying fine-structure constant α and proton-to-electron mass ratio μ.

Mol.	State	R_e (Å)			$\frac{dR_e}{R_e}/\frac{d\alpha}{\alpha}$		$\frac{dR_0}{R_0}/\frac{d\mu}{\mu}$	$\frac{dR_e}{R_e}/\frac{d\mu}{\mu}$
		Exp.[a]	CC	DFT	CC	DFT	Eq. (9.3)	DBOC-CC
Cu_2	$^1\Sigma_g^+$	2.2197(1)	2.216	2.215	-3.19×10^{-2}	-3.18×10^{-2}	-7.15×10^{-4}	-7.31×10^{-6}
Ag_2	$^1\Sigma_g^+$	2.5303(2)	2.522	2.565	-7.66×10^{-2}	-8.21×10^{-2}	-5.34×10^{-4}	-3.38×10^{-6}
Au_2	$^1\Sigma_g^+$	2.4719(1)	2.471	2.501	-3.15×10^{-1}	-3.37×10^{-1}	-2.95×10^{-4}	9.16×10^{-7}
C_2	$^1\Sigma_g^+$	1.24253(2)	1.243	1.254	-2.65×10^{-4}	-3.88×10^{-4}	-1.17×10^{-3}	-6.94×10^{-6}
Si_2	$^3\Sigma_g^-$	2.246	2.255	2.309	8.66×10^{-5}	1.94×10^{-4}	-7.08×10^{-4}	-6.63×10^{-6}
Ge_2	$^3\Sigma_g^-$	2.3667(6)[b]	2.361	2.430	-6.74×10^{-3}	-6.48×10^{-3}	-4.37×10^{-4}	-4.46×10^{-6}
Sn_2	0_g^+	2.746(1)	2.722	2.814	-2.24×10^{-2}	-2.17×10^{-2}	-3.25×10^{-4}	-3.82×10^{-6}
Pb_2	0_g^+	2.9271(2)	2.869	2.960	-1.05×10^{-1}	-1.58×10^{-1}	-3.37×10^{-4}	3.32×10^{-7}

[a] Experimental values from Refs. [32–37].
[b] For Ge_2, only R_0 was available experimentally. This was used together with the experimental B_0 and α_e value of 2.84×10^{-4} cm^{-1} from our CC calculations to calculate R_e.

to illustrate periodic trends, we have also chosen to study the group 11 and 14 elemental solids.

However, we initially investigated the dependence of the equilibrium interatomic distance R_e of diatomic molecules on α and μ. This gave us the opportunity to test the methodology used for the investigation of solids. For molecules, we have the option of using high-level *ab-initio* methodology such as relativistic coupled cluster (CC) theory as a benchmark to our density functional theory (DFT) results. For this part of the study we chose dimers of group 11 and group 14 elements.

In order to investigate the dependence on the fine structure constant, we performed a series of optimizations of the equilibrium bond lengths R_e varying the relativistic parameter $x = (\alpha/\alpha_0)^2 - 1$. In case of the closed shell Cu_2, Ag_2, Au_2, and C_2 we employed the single-reference CCSD(T) method, and for the remaining open-shell systems (Si_2, Ge_2, Sn_2, Pb_2) the Fock space CCSD method was used. For the DFT part, we have used the PBE functional [38, 39] to keep the methodology consistent with the solid-state calculations described below. Dyall's v4z basis sets [40–42] were used for all the systems except Au_2, where the v3z basis was used to conserve computational effort. All the calculations were carried out in the 4-component framework using the relativistic molecular program package DIRAC15 [43]. The results are collected in Table 9.1.

Both CC and DFT calculated bond lengths agree with experiment. The mean absolute symmetric percentage error (MASPE) of CC results with respect to experiment is 0.5%. Correspondingly for DFT, the MASPE is 1.6%. Comparing

the two methods to one another, we obtain the MASPE value of 1.9%, i.e. DFT recovers the more rigorous CC results very well. In case of the derivative property, the α-variation of bond lengths, there are no experimental results. However, comparing the DFT to CC results gives the MASPE of 22%, which we use to evaluate the uncertainty on the predicted DFT α-variation of lattice parameters presented below.

Generally, the magnitude of the α-dependence on R_e increases with increasing atomic number Z, as one expects. In group 11 (Cu, Ag, Au), the effect follows the well-known $\sim Z^2$ dependence as is the case with many other properties [44]. For group 14 elements (C, Si, Ge, Sn, Pb), we observe a non-monotonous trend, although the tendency of increasing α-sensitivity magnitude for heavier elements is clearly present. This is not surprising, as we note the changes in the ground-state electronic structure in the group 14 element sequence.

The main source of the mass dependence of molecular bond lengths comes from the vibrational motion. Assuming that the rotational constant and bond length relationship is $B \sim R^{-2}$, and the vibrationally averaged rotational constant is

$$B_0 = B_e - \frac{\alpha_e}{2}, \tag{9.1}$$

where B_e is the equilibrium rotational constant and α_e is the vibrational-rotational coupling constant, we can express the vibrationally averaged bond length R_0 as

$$R_0 = R_e \sqrt{1 + \frac{\alpha_e}{2B_e - \alpha_e}}. \tag{9.2}$$

Following the scaling of equilibrium constants with reduced mass M, $B_e \sim M^{-1}$ and $\alpha_e \sim M^{-\frac{3}{2}}$ [45], we arrive at the fractional variation of R_0 with varying μ

$$\frac{dR_0}{R_0} = -\frac{\alpha_e}{4(2B_e - \alpha_e)} \frac{d\mu}{\mu}. \tag{9.3}$$

This simple but useful estimate can be evaluated using readily available experimental spectroscopic constants [32–37]. Resulting values are shown in Table 9.1. Due to the negative sign in Eq. (9.3) and the fact that $\alpha_e \ll B_e$ in all realistic diatomics, these are always negative. The magnitude of the effect is relatively uniform in all investigated systems. Following the Pekeris formula [46] derived for the Morse potential,

$$\alpha_e = \frac{6B_e^2}{\omega_e} \left(\sqrt{\frac{\omega_e x_e}{B_e}} - 1 \right), \tag{9.4}$$

we can expect larger fractional variation of R_0 with μ for shallow or strongly anharmonic interatomic potentials.

A small contribution to bond length mass dependence arises from the nuclear kinetic energy terms which are neglected in the Born-Oppenheimer approximation (BOA). Within the BOA, the nuclear motion is separated from the electronic motion, and coupling terms are in practice completely neglected. As a consequence, equilibrium bond lengths are independent of the mass and this near mass-invariance is widely used in the experimental determination of bond lengths from rotational spectra of different isotopologues of the same molecule. Taking the nuclear kinetic energy term into account the R_e is in fact weakly linearly dependent on the inverse reduced mass of the molecule [47]. This directly translates into the μ-dependence $R_e \sim \mu^{-1}$.

To estimate the non-BOA contribution to μ-sensitivity of bond lengths, we included the perturbative diagonal Born-Oppenheimer corrections (DBOC) in optimizations of the investigated molecules. We employed the CCSD methodology as implemented in the program package CFOUR [48, 49] together with Jorge's TZP basis set [50–53]. The current implementation only allows for a non-relativistic treatment of DBOC, and the results for heavier molecules should be considered with some caution. Relativistic effects are known to increase the DBOC in atoms by up to about 40% for the heavy elements considered in this work; however, the trends calculated for diatomic molecules in Ref. [54] are not systematic.

Results for the μ sensitivity of the fractional variation of R_e are collected in Table 9.1. Generally, the size of this effect is comparable in all investigated diatomics. This contribution is at least two orders of magnitude smaller than the fractional variation of R_0 in all investigated systems and therefore it can be safely neglected when considering the μ-sensitivity of vibrationally averaged bond lengths. One can expect this conclusion to be even more justified in solids, where the atoms are further confined by the lattice. We note Lutz and Hutson investigated the role of DBOC in other aspects of diatomic spectroscopy and ultracold physics [55].

We estimate our μ-sensitivity results to be accurate within $\pm 5\%$, considering error bars from experimental determination of spectroscopic parameters and errors introduced by neglecting the higher-order spectroscopic constants (γ_e, ϵ_e, etc.) and the non-BOA effects. The error in α_e determination dominates the resulting compound error of the μ-sensitivity.

9.3 Solid state results

The investigation of the α and μ-sensitivity of lattice parameters of solids was conceptually analogous to the initial study on diatomics. For the α-dependence, series of optimizations of the a_e and c_e equilibrium lattice parameters were performed varying the relativistic parameter x. Technically, this means the value

Table 9.2: Experimental and calculated lattice constants a_e and c_e (c_e shown in the second line for the respective structure) and their corresponding calculated fractional variation with varying fine-structure constant α and proton-to-electron mass ratio μ.

Solid	Structure	Spc. group	a_e, c_e (Å)			$\frac{da_e}{a_e} / \frac{d\alpha}{\alpha}$	$\frac{da_0}{a_0} / \frac{d\mu}{\mu}$
			Exp. (RT)[a]	Exp. (0K)[b]	Calc.		
Cu	Fcc	$Fm\bar{3}m$	3.6146(2)	3.6029(2)	3.634	-1.97×10^{-2}	-1.12×10^{-3}
Ag	Fcc	$Fm\bar{3}m$	4.0857(2)	4.0681(2)	4.160	-4.97×10^{-2}	-8.32×10^{-4}
Au	Fcc	$Fm\bar{3}m$	4.0782(2)	4.0646(2)	4.059	-1.61×10^{-1}	-4.33×10^{-4}
C	Dia.	$Fd\bar{3}m$	3.5669(2)	3.5667(2)	3.576	-2.39×10^{-4}	-2.22×10^{-3}
Si	Dia.	$Fd\bar{3}m$	5.4306(2)	5.4259(2)	5.479	-2.17×10^{-4}	-8.56×10^{-4}
Ge	Dia.	$Fd\bar{3}m$	5.6574(2)	5.6487(2)	5.779	6.21×10^{-4}	-6.02×10^{-4}
Sn	Dia. (α)	$Fd\bar{3}m$	6.4892(2)	6.4752(2)	6.678	-4.46×10^{-4}	-3.29×10^{-4}
	Tet. (β)	$I4_1/amd$	5.8318(2)	5.8048(2)	5.956	7.61×10^{-3}	-7.09×10^{-4}
			3.1818(2)	3.1671(2)	3.251	1.16×10^{-3}	
Pb	Fcc	$Fm\bar{3}m$	4.9502(2)	4.9142(2)	4.715	-2.94×10^{-1}	-5.65×10^{-4}
Al	Fcc	$Fm\bar{3}m$	4.0496(2)	4.0321(2)	4.042	3.65×10^{-4}	-2.11×10^{-3}
Nb	Bcc	$Im\bar{3}m$	3.3004(2)	3.2955(2)	3.317	-2.35×10^{-3}	-3.74×10^{-4}
Ti	Hcp	$P6_3/mmc$	2.9506(2)	2.9461(2)	2.935	-1.18×10^{-3}	-7.06×10^{-4}
			4.6835(2)	4.6764(2)	4.685	-3.47×10^{-3}	
Al_2O_3	Hex.	$R\bar{3}c$	4.7540(5)	4.7507(5)	4.825	-4.06×10^{-4}	-2.06×10^{-3}
			12.9820(6)	12.9731(6)	13.142	-4.88×10^{-4}	
SiC	3C (β)	$F\bar{4}3m$	4.3596(1)	4.3582(1)	4.392	-3.54×10^{-4}	-1.56×10^{-3}
	6H (α)	$P6_3mc$	3.0806(1)	3.0795(1)	3.105	-3.73×10^{-4}	-1.47×10^{-3}
			15.1173(1)	15.1121(1)	15.225	-3.41×10^{-4}	
WC	Hex.	$P\bar{6}m2$	2.9059(1)	2.9051(1)	2.923	-4.39×10^{-2}	-1.26×10^{-3}
			2.8377(1)	2.8369(1)	2.857	-3.19×10^{-2}	

[a] Experimental values from Refs. [56–59].
[b] Finite-temperature experimental lattice parameters extrapolated to 0K [60] using experimental data from Refs. [58, 59, 61–69].

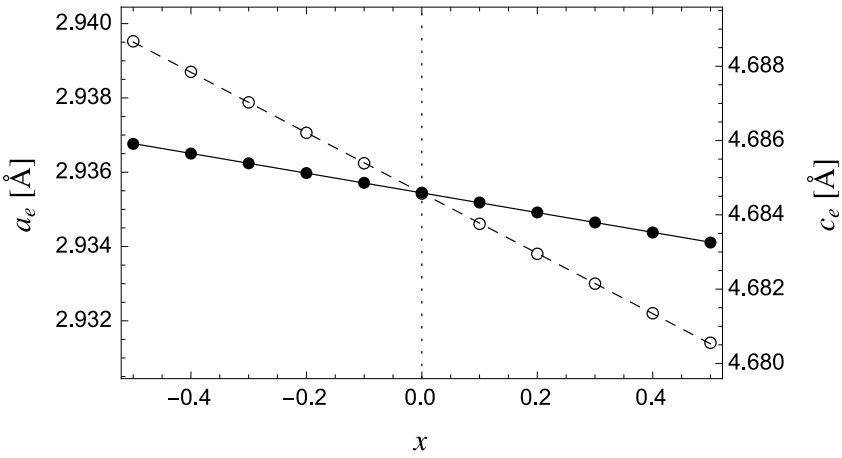

Figure 9.1: Dependence of the lattice constants a_e, c_e (full and open circles, respectively) of bulk Ti on the relativistic parameter x. Slopes are shown to scale.

of the speed of light c was varied in the computations. All calculations were carried out using the relativistic DFT solid-state program package FPLO 14.0, which implements the full-potential local-orbital minimal-basis scheme [70, 71]. We tested several DFT functionals and decided to use the gradient corrected PBE functional [38, 39], which had the smallest error in the equilibrium lattice parameters compared to the available experimental values. In all systems, reciprocal sampling used a k-mesh of $12 \times 12 \times 12$ and 200-point radial mesh. Both were saturated with respect to the equlibrium lattice constants and their derivatives. Optimizations of the lattice constants were performed within a fully relativistic framework, while the internal parameters (atomic positions within the unit cell) were optimized using scalar relativity in each step due to the limitation of the current implementation (the latter only applies to Al_2O_3 and α-SiC). Optimal lattice parameters were determined from minima of polynomial fits through grids of calculated points with nummerical accuracy of 10^{-7} Å. Additionally, we compared the results of our FPLO calculations on Cu, C (diamond), and Si to those obtained from an independent program package SPRKKR 6.3 [72, 73] based on the spin polarized relativistic Korringa-Kohn-Rostoker methodology [74]. The agreement between the two data sets was excellent with discrepancies below 2%.

The results of our DFT solid-state calculations are collected in Table 9.2. The calculated equilibrium lattice parameters are in a very good agreement with experimental values, giving the MASPE value of 1.3%, which is slightly smaller than in the case of diatomic molecules. Relying on the error analysis of diatomics,

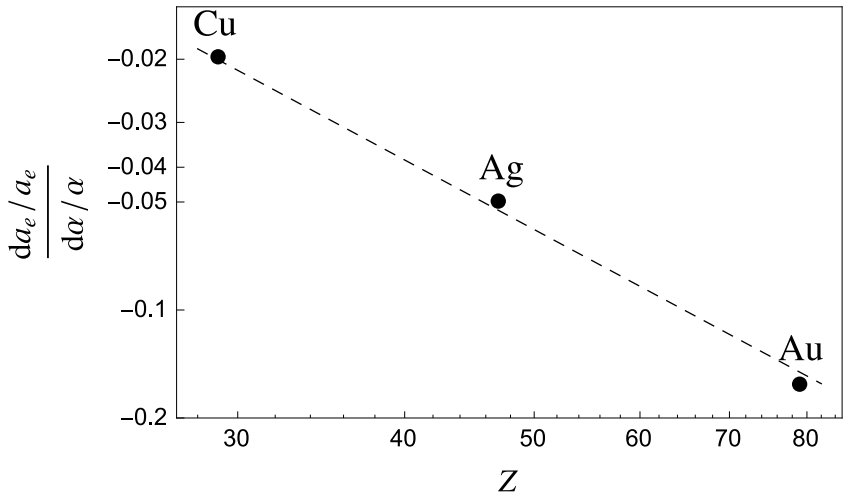

Figure 9.2: Z-scaling of $(da_e/a_e)/(d\alpha/\alpha)$ for group 11 elements (note the log-log scale). Dashed line shows the ideal Z^2 fit.

we thus expect the calculated α-dependence of lattice constants to be accurate within $\pm 20\%$. Figure 9.1 demonstrates that the lattice parameters exhibit close to ideal α^2 scaling, i.e. their dependence on x is almost perfectly linear across a wide range of α values (in the present study, $\sqrt{0.5}\ \alpha_0 \leqslant \alpha \leqslant \sqrt{1.5}\ \alpha_0$). We note that the values of fractional variation $(da_e/a_e)/(d\alpha/\alpha)$ are relatively small ($\ll 1$).

We once more observe the general increase of the α-sensitivity with Z. In the case of group 11 elements, this increase follows the $\sim Z^2$ scaling (Figure 9.2). For group 14, the overall effect is highly non-monotonous. This is also true if we only compare crystal structures with the same space group $Fd\bar{3}m$ (C, Si, Ge, α-Sn), as the bonding character changes significantly along this sequence from strongly covalent to semi-metallic [75]. Another interesting feature is that the α-sensitivity of diamond, the lightest element in the group, is larger than expected from the simple scaling law, and larger than that of its heavier homologue, Si. Comparing the two allotropes of tin, we observe opposite sign of the size dependence on α. Furthermore, the absolute α-sensitivity of β-Sn is higher than that of α-Sn. This can be ascribed to relativistic effects more strongly influencing the distorted-close-pack structure of β-Sn, which has higher s character compared to fully sp^3-hybridized diamond structure of α-Sn [76]. Relativistic effects are strongest in s orbitals with the highest density in the vicinity of the nucleus. Population analysis gives 5s:1.54e, 5p:2.34e for α-Sn and 5s:1.73e, 5p:2.14e for β-Sn, supporting this

interpretation. For the non-cubic crystal structures (corundum, β-tin, α-SiC, WC), we see different α-dependence of the lattice constants a_e and c_e; especially in the case of β-Sn, where the α-sensitivity of a_e is roughly $6\times$ larger than that of c_e. Thus, the character of bonding has a very strong influence on the dependence of the crystal structure parameters on α, and in the general case scaling laws are not sufficient to estimate the size of the effect.

A general practice for removing the dependence on the unit system is to use the ratio of two observed quantities instead of measuring a property of a single system. In this case, we can either compare two different materials (preferably with opposite signs of their α-dependencies, to enhance the sensitivity) or even compare the α-sensitivity in two different directions of a single material (for non-cubic crystals). Additionally, in interferometry, the observed quantity is the phase shift, which is unitless in itself, and one type of measurement would suffice for topological DM detection.

The mass dependence of lattice parameters is due to the vibrational motion of the crystal lattice. It was extensively studied theoretically and experimentally using isotopic substitution. For monoatomic solids at zero temperature (where the mass dependence is largest [77]), London derived an expression for fractional variation of molar volume V with varying isotopic molar mass M [78]

$$\frac{M dV}{V dM} = -\frac{9}{16}\frac{\gamma\kappa}{V} R\Theta_D, \tag{9.5}$$

where γ is the thermodynamic Grüneisen parameter, κ is the compressibility, R is the gas constant, and Θ_D is the Debye temperature. This translates to a final expression for the μ-variation of the lattice constant

$$\frac{da_0}{a_0} \Big/ \frac{d\mu}{\mu} = -\frac{3}{16}\frac{\gamma}{BV} k_B \Theta_D, \tag{9.6}$$

where B is the isothermal bulk modulus, V is atomic volume and k_B is Boltzmann constant. Since all numbers entering this formula are positive, the resulting values are negative for all realistic crystals. Note, the bulk modulus and hence also the μ-variation are assumed to be isotropic.

Results obtained using Eq. (9.6) and available experimental parameters [58, 59, 61–69] are listed in Table 9.2. Considering the errors in experimental determination of solid-state parameters, we estimate the overall presented μ-sensitivity values to be accurate within $\pm 20\%$. Our μ-sensitivity estimates compare well with the results derived from available experimental measurements on diamond, silicon and germanium (-1.8×10^{-3}, -7.8×10^{-4} and -5.5×10^{-4}, respectively) [79–82], as well as with results derived from theoretical path-integral Monte Carlo simulations (C: -1.94×10^{-3}; Si: -1.13×10^{-3}; Ge: -6.55×10^{-4}; β-SiC: -1.37×10^{-3}) [83–86]. The MASPE value of our estimates with respect to the referenced results

is 15%, supporting our error analysis. Out of the investigated materials, diamond, Al and Al_2O_3 (i.e. corundum or sapphire) have the highest μ-sensitivity. All results lie in a relatively small range spanning 1 order of magnitude. Within this range, however, there are no clear systematic trends.

9.4 Conclusion

Precision interferometry can now provide relative sensitivity of parameters such as $\delta L/L$ to VFC beyond that of any other physical apparatus. Combining this with the calculated fractional variation of crystal sizes and the use of silicon, sapphire or other single crystal oscillators or optical cavities offers a new and independent path to testing VFC and search for scalar low-mass dark matter beyond the most stringent limits [17]. For a progress in this field, accurate values for α- and μ-dependence of lattice constants of solid-state materials are required, which we provide in this work.

To illustrate the expected experimental sensitivity to the variation of the fundamental constants, we present an example. Assume that $\delta\alpha/\alpha = 10^{-17}$ yr^{-1} (this value is close to the present best limit on the variation of α [87]). We may compare variation of relative sizes L of two materials with different sensitivity to α-variation, for example, Au and Si with $K_\alpha(\mathrm{Au}) = -0.161$ and $K_\alpha(\mathrm{Si}) = -0.000217$, where the sensitivity coefficients $K = (da_e/a_e)/(d\alpha/\alpha)$ are presented in Table 9.2. The relative variation of the ratio of the sizes is then $[\delta(L_{\mathrm{Au}}/L_{\mathrm{Si}})]/[(L_{\mathrm{Au}}/L_{\mathrm{Si}})] = [K_\alpha(\mathrm{Au}) - K_\alpha(\mathrm{Si})](\delta\alpha/\alpha) = -1.6 \times 10^{-18}$.

This is comparable to the precision of the recent optical cavity experiments [88–90], where the crystal-size variation directly affects the measurement. The highest reported precision for an optical cavity is $5.8(3) \times 10^{-19}$ after an hour of averaging [91]. Longer averaging times may lead to an even higher precision. Therefore, the results presented here support the proposed method as an alternative avenue to test the VFC. Performing a wider search and identifying suitable materials with higher sensitivity coefficients in the future would further improve the prospects of the proposed method.

Currently, the highest instrumental precision is achieved in the large-scale interferometer setups (LIGO, VIRGO), reaching 10^{-22} levels [92]. However, since here the effect of the crystal-size variation is not as direct as for the optical cavities, application of the present method would require some modification of the detection scheme.

As explained in the beginning of this chapter, the sensitivity coefficient for comparison of a resonator frequency and an atomic clock frequency in the non-relativistic limit is given by the difference $K_{\mathrm{resonator}} - K_{\mathrm{clock}} = 1$; i.e., the effect is equal to $\delta\alpha/\alpha = 10^{-17}$. To include the relativistic corrections, we should add to the sensitivity coefficients of the resonator the values presented in Table 9.2 and

for the clock the values presented in Ref. [11]. For the Si optical cavity and Sr clock, the relativistic corrections are not significant; however, for clocks based on heavy elements (such as Hg^+ and Yb^+) relativistic effects increase the sensitivity to $\delta\alpha/\alpha$ several times.

References

[1] L. F. Pašteka, Y. Hao, A. Borschevsky, V. V. Flambaum, and P. Schwerdtfeger, Phys. Rev. Lett. **122**, 160801 (2019).

[2] J.-P. Uzan, Living Rev. Relativity **14**, 2 (2011).

[3] J. D. Barrow, Philos. Trans. R. Soc. A **363**, 2139 (2005).

[4] Y. V. Stadnik and V. V. Flambaum, Phys. Rev. Lett. **115**, 201301 (2015).

[5] Y. V. Stadnik and V. V. Flambaum, Phys. Rev. Lett. **114**, 161301 (2015).

[6] A. Arvanitaki, J. Huang, and K. Van Tilburg, Phys. Rev. D **91**, 015015 (2015).

[7] A. Derevianko and M. Pospelov, Nat. Phys. **10**, 933 (2014).

[8] Y. V. Stadnik and V. V. Flambaum, Phys. Rev. Lett. **113**, 151301 (2014).

[9] Y. V. Stadnik and V. V. Flambaum, Phys. Rev. Lett. **116**, 169002 (2016).

[10] P. Wcisło, P. Morzyński, M. Bober, A. Cygan, D. Lisak, R. Ciuryło, and M. Zawada, Nat. Astron. **1**, 0009 (2016).

[11] V. V. Flambaum and V. A. Dzuba, Can. J. Physics **87**, 25 (2009).

[12] C. Chin, V. V. Flambaum, and M. G. Kozlov, New J. Phys. **11**, 055048 (2009).

[13] P. Jansen, H. L. Bethlem, and W. Ubachs, J. Chem. Phys. **140**, 010901 (2014).

[14] L. F. Pašteka, A. Borschevsky, V. V. Flambaum, and P. Schwerdtfeger, Phys. Rev. A **92**, 012103 (2015).

[15] M. G. Kozlov and S. A. Levshakov, Ann. Phys. **525**, 452 (2013).

[16] M. S. Safronova, D. Budker, D. DeMille, D. Kimball, A. Derevianko, and C. W. Clark, Rev. Mod. Phys. **90**, 025008 (2018).

[17] Y. V. Stadnik and V. V. Flambaum, Phys. Rev. A **93**, 063630 (2016).

[18] A. Arvanitaki, S. Dimopoulos, and K. Van Tilburg, Phys. Rev. Lett. **116**, 031102 (2016).

[19] P. Astone, D. Babusci, L. Baggio, M. Bassan, D. G. Blair, M. Bonaldi, P. Bonifazi, D. Busby, P. Carelli, M. Cerdonio, *et al.*, Phys. Rev. D **68**, 022001 (2003).

[20] P. Astone, D. Babusci, L. Baggio, M. Bassan, M. Bignotto, M. Bonaldi, M. Camarda, P. Carelli, G. Cavallari, M. Cerdonio, *et al.*, Phys. Rev. D **76**, 102001 (2007).

[21] O. D. Aguiar, Res. Astron. Astrophys. **11**, 1 (2011).

[22] M. E. Tobar, P. Wolf, S. Bize, G. Santarelli, and V. Flambaum, Phys. Rev. D **81**, 022003 (2010).

[23] J. G. Hartnett, N. R. Nand, and C. Lu, Appl. Phys. Lett. **100**, 183501 (2012).

[24] E. Wiens, A. Y. Nevsky, and S. Schiller, Phys. Rev. Lett. **117**, 271102 (2016).

[25] T. Kessler, C. Hagemann, C. Grebing, T. Legero, U. Sterr, F. Riehle, M. J. Martin, L. Chen, and J. Ye, Nat. Photon. **6**, 687 (2012).

[26] E. Wiens, Q. Chen, I. Ernsting, H. Luckmann, U. Rosowski, A. Nevsky, and S. Schiller, Opt. Lett. **39**, 3242 (2014).

[27] E. Wiens, Q. Chen, I. Ernsting, H. Luckmann, U. Rosowski, A. Nevsky, and S. Schiller, Opt. Lett. **40**, 68 (2015).

[28] P. Pyykkö, Chem. Rev. **88**, 563 (1988).

[29] T. Söhnel, H. Hermann, and P. Schwerdtfeger, Angew. Chem. Int. Ed. **40**, 4381 (2001).

[30] R. A. King, A. Siddiqi, W. D. Allen, and H. F. Schaefer, Phys. Rev. A **81**, 042523 (2010).

[31] C. Braxmaier, O. Pradl, H. Müller, A. Peters, J. Mlynek, V. Loriette, and S. Schiller, Phys. Rev. D **64**, 042001 (2001).

[32] K. P. Huber and G. Herzberg, *Molecular spectra and molecular structure: IV. Constants of diatomic molecules*.

[33] V. Beutel, H. G. Krämer, G. L. Bhale, M. Kuhn, K. Weyers, and W. Demtröder, J. Chem. Phys. **98**, 2699 (1993).

[34] B. Simard and P. A. Hackett, J. Mol. Spectrosc. **142**, 310 (1990).

[35] D. A. Hostutler, H. Li, D. J. Clouthier, and G. Wannous, J. Chem. Phys. **116**, 4135 (2002).

[36] V. E. Bondybey, M. Heaven, and T. A. Miller, J. Chem. Phys. **78**, 3593 (1983).

[37] M. C. Heaven, T. A. Miller, and V. Bondybey, **87**, 2072 (1983).

[38] J. P. Perdew, K. Burke, and M. Ernzerhof, Phys. Rev. Lett. **77**, 3865 (1996).

[39] J. P. Perdew, K. Burke, and M. Ernzerhof, Phys. Rev. Lett. **78**, E1396 (1997).

[40] K. G. Dyall, Theor. Chem. Acc. **112**, 403 (2004).

[41] K. G. Dyall, Theor. Chem. Acc. **115**, 441 (2006).

[42] K. G. Dyall, Theor. Chem. Acc. **117**, 483 (2007).

[43] DIRAC, A relativistic ab initio electronic structure program, Release DIRAC15 (2015), written by R. Bast, T. Saue, L. Visscher, and H. J. Aa. Jensen, with contributions from V. Bakken, K. G. Dyall, S. Dubillard, U. Ekstroem, E. Eliav, T. Enevoldsen, E. Fasshauer, T. Fleig, O. Fossgaard, A. S. P. Gomes, T. Helgaker, J. Henriksson, M. Ilias, Ch. R. Jacob, S. Knecht, S. Komorovsky, O. Kullie, J. K. Laerdahl, C. V. Larsen, Y. S. Lee, H. S. Nataraj, M. K. Nayak, P. Norman, G. Olejniczak, J. Olsen, Y. C. Park, J. K. Pedersen, M. Pernpointner, R. Di Remigio, K. Ruud, P. Salek, B. Schimmelpfennig, J. Sikkema, A. J. Thorvaldsen, J. Thyssen, J. van Stralen, S. Villaume, O. Visser, T. Winther, and S. Yamamoto (see `http://www.diracprogram.org`).

[44] J. Autschbach, S. Siekierski, M. Seth, P. Schwerdtfeger, and W. H. E. Schwarz, J. Comput. Chem. **23**.

[45] R. Mulliken, Phys. Rev. **25**, 119 (1925).

[46] C. Pekeris, Phys. Rev. **45**, 98 (1934).

[47] J. K. G. Watson, J. Mol. Spectrosc. **45**, 99 (1973).

[48] CFOUR, A quantum-chemical program package written by J.F. Stanton, J. Gauss, M.E. Harding, P.G. Szalay with contributions from A.A. Auer, R.J. Bartlett, U. Benedikt, C. Berger, D.E. Bernholdt, Y.J. Bomble, L. Cheng, O. Christiansen, M. Heckert, O. Heun, C. Huber, T.-C. Jagau, D. Jonsson, J. Jusélius, K. Klein, W.J. Lauderdale, F. Lipparini, D.A. Matthews, T. Metzroth, L.A. Mück, D.P. O'Neill, D.R. Price, E. Prochnow, C. Puzzarini, K. Ruud, F. Schiffmann, W. Schwalbach, C. Simmons, S. Stopkowicz, A. Tajti, J. Vázquez, F. Wang, J.D. Watts and the integral packages MOLECULE (J. Almlöf and P.R. Taylor), PROPS (P.R. Taylor), ABACUS (T. Helgaker,

H.J. Aa. Jensen, P. Jørgensen, and J. Olsen), and ECP routines (A. V. Mitin and C. van Wüllen), (see `http://www.cfour.de`).

[49] J. Gauss, A. Tajti, M. Kállay, J. F. Stanton, and P. G. Szalay, J. Chem. Phys. **125**, 144111 (2006).

[50] A. C. Neto, E. Muniz, R. Centoducatte, and F. Jorge, J. Mol. Struct. **718**, 219 (2005).

[51] G. G. Camiletti, S. F. Machado, and F. E. Jorge, J. Comput. Chem. **29**, 2434 (2008).

[52] C. Barros, P. de Oliveira, F. Jorge, A. C. Neto, and M. Campos, Mol. Phys. **108**, 1965 (2010).

[53] A. C. Neto and F. Jorge, Chem. Phys. Lett. **582**, 158 (2013).

[54] Y. Imafuku, M. Abe, M. W. Schmidt, and M. Hada, J. Phys. Chem. A **120**, 2150 (2016).

[55] J. J. Lutz and J. M. Hutson, J. Mol. Spectrosc. **330**, 43 (2016).

[56] H. W. King, "Crystal structures and lattice parameters of allotropes of the elements," in *CRC Handbook of chemistry and physics*, edited by W. M. Haynes (CRC Press, 2013).

[57] E. N. Maslen, V. A. Streltsov, N. R. Streltsova, N. Ishizawa, and Y. Satow, Acta Crystallogr. Sect. B **49**, 973 (1993).

[58] O. Madelung, U. Rössler, and M. Schulz, *Group IV elements, IV-IV and III-V compounds (Part b): Electronic, transport, optical and other properties* (Springer-Verlag, 2002).

[59] K. D. Litasov, A. Shatskiy, Y. Fei, A. Suzuki, E. Ohtani, and K. Funakoshi, J. Appl. Phys. **108**, 053513 (2010).

[60] G. B. Mitra and A. K. Giri, J. Phys. D **19**, 1065 (1986).

[61] C. Kittel and P. McEuen, *Introduction to solid state physics*, 8th ed. (John Wiley & Sons, 1996).

[62] D. C. Wallace, *Statistical physics of crystals and liquids: a guide to highly accurate equations of state* (World Scientific, 2002).

[63] I. V. Aleksandrov, A. F. Goncharov, A. N. Zisman, and S. M. Stishov, Zh. Eksp. Teor. Fiz **93**, 680 (1987).

[64] S. M. Stishov, J. Exp. Theor. Phys. Lett. **71**, 15 (2000).

[65] A. F. Goncharov, Usp. Fiz. Nauk **30**, 525 (1987).

[66] U. Rössler, D. Strauch, and M. Schulz, *Group IV elements, IV-IV and III-V compounds (Part a): Lattice propertiesp* (Springer-Verlag, 2001).

[67] J. A. Rayne and B. S. Chandrasekhar, Phys. Rev. **120**, 1658 (1960).

[68] L. V. Al'Tshuler, A. A. Bakanova, and R. F. Trunin, J. Exp. Theor. Phys. **15**, 65 (1962).

[69] R. Tarumi, H. Ledbetter, H. Ogi, and M. Hirao, Philos. Mag. **93**, 4532 (2013).

[70] K. Koepernik and H. Eschrig, Phys. Rev. B **59**, 1743 (1999).

[71] H. Eschrig, M. Richter, and I. Opahle, "Relativistic solid state calculations," in *Relativistic electronic structure theory (Part 2): Applications*, Vol. 14, edited by P. Schwerdtfeger (Elsevier, 2004) pp. 723–776.

[72] H. Ebert *et al.*, *The Munich SPR-KKR program package (Version 6.3): A spin polarized relativistic Korringa-Kohn-Rostoker (SPR-KKR) code for calculating solid state properties* (Universität München, 2018).

[73] H. Ebert, D. Ködderitzsch, and J. Minár, Rep. Prog. Phys. **74**, 096501 (2011).

[74] H. Ebert, "Fully relativistic band structure calculations for magnetic solids: Formalism and application," in *Electronic structure and physical properties of solids* (Springer-Verlag, 2000) pp. 191–246.

[75] A. Hermann, J. Furthmüller, H. W. Gäggeler, and P. Schwerdtfeger, Phys. Rev. B **82**, 155116 (2010).

[76] F. Legrain and S. Manzhos, AIP Adv. **6**, 045116 (2016).

[77] P. Pavone and S. Baroni, Sol. St. Comm. **90**, 295 (1994).

[78] H. London, Zeitsch. Phys. Chem. **16**, 302 (1958).

[79] H. Holloway, K. C. Hass, M. A. Tamor, T. R. Anthony, and W. F. Banholzer, Phys. Rev. B **44**, 7123 (1991).

[80] H. Holloway, K. C. Hass, M. A. Tamor, T. R. Anthony, and W. F. Banholzer, Phys. Rev. B **45**, 6353 (1992).

[81] H.-C. Wille, Y. V. Shvyd'ko, E. Gerdau, M. Lerche, M. Lucht, H. D. Rüter, and J. Zegenhagen, Phys. Rev. Lett. **89**, 285901 (2002).

[82] M. Y. Hu, H. Sinn, A. Alatas, W. Sturhahn, E. E. Alp, H. C. Wille, Y. V. Shvyd'ko, J. P. Sutter, J. Bandaru, E. E. Haller, V. I. Ozhogin, S. Rodriguez, R. Colella, E. Kartheuser, and M. A. Villeret, Phys. Rev. B **67**, 113306 (2003).

[83] C. P. Herrero, J. Phys.: Cond. Mat. **13**, 5127 (2001).

[84] C. Herrero, Sol. St. Comm. **110**, 243 (1999).

[85] J. C. Noya, C. P. Herrero, and R. Ramírez, Phys. Rev. B **56**, 237 (1997).

[86] C. P. Herrero, R. Ramírez, and M. Cardona, Phys. Rev. B **79**, 012301 (2009).

[87] A. D. Ludlow, M. M. Boyd, J. Ye, E. Peik, and P. O. Schmidt, Rev. Mod. Phys. **87**, 637 (2015).

[88] J. M. Robinson, E. Oelker, W. R. Milner, W. Zhang, T. Legero, D. G. Matei, F. Riehle, U. Sterr, and J. Ye, Optica **6**, 240 (2019).

[89] W. Zhang, J. M. Robinson, L. Sonderhouse, E. Oelker, C. Benko, J. L. Hall, T. Legero, D. G. Matei, F. Riehle, U. Sterr, and J. Ye, Phys. Rev. Lett. **119**, 243601 (2017).

[90] D. G. Matei, T. Legero, S. Häfner, C. Grebing, R. Weyrich, W. Zhang, L. Sonderhouse, J. M. Robinson, J. Ye, F. Riehle, and U. Sterr, Phys. Rev. Lett. **118**, 263202 (2017).

[91] E. Oelker, R. B. Hutson, C. J. Kennedy, L. Sonderhouse, T. Bothwell, A. Goban, D. Kedar, C. Sanner, J. M. Robinson, G. E. Marti, *et al.*, arXiv:1902.02741 (2019).

[92] J. Aasi, B. P. Abbott, R. Abbott, T. Abbott, M. R. Abernathy, K. Ackley, C. Adams, T. Adams, P. Addesso, R. X. Adhikari, *et al.*, Class. Quant. Grav. **32**, 074001 (2015).

Chapter 10

Conclusion and Outlook

The present work focuses on theoretical aspects of testing fundamental symmetries of the SM and searching for new phenomena beyond the SM using diatomic molecules. Although the SM provides a successful description of existing data to a remarkably high precision at the electroweak energy scale, it is considered as an incomplete theory, due to the fact that it cannot answer many open questions. In order to answer such questions, many new physics models that extend the SM have been proposed. Compared with the SM, some new physics models beyond the SM are characterized by more significant symmetry-breaking effects, such as a larger electron electric dipole moment (eEDM), etc. In other cases, the new physics models, such as quantum gravity, etc., which attempt to unify gravity with the remaining fundamental interactions are characterized by novel physical phenomena such as the variation of fundamental constants. In this work, we have demonstrated that diatomic molecules have a very promising application to the tests of fundamental symmetries of the SM and to the searches for new phenomena beyond the SM. To be more specific, the measurements of the symmetry-breaking effects, such as the ones arising from the nuclear anapole moment and the electron electric dipole moment, can be used to test fundamental symmetries of the SM. The searches for the new physical phenomena, such as the variation of fundamental constants, can put constraints on new physics models that extend the SM and can also provide new insights into the construction of new physics theories that attempt to unify gravity with the remaining fundamental interactions.

In order to extract the magnitude of nuclear anapole moment effect from measurements, a $\hat{\mathcal{P}}$-odd interaction parameter W_A, which depends on molecular structure, needs to be calculated with high accuracy. The accuracy of the calculations is demonstrated with application to the selected diatomic molecules such as

BaF, BeCl, etc. In this work, the interplay of various computational parameters has been explored. We find that, compared with other factors, electron correlation plays a dominant role in accurately determining W_A, because inclusion of electron correlation raises the calculated W_A value by about 20%. For this reason, we focus our attention on the performance of various electron correlation methods that have been widely employed, including DFT, MP2, CCSD, CCSD(T), FSCC, etc. Among such methods, the coupled cluster method is considered as a powerful tool for the treatment of electron correlation and thus is suitable for calculating W_A with high accuracy. Since the difference between the CCSD and CCSD(T) values is very small, we conclude that triple excitations are not important in determining W_A. We have also investigated the scaling behavior of the W_A parameter for the alkaline-earth-metal fluorides, and found it to be close to the expected Z^2 behavior. In addition to examining various correlation methods, we also analyze the effects from the truncation of the occupied and virtual orbitals on the calculated W_A parameter. We find that the inner orbitals are very important for determining W_A and thus all the electrons should be included into correlation scheme. In order to extract the final values of the nuclear anapole moment effect from experiments, the measured quantities need to be combined with the calculated W_A parameters, where the total uncertainty needs to be included by summing the experimental and theoretical uncertainties in quadrature. For the calculated W_A parameter of BaF, we have devised a new scheme that allows us to set uncertainties on the calculated W_A values. The small uncertainties of $\sim 2\%$ will help us to put strong constraints on the measured effects. Finally, we have also pointed out that different factors contribute differently to the uncertainty for different molecules. For light molecules, the theoretical uncertainty might be dominated by the basis set effects while for molecules containing heavy elements, the leading contribution to the theoretical uncertainty may come from the correlation and relativistic effects.

In the search for the eEDM, one of the paths to a successful measurement requires the molecules under study to be effectively laser-cooled so that longer coherent interaction time could be achieved, resulting in an increase in the measurement sensitivity. In order to develop laser systems more efficiently, highly accurate theoretical calculations of the molecular spectroscopic constants are necessary. In order to determine the spectroscopic constants accurately, the potential energy curves (PECs) of diatomic molecules need to be calculated using a sufficiently accurate method. We demonstrate that the X2C Hamiltonian can decrease the computational effort considerably without losing too much accuracy. We show that our calculated spectroscopic constants are in excellent agreement with available experimental values. This indicates that our calculation has sufficient predictive accuracy to propose a scheme for laser cooling. In practice, a good candidate for laser-cooling should satisfy a number of requirements such as

strong one-photon transitions, highly-diagonal Franck-Condon factors, absence of intervening electronic states (or suppressed transition leaks), etc. We examine different possible schemes for laser-cooling and identify the ones that satisfy these requirements. An important difference in the electronic structure of the three molecules (CaF, SrF, and BaF) is in the location of the $A'^2\Delta$ states. For CaF and SrF, these states are higher in energy than the $A^2\Pi$ states, and even higher than the $B^2\Sigma^+$ states. However, for BaF, the $A'^2\Delta$ states are lower in energy than the $A'^2\Delta$ states and thus transitions to the $A'^2\Delta_{3/2}$ state could constitute a leak in the cooling cycle. We conclude that although the $B^2\Sigma^+_{1/2} - X^2\Sigma^+_{1/2}$ cooling transition was shown to be extremely efficient for CaF, laser-cooling on this transition is impractical for BaF, due to the non-diagonal nature of the FCFs for this transition. The location of the $A'^2\Delta$ states in BaF gives rise to leaks and restricts the number of scattered photons for the $A^2\Pi_{1/2} - X^2\Sigma^+_{1/2}$ cooling transition, making it unsuitable for longitudinal cooling. However, based on our estimate, this cooling transition in BaF can scatter sufficient number of photons for transverse laser-cooling, if two repump lasers are added to higher vibrational levels to compensate for the leaks.

New physics models that attempt to unify gravity with the remaining fundamental interactions are usually featured with new phenomena, such as the variation of fundamental constants. As a new alternative method to the analysis of atomic clocks and quasar spectra, precision laser interferometry may provide competitive sensitivity to the variation of fundamental constants through the comparison of the phase differences between two light beams. The variation of fundamental constants could influence the crystal lattice parameters in a solid. Therefore, it could change the size of the solid-state materials employed in the optical cavity of a laser interferometer and lead to a shift in the phase between two light beams. Ideally, the dependence of the crystal lattice parameters on fundamental constants in a solid needs to be examined by highly accurate computational methods, such as the coupled cluster method, etc. Such studies can help to identify promising candidate materials which lead to great discovery potential. However, comprehensive and systematic calculations on solid-state materials using the coupled cluster method are not computationally affordable or tractable. Instead, the DFT method has been widely used to predict the solid-state properties, but the accuracy of the DFT results should be assessed. In principle, the exact lattice parameters in a solid depend on the specific crystal structure and on the actual thermal environment. Nonetheless, if we assume that the distance between two nearest atoms (lattice points) in a solid can be approximated by the equilibrium bond distance in a diatomic molecule formed by these two atoms, the coupled cluster calculations of the equilibrium bond distances for diatomic molecules can be used to benchmark the performance of the DFT calculations of the lattice parameters for solid-state materials. Our calculations show that

the material sizes can be well modeled by the equilibrium bond distances of diatomic molecules and the DFT calculations can provide the expected accuracy in predicting the dependence of the material sizes on the variation of fundamental constants. We also provide the accurate values for the dependence of lattice constants on α and μ in a variety of solid-state materials, such as Cu, Si, Al, Nb, Al_2O_3, etc. The choice of these solid-sate materials is motivated by the highly precise experimental setups aiming to search for new physics beyond the SM [1]. Finally, we present the possible experimental setups for the detection of the variation of fundamental constants and reveal the corresponding discovery potential.

In the measurements of symmetry-breaking effects, the improvement in the measurement sensitivity cannot be accomplished without high-accurate determination of the needed parameters. For example, in the measurement of the nuclear anapole moment effect, the measured quantities have to be combined with theoretical values, where the total uncertainty needs to be included by combining the experimental and theoretical uncertainties together. In order to extract the effective coupling constant κ_A precisely from the measured signals, the W_A parameter needs to be known with high accuracy. From a theoretical point of view, significant improvement in the accuracy of the calculated parameters can be achieved in a number of ways. First of all, the development of various electron correlation methods that can handle correlation effects more accurately and more efficiently could be an active research area in the future. Our calculated excitation energies T_e are generally higher than the experimental values for the selected alkaline-earth-metal fluorides, although the relative discrepancy is very small (only a few percent). This might be due to the fact that the triple and higher-order excitations have not been implemented into the CC equations in an iterative way in the present version of the DIRAC program. As a matter of fact, the triple excitations have been only added into the calculations perturbatively based on the CCSD amplitudes. The lack of iterative triple and higher-order excitations may also help to explain the fact that although our calculated results show a good agreement with the experimental data for all the electronic states, the agreement is slightly worse in such results for the excited states, comparing with the ground state. Therefore, implementation of triple or higher-order excitations into the CC equations in an iterative way could be the subject of intensive research. Remarkably, there is a large discrepancy between the calculated and measured lifetimes for the molecules under discussion. This might be due to the fact that the calculated transition dipole moments (TDMs) for the allowed transitions are generally too large to account for the experimental values, while the calculated TDMs for the forbidden transitions are too small. Since the calculations of TDMs involve the transition moment integral between different electronic states, electronic structure methods which are capable of calculating

multiple electronic states simultaneously are preferable. In the present version of the DIRAC program, the FSCCSD and CISD methods are two tractable frameworks for the calculation of TDMs. Since, currently, the implementation of TDMs with the FSCC method is not available, the calculations of TDMs in the present work are carried out using the CISD method. However, the CISD method faces numerous problems such as the lack of size-consistency and size-extensivity. Furthermore, in the CISD method, all the electron correlation effects beyond double excitations are excluded. In order to overcome such deficiencies, new implementations of the TDM using the state-of-the-art correlation methods, such as the FSCCSD method, are needed. In this improvement effort, the computation of the TDM can be accomplished by two steps. In the first step, the perturbed wavefunctions can be obtained by adding the TDM term as a perturbation to the coupled cluster equations. Then, the TDM can be evaluated by taking the transition moment integral between two perturbed wavefunctions. Besides the above directions, inclusion of high order relativistic corrections and construction of high quality basis sets may also help to significantly improve the accuracy of the calculated parameters.

Recent advances in precision measurements and availability of highly accurate computational methods have provided a unique window for the tests of the SM and for new physics searches using molecular properties. Identification of promising molecular candidates that allow precision measurements of the $\hat{\mathcal{P}}$ or $\hat{\mathcal{T}}$ violating interactions with sufficiently high sensitivity could be another subject of future work. It has been demonstrated that triatomic molecules (or polyatomic molecules) have significant additional advantages in the precision measurement of the $\hat{\mathcal{P}}$ or $\hat{\mathcal{T}}$ violating effects [2, 3]. This is mainly due to the fact that triatomic molecules have opposite-parity molecular levels with their energies a few orders of magnitude closer than the ones for diatomic molecules, making them easier to be brought into degeneracy by smaller magnetic fields. Smaller magnetic fields allow the elimination of the inhomogeneities more easily upon the reversal of the fields and thus can help to decrease the systematic uncertainties and increase the measurement sensitivities. Furthermore, the existence of internal comagnetometer states in triatomic molecules, such as YbOH, etc., enables the measurement of the eEDM without reversing the external fields and allows us to control systematic errors more easily [2]. In addition, because of the favorable electronic structure, such molecules can achieve full polarization in smaller electric fields, where the measurement sensitivity can be improved. Finally, the use of triatomic molecules, such as BeNC, MgNC, etc. [3], might help to distinguish the nuclear anapole moment effect from the remaining NSD-PV effects by measuring the effects on different nuclei. Due to these considerations, extending the applications to triatomic molecules might be a promising direction of future work.

Besides triatomic molecules, molecules containing light elements, such as

BeCl, BeI, etc., are also considered as promising candidates for the measurement of the nuclear anapole moment effect. The nuclear anapole moment effect can be used to test nuclear theories by a direct comparison between the experimental and theoretical values of the effective coupling constant κ_A. Any deviation may suggest the incompleteness of our knowledge about nuclear models or even imply hints for new physics beyond the SM. However, no meaningful comparison can be made unless κ_A is precisely determined from experiments and accurately calculated from theories. The practical advantage of using such molecules is that nuclear calculations for light elements are more computationally tractable. In this case, the effective coupling constant κ_A can be more accurately calculated from nuclear theories and thus a more meaningful comparison can be made. Furthermore, molecules containing heavy elements, such as RaF [4], etc., are also considered as good candidates for the measurement of the nuclear anapole moment effect. This is due to the fact that the nuclear anapole moment effect tends to increase dramatically with the nuclear mass number and a larger effect allows easier detection and easier separation from the remaining NSD-PV effects. In addition, the searches for exotic phenomena with molecules cover a wide range of research topics, such as the test of the $\hat{\mathcal{C}}\hat{\mathcal{P}}\hat{\mathcal{T}}$ and Lorentz invariance, and would become very active in the future. Last but not least, in precision measurements like the search for the eEDM, some important hyperfine structure parameters need to be known to a very high degree of precision. Among such parameters, the nuclear electric quadrupole moment (NQM) is related to a term in the multipole expansion of nuclear charge distribution and plays an important role in nuclear structure research. A non-zero NQM indicates that the charge distribution of a nucleus is not spherically symmetric. With the help of the theoretically determined electric field gradients (EFG) from molecular calculations, the NQM can be extracted from the experimentally determined nuclear quadrupole coupling constants through the analysis of rotational spectra [5]. Another important parameter is the magnetic hyperfine structure constant, which plays a significant role in precision measurements and in benchmark assessment of the accuracy of *ab initio* calculations. Theoretical investigations of such hyperfine structure parameters with high accuracy could possibly be the fruitful directions for future work.

Search for new physics beyond the SM with diatomic molecules is an exciting field and has attracted enormous attention recently [6]. In the present work, we show that theoretical investigations of molecular properties play a crucial role in the successful measurements of symmetry-breaking effects and in the searches for new physical phenomena. To begin with, the theoretically determined molecular properties can help to design an experimental setup for precision measurements with enhanced sensitivity. For example, highly accurate calculations of molecular properties can help to develop laser systems more efficiently in the measurement

of the eEDM so that the molecules can be effectively laser-cooled throughout the measurements. In this case, longer interaction time can be achieved and improved sensitivity can be gained. Furthermore, highly accurate calculations of molecular properties can be used to interpret the results of the precision measurements more correctly. For example, in the measurement of the nuclear anapole moment effect, a $\hat{\mathcal{P}}$-odd interaction parameter W_A, which depends on molecular structure, needs to be calculated with high accuracy in order to extract the final values of the effective coupling constant from the measured signals. In this case, the total uncertainty is contributed by both the experimental part and the theoretical part. The evaluation of theoretical uncertainty can help us to make a valid comparison between theories and experiments so that reliable conclusions can be obtained. Thirdly, the advanced computational methods enable careful examinations of electronic structure and can help to understand the possible mechanisms for the influence of new physics interactions on molecular properties. In this case, based on highly accurate calculations, comprehensive strategies for new physics searches can be designed and promising candidates with enhanced sensitivity can be identified. Last but not least, in the search for the variation of fundamental constants, the calculations of molecular properties can be used to find new measurement strategies and identify promising candidate materials. To conclude, theoretical efforts with diatomic molecules would have great potential to provide new insights on the problems that cannot be answered by the SM and thus open a window to new physics beyond the SM.

References

[1] L. F. Pašteka, Y. Hao, A. Borschevsky, V. V. Flambaum, and P. Schwerdtfeger, Phys. Rev. Lett. **122**, 160801 (2019).

[2] I. Kozyryev and N. R. Hutzler, Phys. Rev. Lett. **119**, 133002 (2017).

[3] E. B. Norrgard, D. S. Barker, S. Eckel, J. A. Fedchak, N. N. Klimov, and J. Scherschligt, Commun. Phys. **2**, 77 (2019).

[4] T. A. Isaev, S. Hoekstra, and R. Berger, Phys. Rev. A **82**, 052521 (2010).

[5] R. L. A. Haiduke, Chem. Phys. Lett. **544**, 13 (2012).

[6] M. S. Safronova, D. Budker, D. DeMille, D. F. J. Kimball, A. Derevianko, and C. W. Clark, Rev. Mod. Phys. **90**, 025008 (2018).

Appendix A: Dunham expansion

The vibrational-rotational levels of a diatomic molecule can be expressed by the Dunham expansion [1–6],

$$E(v,J) \equiv \sum_{\alpha,\beta\in\mathbb{Z}} Y_{\alpha\beta}\Big(v+\frac{1}{2}\Big)^{\alpha}\Big[J(J+1)\Big]^{\beta}, \quad Y_{\alpha\beta}\in\mathbb{R}, \tag{X.1}$$

where $Y_{\alpha\beta}$ represents the Dunham coefficients, which depend on molecular structure. The parameter v is the vibrational quantum number and the parameter J is the rotational quantum number. In practice, the following Dunham expansion has been widely used to model the potential energy curves [1–3, 7–12],

$$E(R) = T_e + a_0\Big(\frac{R-R_e}{R_e}\Big)^2\Big[1+\sum_{k=1}^{\infty} a_k\Big(\frac{R-R_e}{R_e}\Big)^k\Big], \tag{X.2}$$

where $E(R)$ represents the potential energy as a function of the internuclear distance R. R_e represents the equilibrium internuclear distance (bond length). T_e represents the potential energy at R_e. The parameters a_k ($a_k \in \mathbb{R}$) are the expansion coefficients.

One the one hand, the Dunham coefficients $Y_{\alpha\beta}$ are related to the conventional spectroscopic constants [1, 3–6]. On the other hand, by ignoring higher order corrections, the spectroscopic constants can be calculated from the expansion

coefficients according to the following expressions [1, 3, 4, 12, 13]:

$$B_e \simeq Y_{01} \simeq \frac{h}{8\pi^2 \mu c R_e^2}, \tag{X.3}$$

$$\omega_e \simeq Y_{10} \simeq 2\Big(a_0 B_e\Big)^{\frac{1}{2}}, \tag{X.4}$$

$$\omega_e \chi_e \simeq -Y_{20} \simeq \frac{3B_e}{2}\Big(\frac{5a_1^2}{4} - a_2\Big), \tag{X.5}$$

$$\alpha_e \simeq -Y_{11} \simeq -\frac{6B_e^2}{\omega_e}\Big(1 + a_1\Big), \tag{X.6}$$

$$D_e \simeq -Y_{02} \simeq \frac{4B_e^3}{\omega_e^2}. \tag{X.7}$$

Here, μ is the reduced mass of the molecule. B_e represents the rotational constant. ω_e and $\omega_e \chi_e$ represent the harmonic and anharmonic frequencies, respectively. α_e represents the vibration-rotation coupling constant. D_e is the centrifugal distortion constant.

References

[1] J. L. Dunham, Phys. Rev. **41**, 721 (1932).

[2] I. Sandeman, Proc. Roy. Soc. (Edinburgh) **60**, 210 (1940).

[3] H. M. Hulburt and J. O. Hirschfelder, J. Chem. Phys. **9**, 61 (1941).

[4] G. Herzberg, *Molecular spectra and molecular structure*, Vol. 1 (Read Books Ltd., 1950).

[5] J. M. Brown, J. M. Brown, and A. Carrington, *Rotational spectroscopy of diatomic molecules* (Cambridge University Press, 2003).

[6] W. Demtröder, *Atoms, molecules and photons* (Springer, 2010).

[7] G. Simons, R. G. Parr, and J. M. Finlan, J. Chem. Phys. **59**, 3229 (1973).

[8] H. Lefebvre-Brion and R. W. Field, *The spectra and dynamics of diatomic molecules* (Elsevier, 2004).

[9] O. K. Voitsekhovskaya, D. E. Kashirskii, and V. S. Korchikov, Mos. Uni. Phys. Bullet. **65**, 386 (2010).

[10] S. N. Yurchenko, L. Lodi, J. Tennyson, and A. V. Stolyarov, Comp. Phys. Comm. **202**, 262 (2016).

[11] J. F. Ogilvie, arXiv:1905.01761 (2019).

[12] F. G. Pashaev, A. I. Ahmadov, A. G. Gasanov, D. B. Bairamova, S. G. Rahimzade, and U. T. Agayeva, Russ. Phys. J. **62**, 747 (2019).

[13] P. F. Bernath, *Spectra of atoms and molecules* (Oxford University Press, 2005).

Appendix B: Units

Throughout the present work, different systems of units are involved. In Section 2.2, all the equations are expressed in the natural units ($\hbar \equiv 1$, $c \equiv 1$). In the field of parity-violating effects, all the equations are expressed in the atomic units ($\hbar \equiv 1$, $m_e \equiv 1$, $e \equiv 1$, etc.) or equivalently in the natural units [a]. Except for the above-mentioned equations, all other equations, mainly associated with the electromagnetic interactions and the electronic structure, are expressed in the system of Gaussian units. Since in the computational packages all the equations are implemented in the system of atomic units, the calculated molecular properties are expressed in atomic units.

[a] This is because, except for $\hbar$, the constants m_e and e are not involved in such equations.

Acknowledgement

During my PhD study, lots of people provided help and support. First of all, I would like to thank my supervisors Dr. Anastasia Borschevsky and Prof. Rob G. E. Timmermans for their help and support. Then, I would like to thank all the people in the NL-eEDM collaboration: Parul Aggarwal, Dr. Hendrick L. Bethlem, Alexander Boeschoten, Dr. Malika Denis, Kevin Esajas, Pi A. B. Haase, Prof. Steven Hoekstra, Prof. Klaus Jungmann, Virginia R. Marshall, Thomas B. Meijknecht, Maarten C. Mooij, Anno Touwen, Prof. Wim Ubachs, Prof. Lorenz Willmann, Dr. Yanning Yin, and Dr. Artem Zapara. I also would like to thank all our collaborators: Prof. Julian Berengut, Prof. Ephraim Eliav, Prof. Victor V. Flambaum, Eugene Gvozdetsky, Emily Kahl, Dr. Miroslav Iliaš, Dr. Lukáš F. Pašteka, Prof. Peter Schwerdtfeger, and Prof. Lucas Visscher. In addition, I would like to thank the secretaries in VSI, Ms. Annelien Blanksma, Ms. Iris de Roo-Kwant, and Ms. Hilde van der Meer for their help during my PhD study. After that, I would like to thank all the PhD students in VSI. Especially, I would like to thank Femke Oosterhof, Martijn Reitsma, and Ruud Peeters for their help on the Dutch summary. Finally, I would like to thank my family for their understanding and support.

Publications

The present PhD thesis is based on the following publications:

1. **Yongliang Hao**, Miroslav Iliaš, and Anastasia Borschevsky, Correlation trends in the nuclear anapole moment interaction of the Be atom in BeCl, Proceeding of Science, International Conference on Precision Physics and Fundamental Physical Constants, **FFK2019**, 057 (2019). For this paper, I performed the calculations, analyzed the results, and prepared the manuscript.

2. **Yongliang Hao**, Lukáš F. Pašteka, Lucas Visscher, Parul Aggarwal, Hendrick L. Bethlem, Alexander Boeschoten, Anastasia Borschevsky, Malika Denis, Kevin Esajas, Steven Hoekstra, Klaus Jungmann, Virginia R. Marshall, Thomas B. Meijknecht, Maarten C. Mooij, Rob G. E. Timmermans, Anno Touwen, Wim Ubachs, Lorenz Willmann, Yanning Yin, Artem Zapara, High accuracy theoretical investigations of CaF, SrF, and BaF and implications for laser-cooling, J. Chem. Phys. **151**, 034302 (2019). For this paper, I performed the calculations, analyzed the results, and prepared the manuscript.

3. Lukáš F. Pašteka, **Yongliang Hao**, Anastasia Borschevsky, Victor V. Flambaum, and Peter Schwerdtfeger, Material Size Dependence on Fundamental Constants, Phys. Rev. Lett. **122**, 160801 (2019). For this paper, I performed the calculations for diatomic molecules, analyzed the results for diatomic molecules, and prepared the molecular part of the manuscript.

4. **Yongliang Hao**, Miroslav Iliaš, Ephraim Eliav, Peter Schwerdtfeger, Victor V. Flambaum, and Anastasia Borschevsky, Nuclear anapole moment interaction in BaF from relativistic coupled-cluster theory, Phys. Rev. A **98**, 032510 (2018). For this paper, I performed the calculations, analyzed the results, and prepared the manuscript.

Samenvatting

Samengevat richt dit proefschrift zich op het theoretisch onderzoek voor het testen van de fundamentele symmetrieën van het Standaardmodel (SM) met behulp van diatomaire moleculen. In Hoofdstuk 1 geven we de achtergrond en motivatie voor dit onderzoek. Hoewel het SM erg succesvol is in het beschrijven van de fundamentele deeltjes en hun interacties, zijn er veel openstaande vragen die dit model niet kan beantwoorden en daarom wordt het als een onvolledige theorie beschouwd. Theoretisch onderzoek met moleculen heeft grote potentie om nieuwe inzichten te bieden in de vragen die het SM niet kan beantwoorden, wat een deur opent naar nieuwe natuurkunde voorbij het SM. In Hoofdstuk 2 bespreken we in het kort enkele belangrijke concepten van het SM en de relevante aspecten van fundamentele symmetrieën daarin. Vervolgens introduceren we de aard van symmetrie-brekende effecten die kunnen worden gebruikt om het SM te testen en om nieuwe natuurkunde voorbij het SM te vinden. In Hoofdstuk 3 bespreken we de computationele methoden die voor de berekening van moleculaire eigenschappen worden gebruikt. We geven een overzicht van de factoren die de nauwkeurigheid van het theoretische onderzoek bepalen, en demonstreren de bepaling van de theoretische onzekerheid. In Hoofdstuk 4 introduceren we een aantal moleculaire symbolen die voor dit werk relevant zijn en behandelen we de algemene vorm van de moleculaire Hamiltoniaan, die de basis vormt voor de rest van dit onderzoek. In Hoofdstuk 5 vatten we de belangrijkste onderwerpen van het huidige werk samen, waaronder het meten van het nucleaire anapoolmoment en het elektron-elektrisch dipoolmoment (eEDM) en het zoeken naar variatie van fundamentele constanten. We benadrukken dat het belangrijkste doel van dit onderzoek is om de benodigde moleculaire parameters te bepalen voor succesvolle metingen van verschillende constanten en voor rigoureuze interpretaties van de metingen, met behulp van toonaangevende computationele methoden. In Hoofdstuk 6 presenteren we relativistische coupled-cluster-berekeningen van hoge nauwkeurigheid van de $\hat{\mathcal{P}}$-oneven W_A-parameter voor het BaF molecuul. De invloed van verschillende rekenparameters op de berekende W_A-parameter wordt geanalyseerd. In dit hoofdstuk wordt ook de

berekening van de onzekerheid uitgevoerd. In Hoofdstuk 7 bespreken we de details van de correlatietrends van de nucleaire anapoolmomentwisselwerking voor het BeCl-molecuul. We benadrukken het belang van elektronencorrelatie bij de bepaling van de W_A-parameter door de berekende resultaten met een verschillende behandeling van elektronencorrelatie te vergelijken. In Hoofdstuk 8 presenteren we zeer nauwkeurig theoretisch onderzoek naar de spectroscopische constanten voor bepaalde aardalkalimetaalfluoriden en bespreken we hun toepassing op laserkoeling. We laten zien dat bij het zoeken naar het eEDM met een langzame bundel van koude BaF-moleculen kennis van de moleculaire eigenschappen van BaF nodig is om de metingen te plannen, en in het bijzonder om de optimale laserkoelingsschema's te bepalen. In Hoofdstuk 9 richten we ons op theoretisch onderzoek naar de variatie van fundamentele constanten door te onderzoeken hoe kristalparameters in vaste stoffen en de evenwichtsbindingsafstand in diatomaire moleculen variëren aan de hand van fundamentele constanten (α en μ). Als we aannemen dat de afstand tussen twee dichtstbijzijnde atomen (roosterpunten) in een vaste stof kan worden benaderd door de evenwichtsbindingsafstand in een door deze twee atomen gevormd diatomair molecuul, dan kunnen de coupled cluster-berekeningen van de evenwichtsbindingsafstanden voor diatomaire moleculen worden gebruikt om de kwaliteit van de DFT-berekeningen van de roosterparameters voor vaste stoffen te beoordelen. Ten slotte presenteren we in Hoofdstuk 10 de conclusie van dit onderzoek en geven we perspectieven voor toekomstig werk.